Active Patch Array Design and Indoor Channel Modeling for Future Wireless Communications

Thesis by

Dai Lu

In Partial Fulfillment of the Requirements

For the Degree of

Doctor of Philosophy

California Institute of Technology

Pasadena, California

2004

(Defended May 17, 2004)

Acknowledgements

First, I want to thank my advisor, Professor David Rutledge, for giving me this opportunity to pursue the PhD at Caltech, and to be a member of his research group. Without his valuable advice and guidance, without the many intuitive discussions with him during weekly group meeting, and without the excellent research environment he created in the RF and microwave group, this thesis would not have been possible. His keen insight, nice personality, unlimited patience and support made the work under his supervision a really enlightening and pleasant experience. I would also like to thank the Lee Center for Advanced Networking for the financial support of my research at Caltech.

I would like to acknowledge those people who have given me lots of support and assistance at Caltech. I am grateful for the help of Kent Potter. Without his excellent mechanic work, our compact anechoic chamber would not have been made. Also, I cannot finish my indoor wireless channel measurement without his help on the automatic testing robot. Besides, I would like to thank Lawrence Cheung. He is really a sincere and kind person. He deserves much credit for his valuable assistance and help during the early stage of this work. Also I really enjoy the discussions with him about our current research. I want to thank Sander Weinreb for his valuable advice during the group seminars. In addition, John Davis, Blythe Deckman, Taavi Hirvonen, Ichiro Aoki, Scott Kee, Matt Morgan deserve thanks for their great help in showing me how to work in the lab. I also want to thank Dale Yee for her wonderful work on helping me solve software problems in my machine. Finally, I would like to give my great appreciation to my

friends in the group including Milan Kovacevich, Takahiro Taniguchi, Feiyu Wang, Sanggeun Jeon, Edwin Soedarmadji, Yulung Tang, Glenn Jones, Paul Laufer, Guangxi Wang, and Niklas Wadefalk. Also, I want to thank Carol Sosnowski and Heather Hein for their valuable help on my conference schedule and registration. Last but not least, heartfelt thanks go to my good friends at Caltech who have given me lots of supports in the past: Jun Xie, Zhigang Han, Weiqiao Deng, Hossein Hashemi, Donhee Ham, Chris Write, Hui Wu, Yindi Jing, Andrew Jiang, Qingsong Zhang, Jiao Lin, Ying Tang, Fu Liu.

Finally, I want to express my gratitude to my family. The encouragement and patience of my wife, Dizhou, has been a great source of strength for me. You always have the right words and thoughts to keep me focused on my work. My mother Minna Li and my father Hezhi Lu, have always been my great support for both my life and work. Thank you for all your love, understanding, and support during this endeavor.

I would like to express my warmest regards and best wishes to all those above for the future.

Abstract

Indoor wireless LAN systems currently operate at ranges of up to 30 meters, with practical data rates of 10 Mbps. In order to achieve higher data rates, higher frequencies are under consideration. Smaller antennas are required at these frequencies, but path loss increases. To combat the large path loss and multipath, 24 GHz phased arrays are being considered. The advantage of a phased array is that it can form narrow beams to favored directions, and nulls to combat interference. A 24 GHz active antenna with a 5-element patch array is demonstrated that includes an integrated GaAs MMIC power amplifier and low noise amplifier chip. Bias switching is used for changing from transmit to receive. The measured active gain is 31 dB in receive and 35 dB in transmit. The measured noise figure in receive is 3.5 dB and the maximum output power in transmit is 22 dBm (158 mW). Indoor wireless channels are investigated at five different frequency bands. The understanding of the channel will help link budgeting and system planning for future wireless communication. An automatic testing system has been developed using remote control by LABVIEW. This increases testing efficiency and reduces near field interference from the operator. A combined E/H plane 2-D ray-tracing method is proposed to predict the channel performance. This approach accurately predicts path loss for both line-of-sight and non-line-of-sight paths. It predicts the delay spread in line-of-sight paths well but fails for non-line-of-sight paths. This could be due to the ignorance of some higher order paths with small amplitudes but near random phases. In addition, a 3-D simplified ray-tracing code is developed to for access point optimization and to predict human shadow effects.

Contents

List of Figures

Chapter 1: Introduction

Chapter 2: A 24 GHz Patch Array with A Power/Low Noise Amplifier MMIC

Chapter 3: Concepts of Indoor Channel Modeling for Future Wireless Communications

Chapter 4: Empirical Explorations of Indoor Wireless Channels

Chapter 6: Access Point Optimization and Study of Human Body Effects at 2.4 and 24GHz

Appendix A: Design of a Compact Anechoic Chamber System

Appendix B: Automatic Indoor Measurement

Appendix C: Ray Tracing Programming by MATLAB

List of Tables

Chapter 1: Introduction

Chapter 2: A 24 GHz Patch Array with A Power/Low Noise Amplifier MMIC

Chapter 3: Concepts of Indoor Channel Modeling for Future Wireless Communications

Chapter 4: Empirical Explorations of Indoor Wireless Channels

Chapter 1

Introduction

Wireless has now become an important part of people's life. Wi-Fi, or Wireless Fidelity, is freedom that allows you to connect to the Internet from your couch at home, a bed in a hotel room or a conference room at work without wires. Wi-Fi is a wireless technology like a cell phone. Wi-Fi enabled computers send and receive data indoors and out; anywhere within the range of a base station.

The original version of Wi-Fi, also known as 802.11b (2.4 GHz), transmits data at 11 megabits per second, though, as is true for all forms of wireless, your actual speed is likely to be about half of the posted rate. A newer version, 802.11g, runs at up to 54 Mbps and works interchangeably with 802.11b gear. Buying "g" instead of "b" has no real downside now that early compatibility bugs seem to have been worked out, though the equipment tends to be bit more expensive. Another variant, 802.11a (5 GHz), also runs at 54 Mbps but operates at a different radio frequency, so it's not compatible with "b" or "g." The higher frequency is immune to interference from microwave ovens and cordless phones, but provides shorter range. Companies are pushing the available standard product even further recently. US. Robotics, a company headquartered in Chicago has just announced its boosted 802.11g product with speed of 125 Mbps by packet aggregation in March 2004. Motia, a California company also demonstrated its smart antenna technology called Javelin to enhance WiFi (802.11b and g) by extending 2-

3 times of its operating range. At the same time, people are working in-group on other wireless standard (Figure 1.1).

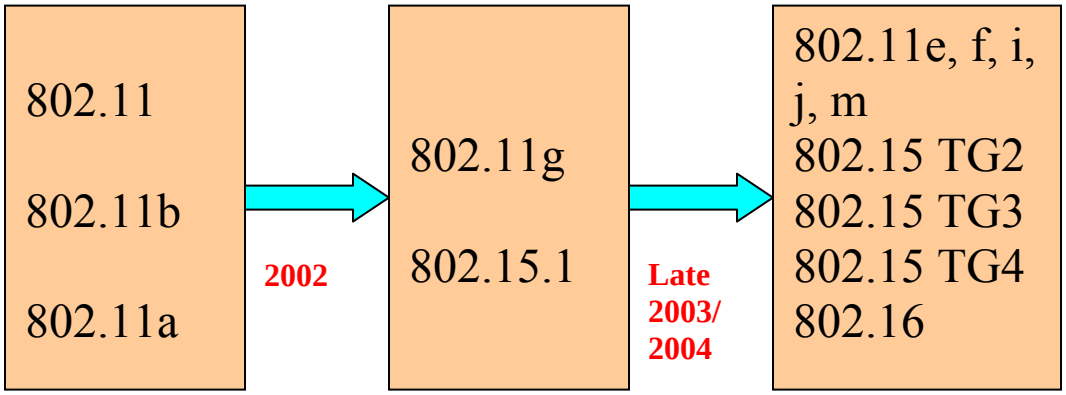

Figure 1.1 Development of wireless standards[1]

There are two general ways to improve the performance of wireless systems such as operating range and data rate. The first is using advanced antenna technology. The second is designing the system at a higher frequency where a larger channel bandwidth is available. My graduate research at Caltech actually aims in these directions to improve the performance of future wireless systems.

First, my research is started with active antenna. An active antenna is a structure which combines the active devices with passive antenna to improve its performance or introduce new functionality directly into the antenna. Such antennas are currently of increasing interest, as system designers require increased functions and a compact space [1]-[4]. Also, the new high-volume commercial applications such as wireless LAN and collision avoidance radars require low-cost and light-weight solutions, and the high level

[1] 802.11: Wireless LAN, 802.15: Wireless Personal Area Networks, 802.16: Broadband Wireless Access

of integration achievable with active antennas inherently fulfill these requirements [5]-[6].

Phased array technology has been received considerable attention by the military and industry for airborne-, space-, surface-, and ground-based applications due to its agile beams of electronically scanning which provide significant system advantages [7]-[12]. The current prosperity of phased array systems is partially caused by the advancement of IC technology as more high performance ICs are made available for a lower price. One promising application for phased arrays is WLAN. The phased array with a phasing network embedded will be a key component of a high data rate WLAN in future. With a fast and adaptive beam scanning, a mobile computer can find its target (another mobile computer, or an access point) easily, which improves its efficiency and mobility (Figure 1.2). Nulls can be formed to avoid interference.

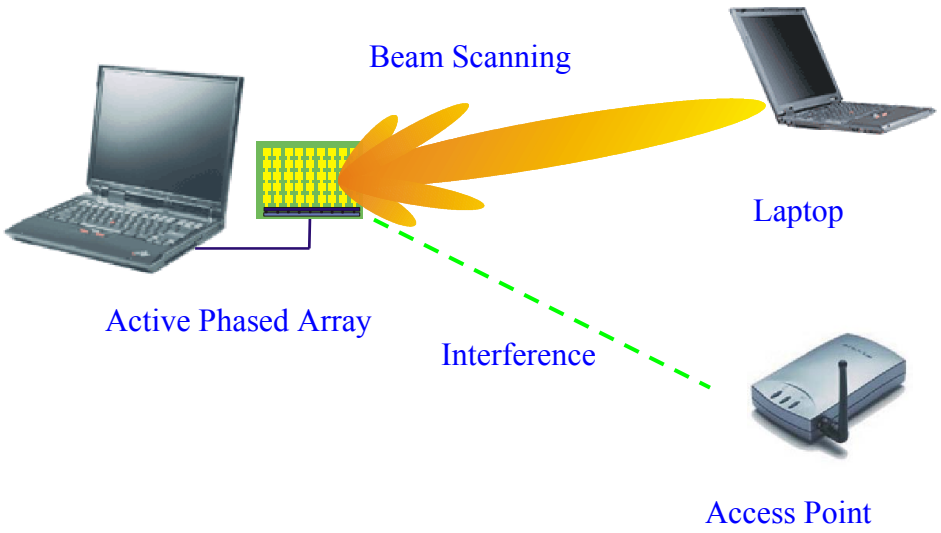

Figure 1.2 Phased array for the wireless LAN (WLAN)

The Caltech RF and Microwave group has proposed a WLAN project at 24 GHz, an ISM (Industrial, Scientific and Medical) band which has a bandwidth of 250 MHz. The schematic of this WLAN system is shown in Figure 1.3. This dissertation will present the design and testing results associated with this front active patch array in details.

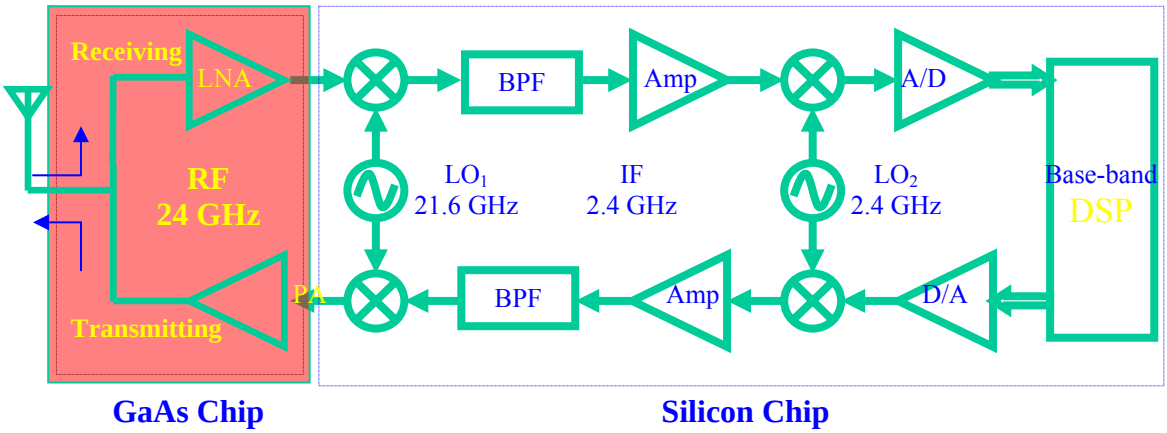

Figure 1.3 Schematic of the Caltech 24 GHz WLAN system

Second, any wireless communication system has to cope with the difficulties caused by the communication medium. This difficulty is especially serious for the indoor wireless communication. For such a system, the media is a multi-path channel where, due to the propagation phenomena, the transmitted signal suffers from interference, fading and noise. Moreover, the real indoor channel is time-, frequency- and space-variant. Therefore, an appropriate characterization of the channel is indispensable during the design process of any communication system. Knowing the channel characteristics and properties ahead can help people design the system, match to the environment impairments and therefore will be more efficient and robust. The second part of this dissertation will cover my research on the indoor wireless channel investigation. A site

specific theoretic model based on ray-tracing and verified by measurements will be presented.

1.1 Organization of the Dissertation

Chapter 2 discusses the 24 GHz phased array based WLAN proposal at Caltech. First the design issues regarding the Power Amplifier and Low Noise Amplifier GaAs chip are presented. Measurement results are shown in comparison with simulation. The concept of a series fed patch array is explained and both the simulation and measurement results are plotted. Since this is a phased array project, beam-shifting simulation is also done to verify its function and also gives limitations of application by gain drop and grading lobes. Finally, the patch array is combined with the power amplifier and low noise amplifier MMIC and tested and the results are shown.

Chapter 3 explains some basic concepts used frequently in the channel modeling. For example, different propagation mechanisms (reflection, diffraction and scattering) and effects of multipaths are discussed. Important terms such as Power Delay Profile and RMS delay spread are defined. Types of channel models are explained.

Chapter 4 introduces the automatic measurement setups for the indoor channel investigation and five frequency bands from 2.4 to 24 GHz under test. In addition, the path loss measurement results in three different scenarios (floor to floor, LOS – hallway, NLOS – hallway) are presented. RMS delay spreads in the 3rd floor hallway (LOS and NLOS) are also given with a brief analyzing summary.

Chapter 5 explains in details a combined 2-D E/H plane ray-tracing method which can be applied to do the channel prediction. First, calibration measurement is done to characterize indoor materials such as plasterboard, glass and wood. Then, with enhanced numerical calculation of Fresnel integral, ray-tracing results are computed and compared with previous measurements.

Chapter 6 introduces currently unfinished research work and some work for future. For example, a simplified 3-D ray-tracing code is developed, aiming to improve the accuracy of the previous combined 2-D ray-tracing program. Interesting topics such as "access points optimization" and "human body effects" are also covered in that chapter.

There are three appendixes in this dissertation. Appendix A covers the designing and testing of a compact anechoic chamber. Appendix B shows the automatic indoor channel testing system built and also the safety concern during the testing. Appendix C explains the issues concerning in the development of ray-tracing codes.

Chapter 2

A 24 GHz Patch Array with A Power/Low Noise Amplifier MMIC

In this chapter, the focus is on the design of the 24 GHz power amplifier and low-noise amplifier chip and its integration with the microstrip patch array. (Milan Kovacevic, a master student at Caltech did the primary chip design.) The designs of other WLAN components can be found in the reference [13]-[16].

The transmit/receive (T/R) module provides the final stage of amplification for transmitted signals and the first stage of amplification for received signals. Aside from amplification, it controls the phase and amplitudes of these signals to electronically steer the antenna beam [17]. Low module cost is desirable due to the large number of modules required in a typical phased-array application. For these reasons, T/R modules are a critical element for phased-array antennas, and the T/R module cost-performance trade greatly affects the entire phased-array antenna architecture. In the past, the transmit/receive function of a communication system has usually been realized by connections of separate modules, such as T/R switch, power amplifier and low noise amplifier [18]-[19]. Even recently, these modules have been realized as separate MMIC chips, they still need to be connected by wire-bonding. Integration of these modules [20] into one MMIC chip can further reduce the size and cost. But a practical realization of this integration is challenging:

- First, an appropriate IC process with both good low-noise and power performance is needed.
- Second, an appropriate design methodology must to be used to keep good bi-directional impedance matching and isolation between T/R channels.

Some researches have been done on the on-chip T/R switches in recent years [21]-[22]. Also, researchers have successfully designed the PA/LNA chip on the AlGaAs/GaAs HBT process and a full transceiver on GaAs at 1.9 GHz [23]-[24]. But implementing such a T/R module at high frequencies as 24 GHz is still quite challenging.

2.1 PALNA: Power Amplifier and Low Noise Amplifier on the Same Chip

The GaAs PHEMT (Gallium Arsenide Pseudomorphic High Electron Mobility Transistor) has a well-established use as a high-performance device which can work at frequencies up to W-band (75-110 GHz) [25]-[27]. The combination of those terrific material properties, such as high mobility and low loss substrate, as well as property such as shot gates from fabrication techniques, i.e., Electron Beam Lithograph (EBL), determines its unique performance. Initially used for low noise amplifier applications, more recently GaAs PHEMTs have found applications in the low to medium power applications at millimeter wave frequencies with respectable power added efficiency [28]-[29]. So it is potentially a good candidate to integrate both power amplifier and low noise amplifier in a single chip.

In this work, the power amplifier (PA) and low noise amplifier (LNA) chip is designed on Rockwell GaAs PHEMT process at 24 GHz. A set of DC bias control is used

to switch between PA and LNA. On and OFF transistor S-parameters are used to design the impedance matching network and isolation for the T/R channels. While the T/R switch loss is greatly reduced, the size of the whole module decreases to 2.3 mm^2 (1.2 × 1.9 mm^2).

This design used the standard MMIC elements: microstrip lines, metal-insulator-metal (MIM) capacitors, ion-implant resistors, via holes for low impedance ground connection, two metal layers and air bridge crossovers (Table 2.1). The GaAs wafer is 4 inch and 75 μm thick. The substrate material is grown by molecular beam lithograph (EBL). In order to achieve high breakdown voltage, gates were double recessed, with the final etch performed using plasma. The use of dry gate recess improved the uniformity of the devices to better than 5% across the entire wafer.

Design Components	**Details**
MIM Capacitor	300 pF / mm^2
Resistor	N+, 220 Ohm / Square
Metal Layer	First layer: 0.7 μm, Second layer: 2 μm

Table 2.1 Design parameter for Rockwell PHEMT process

2.1.1 Transistor Models

The PALNA chip (Figure 1.3) is designed in ADS using the table based S-parameter for on/off-state small signal simulations and EE_HEMT1 transistor model [30] for on-state large signal simulations (Figure 1.4). The output impedance of the PA when biased off is purely inductive. Cascaded transmission line is added to the output of PA for the desired high-impedance state. This part of transmission line combines with LNA input

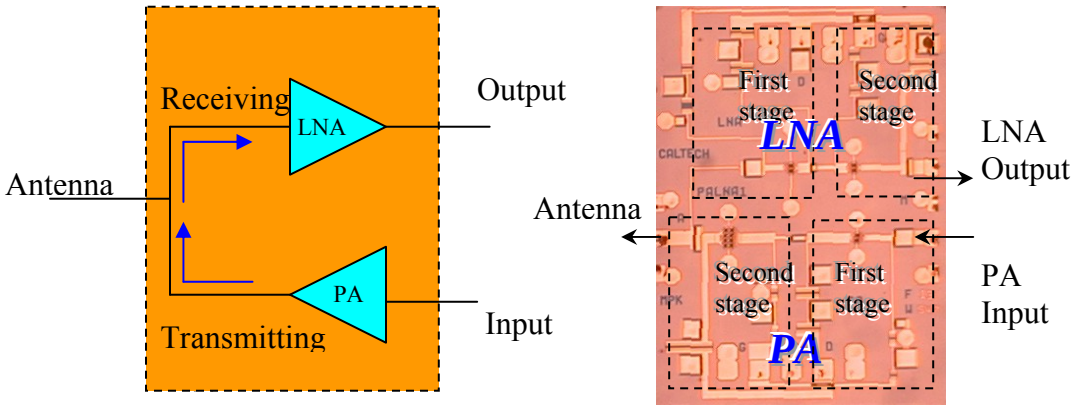

Figure 2.1 PALNA chip on Rockwell GaAs PHEMT process (Die size: 1.2 × 1.9 mm^2): (a). Schematic; (b). Photo;

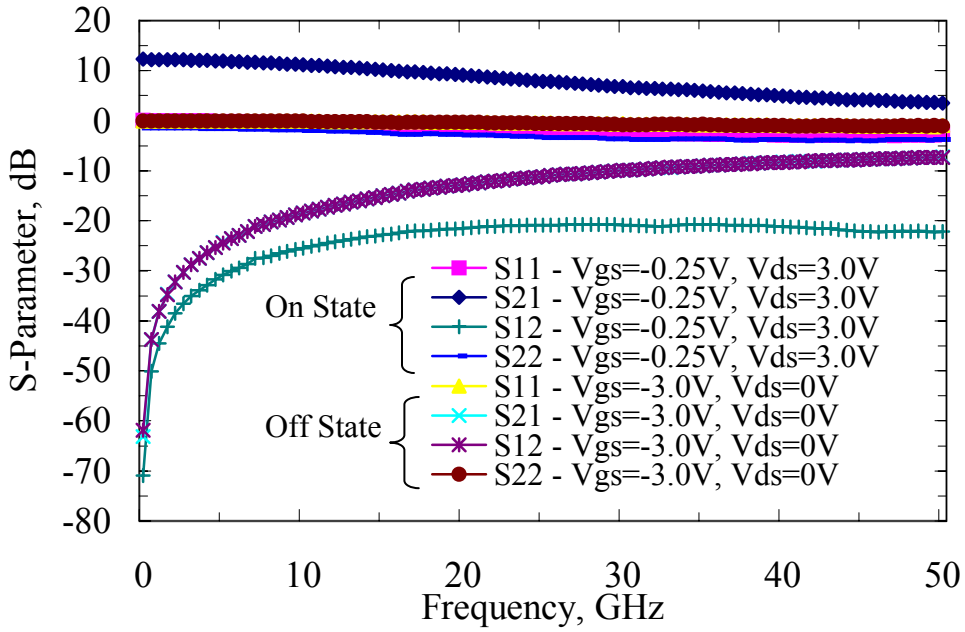

(a)

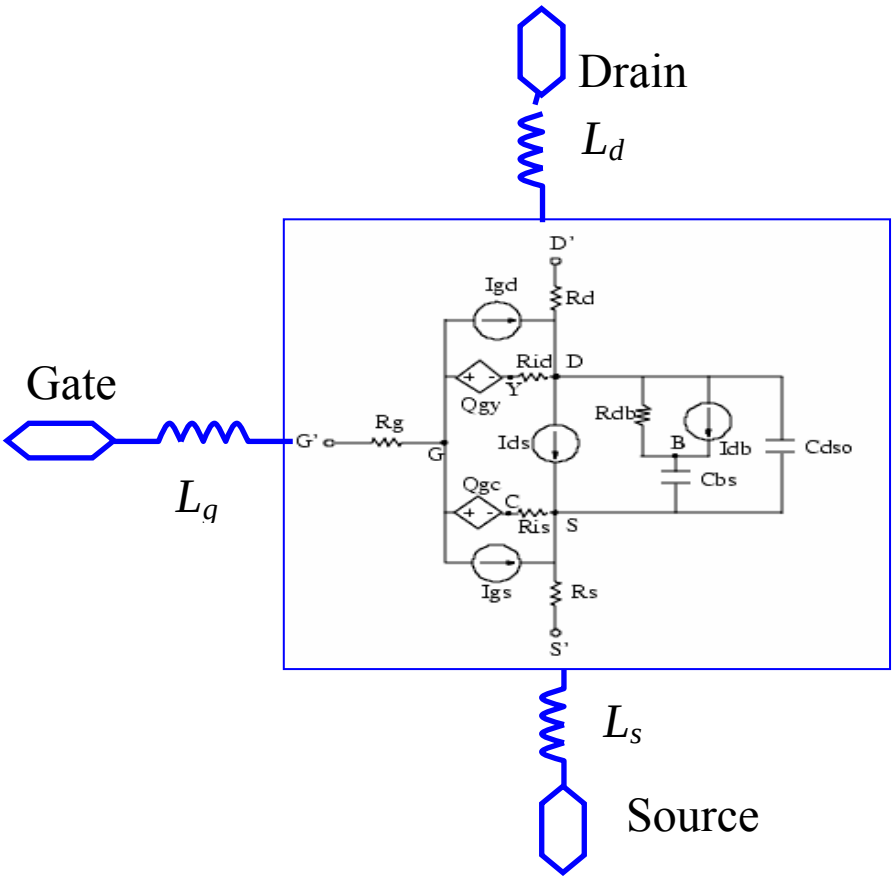

(b)

Figure 2.2 (a). Table based S-parameters for the GaAs PHEMT (4x20 μm)
(b). EE_HEMT1 model used in the PA design

for 50 Ohm matching, while itself does not degrade the performance of the PA. There is another section of transmission line cascaded with LNA input for similar purpose. High isolation is provided between LNA and PA.

2.1.2 Low Noise Amplifier Design

A two-stage (common source) topology is used for the LNA design, with the first stage matched for noise and the second stage matched for gain. Input, output and inter-stage impedance matching is accomplished by cascading and parallel transmission lines.

A gate width of 80 μm is chosen for the trade-off between high gain and low noise. 2pF MIM capacitors are used for decoupling the DC and RF. Stability simulation is also carried out for DC to 50 GHz and around 24 GHz. In this design (Figure 1.6), we use source inductive degeneration for stabilization, impedance and noise matching.

2.1.2.1 Inductive Source Degeneration

Inductive Source Degeneration (ISD) has been used in LNA design for a couple of years. People have done lots of research on this topic [31]-[33] in the past.

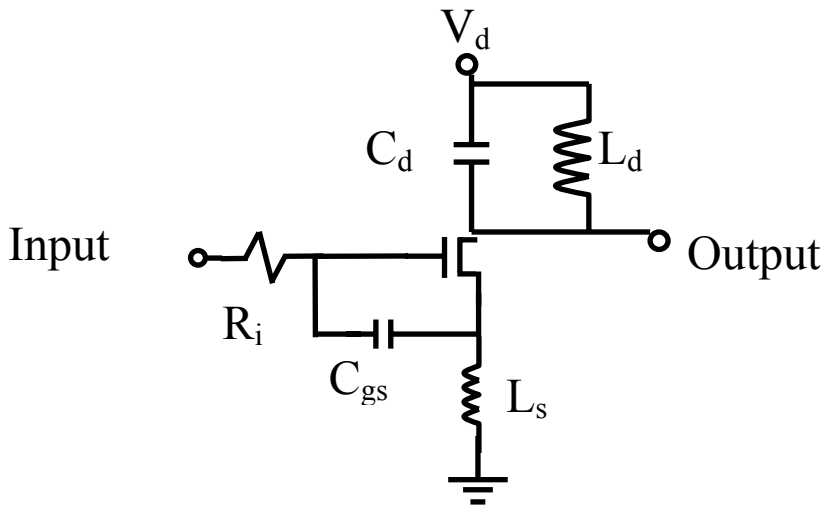

Figure 2.3 Input impedance of a PHEMT with inductive source degeneration

If we ignore the capacitance between gate and drain, we can derive the input impedance of this common source amplifier easily by the small signal model (Figure 2.5).

$$Z_{in} = R_i + j\omega(L_s + L_d) + \frac{1}{j\omega C_{gs}} + \frac{L_s}{C_{gs}} \cdot g_m \tag{2.1}$$

where g_m is transistor transconductance, C_{gs} is the gate-source capacitor, and L_s and L_d are the source and drain inductor. For input power match $R_i + \frac{L_s}{C_{gs}} \cdot g_m$ must be equal to R_s, or $\Delta R = R_s - R_i = \frac{L_s}{C_{gs}} \cdot g_m$. The reactive part can be compensated at the frequency of operation, ω_o, by selecting the gate and drain inductor, L_s and L_d such that

$$\omega_o = \sqrt{\frac{1}{(L_s + L_d) \cdot C_{gs}}} \tag{2.2}$$

The minimum achievable noise figure of this common source configuration can be estimated by applying constant-power optimization method [34], resulting in:

$$F_{\min} \cong 1 + 1.426\sqrt{\delta\gamma}\left(\frac{\omega_o}{\omega_T}\right) \tag{2.3}$$

From this formula, we can see that the minimum noise figure is a function of δ, γ and the ratio of ω_o and ω_T. Researchers have tried to reduce the (ω/ω_T) ratio by introducing additional gate to source capacitance (increasing C_{gs}) to get a small F_{min} [35]. It is also possible to reduce ωo by increasing L_s but the source (antenna) impedance must be changed to get a good match [36]. In our design, an electrically-small shorted line with an impedance $Z_L = jZ_0 \tan\beta l$ is used as an inductor (1.4):

$$L = Z_o \frac{\beta}{\omega} l \tag{2.4}$$

Thus, the gate input resistance can be increased by ΔR to converge with optimum noise resistance using a line of fractional wavelength:

$$\frac{l}{\lambda_g} = \frac{C_{gs} f \Delta R}{g_m Z_o} \approx \frac{\Delta R}{2\pi Z_o} \frac{f}{f_T} \tag{2.5}$$

It is important to notice that the gate impedance matching strongly depends upon the device cut-off frequency f_T and transmission line parameters, both of which are highly repeatable from wafer to wafer in the MMIC process.

Amplifier	**Degenerate L, nH**	**Z_o, Ohm**	**Electrical Length**
LNA –1st stage	0.090	83.35	9.34°
LNA – 2nd stage	0.024	83.35	2.14°

Table 2.2 Dimension of the source degeneration inductors on GaAs[2] .

2.1.2.2 Bias Network for LNA and PA Design

During the design of LNA, the PA stage is totally biased off to provide big impedance isolation for the signal receiving. The similar procedure is used in the PA design. The bias network used is shown in Table 2.3.

	V_{Gate_LNA}, V	**V_{Drain_LNA}, V**	**V_{Gate_PA}, V**	**V_{Drain_PA}, V**
LNA	-0.25	3.0	-1.7	0
PA	-1.0	0	-0.1	3.0

Table 2.3 DC bias for the LNA and PA design

[2] GaAs substrate parameters: H=75 um, ε_r=12.8, Cond=6.56 E07, T=2 um, TanD=0.0005.

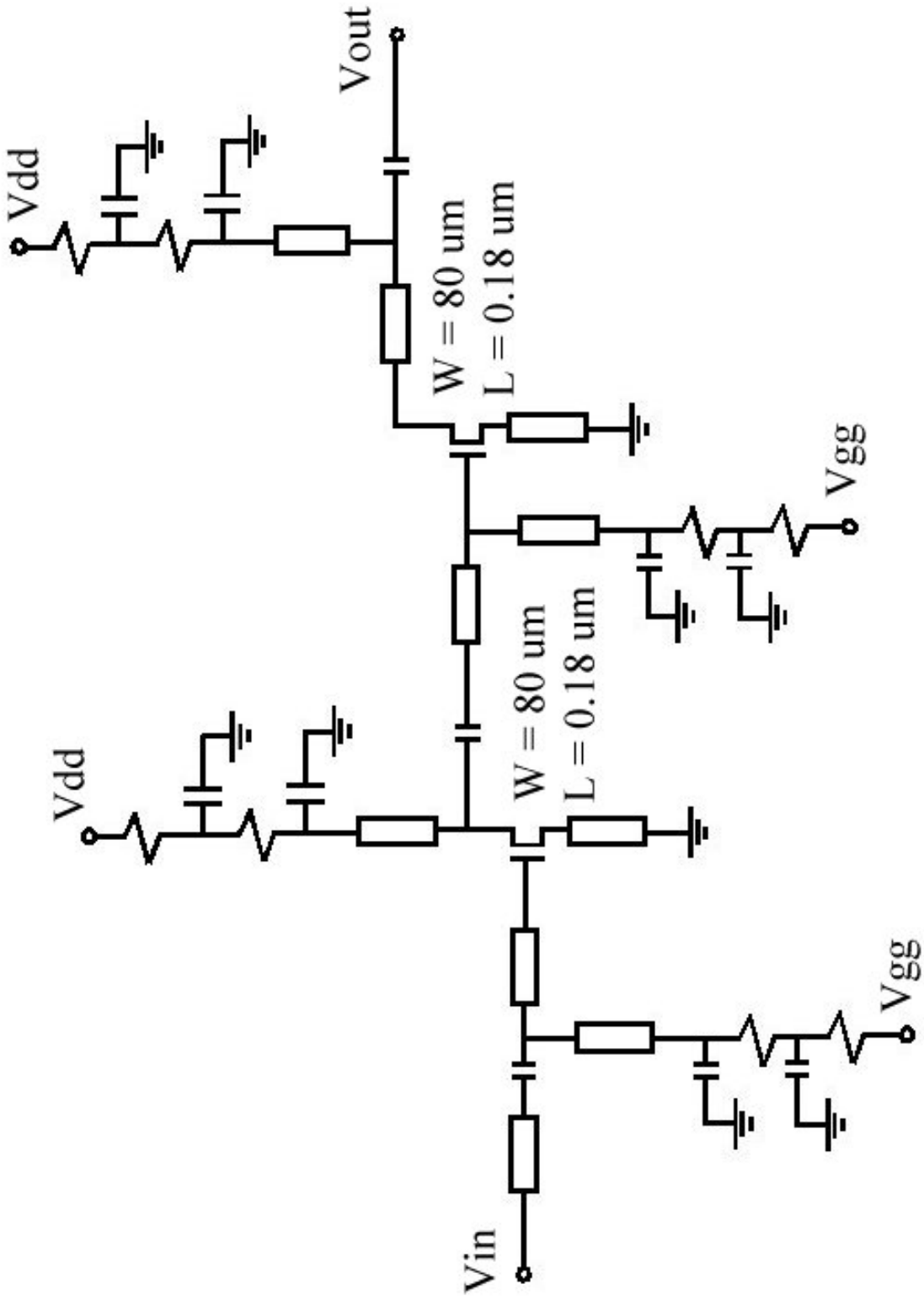

Figure 2.4 The LNA schematic

2.1.3 Power Amplifier Design

A circuit topology for the two-stage PA is presented in Figure 2.17. The first stage employs an 80 μm PHEMT, whereas the second stage employs a 320 μm PHEMT, in order to output more than 50 mW at 24 GHz. The first stage is optimized for gain. The second stage is designed to maximize output power. Input, output, and interstage impedance matching is accomplished using cascade and shunt parallel transmission lines. 2 pF capacitors have been used for decoupling the DC and RF signals. RC bias networks were also designed to ensure lower frequency stability. Input and output matching circuits were designed so that the corresponding return losses are lower than -6 dB. The optimization criterion for the two-stage amplifier stability was a stability factor $\mu>1$ in the frequency range from DC to 30 GHz, and $\mu>3$ for frequencies near 24 GHz.

2.1.3.1 PA Performance under Different Bias Condition

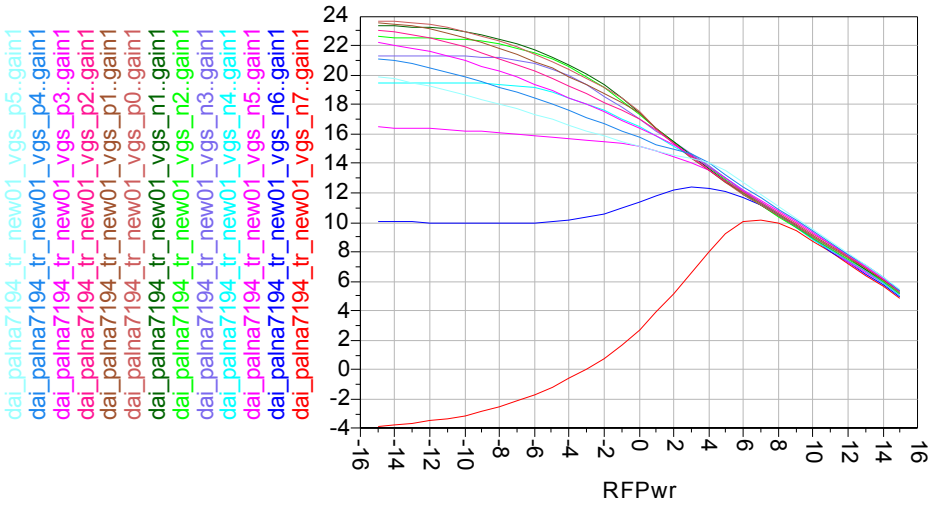

Figure 2.5 PA gain vs. p_{in} as Vgs sweeping from –0.7 V to 0.5 V.

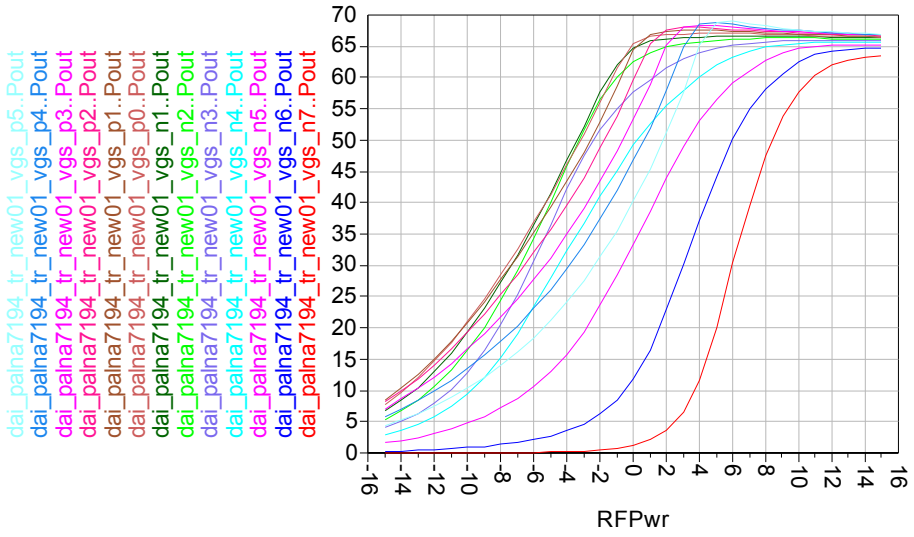

Figure 2.6 Pout vs. p_{in} as Vgs sweeping from –0.7 V to 0.5 V.

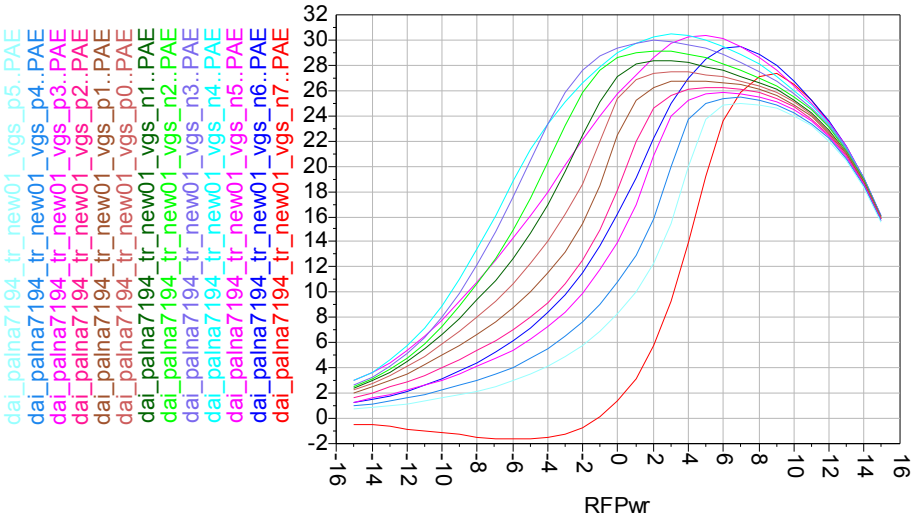

Figure 2.7 PAE vs. p_{in} as Vgs sweeping from –0.7 V to 0.5 V.

As can be seen from the above simulation results on the Vgs sweeping, the best performance of gain and Pout happen at Vgs ≈ -0.1 – 0.2 V and the best PAE occurs even lower between –0.3 and -0.2 V. In our design, a –0.1 V is chosen for V_{gs} of PA.

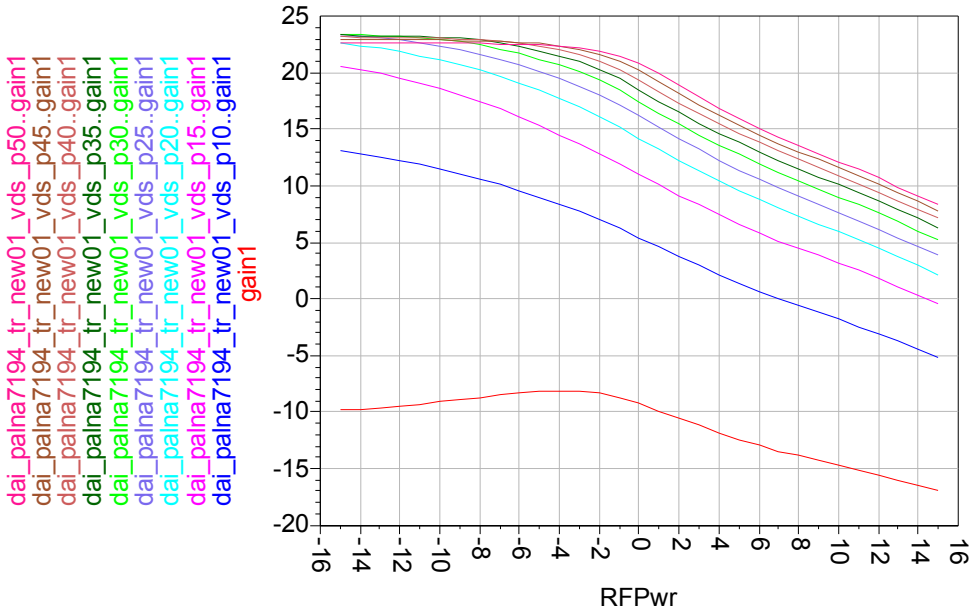

Figure 2.8 Gain vs. p_{in} as Vds sweeping from 0.5 V to 5.0 V.

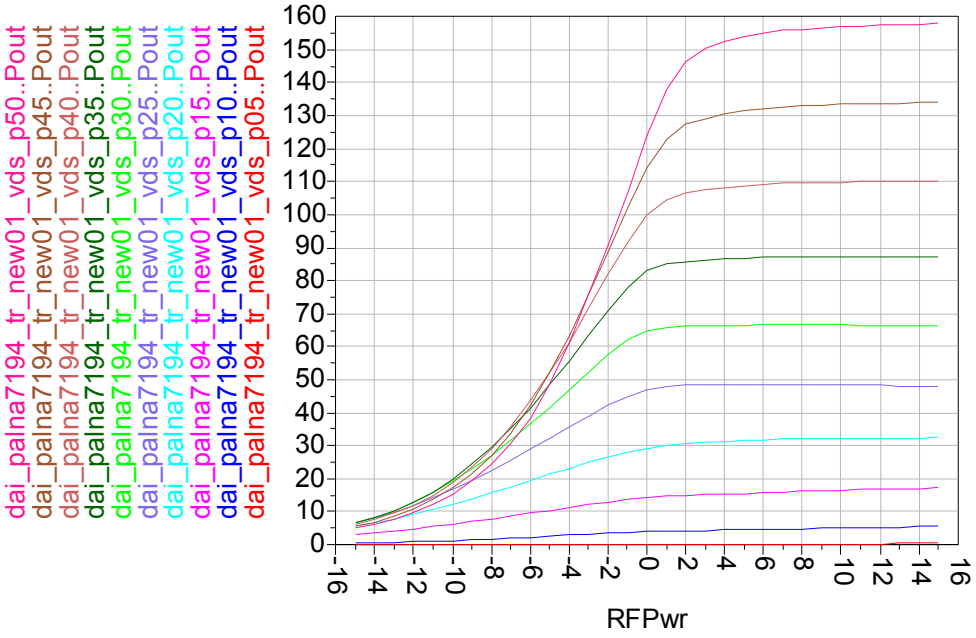

Figure 2.9 Pout vs. p_{in} as Vds sweeping from 0.5 to 5.0V

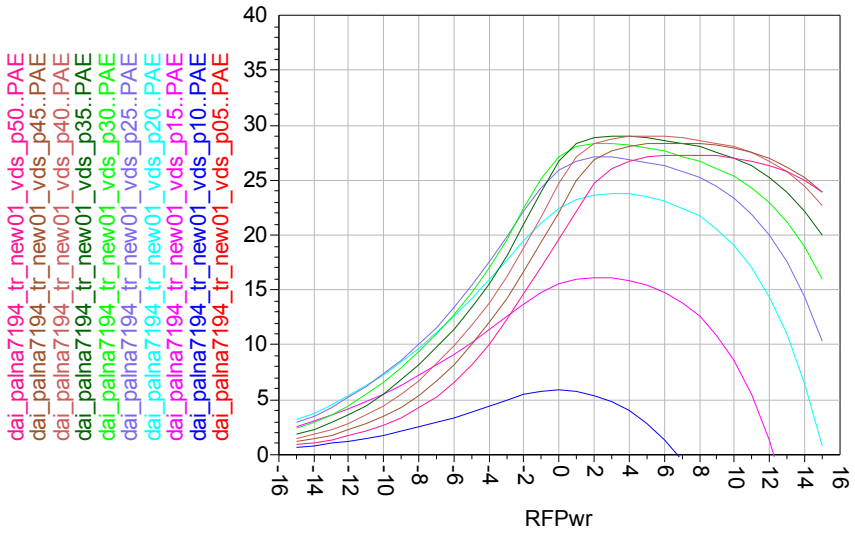

Figure 2.10 PAE vs. p_{in} as Vds sweeping from 0.5 V to 5.0 V.

Figure 2.10 to 2.12 give gain, Pout and PAE simulation results on Vds sweeping. It is clear from simulation that the higher the Vds, the larger the PA gain and Pout. But the best PAE is achieved at an intermediate level of Vds = 3.5 V, instead of 5.0 V.

2.1.3.2 Load-Pull Simulation by ADS

The transistor model used in ADS simulations is EE_HEMT1. This model was empirically constructed from small-signal S-parameters taken at different bias conditions. The resulting bias-dependent nonlinear model was validated by a load-pull measurement. Here, ADS is used as a simulation tool to verify the load-pull measurement result in the model. Five harmonics are applied in this ADS simulation and each of them is terminated with 50 Ohm. After finding the optimal output power, 10 different power levels with 1 dB difference are chosen to get the load-pull plots on the Smith chart (Figure 2.13).

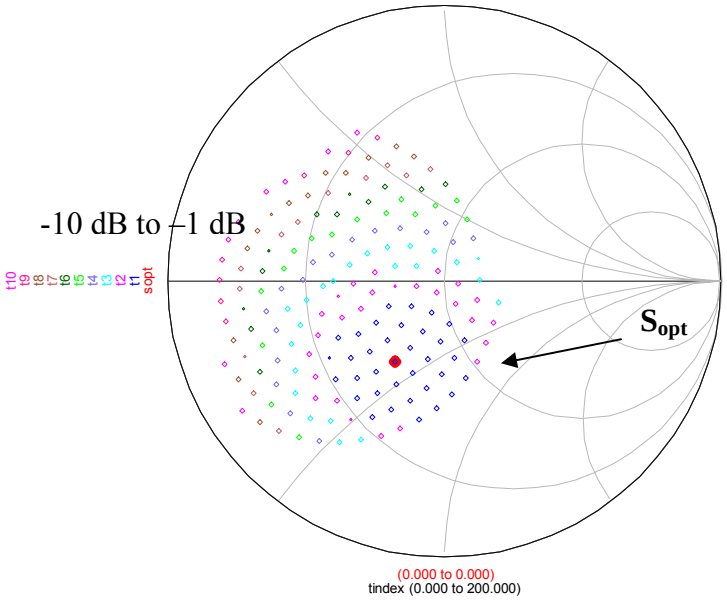

Figure 2.11 Load-Pull simulation by ADS

The optimal power match is found to be $S_{opt} = 0.342 / -121.67$ with P_{opt}=18 dBm.

So the optimal load for the output is $Z_{opt} = 50 * (0.5982 - j * 0.3944)\Omega$.

2.1.3.3 Harmonic Balance Simulation by ADS

With the large signal model (EE_HEMT1) for the transistor, we can do lots of useful PA simulation by harmonic balance method in ADS. Figure 2.14 shows the simulated gain, Pout and PAE of this PA as a function of input power sweeping. The input 1dB compression point is around -1 dBm. At this power level, the output power is around 65 dBm, more than what we have proposed. The gain and PAE are 18 dB and 25%.

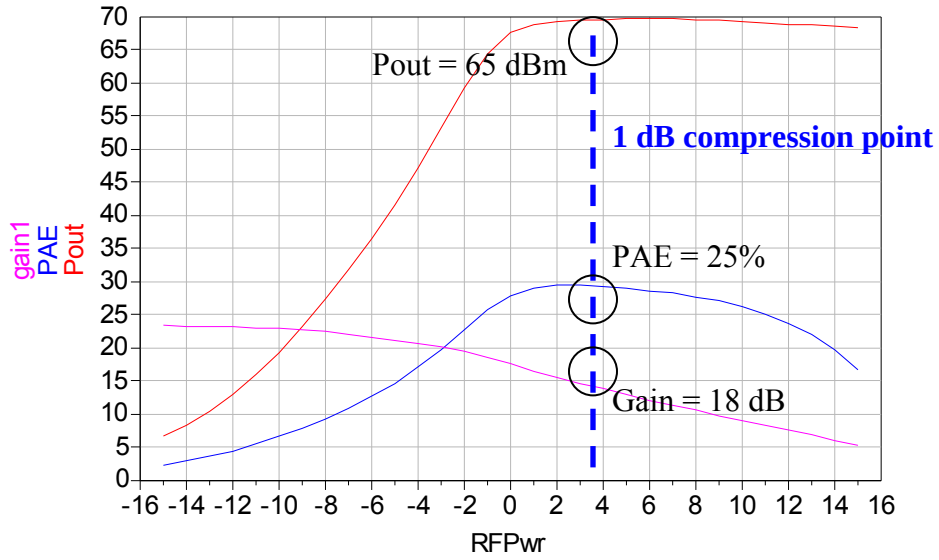

Figure 2.12 Pout, PAE and gain vs. Pin.

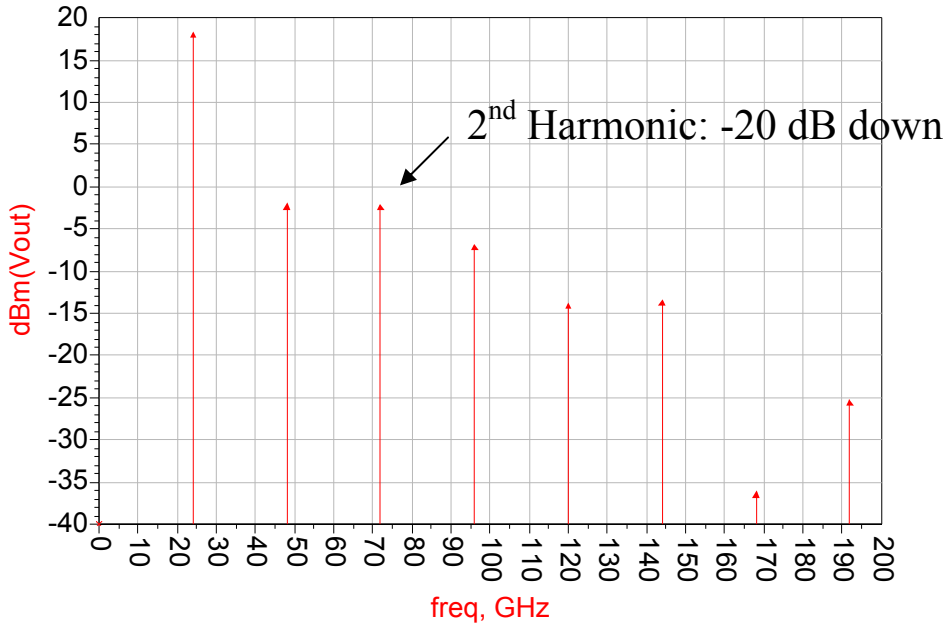

Figure 2.13 Output spectrum at 1 dB compression point (Pin ≈ 0 dBm).

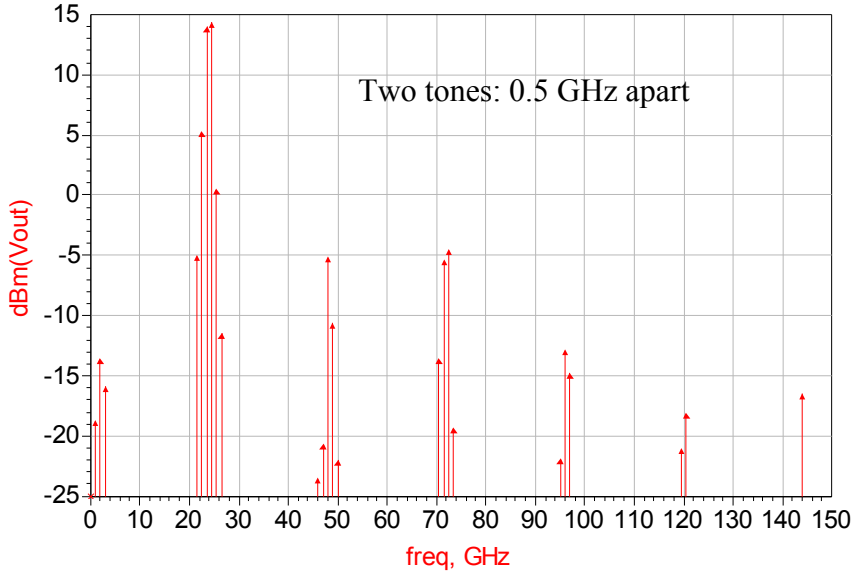

Figure 2.14 Two tone spectrum at input = 0 dBm.

Another very important characteristic of PA is linearity. Harmonic balance simulation is applied to find to linearity of this PA. We can see from the Figure 2.15 that the 2nd and 3rd harmonic is about 20 dB down from the fundamental, which is not so great but bearable for the first design.

Two tone ADS simulation is applied to find the intermodulation products of this PA:

First tone: $f_1=f_o-\Delta f=24-0.01=23.39$ GHz, $P_{in1}=-10$dBm, Order=5;

Second tone: $f_2=f_o+\Delta f=24+0.01=24.01$ GHz, $P_{in1}=-10$dBm, Order=5;

$P_{out\_fund}=11.36$ dBm, $P_{out\_IM3}=-10.49$ dBm, so the IP3 results [37] are:

$$IIP_3\big|_{dBm}=\frac{\Delta P\big|_{dB}}{2}+P_{in}\big|_{dBm}=\frac{11.36+10.49}{2}-10=0.925dBm\text{, or }OIP_3\big|_{dBm}=22.28dBm.$$

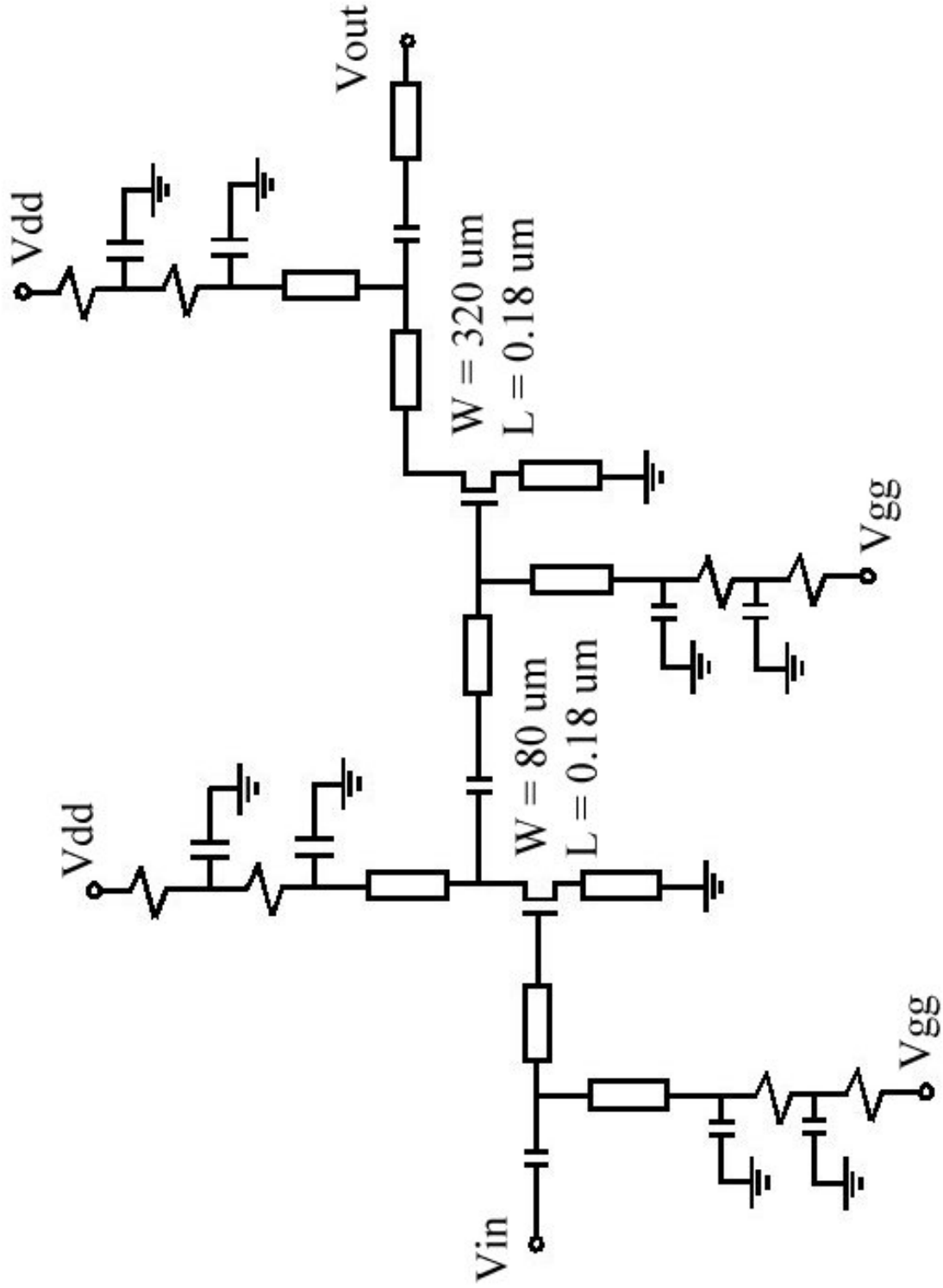

Figure 2.15 The PA schematic

2.1.4 Stability Analysis

In his famous paper [38], Marion Lee Edwards has defined a stability parameter μ for linear 2-port circuits. It is proven that μ > 1 alone is necessary and sufficient for a circuit to be unconditionally stable, where

$$\mu = \frac{1-\left|S_{11}\right|^2}{\left|S_{22}-S_{11}^{*}\Delta\right|+\left|S_{21}S_{12}\right|} \tag{2.6}$$

And $\Delta = S_{11}S_{22} - S_{12}S_{21}$. This criteria for stability is realized in ADS (Advanced Design System) as "Mu(S)", and the simulation results for LNA and PA is shown in Figure 1.18.

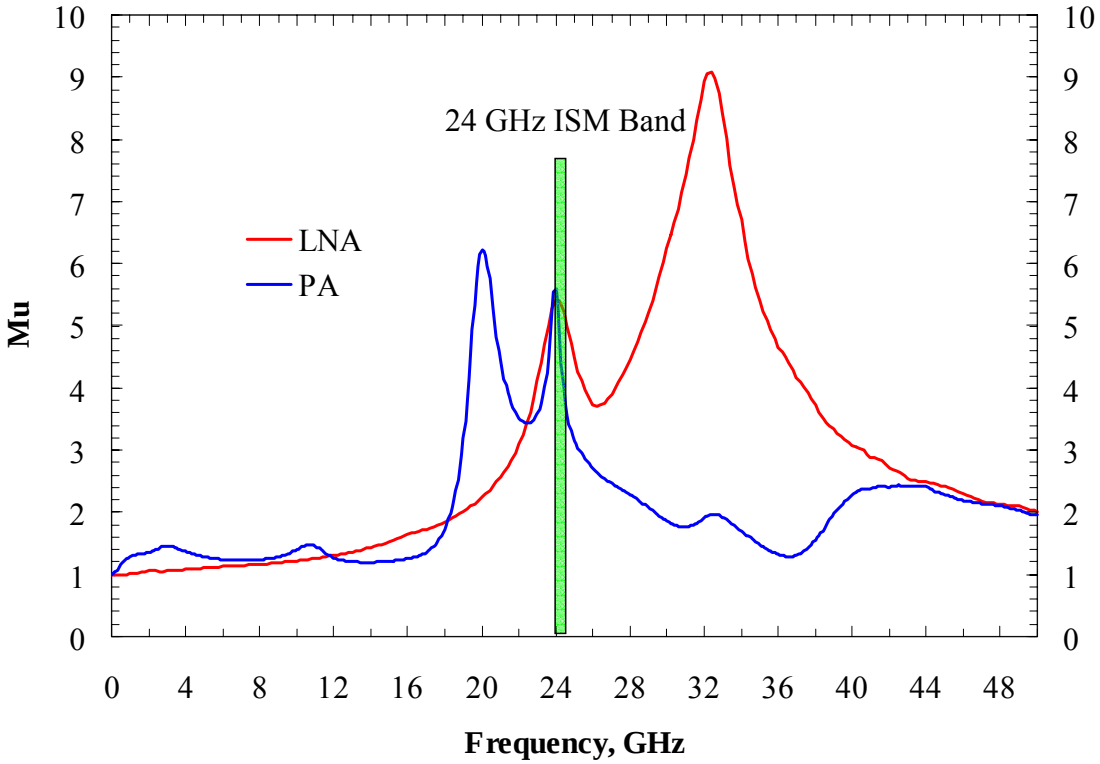

Figure 2.16 Stability simulations for LNA and PA

2.1.5 Measurement Results of PALNA

The measurement results of this chip are compared with simulations in Figure 2.19.

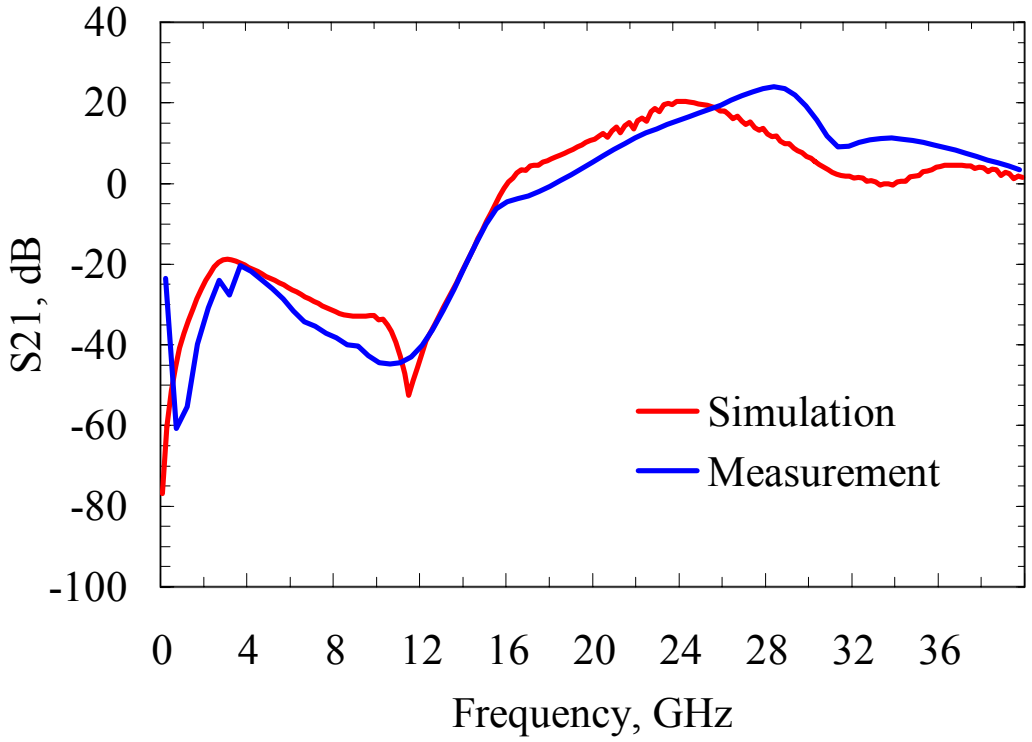

(a)

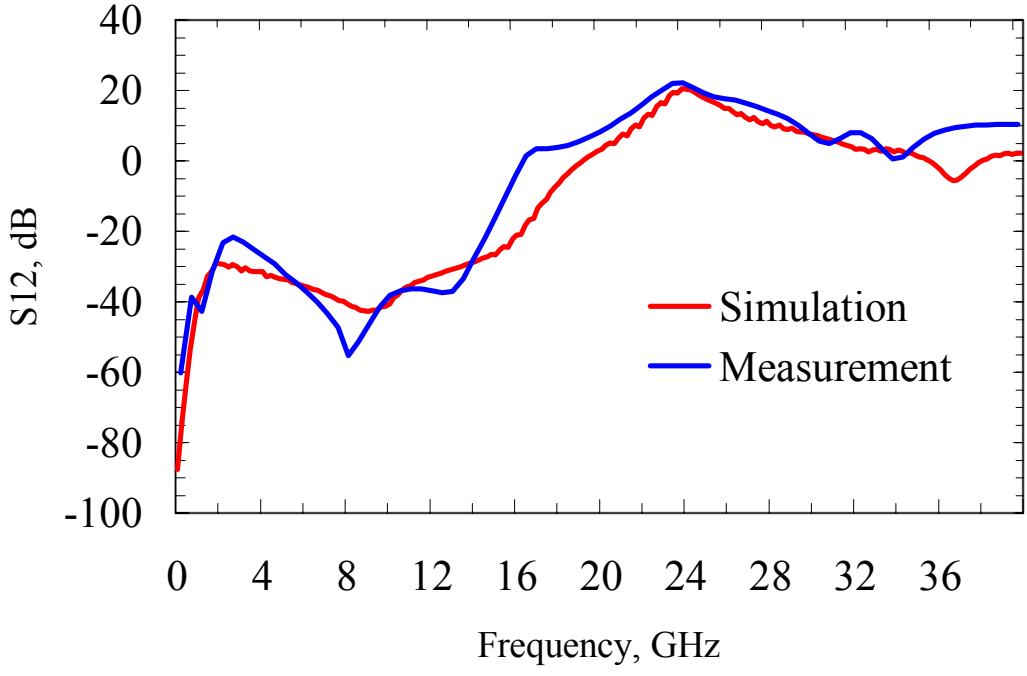

(b)

Figure 2.17 (a). Small signal gain of LNA (b). Small signal gain of PA.

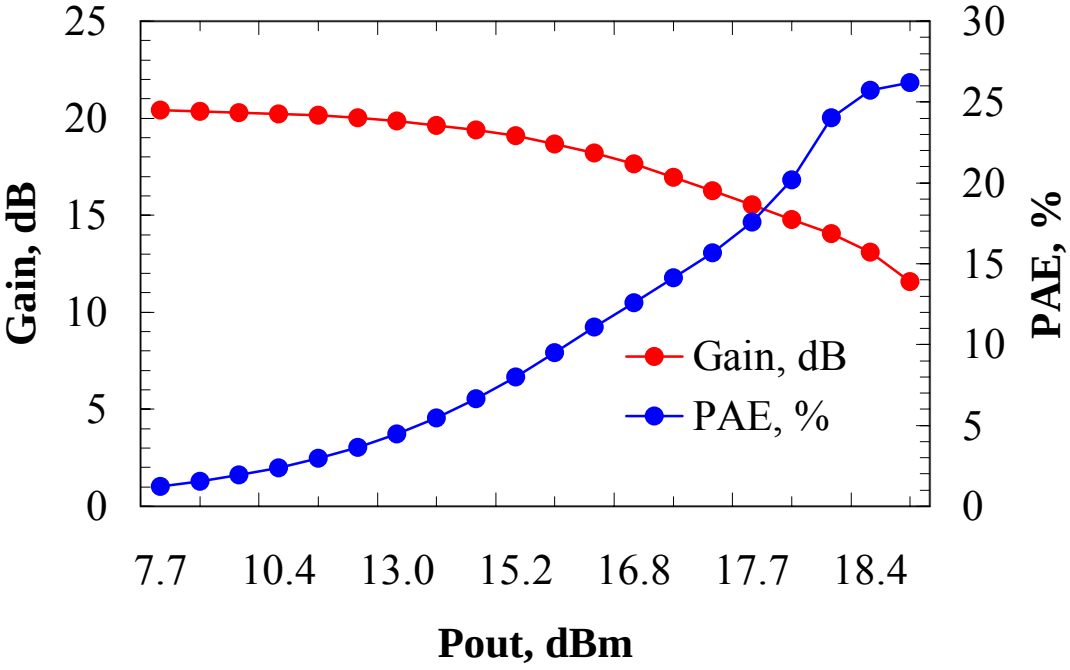

(a)

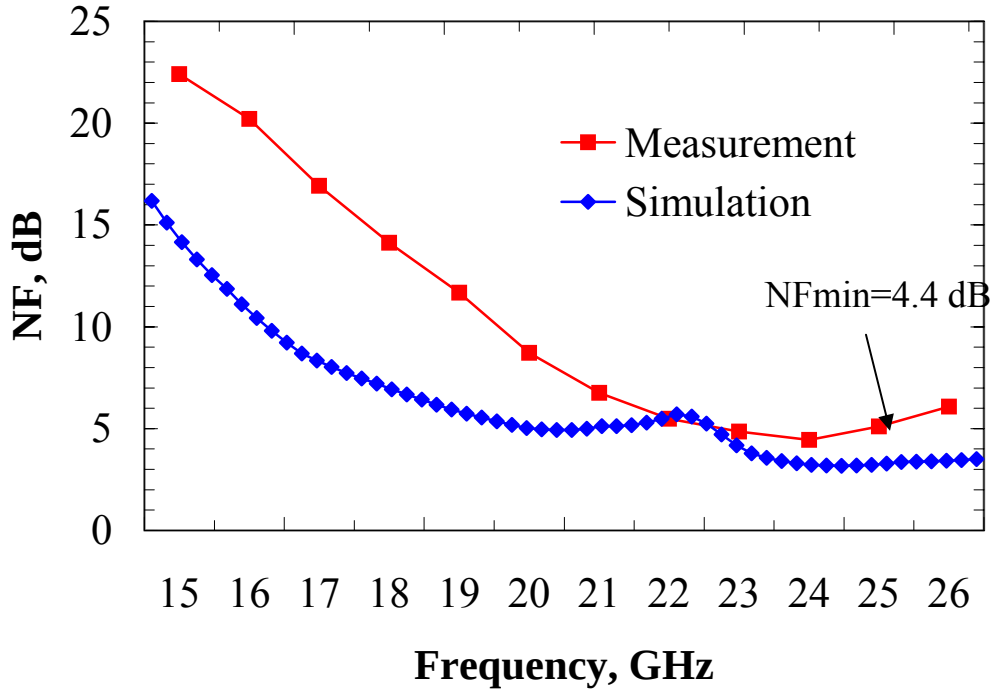

(b)

Figure 2.18 (a). PAE and gain of PA (b). Noise figure of LNA.

As can bee seen from the plots, the chip works well in both transmitting and receiving. The small signal gain of LNA and PA are both above 20 dB. But for LNA, the gain peaks at around 28 GHz, which is higher than 24 GHz predicted in simulation. The shape of S_{12} and S_{21} agrees quite well between simulation and measurement. The output power goes up to 18 dBm (63 mW) and PAE maximum is 26%. A minimum 4.4 dB noise figure is achieved at 24 GHz. This noise performance of the LNA is not so great since we don't have an accurate noise model for the transistor in the noise simulation. The impedance matching at 24 GHz is –7 dB for the LNA and –4.5 dB for the PA. The input impedance is designed intentionally capacitive to cancel the inductance from the wire bonding, which can also affect the noise performance of the chip.

2.2 Design of a 24 GHz Patch Array

In the proposed 24 GHz WLAN system, a patch array is needed to be able to scan in the H-plane to find the target and maximize the received signal level in that direction and null the other possible directions of interference. So the patch array should have a broad H-plane for target tracking and a narrow E-plane for good scanning resolution. A series fed (resonant) patch array [39] has all these properties, and in addition, its input impedance can be matched to 50 Ohm in a systematic way.

2.2.1 Theory of Series Resonant Patch Array

The series array configuration offers unique advantages to the microstrip antenna designers [40]. First, for a single input, the feed line lengths are greatly reduced, and thus reducing the radiation and dissipation losses which may decrease array efficiency.

Further, in the series resonant arrays the high impedance feed lines have the same current directions which may cause less coupling between each other as compared to the case in parallel feeding array. The disadvantages of this type of feed are narrow bandwidth and inherent bean shift with frequencies due to the insertion phase shift of the patch in the series configuration. However, by appropriate adjustment of the parameters of the array, the beam squint can be kept low.

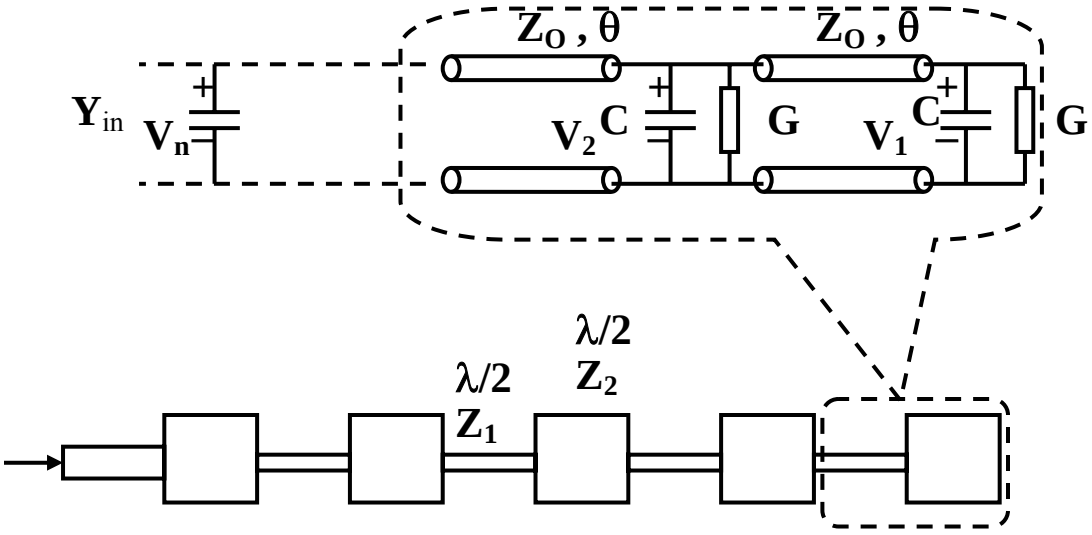

Figure 1.19 Layout for the resonant microstrip array

Figure 2.21 shows the transmission line model of this kind of patch array. The feeding lines connecting the patches are now narrow high impedance lines so as to reduce the disturbance to the radiation fields. The array factor is given by [41]

$$AR = \sum_{i=1}^{N} V_i \exp\left[j \cdot k_o \cdot d_i \cdot \cos\theta\right] \tag{2.7}$$

where V_i is the voltage across the ith patch, k_o is the free space propagation constant and d_i is the distance between first and the ith patch. For the broadside array, the dimension of

the radiating elements and connecting transmission line can be optimized to maximize the array gain by optimizing the function

$$G_T = \frac{\left|\sum_{i=1}^{N} V_i\right|^2 \cdot G}{\left|V_N\right|^2 \cdot \mathrm{Re}(Y_{in})} \tag{2.8}$$

where G is the radiation conductance of the slot and Y_{in} is the input admittance (Figure 2.21). The array factor contribution to directivity is

$$D_T = \frac{\left|\sum_{i=1}^{N} V_i\right|^2}{\sum_{i=1}^{N} V_i^2} \tag{2.9}$$

If V_i is the same for all i, we can see the directivity of this array is N. In our case, 5 patch elements are used for impedance matching, so we should have a theoretic array factor of $D_T = 5 = 7$ dB.

2.2.2 Simulation and Measurement Results

The layout of the microstrip resonant array is shown in Figure 2.21. The simulation is done in both ADS Momentum and IE3D to confirm the performance of the array. As can be seen from Figure 2.21, the cascaded transmission line structure actually acts as an impedance transformer. And it transforms the high impedance at the edge of the last square patch, which resonates at 24GHz, to a near 50 ohm for matching at the first patch element. As the number of elements increasing, we can also expect the impedance goes down and the gain of the antenna goes up. The simulation result by ADS Momentum is shown in Figure 2.22(a).

The microstrip patch array is made on Duroid material with a low dielectric constant of 2.2. The simulation gives about –15 dB return loss at 24 GHz and 2% impedance bandwidth ($S_{11} < -10$ dB), while the measurement actually shows the resonant frequency shifting up to 24.31 GHz with a better matching of –27 dB. This shift may be due to the backside probe feed mounting of the 3.5 connector which is not characterized in the EM simulation. The simulated and measured return loss are both shown in the Figure 2.22(b) for a comparison.

For this 1×5 patch array, we can expect a narrow E plane with 4 side lobes and a broad H plane (Figure 2.23). The measured performance of the prototype antenna is summarized in Table 2.4. It seems that the sidelobe in measurement is 1.2 dB higher than what is predicted. This pattern degradation may be caused by the imperfection of the transition from back-side connector to the microstrip on the board which causes unwanted radiation.

	Gain at 24GHz	**Sidelobe**	**HPBW (E-plane)**	**HPBW (H-plane)**
Simulation	13.0 dB	–9.8 dB	17^{O}	74^{O}
Measurement	12.8 dB	–8.6 dB	16^{O}	67^{O}

Table 2.4 Performance summary for 1×5 patch array

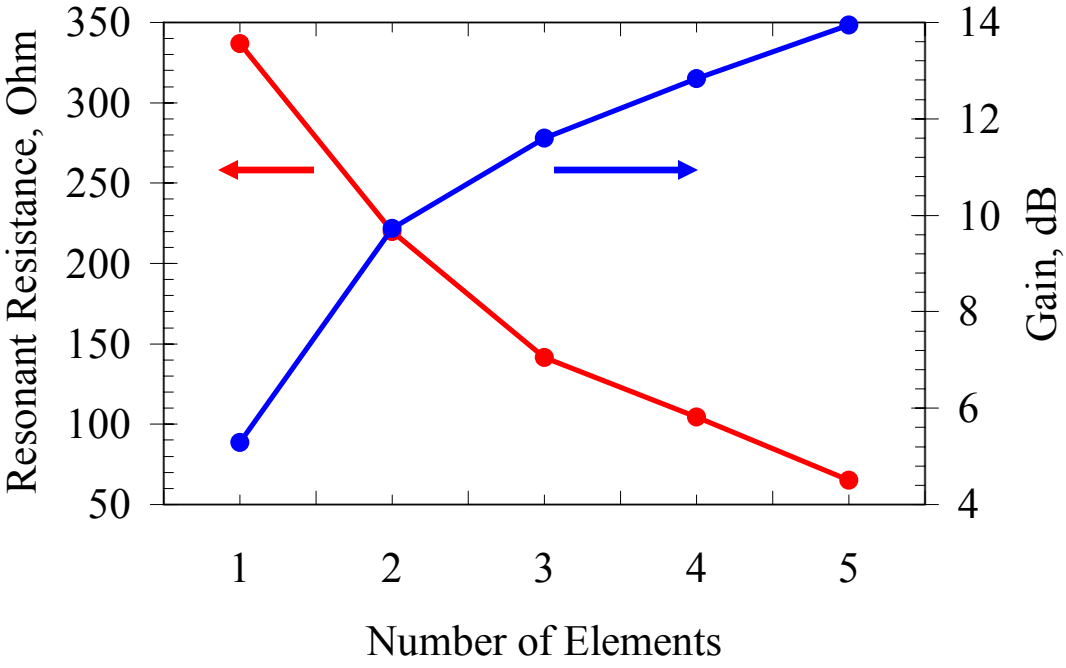

(a)

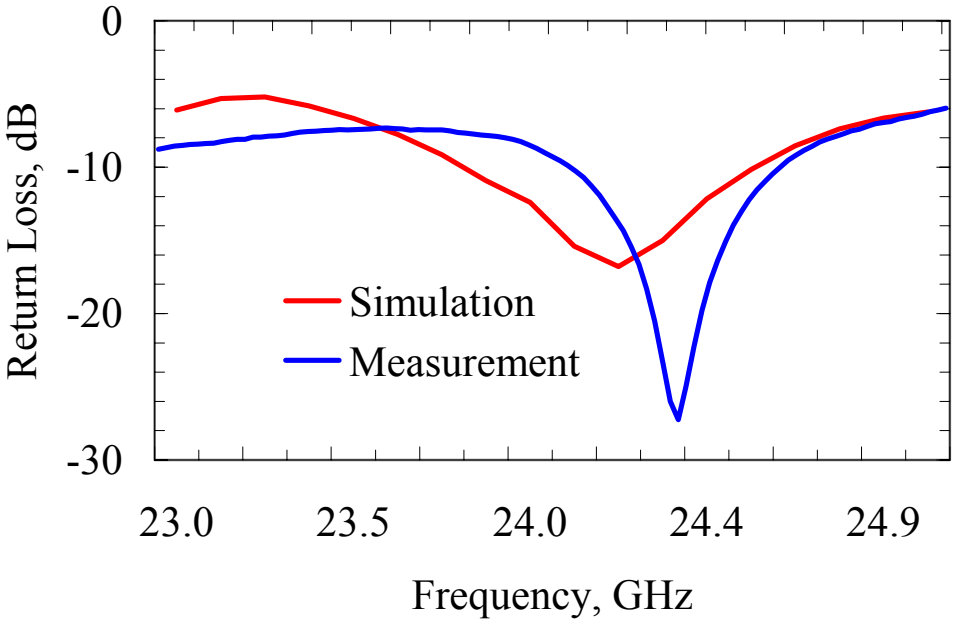

(b)

Figure 2.20 (a). Calculated gain and resistance vs. number of elements;
(b). Calculated and measured return loss;

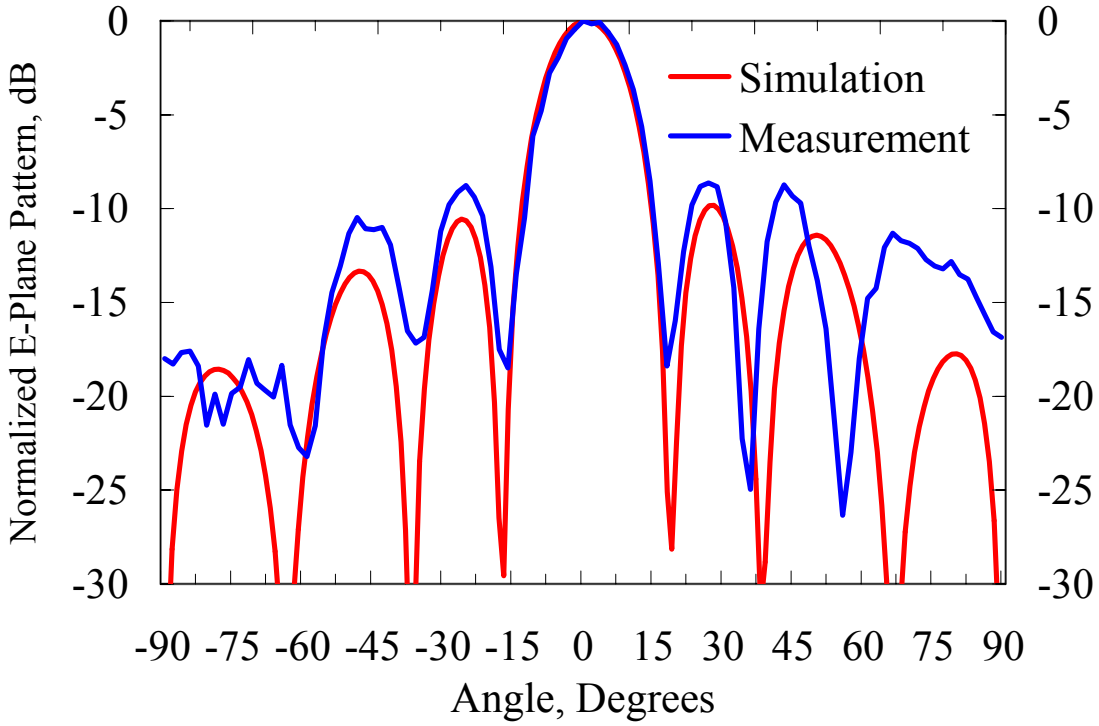

(a)

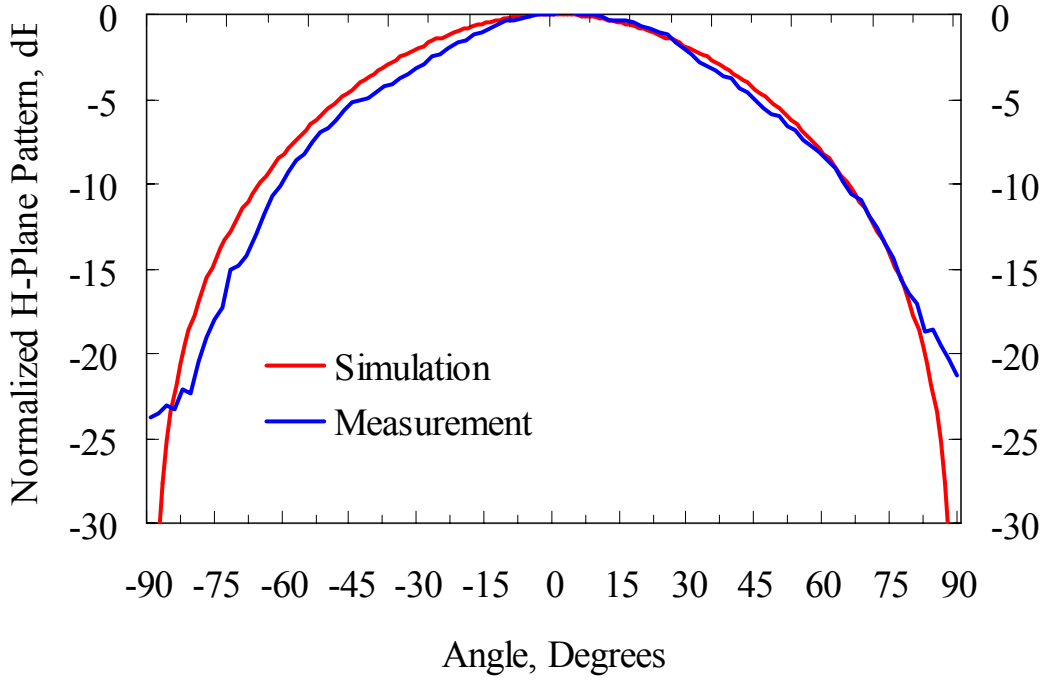

(b)

Figure 2.21 E and H plane of 1×5 element patch array at 24 GHz.

In simulation, the 1x5 patch array gives 13-dB gain at 24GHz. This is proved by measurement (Figure 2.24). If a high antenna gain and beam steering are required for applications such as WLAN, 2-dimensional patch array should be made (Figure 2.25).

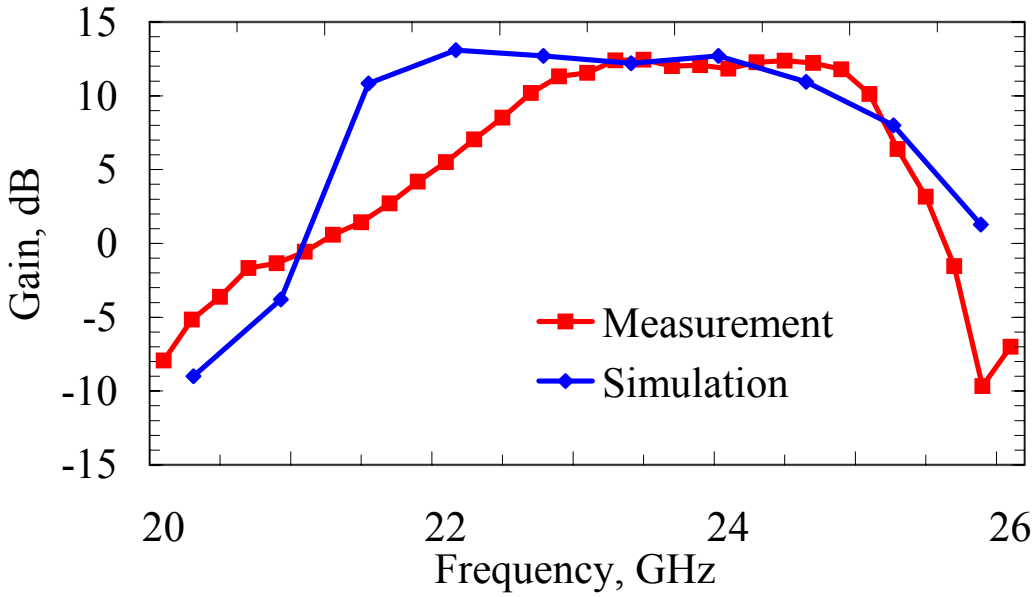

Figure 2.22 Gain of the 1×5 patch array: simulation vs. measurement

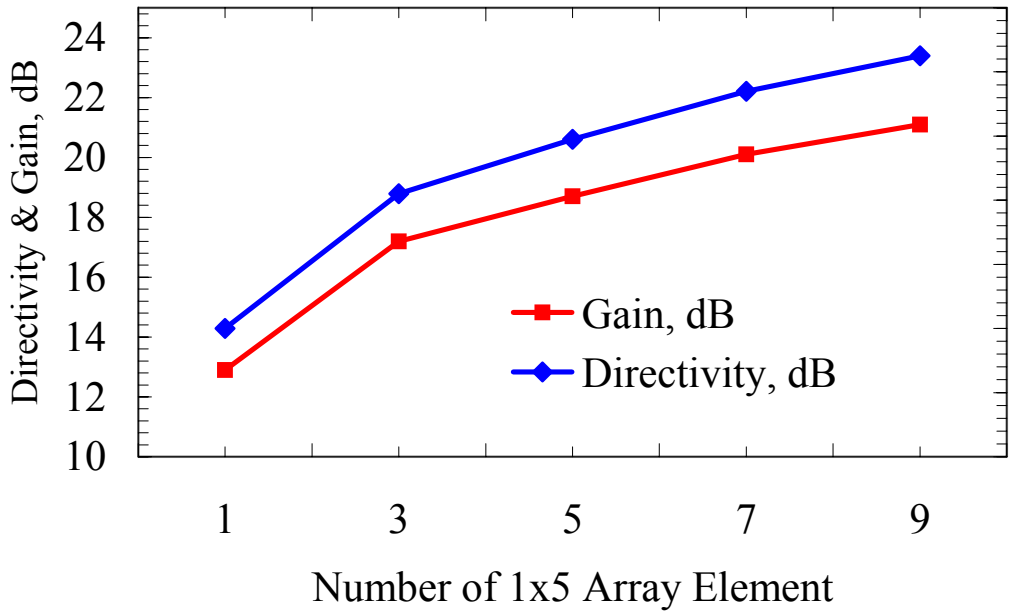

Figure 2.23 Directivity and gain when the number of 1×5 patch elements increases.

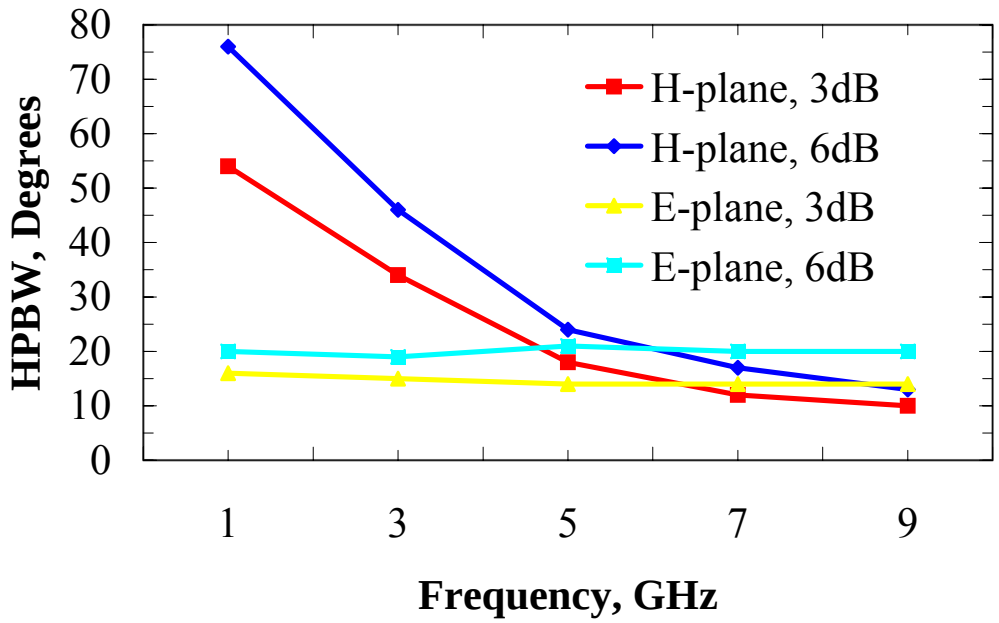

Figure 2.24 Change of HPBW as the number of array increases (E/H Plane).

An 8×5 passive patch array is built with the Wilkinson power combiner [42], which demonstrates a 20dB gain at 24GHz (Figure 2.28). Table 2.5 shows the results from measurements. It can be seen from Figure 2.28 that the gain variation is small over the 24 GHz band. If the insertion loss of combiner is subtracted from the total gain, this array should have a gain of 21-22 dB at 24 GHz.

Num of El	Size,	Bandwidth	Gain,	SL,	E-	H-
8×5	5×5=25	23.6 – 24.2GHz	20	10	20^{o}	16^{o}

Table 2.5 Measurement of the 8×5 Wilkinson combined patch array.

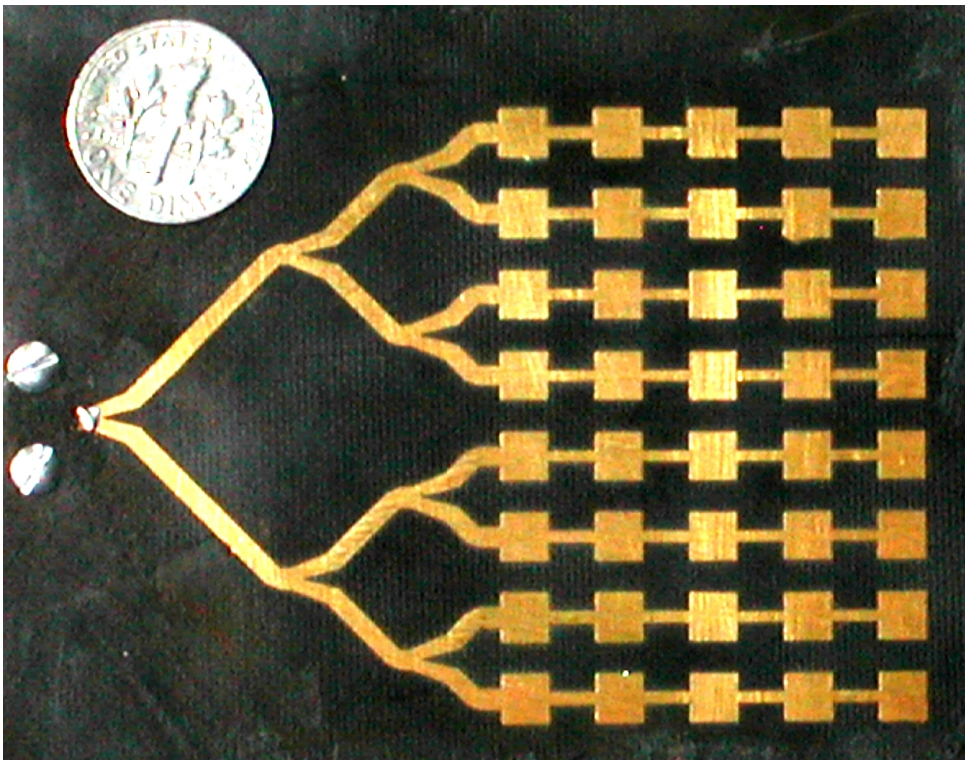

Figure 2.25 8×5 patch array by Wilkinson power divider.

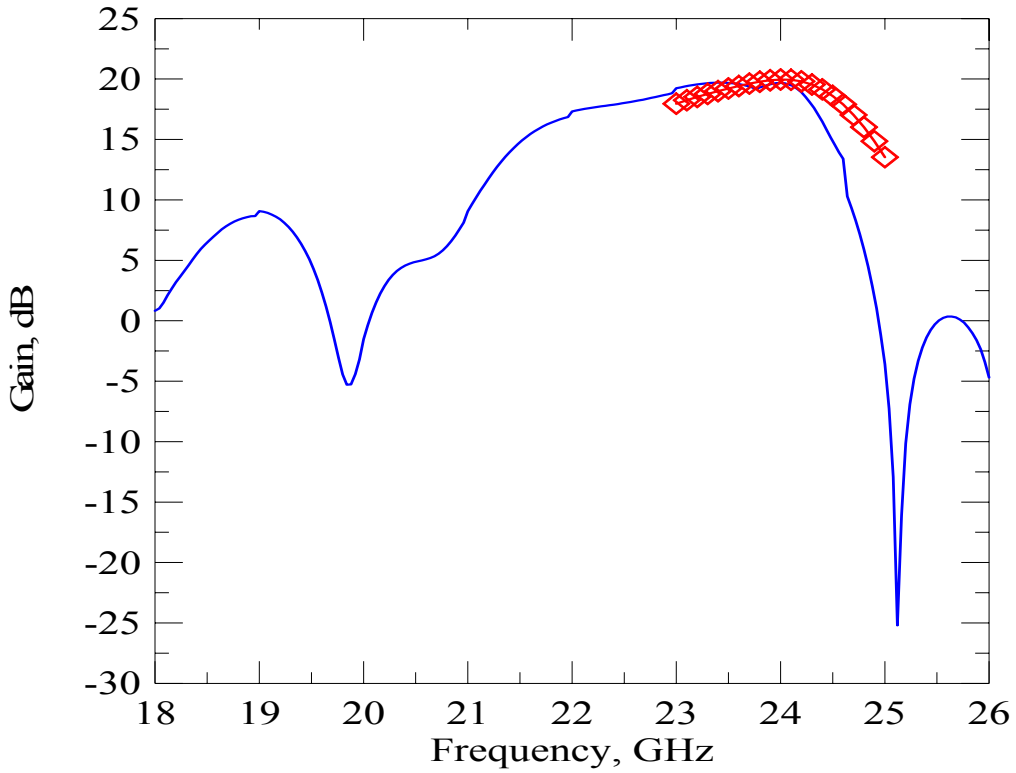

Figure 2.26 Antenna gain of the 8×5 patch array with Wilkinson power divider.

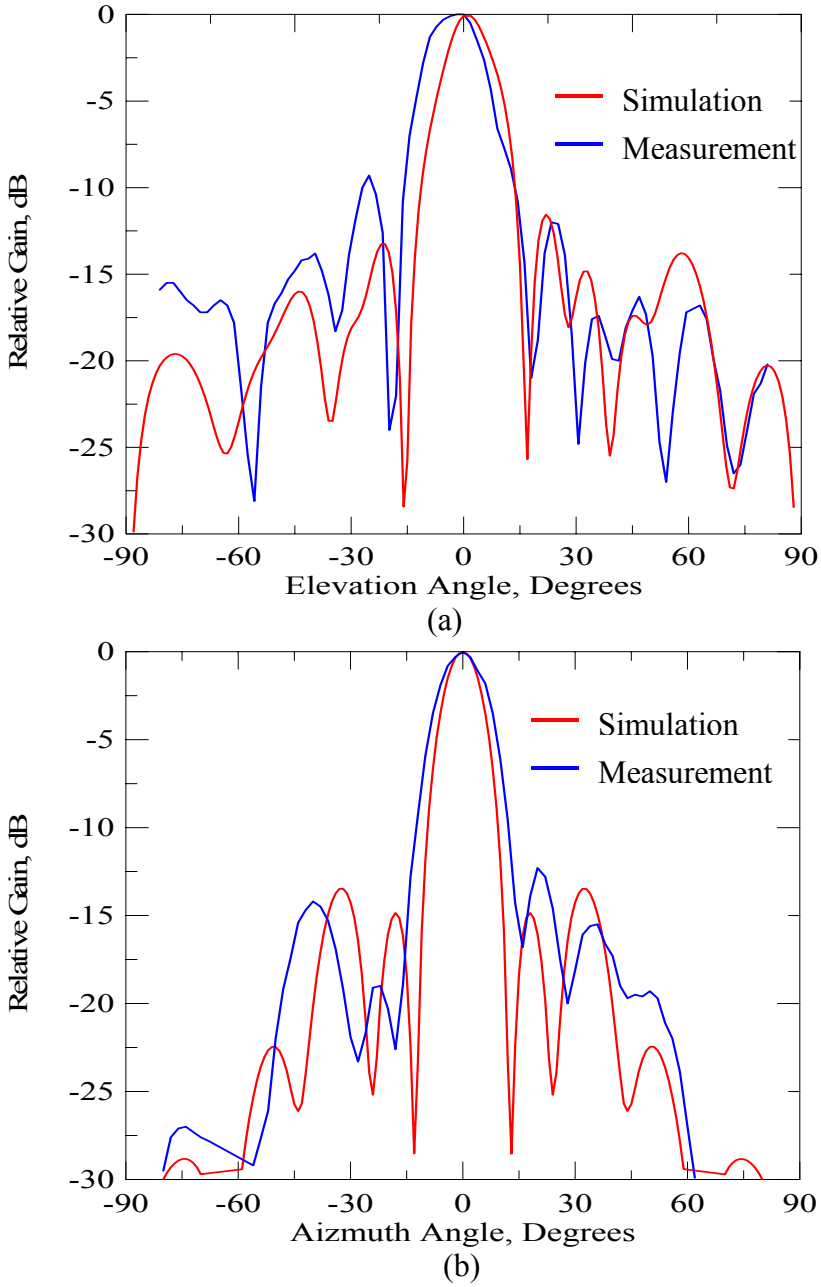

Figure 2.27 (a) E and (b) H plane of the Wilkinson combined 8×5 patch array.

2.2.3 Design of 24 GHz Phased Array

ADS Momentum and IE3D are used to simulate the input impedance and mutual coupling between the patch elements (Figure 2.30). It is found that the return loss for each element is pretty close. And the max mutual coupling is about –13.5dB. Beam scanning simulation is done with equal phase lagging between each patch elements. It

shows that the most appropriate scanning range of this array is –45° to 45° (Figure 2.31). Another limiting factor for the range of beam scanning is the gain drop. Simulation shows that the gain will drop 3dB with 45 degree scanning (Figure 2.32). The sidelobe level also gets worse when the main beam is shifted from the center.

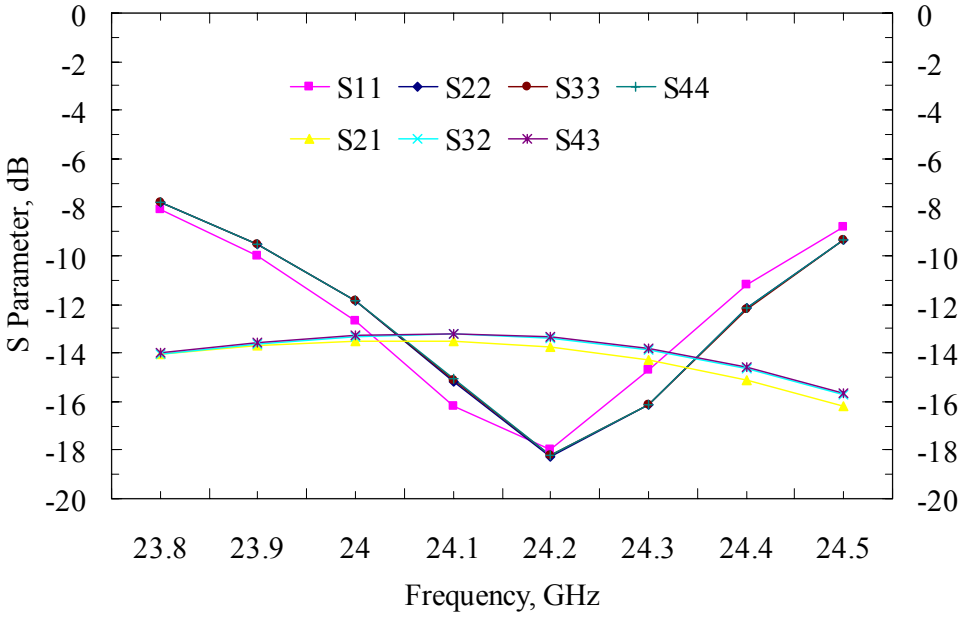

Figure 2.28 Return loss and mutual coupling of each 1×5 patch elements

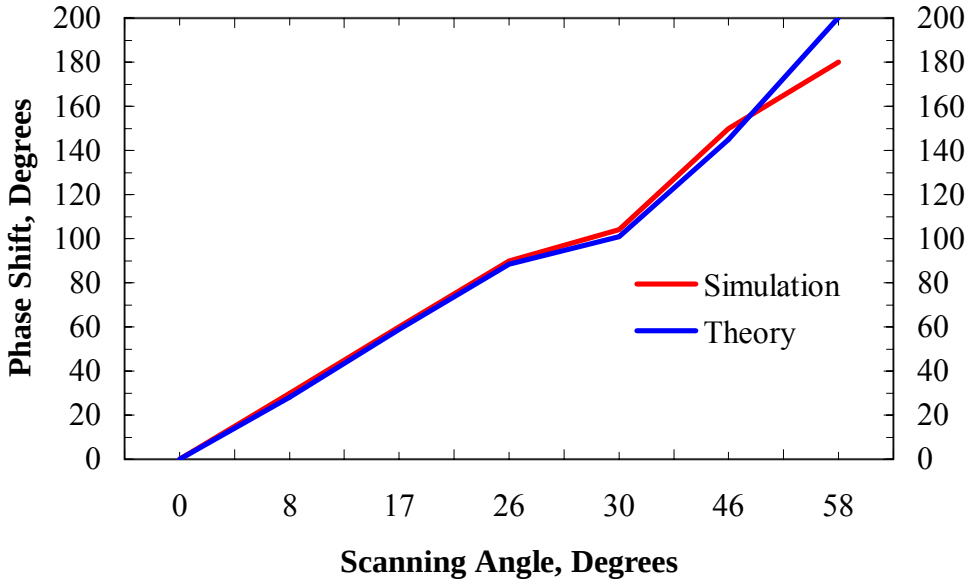

Figure 2.29 Scanning angle as a function of phase shifts.

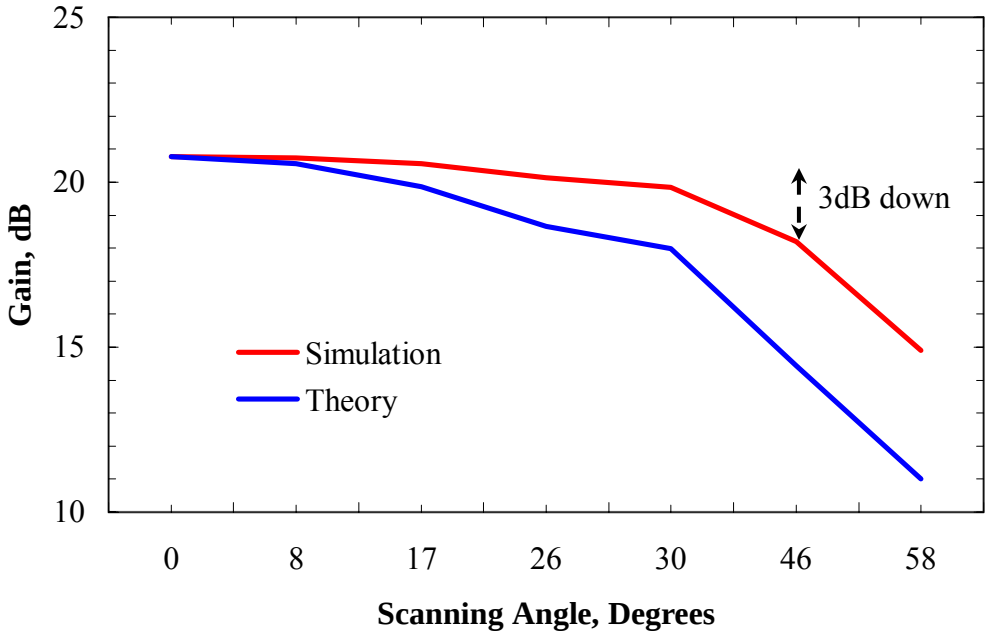

Figure 2.30 Gain drop during the beam scanning

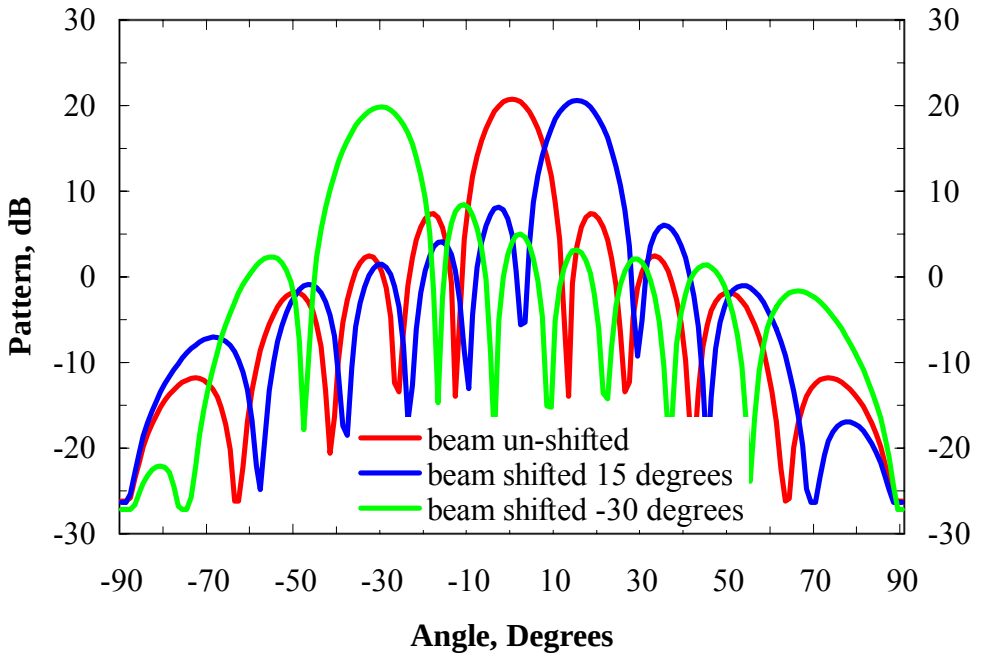

Figure 2.31 Array pattern during the shift of the main beam

2.3 Active Patch Array with PALNA

A 24 GHz “active” patch array is made by combining the PALNA MMIC chip and the 1×5 patch array through wire bonding on a gold plated brass board. The performance of this active antenna is obtained by small-signal, power and noise measurement inside the Caltech aneichoic chamber (Appendix A). Combined with mixer, oscillator and A/Ds, this active antenna can be made an effective phased array element for 24GHz WLAN.

2.3.1 Board Design

A prototype board is made to test this active patch array with PALNA. The board is machined on a thick brass plate with gold plating (Figure 2.34). As can be seen from the figure, different dimensions are for different circuit boards to fit in. The small island region is specially made for the PALNA MMIC chip so that it can be sit with the same top height as other Duroid boards besides.

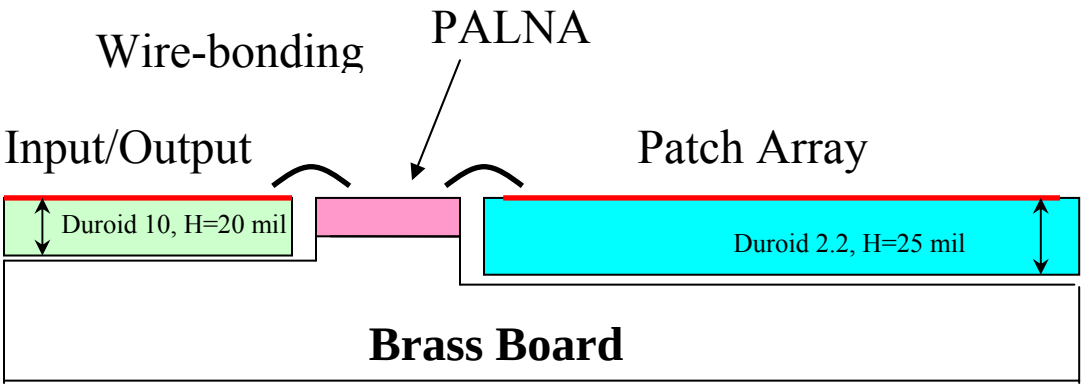

Figure 2.32 Board design for the active patch array

active antenna is built by cascading the patch array with the PALNA chip (Figure 2.3). We use wire bonding to make the inter-connections between GaAs to the Duroid boards for both RF and DC signal transmission. Four DC Bias are used to switch the chip

between transmitting and receiving states. The total size of the active patch array is 6×2.5 cm^2.

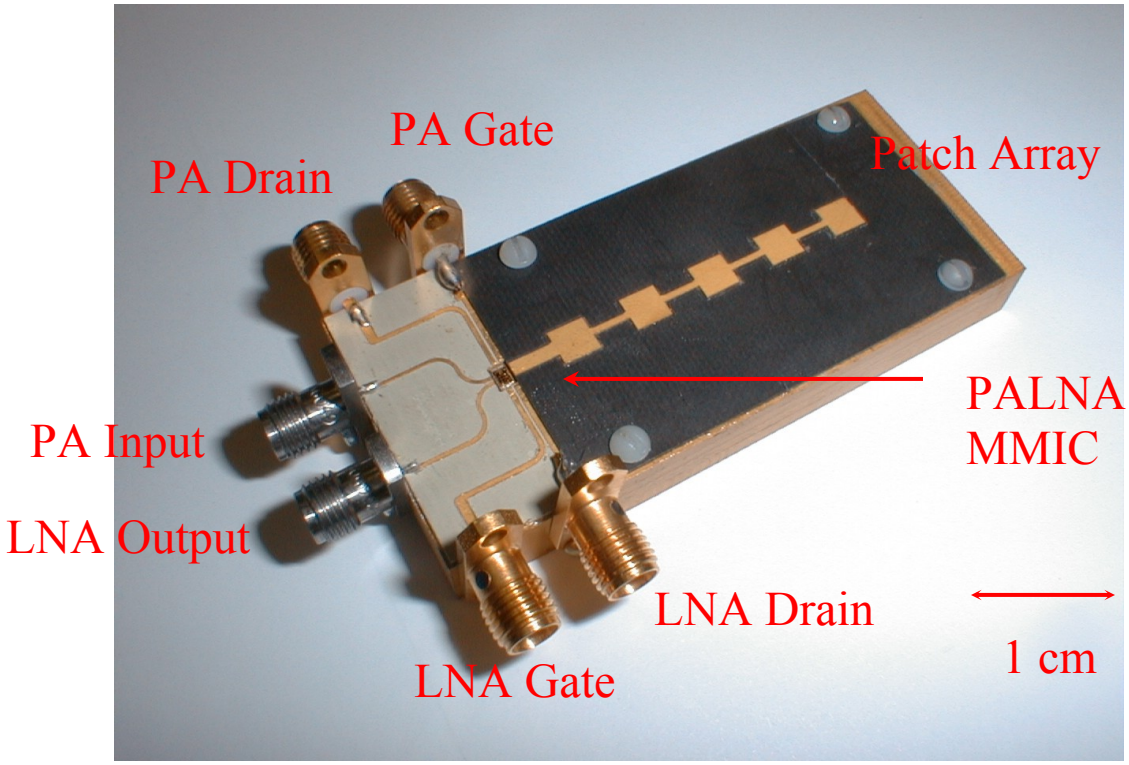

Figure 2.33 Active patch array with PALNA

2.3.2 Small Signal Active Gain

Two-port S-parameter measurement inside the chamber gives the small signal performance of the active antenna. We use Friis transmission formula to extract the active gain of this antenna after de-embedding the radiation loss. Both of the transmitting and receiving measurements shows a gain peak at 24GHz, which is 20dB above the passive patch array (Figure 2.36). The active gain in transmitting mode is 3.5dB higher than in receiving mode. This may be due to the better transition match between the PA than the LNA to the microstrip line.

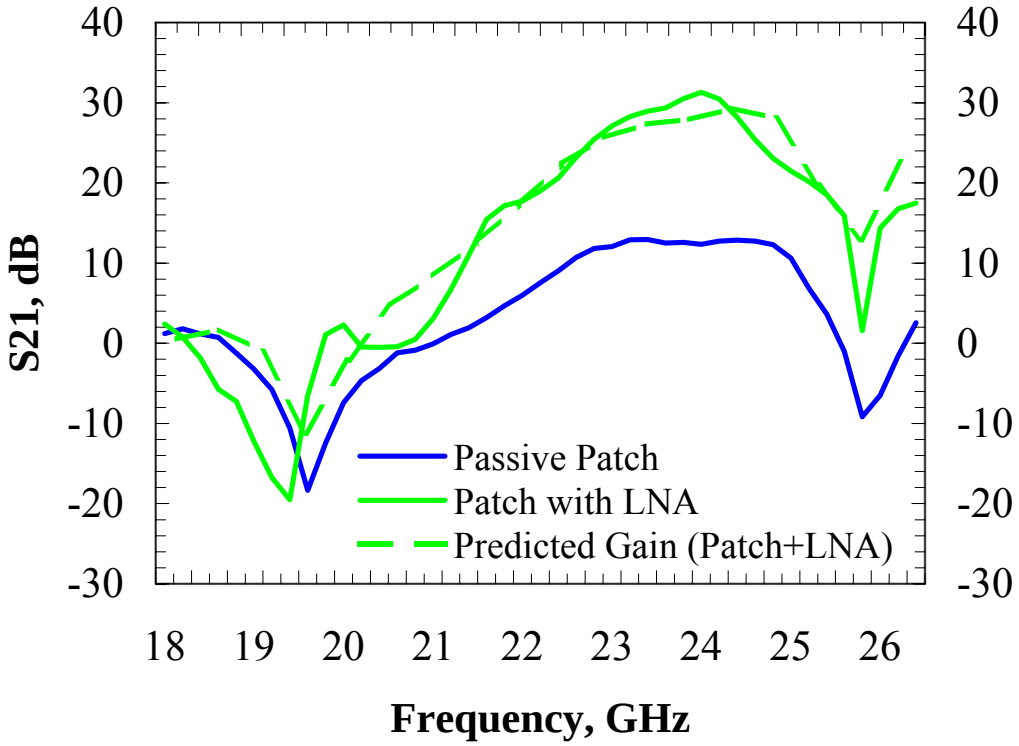

(a)

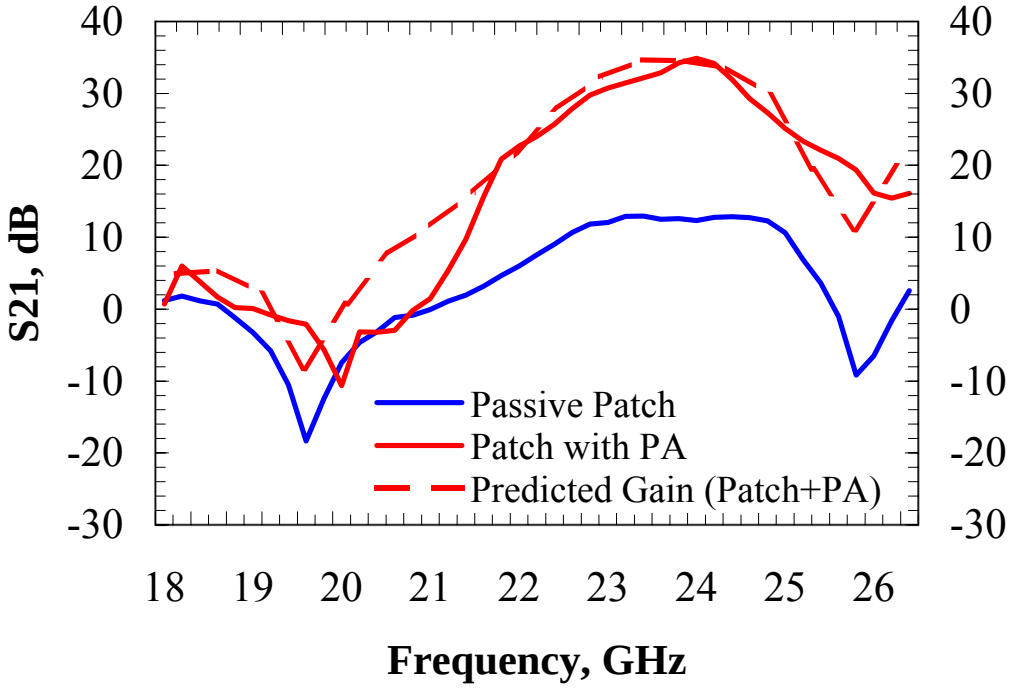

(b)

Figure 2.34 Patch array with PALNA in receive (a) and transmit (b) modes

E and H plane pattern comparisons are made between passive and active patch antenna (Figure 2.37). The nulls in the E plane are almost in position but the sidelobe amplitude ratios have changed. It seems from the plot that a sidelobe level of 10 dB is reached for both transmit and receive modes, which is better than the original passive patch. The H plane pattern looks quite similar. There are a few small ripples at large angles in the transmit mode which may due to the connector loose caused by trembling effects during the turning of step motor.

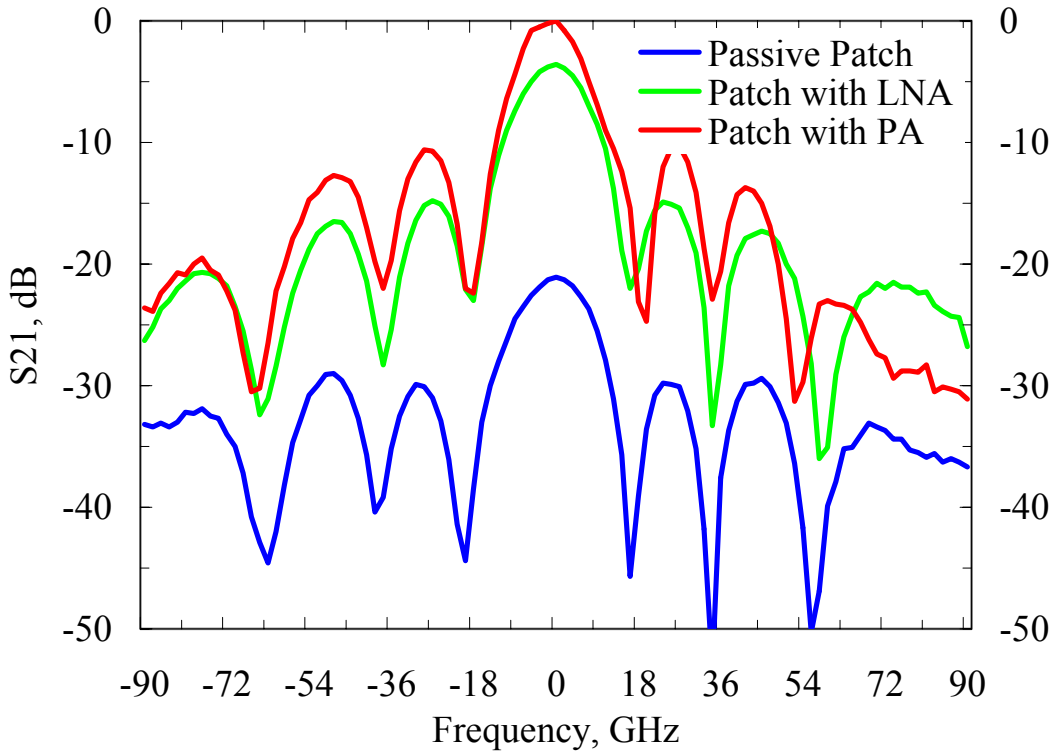

(a)

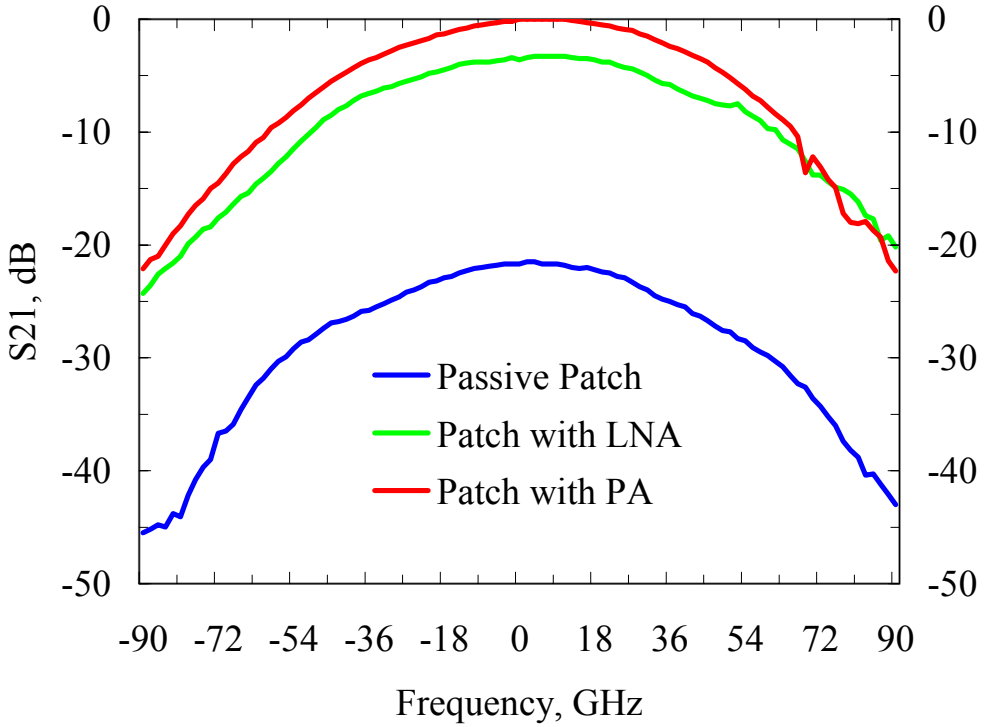

(b)

Figure 2.35 Normalized E-Plane (a) and H-Plane (b) patterns at 24 GHz

2.3.3 Power Measurement

To see how the power amplifier works with the antenna, a power sweeping is done in the anechoic chamber. 1 dB and 3 dB compression points can be found from the measurement (Figure 2.38(a)). EIRP (*Equivalent Isotropically Radiated Power*) is used to characterize the performance of the radiation, which is defined by

$$EIRP = P_{rad} \cdot Gain \tag{2.10}$$

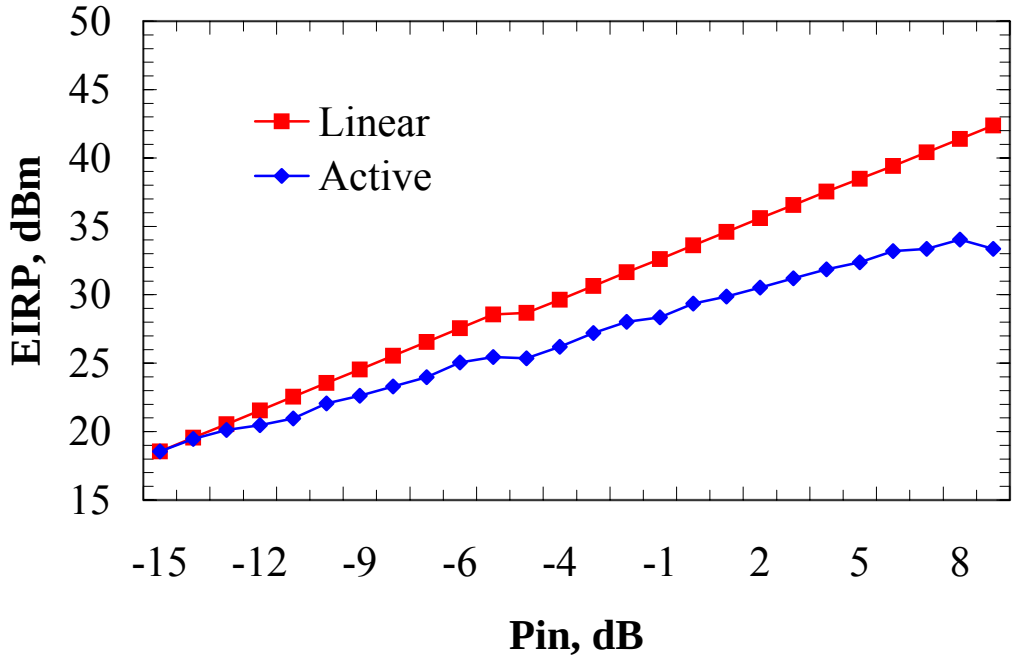

(a)

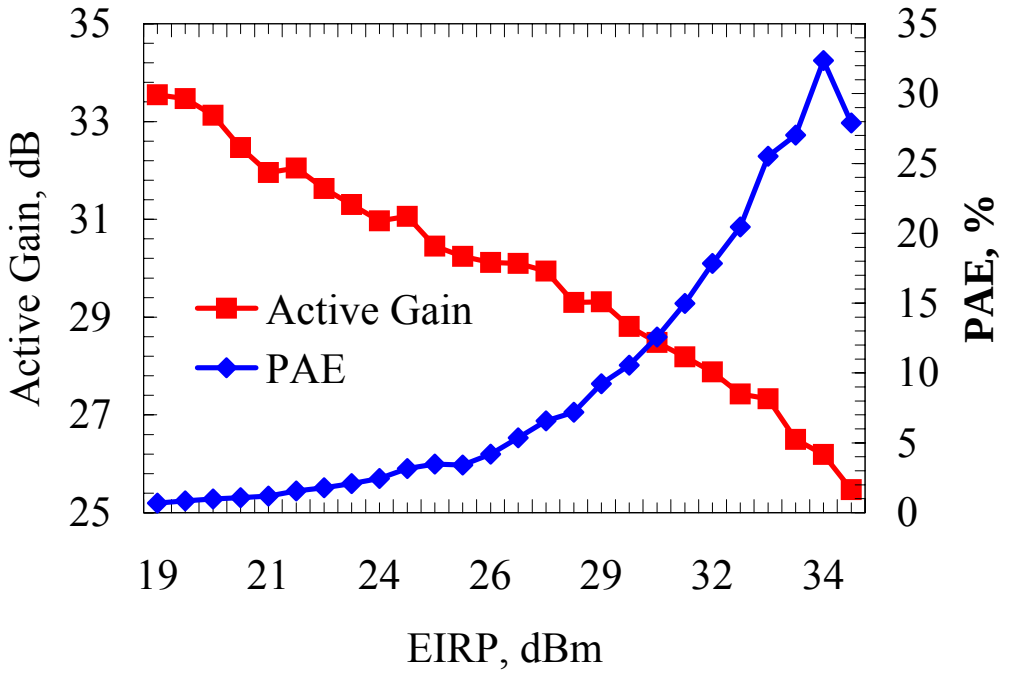

(b)

Figure 2.36 (a).EIRP vs. Pin; (b) Active gain and PAE vs. EIRP

By definition, EIRP is the power needed to feed in the isotropic radiator if the same amount of power is to be received. The maximum of EIRP of this active antenna can achieve is 34 dBm. This indicates that the total radiated power is 22 dBm, since we have 12 dB antenna gain. Also PAE (*Power Added Efficiency*) is calculated from the measurement data (Figure 2.38(b)). We measured all bias voltages and currents in the transmit mode to obtain the DC power consumption of active array. Treating the active antenna as a two-port device, with the known input RF power and DC power and total radiated power calculated from Friis formula, we can get power added efficiency by

$$PAE = \frac{P_{radiated} - P_{input}}{P_{DC}} \times 100\% \tag{2.11}$$

The maximum PAE we got is 32%, when the active gain drops to about 25 dB. All the measurements are done at 24 GHz.

2.3.4 Noise Figure Measurement

Noise figure is a very important performance factor for the receiver. The noise measurement has been done in the chip level, which gives about 4.4dB noise figure at 24GHz. This high noise value may partially due to the bad impedance matching to 50Ω. A more reliable noise measurement is done after inter-connection of the active device and antenna. The following setup (Figure 2.39) is used to do the do the Y-factor noise measurement [43]. The active antenna is facing down inside Styrofoam box with absorber materials filled. The output of the LNA is amplified by another two amplifiers and then sent to the spectrum analyzer. The first is a solid-state amplifier and the second is a TWT amplifier, which provides a total gain about 70dB cross the 18-35 GHz band.

This high amount of gain is necessary to bring the noise from LNA above the noise floor of the spectrum analyzer. The two amplifiers are calibrated before the measurement to obtain their noise figure and gain. When the active antenna is in receiver mode, two kinds of power measurement are done by the spectrum analyzer. One is at normal temperature, the other is at 77K by pouring liquid nitrogen (LN_2) inside the box to make a cold radiating source. The power ratio gives us the Y-factor. After de-embedding the noise of the post-amplifiers, the noise figure of the active antenna is obtained (Figure 2.40). We get a 3.5-dB minimal noise figure at 24GHz.

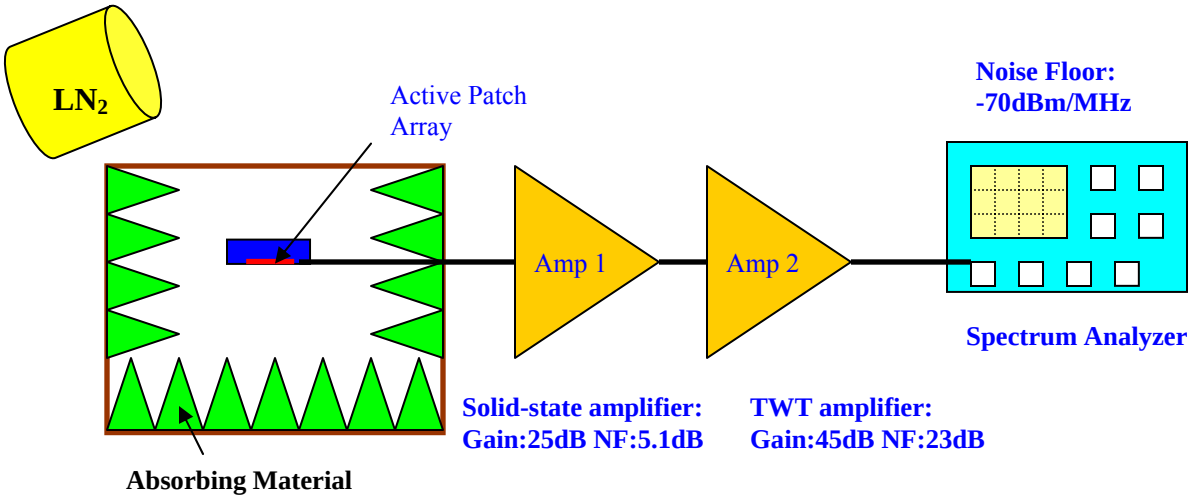

Figure 2.37 Setup for the noise figure measurement

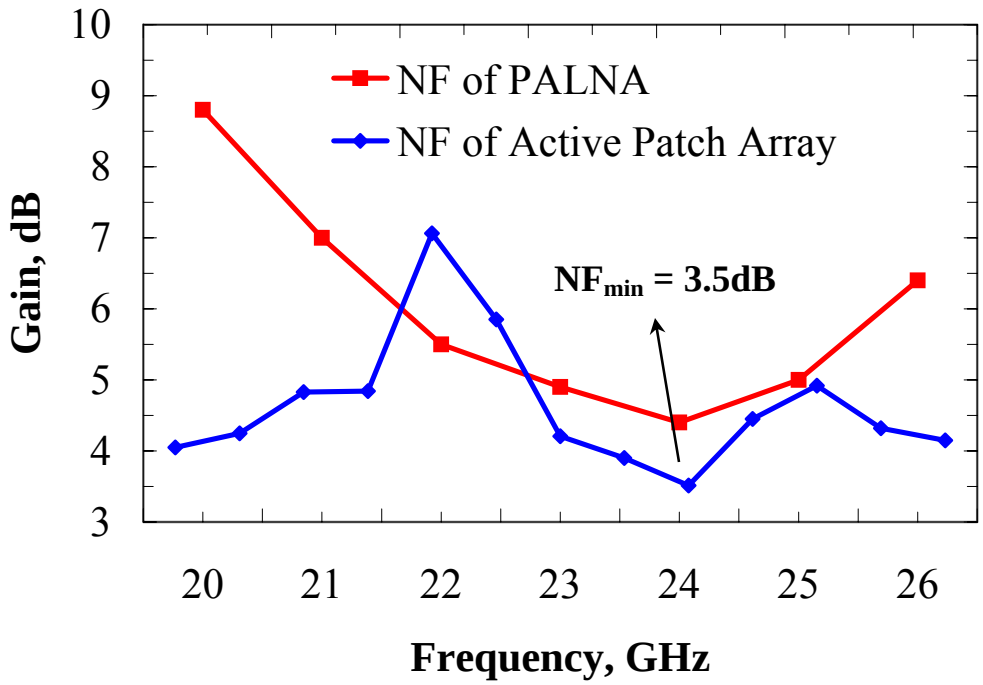

Figure 2.38 Noise figure of the active antenna in receiver mode

2.4 Conclusion and Future Work

An active patch array is built for 24GHz WLAN. This active antenna has demonstrated a 34dB gain in the transmit mode and 31dB gain in the receive mode. The total radiated power has a maximum of 22dBm with a PAE of 32%. The Y-factor method is used to measure the noise performance of this active antenna. A 3.5dB noise figure is obtained at 24GHz. This antenna is proved to be working successfully both as a transmit and receive active antenna.

There are many places that require future research work. For example, the PALNA design has to be revised to improve the return loss for both LNA and PA at 24 GHz. In addition, analysis must be carried out to find the reason of frequency shifting in the LNA

gain to 28 GHz. It must be understood whether this was due to inaccurate transistor model or ADS circuit model. If it is former, a transistor based characterization must be made to extract more accurate model for design. If it is the latter, part or all circuit (most transmission lines) must be re-modeled using full wave EM simulator. The series fed microstrip antenna is also a place that needs re-thinking. As we know, microstrip antenna has a very strict narrow impedance bandwidth. It is highly likely that the resonant frequency will be off due to un-expected effect such as back-side feeding of connector. It should be modeled accurately by 3D simulator such as HFSS or a broadband design with less sensitivity must be made. The 24 GHz WLAN system needs future work on the additional components such as VCO, mixer etc. Hossein Hashemi, a former Caltech graduate student has done some research work on the 24 GHz receiver [44]. That will be a good start to follow for a future design.

Chapter 3

Concepts of Indoor Channel Modeling for Future Wireless Communications

The current and future generation wireless standards require the support for a data transmission rate ranging from 2 to over 100 Mb/s [45]. Due to this increasing demand for high-speed wireless service, considerable efforts have been made in the field of channel investigation of radio waves, especially for the indoor environment.

3.1 Why a High-Frequency Band Is Needed

As we know, the maximum bit rate of the wireless link is imposed by the properties of the communication channel used and its upper bound can be calculated from the famous Shannon's channel capacity formula [46]:

$$C = B \cdot \log_2(1 + SNR) \tag{3.1}$$

where B is the bandwidth of the channel and SNR is the signal to noise ratio at the receiver. It means that a high bit rate transmission can be achieved by increasing either the signal to noise ratio (SNR) or the bandwidth of the communication channel. Due to safety considerations, the maximal power available for the transmission is limited by government regulations. Table 3.1 shows the maximum transmitter power for communication devices by the Federal Communications Commission (FCC) and the European Conference of Postal and Telecommunications Administrations [47]-[49]. This puts a limitation on the range of operation when the SNR required by the system is fixed.

Frequency	Band	Maximum Transmitter Power
2.4 GHz	802.11b, g	EIRP < 1W for antenna gain < 6 dB
		EIRP < 4 W for antenna gain > 6 dB
5.2 GHz	802.11a	5.15-5.25 GHz: 50 mW (FCC)
		5.25-5.35 GHz: 250 mW (FCC)
		5.725-5.825 GHz: 1W (FCC)
10 GHz	Amateur	1 W (FCC)
17 GHz	HIPERLAN	10 W (CEPT/ERC)
24 GHz	ISM	1 W (FCC)
3.1-10.6 GHz	UWB	-41.3 dBm / MHz (FCC)

Table 3.1 Transmitter-power limits

Also increasing the transmitter output power is not a best solution to improving data rates at the mobile part since the power consumption is a real concern for a battery life. Therefore, a higher bit rate is achieved instead by increasing the available channel bandwidth. The whole radio frequency spectrum has been already divided among various communication services by the FCC [50]. When the frequency is high, it is more likely that a larger channel bandwidth is available. The recent released UWB (Ultra Wide Band) standard [51] starts from 3.1 GHz up to 10.6 GHz, with a bandwidth of 7.5 GHz. As discussed in Chapter 2, the 24 GHz ISM (Industry, Scientific and Medical) band is chosen in our WLAN project, which has an available bandwidth of 250 MHz.

3.2 The Purpose of Indoor Channel Investigation

Any communication system has to cope with the difficulty caused by communication mediums. This difficulty is especially serious for indoor wireless communications. In a

typical indoor wireless system, the media is a multi-path channel where, due to the propagation phenomena, the transmitted signal suffers from interference, fading and noise. Moreover, the physical indoor channel is time-, frequency- and space-variant. Therefore, an appropriate characterization of the channel is indispensable during the design process of any communication system. Knowing the channel characteristics and properties ahead can help people design the wireless system, match to the environment impairments and therefore make it more efficient and robust.

3.3 Indoor Channel Modeling

As described before, the channel property is very important since it imposes constraints on the system's transmission rate, error probability and the distance over which the system can operate. Normally, we can use a linear filter with additive white Gaussian noise depicted in Figure 3.1 to model the channel. As can be seen in the figure, it is fully described by a time-variant impulse response function h(τ;t) [52] (where τ indicates the delay and t is the time variation of the function) and the noise statistics.

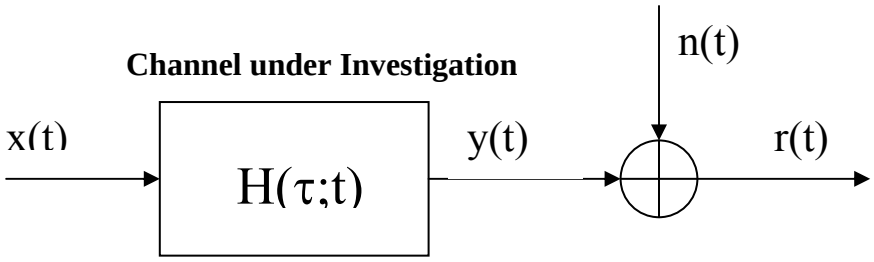

$$y(t) = \int_{-\infty}^{t} h(\tau;t) \cdot x(t-\tau) d\tau$$

Figure 3.1 The channel model for the radio waves

In the complex indoor environment, the transmission between transmitter and receiver is through many paths, which are caused by reflection, diffraction and scattering. These phenomena are explained below.

- Reflection occurs when a propagating electromagnetic wave impinges upon an object that has very large dimensions compared to those of the wavelength of the propagating wave. Reflection occurs from the surface of the ground, walls and furniture. When reflection occurs, the wave may also be partially refracted. The coefficient of reflection and refraction is a function of the material properties of the medium, and generally depends on the wave polarization, angle of incidence, and the frequency of the propagating wave.
- Diffraction occurs when the radio path between a transmitter and receiver is obstructed by a surface that has sharp edges. The waves produced by the obstructing surface are present throughout the space and even behind the obstacle, giving rise to bending of waves around the obstacle, even when a line-of-sight (LOS) path does not exist between the transmitter and receiver. At high frequencies, diffraction, like reflection, depends on the geometry of the object as well as the amplitude, phase, and polarization of the incident wave at the point of diffraction.
- Scattering occurs when the medium through which the wave propagates consists of objects with dimensions that are small compared to the wavelength, and where the number of obstacles per unit volume is large. Scattered waves are produced by rough surfaces, small objects, or by other irregularities in the channel. In practice, foliage, lampposts and stairs within buildings, light wedges can introduce scattering in the

mobile communication systems. In most cases of indoor communication, scattering can be neglected.

A transmitted signal, which experiences the influence of reflection, refraction and scattering, reaches the receiver via many different paths. This is what we called multipath propagation [53] and is depicted in Figure 3.2. Each replica of the signal arrives at the receiver over a different distance and thus has different amplitudes, phases, and time delay. The superposition of all these multipath (3.2) will determine whether the signal is enforced or reduced (multipath fading [54]).

$$\vec{E}_{receive} = \sum_i \vec{E}_i = \sum_i E_O G_{Tx}(\theta_i, \varphi_i) \cdot G_{Rx}(\theta_i, \varphi_i) L_i(d_i) \cdot \prod \Gamma_i^{\,j} \cdot \prod T_i^{\,k} \cdot e^{-jkd_i} \qquad (3.2)$$

where E_o is the amplitude of the reference incident field, G_{Tx}, G_{Rx} are radiation patterns of the transmitting and receiving antennas, $L_i(d_i)$ is the path loss of i^{th} multipath, and Γ and T are reflection and transmission coefficients through the i^{th} multipath component.

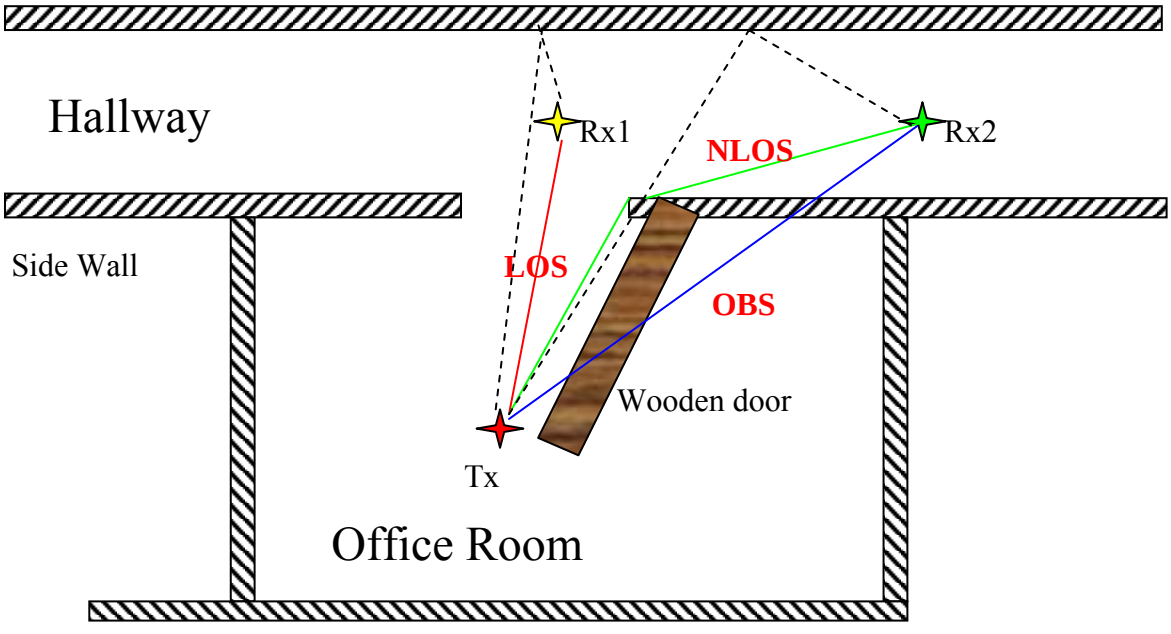

Figure 3.2 Multipath propagation in the building (Tx – transmitter, Rx – receiver)

As can be seen from Figure 3.2, there are three signal paths related to the locations of the transmitter and receiver. They are LOS (line of sight), NLOS (non-line of sight), and OBS (obstructed line of sight). In the following part, OBS and NLOS are treated together as NLOS for simplicity.

3.4 The Effects of the Multipath Propagation

As can be expected, the multipath introduced by the complex indoor environment affects a lot on the performance of communications inside buildings. This effect is further analyzed in both time and frequency domain.

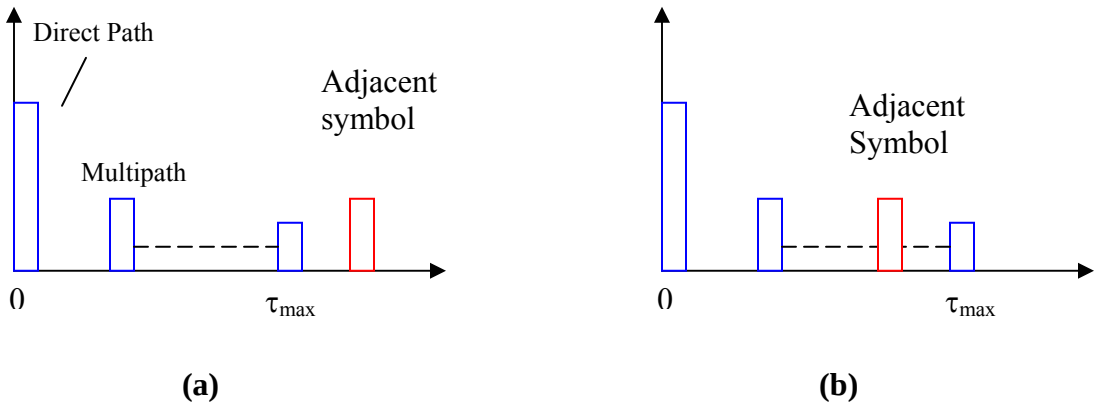

Figure 3.3 Received signal in the time domain: (a). slow rate transmission; (b). high-rate transmission.

First, it is easy to understand the multipath effect in the time domain. Since the multipath reaches the receiver at different time delay, the received symbols are spread over time. This may cause adjacent symbols to overlap, which is called ISI (Inter-Symbol Interference). If the data rate is slow, the symbol duration is long compared to the delay

spread of the channel, the delayed symbol will not affect the next coming symbol. However, if the data are transmitted at a high rate, the receiver is not able to resolve the the next symbol and the delayed multipath, since they overlap in time. This is why a lower delay spread is always required for a wireless communication system to achieve a high bit-rate transmission.

This effect in the frequency domain becomes the frequency selectivity of the channel. Due to multipath propagation in the channel, the transmitted signal will get enforcement at some frequencies but suppression (deep fades) at others.

In addition to the already presented description in the time domain, an equivalent description in the frequency domain can be provided. By applying the Fourier transform to the channel response h(τ;t), the time-variant channel transfer function H(f;t) is obtained

$$H(f;t) = \int_{-\infty}^{\infty} h(\tau;t) \cdot e^{-j2\pi f\tau} d\tau \tag{3.3}$$

There are many useful channel correlation functions that can be explored in the channel characterization. Since the nature of the channel is random, it is better to describe the unpredictable behavior of the channel by the autocorrelation functions. The autocorrelation function of h(τ;t) is then defined as follows

$$\phi(\tau_1, \tau_2; t_1, t_2) = \frac{1}{2} E\left[h^*(\tau_1; t_1) \cdot h(\tau_2; t_2)\right] \tag{3.4}$$

where x^* denotes the complex conjugation. In many cases, the channel is **Wide Sense Stationary** (WSS) [55]. This implies that the given autocorrelation function does not

depend on the particular time instants t_1 and t_2, but only on the time difference between them. Also, another good assumption is **Uncorrelated Scattering** (US), which means that the signal coming via different paths experience uncorrelated attenuations, phases and time delays, the formula transforms to

$$\phi(\tau_1,\tau_2;t_1,t_2)=\frac{1}{2}E\left[h^*(\tau_1;t)\cdot h(\tau_2;t+\Delta t)\right]=\phi_h(\tau_1;\Delta t)\cdot\delta(\tau_1-\tau_2) \tag{3.5}$$

In this case, the channel is said to be a Wide Sense Stationary Uncorrelated Scattering channel [56]-[57]. If the time difference is set to zero, the resulting autocorrelation function describes the time spread of the channel. This function is called multipath intensity profile or the **Power Delay Profile** (PDP) and represents the average power output of the channel as a function of the time delay τ. Hence, the function provides a measure for the time dispersion of the channel. The measure is called **RMS delay spread** of the channel [58], and is denoted by τ_{rms} and defined as the square root of the second central moment of the power delay profile by the formula

$$\tau_{rms}=\sqrt{\int_{-\infty}^{\infty}\frac{(t-\tau_m)^2\,PDP(t)}{\overline{P_c}}dt} \tag{3.6}$$

where τ_m is the average delay time, $\overline{P_c}$ is the average channel power response and $PDP(t)=|h(t)|^2$ is the power delay profile. The same procedure can be repeated in the frequency domain. The equivalent autocorrelation function in the frequency domain is defined by

$$\phi_H(f_1,f_2;\Delta t)=\frac{1}{2}E\left[H^*(f_1;t)\cdot H(f_2;t+\Delta t)\right]\xrightarrow{\Delta f=f_2-f_1}\phi_H(\Delta f;\Delta t) \tag{3.7}$$

This is called the spaced-frequency, spaced-time correlation function. As the channel transfer function and the channel impulse response are a Fourier pair, it is not surprising

that their autocorrelation functions $\phi_h(\tau, \Delta t)$ and $\phi_H(\Delta f; \Delta t)$ are also a Fourier pair. Again, if $\Delta t = 0$, the derived function $\phi_H(\Delta f) = \phi_H(\Delta f; 0)$ is the Fourier transform of the multipath intensity profile. It provides the information about the channel's coherence in the frequency domain. The measure for this coherence is called the coherence bandwidth of the channel B_c, which is related to the RMS delay spread as

$$B_c \approx \frac{1}{\alpha \tau_{rms}} \tag{3.8}$$

where $\alpha = 2\pi$ in case of the exponentially decaying PDP [59]. The coherence bandwidth is an important measure in the characterization of the channel since it givers an indication whether the channel is frequency selective or frequency nonselective with respect to the bandwidth of the transmitted signal. When the coherence bandwidth is small compared to the bandwidth of the transmitted signal, different frequencies of the signal spectrum are affected by the channel differently; the channel is said to be frequency selective. However, if the bandwidth of the transmitted signal is narrow compared to the coherence bandwidth of the channel, all the frequency components of the signal undergo the same attenuation; the channel is said to be frequency selective.

The time variations of the channel can also cause Doppler shift. Due to the slow movements in normal indoor environment and high frequency bands for communication, the Doppler shift is always quite small. This effect is ignored in the following research.

To give a complete picture of the channel functions involved, a summary diagram is shown in Figure 3.4.

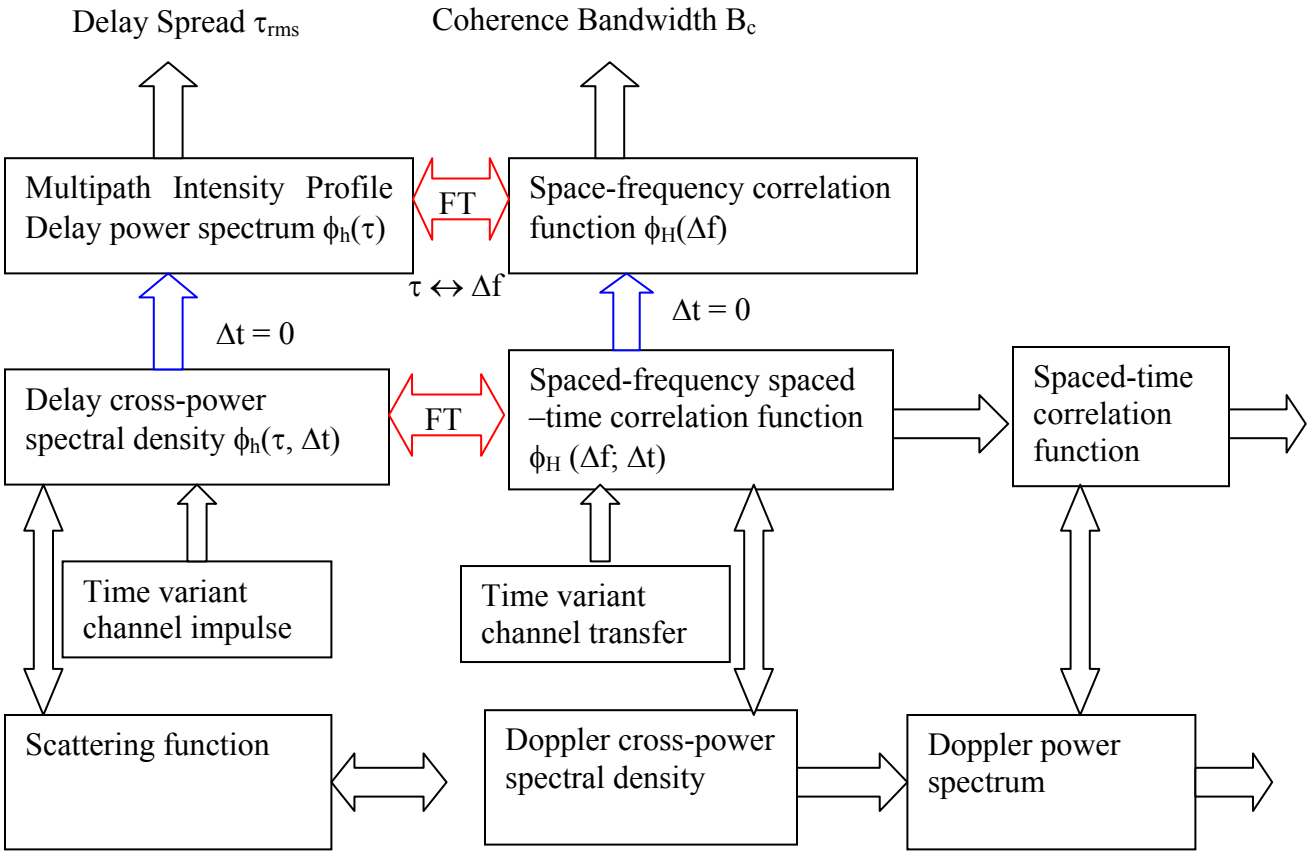

Figure 3.4 The relations between channel correlation functions

3.5 Types of Channel Models

There are various channel models in the literature, which are convenient to describe and parameterize the behavior of the multipath medium. The most frequently used is the time domain model, which originates from a description of the multipath phenomenon in the time domain. However, frequency domain model can also be found. The description in the frequency domain can be beneficial in some cases, i.e. when the description of the communication system take place in this domain, as it is the case for OFDM systems.

3.5.1 Time Domain Model

The description of the time domain modeling is directly related to the impulse response function of the channel $h(\tau,t)$, presented in the previous section. Since the parameters of the impulse response are random process, the appropriate statistic process has to be determined. That process can be found empirically by measurement.

The most commonly used distribution for the impulse response variables of the channel are the following. The phase is uniformly distributed over $[0, 2\pi)$. The distribution of the path arrival times can be modeled as a standard Poisson process or modified Poisson process. The average path amplitude can be modeled as a decaying function (e.g. exponentially decaying). On top of it, small-scale variations in the amplitudes are usually modeled as a Rayleigh or Ricean process.

3.5.2 Frequency Domain Model

An equivalent model can be built in the frequency domain. In this case, the frequency transfer function is used as a representation of the linear time-variant filters in the frequency domain. It is possible to make transition to time domain by applying inverse Fourier transform. The spaced-frequency, spaced-time correlation function $\phi_H(\Delta f;\Delta t)$ is a convenient description, since the function represents the frequency selectivity and the time variability of the channel transfer function. Further details about the frequency domain modeling can be found in [60] and [61].

3.6 Signal Variation in Space

The effect of the space variations is explained in this section. The types of the signal variation are divided with respect to the wavelength of the transmitted signal.

3.6.1 Large-scale Fading

Large-scale fading represents loss in average signal power with an increasing distance. A commonly used formula describing the large-scale fading effects is

$$PL(d) \propto \left(\frac{d}{d_o} \right)^{\alpha} \tag{3.9}$$

where α is the path loss factor, d_o is the reference distance (usually d_o=1 m) and d is the distance between the transmit and receive antennas. The path loss component indicates how fast the signal power is decaying as a function of distance. In logarithmic scale, the equation transforms to

$$PL_{dB}(d) = PL_{dB}(d_o) + 10\alpha \log_{10}\left(\frac{d}{d_o} \right) \tag{3.10}$$

with a reference distance d_o (corresponding to the point located in the far field of the antenna).

3.6.2 Shadowing Effect

According to the previous equation, the receiver always experiences the same signal power at two different locations, each having the same Tx-Rx distance. The results obtained at various sites with the same antenna separation have shown that the received signal power can vary significantly. Moreover, this type of variation tends to be unpredictable. To model them statistically, an appropriate random process has to be

chosen. The measurement has shown a good agreement of the signal power variations around the average path loss with the log-normal distribution (the Gaussian distribution in logarithmic scale). Therefore, the shadowing effect is usually modeled as a log-normal random process. The path loss model is

$$PL_{dB}(d) = PL_{dB}(d_o) + 10\alpha \log_{10}\left(\frac{d}{d_o}\right) + X_\sigma \tag{3.11}$$

where X_σ is a zero-mean Gaussian variable in the logarithmic scale with a standard deviation σ.

3.6.3 Small-scale (fast) Fading

Small-scale fading occurs over very small distances, usually in the order of a wavelength. Small displacements of one of the antennas can lead to dramatic changes in the signal reception due to multipath propagation. This not because of the change in number of multipath components, the amplitudes, but because of their phases have significant changes. This can be illustrated as in Figure 3.5.

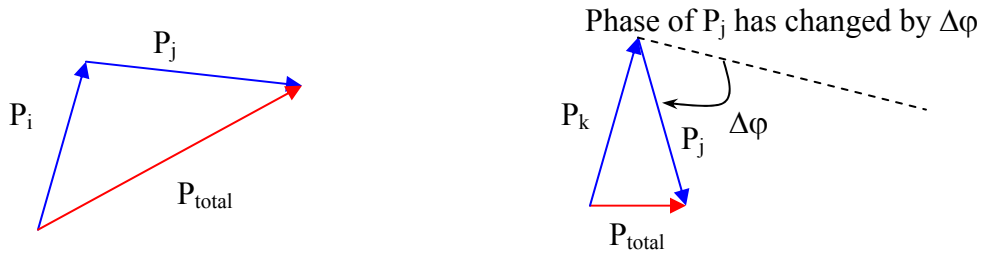

Figure 3.5 The small-scale fading effect

Applying the theory of random process, we can find out that if channel is a complex Gaussian zero-mean random process, the magnitudes of coming signal is Rayleigh distributed, whereas the phase is uniformly distributed over the interval [0, 2π),

3.7 Classification of the Channels

The channels can be classified into the following groups: time flat, frequency-flat, flat-flat and non-flat. This is according to the flatness of the signal in each domain. For example, if the channel is flat in both time and frequency domain, it is called a flat-flat channel. The introduced types of the channels are summarized in Figure 3.6.

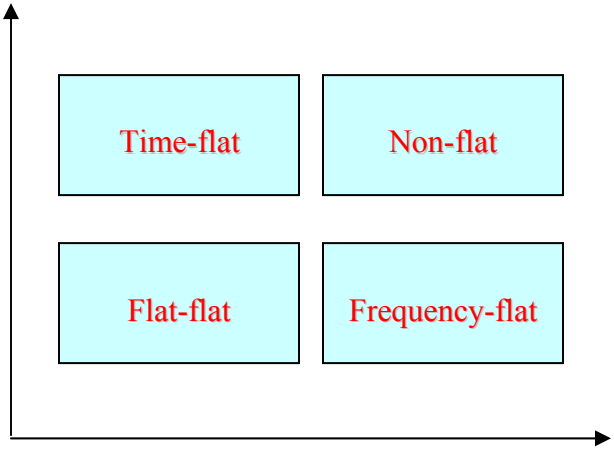

Figure 3.6 Classification of the channels

3.8 Techniques for Channel Measurement

The important channel parameters have been introduced in the previous sections. The values of these parameters have to be obtained from the channel measurement. There are many types of measurement techniques available. The choice of a particular technique depends on the desired parameters and their prospective application.

3.8.1 Narrowband Channel Sounding

This method is based on the transmission of an unmodulated carrier wave (CW) over the channel. The receiver is usually movable, allowing the channel statistics to be gathered over large areas in a relative fast way. The narrowband techniques are suitable for the measurement of path loss effect, mid-scale fading statistics and Doppler effects. This is the method the author has used to do the channel modeling in the 3rd floor of Moore lab. The receiver is sitting on a movable cart by automatic controlled motor.

3.8.2 Wideband Channel Sounding

The wideband channel sounding techniques are used when the wide band description of the channel is required. This technique can be categorized with respect to the domain in which the measurement is performed.

3.8.2.1 Time Domain (pulse) Sounding

This is the most commonly used technique in channel measurements. The method is based on the transmission of a single pulse. The signal detected at the receiver consists of a number of delayed pulses. From the received signal, the channel impulse response power delay profile is determined. Even though there are power and time limitation of this method, it is fast and well suited for determining the power delay profile (PDP).

3.8.2.2 Coherence Frequency Domain Sounding

This technique is based on sweeping the measured bandwidth with a single sine-wave signal. As the result, the channel transfer function is solved. The technique implies coherent measurements and therefore the information about both amplitude and phase is required. Having the complex transfer function in the frequency domain, a transfer to the time domain is possible. The advantage of this method over the time domain measurements is that the accuracy of the time domain representation is only limited by the frequency range of the sweep. More over, it provides phase information while others don't. The disadvantage of this method is that the channel has to be remain unchanged during the operation. Consequently, no Doppler effects can be measured. Another disadvantage is that cables used to keep the reference phase have limited the distance between transmitter and receiver.

3.8.2.3 Non-coherenet Frequency Domain Sounding

In this modified approach, only the received signal power is measured over the considered frequency range. Although phase information is missing, through the data process, it is still possible to estimate the channel properties ([60], [61]) by calculating LCR (Level Crossing Rate).

3.8.2.4 Correlation Sounding

This technique employs spread spectrum transmission. A sine-wave signal is modulated with a pseudo-random sequence and sent over a channel. At the receiver, the same pseudo-random code is used to retrieve the transmitted signal. The code generator runs, however slightly slower than the transmitter. As a result, different multipath

components are sequentially correlated with code. The method is often used to perform measurements in frequency bands that are occupied by the existing communication systems.

Chapter 4

Empirical Explorations of Indoor Wireless Channels

In chapter 3, we have introduced some basic concepts in the channel modeling. Some of the channel parameters such as path loss exponents and RMS delay spread are derived from the measurement data and shown in this chapter. On frequency bands, we are particularly interested in 24 GHz since it is the ISM band we proposed for our phased array based WLAN project [62] (Chapter 2) at RF and Microwave group. For comparison, measurements have also been done at 2.4 GHz (802.11b, ISM), 5.2 GHz (802.11a U-NII) 10 GHz (US Amateur) and 17 GHz (HIPERLAN II) bands for a comparison (Table 3.1). Wysocki, Lobeira and other researchers have done channel modeling at these frequencies before [63]-[65]. But comparison has not been done.

On measurement techniques, we have applied both coherent frequency domain sounding and non-coherent frequency domain sounding in order to obtain both path loss and delay spread information.

4.1 Measurement Setup (Appendix B)

Two different measurement setups are used in the channel investigation. They are scalar and vector measurement setups (Figure 4.1). The scalar measurement is applied to find the narrowband channel information such as excess path loss and path loss

exponents. And the vector measurement is applied to find out the wideband channel information such as RMS delay spread. In the scalar measurement setup, an Anritsu 68397 signal generator (10MHz-65GHz) provides the CW wave for the transmitting signal. Depending on the frequency of operation, this signal is amplified by either an HP8349B amplifier (2-20 GHz) or a Litton TWT (18-40GHz) to boost the output power at the antenna. The total output power varies between 100mW and 1W (FCC rule). An HP8563 spectrum analyzer is used in the receiver. A pair of AEL broadband horns that cover all bands with a gain of 6-9dB are used for transmitting and receiving. In the vector measurement setup, an HP8722 vector network analyzer is used to extract the Power Delay Profile by coherent frequency domain sounding. The PDP data can be used later to calculate the RMS delay spread (τ_{rms}). LABVIEW programs are written to realize two functions: data acquisition and motor control. First, it is used to extract raw measurement data from testing instrument such as spectrum analyzer and network analyzer and save them in the computer file. Second, it is applied to control the movement of the receiver cart. The client program on the transmitter side can send this command to the server on receiver cart through WLAN to avoid near-field interference.

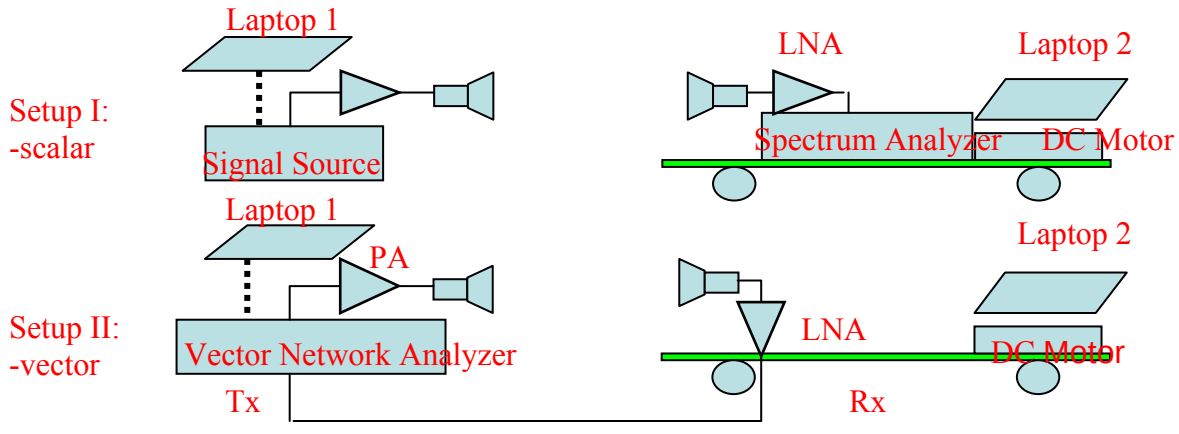

Figure 4.1 Measurement setups for indoor channel investigation

4.2 Path Loss Measurements

The wireless indoor channel investigation is done in the Moore Lab, which is the Electrical Engineering Department at Caltech (Figure 4.2). Three different scenarios have been chosen in the path loss measurements.

Figure 4.2 Moore Laboratory – Electrical Engineering Department, Caltech

The first scenario is floor to floor. Two typical areas in the Moore Lab are considered. The first is the pipeline area, where pipes for AC and water go along the ceiling. The second is the clean area (no pipes) at both ends of the hallway. Table 4.1 shows the excess path loss through one floor in pipe area. This excess path loss is calculated by subtracting free space path loss from the total path loss. As we can see, polarization does not affect much in the result. The loss increases rapidly with frequency from 15 dB at 2.4 GHz to 50 dB at 24 GHz. The data indicates that the low-frequency bands are better for a multi-story wireless system. But high ones provide a high system isolation.

Tx Antenna Polarization	2.45GHz	5.25GHz	10GHz	17GHz	24GHz
Parallel to hallway	16	19	27	45	50
Perpendicular to hallway	15	18	24	44	52

Table 4.1 Excess path loss in dB from the 3rd floor to the 2nd floor.

We also measured the path loss through floors from 3rd floor to the subbasement with antenna polarization parallel to the hallway. The result is given in Table 4.2. There are blank spaces in the table because we cannot detect the signal at that location with the maximum power we can provide. The path loss increases rapidly with the number of floors in a non-linear way as what was recorded in Seidel and Rappaport's paper [66].

Frequency, GHz		**2.45**	**5.25**	**10**	**17**	**24**
Pipe area	3rd to 2nd	28	28	42	50	40
	3rd to 1st	35	46	N/A	N/A	N/A
	3rd to basement	53	66	N/A	N/A	N/A
	3rd to sub basement	67	N/A	N/A	N/A	N/A
Clean area	3rd to 2nd	15	13	24	40	38
	3rd to 1st	27	32	53	N/A	N/A

Table 4.2 Excess path loss in dB for different numbers of floors at 2.45GHz.

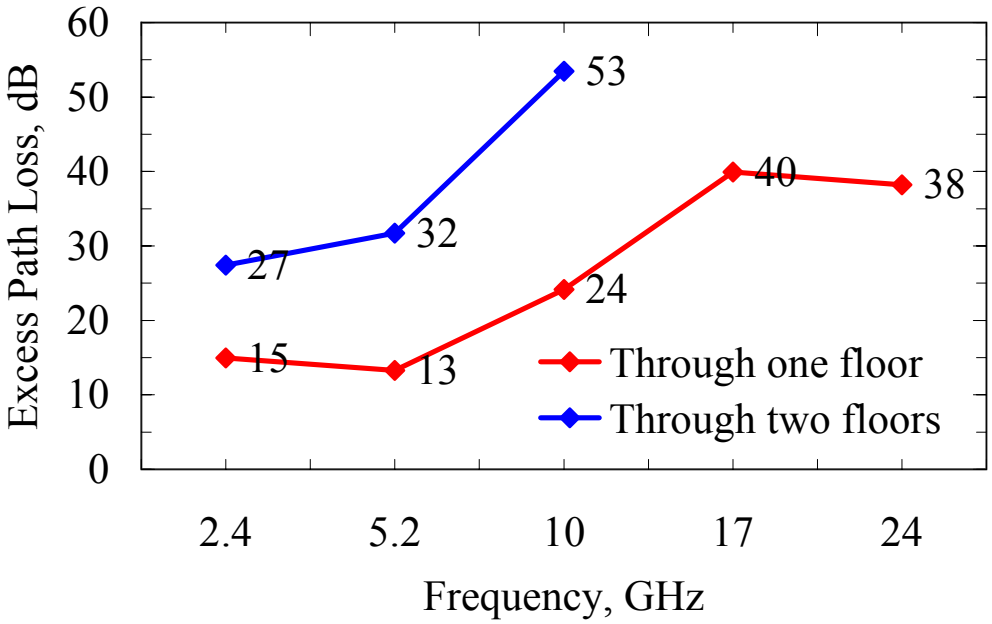

Figure 4.3 Floor to floor excess path loss in clean area

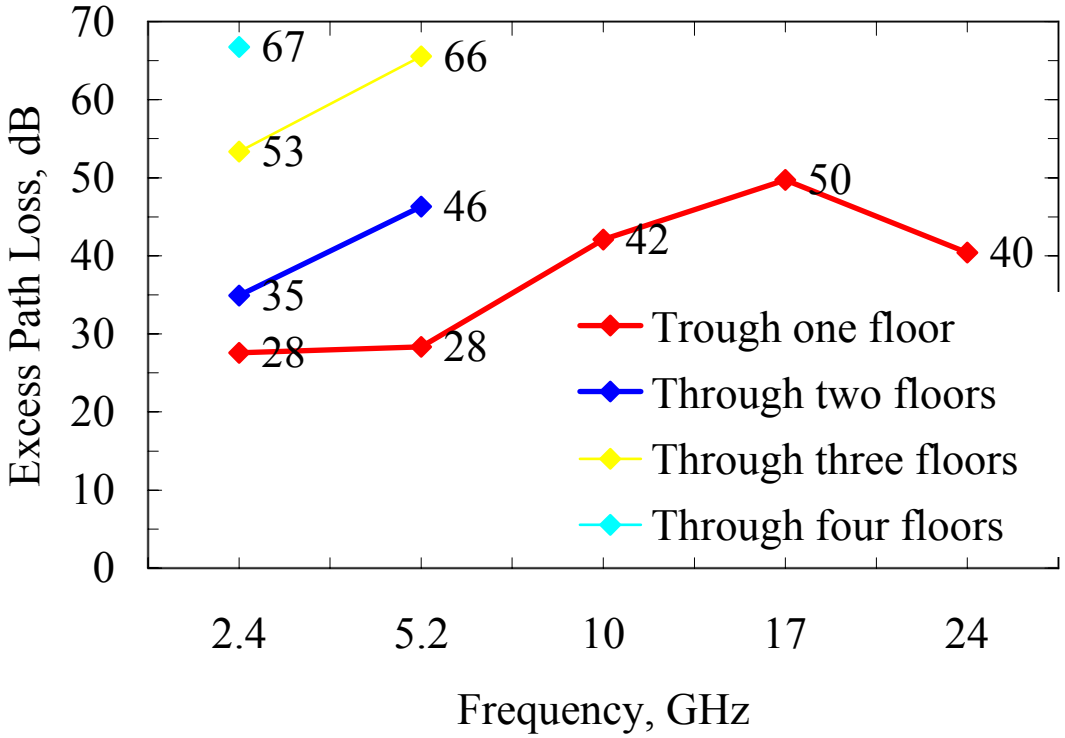

Figure 4.4 Floor to floor excess path loss in pipe area

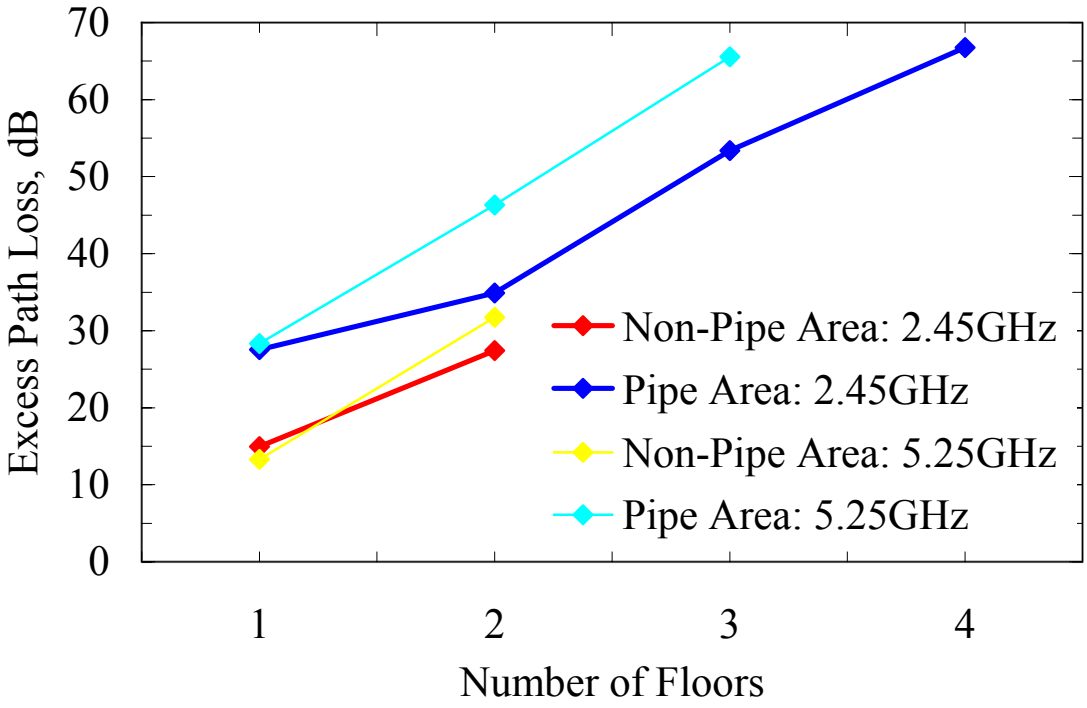

Figure 4.5 Comparison of excess path loss in 802.11b (2.4 GHz) and 802.11a (5.2 GHz).

Next we considered a line-of-sight (LOS) path along the hallway and a non-line-of-sight (NLOS) path from an office to the hallway, with the door open and closed (Figure 4.6). The Rx is sitting on a cart which can move along the hallway by LABVIEW programs. The sampling space we chose is 3.8cm / point. The excess path losses, averaged over hall distances from 3 meters to 33 meters, are given in Table 4-3. For the LOS path, the excess path loss is slightly negative, indicating a small guiding effect of the hallway. For the non-LOS path, the excess path loss increases with frequency, from 18 dB at 2.45 GHz to 28 dB at 28 GHz with the door open. The loss increased with the door closed. This increase was small at 2.45 GHz, only 1 dB, but substantial at 24 GHz (9 dB). These values are consistent with transmission-loss measurements we made through the solid wood door, where the loss increased from 2 dB at 2.4 GHz to 10 dB at 24 GHz. Also we did the path loss measurement when the doors of all offices along the hallway are open and closed. The difference, even increases with frequency, is not so big which indicates that the wooden office door does not contribute too much in the path loss.

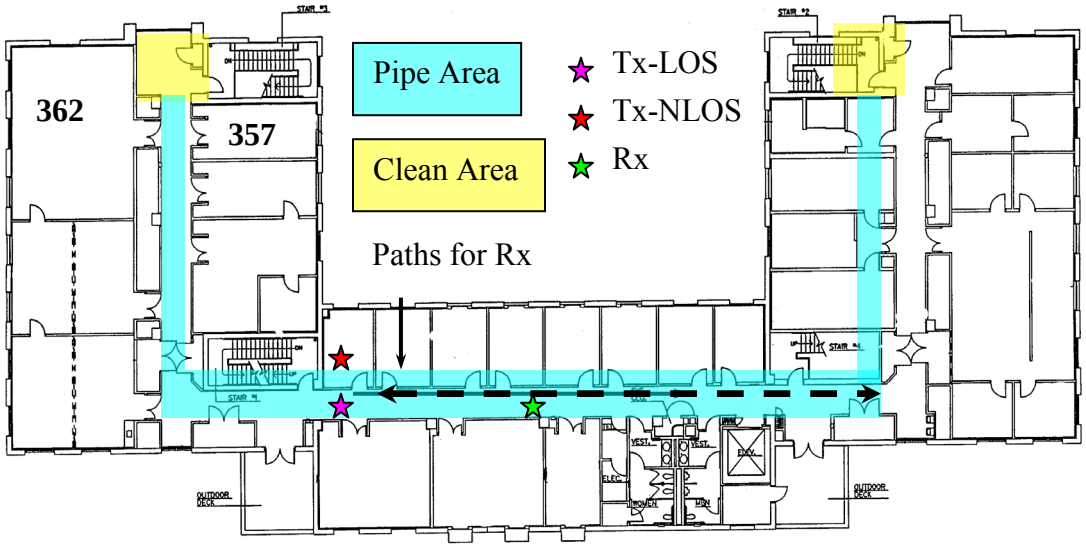

Figure 4.6 The 3rd floor of the Moore Laboratory, Caltech.

Path	2.45GHz	5.25GHz	10GHz	17GHz	24GHz
LOS	−4.0	−2.0	−1.6	−1.0	-1.4
NLOS (open door)	18	20	23	25	28
NLOS (closed door)	19	24	27	31	37

Table 4.3 Excess path loss for the LOS and the NLOS paths.

We also characterized loss for these paths by fitting a path-loss exponent *n* and standard deviation σ (Tables 4.4 and 4.5). The LOS path has an exponent less than 2, indicating a guiding effect of the hall. It increases with frequency, from 1.3 at 2.45 GHz to 1.7 at 24 GHz, which means less waveguide effect at high frequencies. For the NLOS path, the exponent is 2.5 at the lower frequencies, presumably related to diffraction at the door. It drops at the higher frequencies, reaching 2.1 at 24 GHz. The value of exponent here is similar to what is published in [65] and [67]. The small n at 2.45 GHz for LOS may also due to the big metal section of elevator in the hallway.

	2.45GHz	5.25GHz	10GHz	17GHz	24GHz
n	1.3	1.8	1.7	1.8	1.7
σ, dB	6.0	5.8	5.2	5.1	4.3

Table 4.4 Fitted path-loss exponent *n* and standard deviation σ in dB for the LOS path.

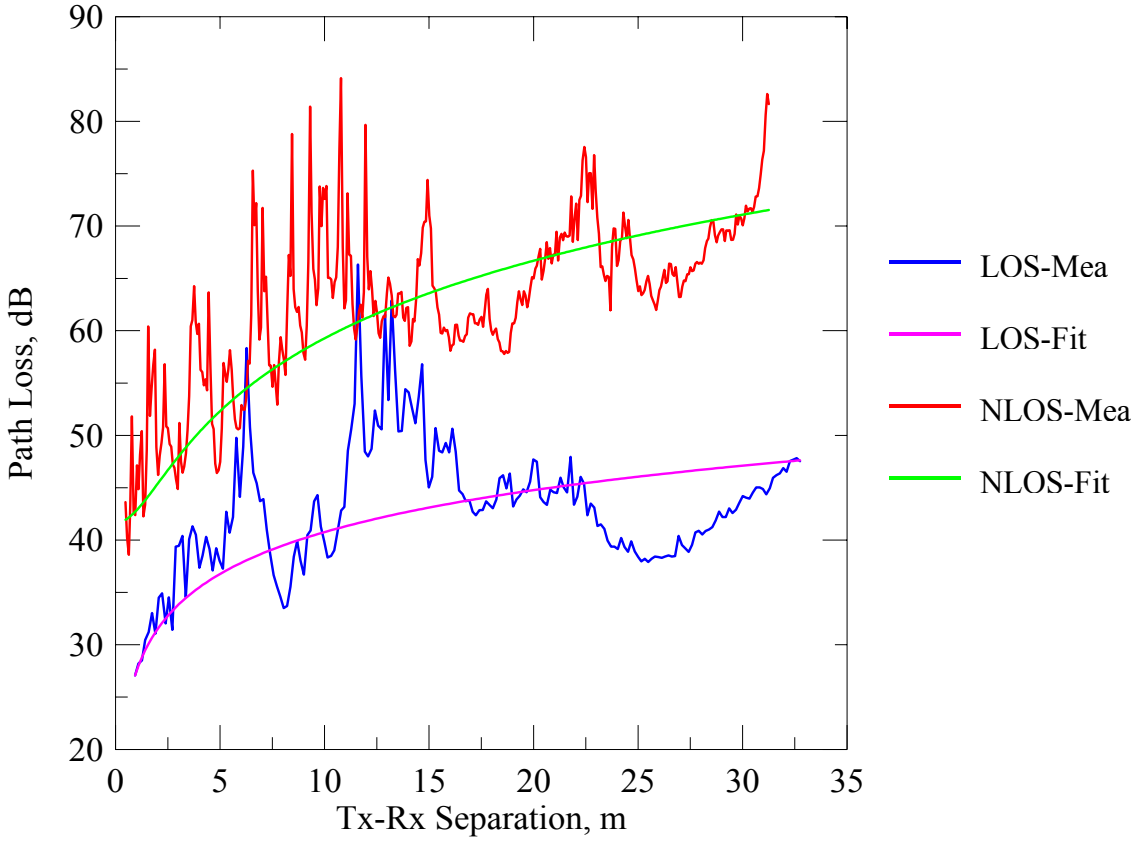

Figure 4.7 Path loss at 2.4 GHz: LOS and NLOS.

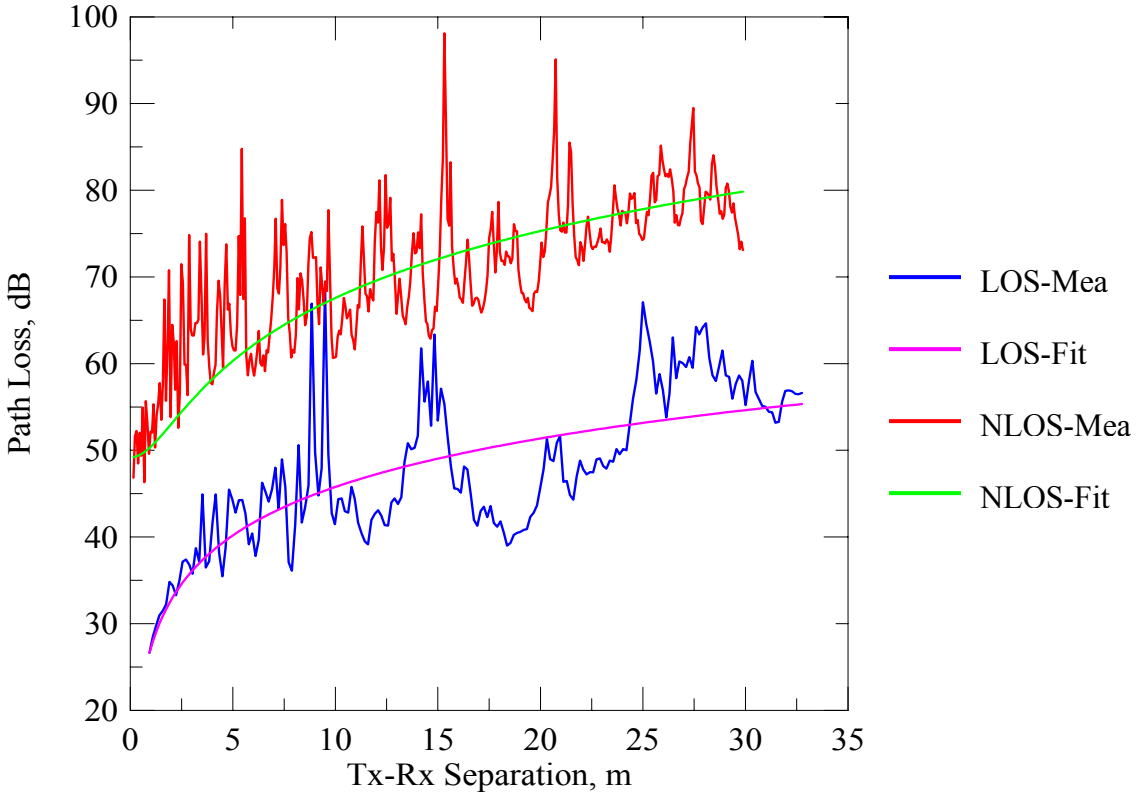

Figure 4.8 Path loss at 5 GHz: LOS and NLOS.

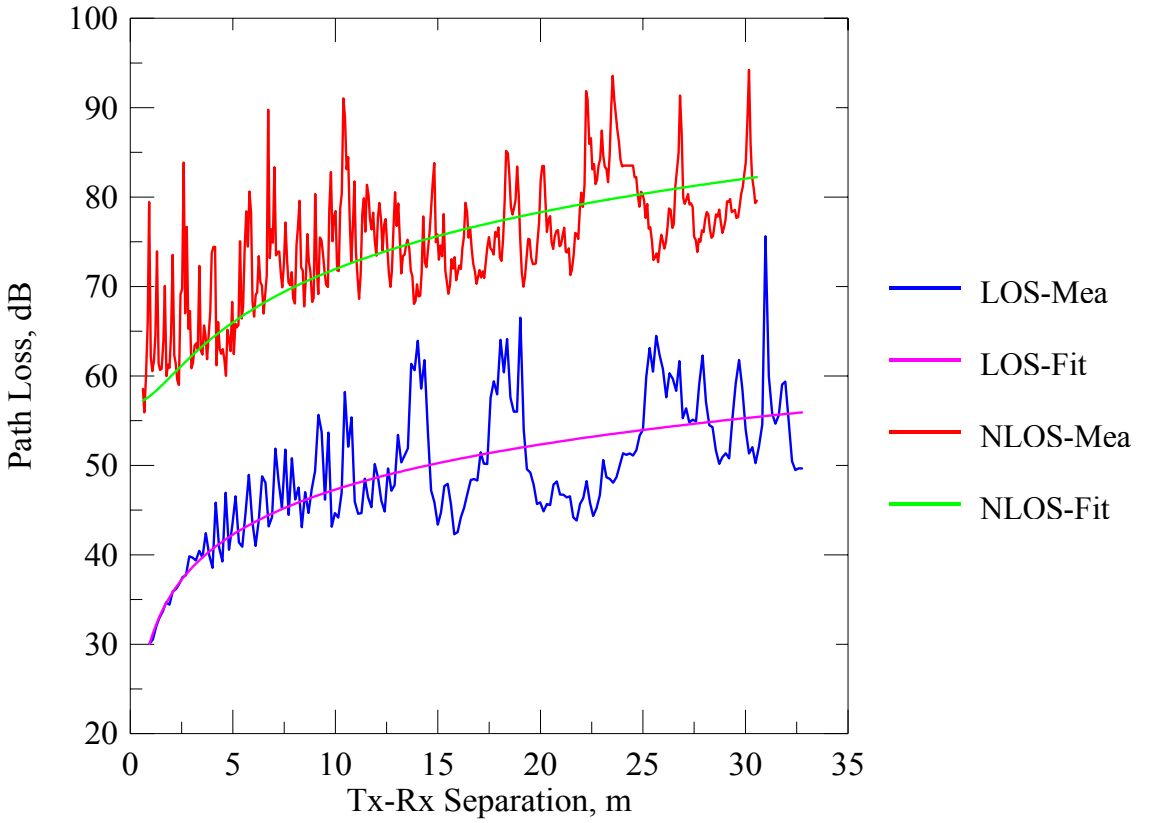

Figure 4.9 Path loss at 10 GHz: LOS and NLOS.

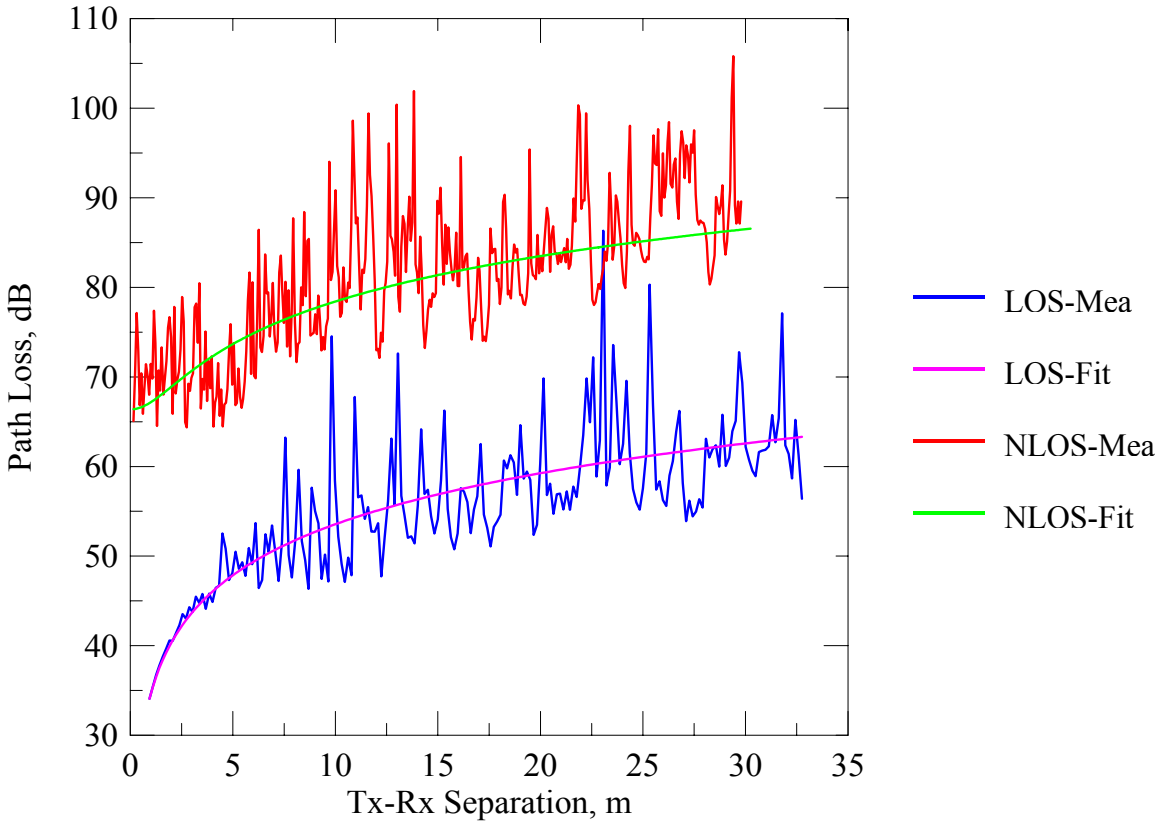

Figure 4.10 Path loss at 17 GHz: LOS and NLOS.

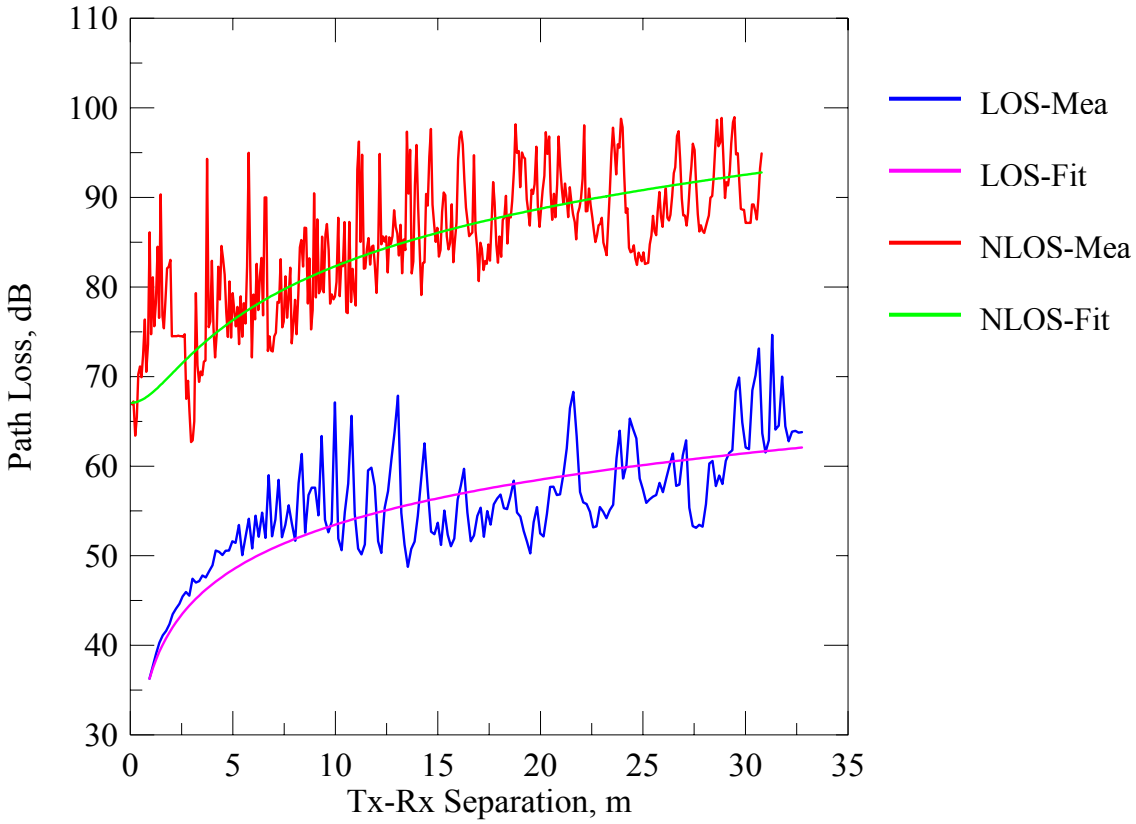

Figure 4.11 Path loss at 24 GHz: LOS and NLOS.

	2.45GHz	**5.25GHz**	**10GHz**	**17GHz**	**24GHz**
n	2.5	2.6	2.1	2.1	2.1
σ, dB	5.7	5.7	5.4	3.5	5.1

Table 4.5 Fitted path-loss exponent *n* and standard deviation σ in dB for the NLOS path (open door).

Figure 4.7 to 4.11 give the path loss comparison between LOS and NLOS from 2.4 to 24 GHz. The log-normal path loss models are also drawn in the plots. It can be seen from the plots that even the difference between path loss values of LOS and NLOS are quite big, the shape of the curves are very similar, indicating the frequency dependence of path loss for a specific indoor environment. The fading effect is generally stronger at higher frequencies than lower ones. For a better path loss measurement at 24 GHz, we may need to increase the sampling resolution compared to its wavelength.

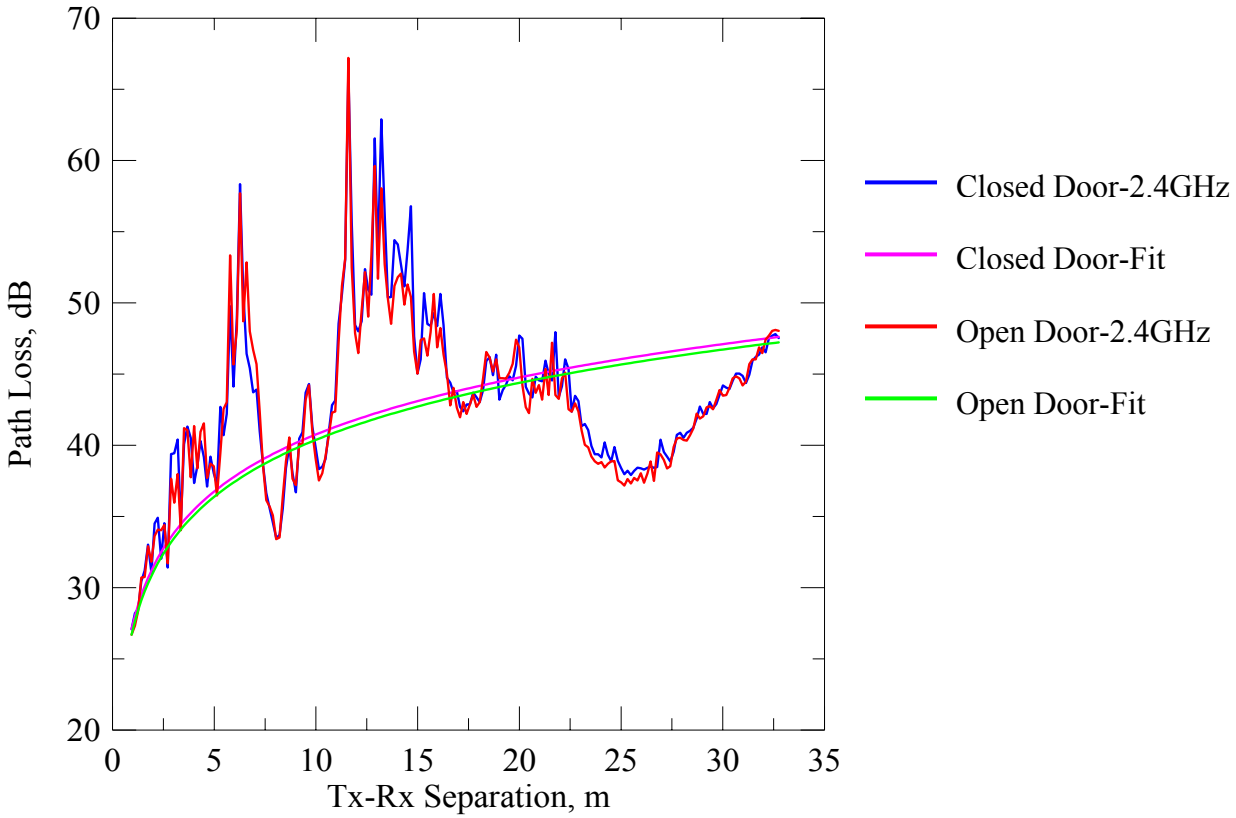

Figure 4.12 Path loss in LOS: open doors vs. closed doors (2.4 GHz)

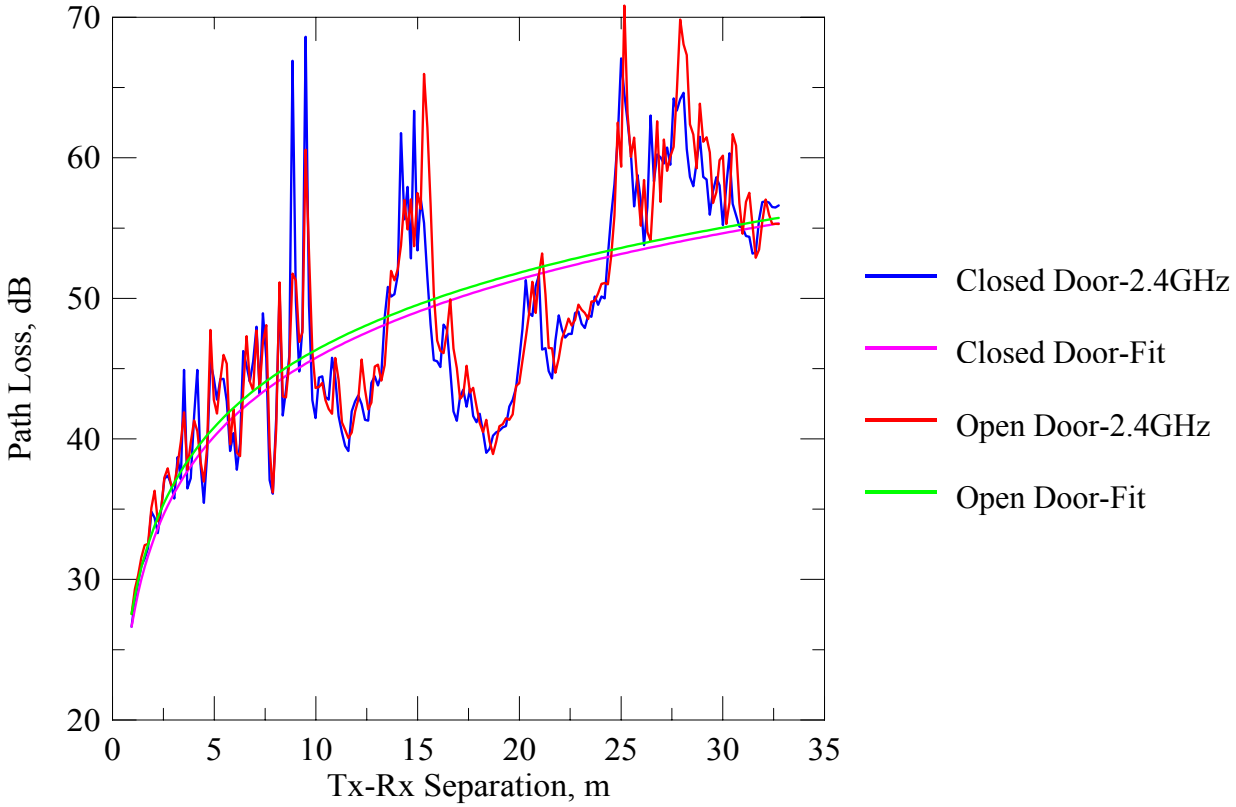

Figure 4.13 Path loss in LOS: open doors vs. closed doors (5.2 GHz)

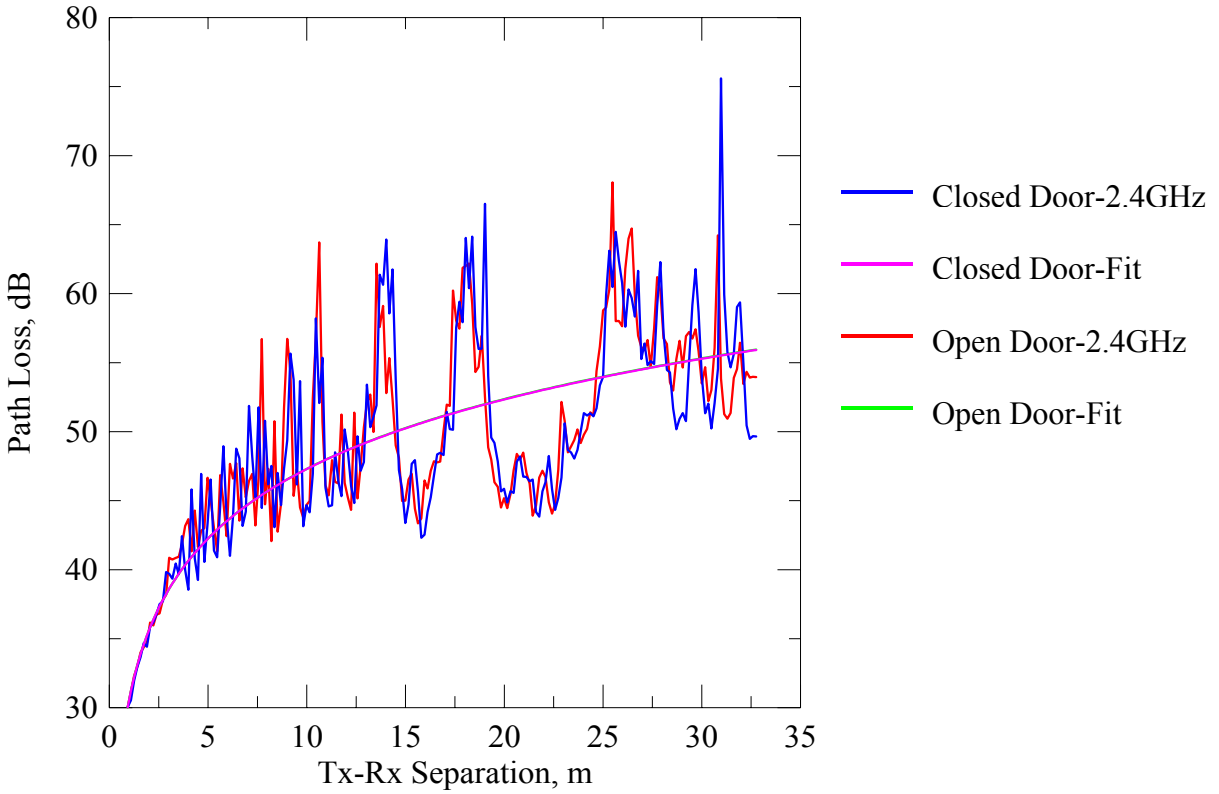

Figure 4.14 Path loss in LOS: open doors vs. closed doors (10 GHz)

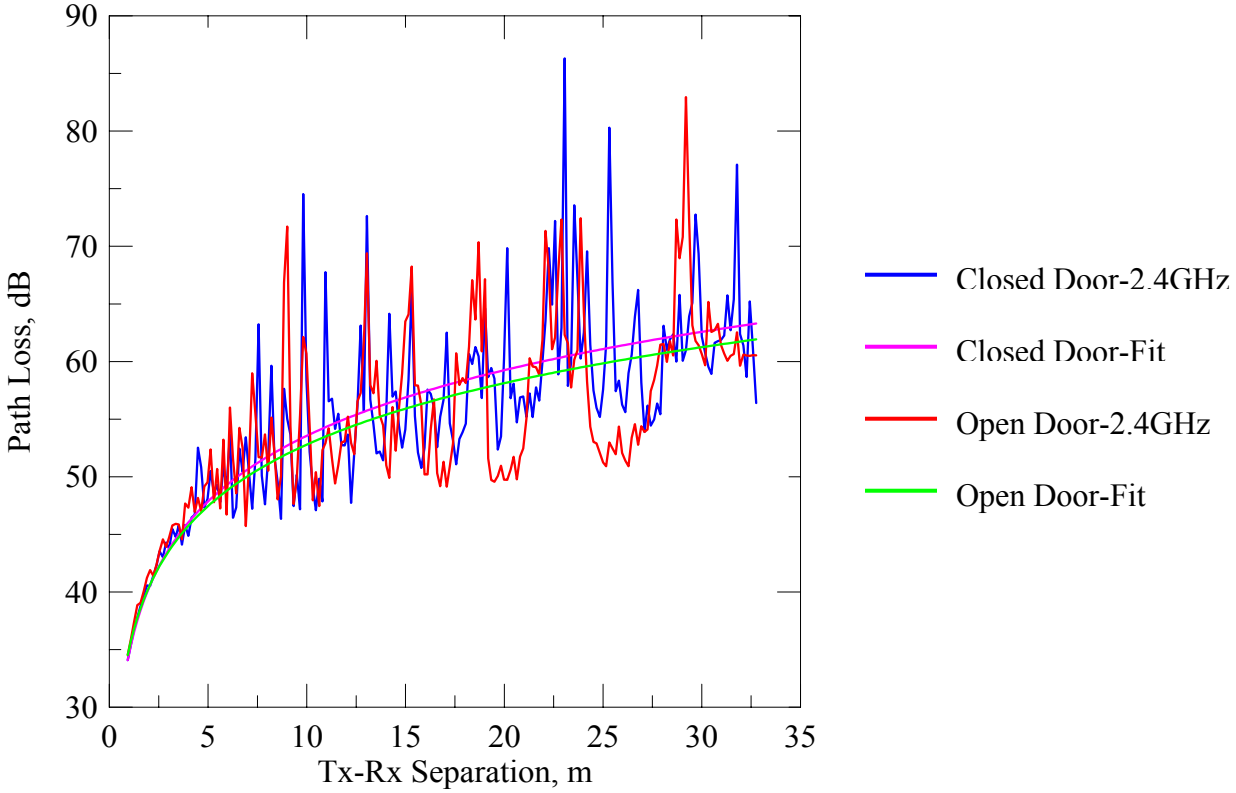

Figure 4.15 Path loss in LOS: open doors vs. closed doors (17 GHz)

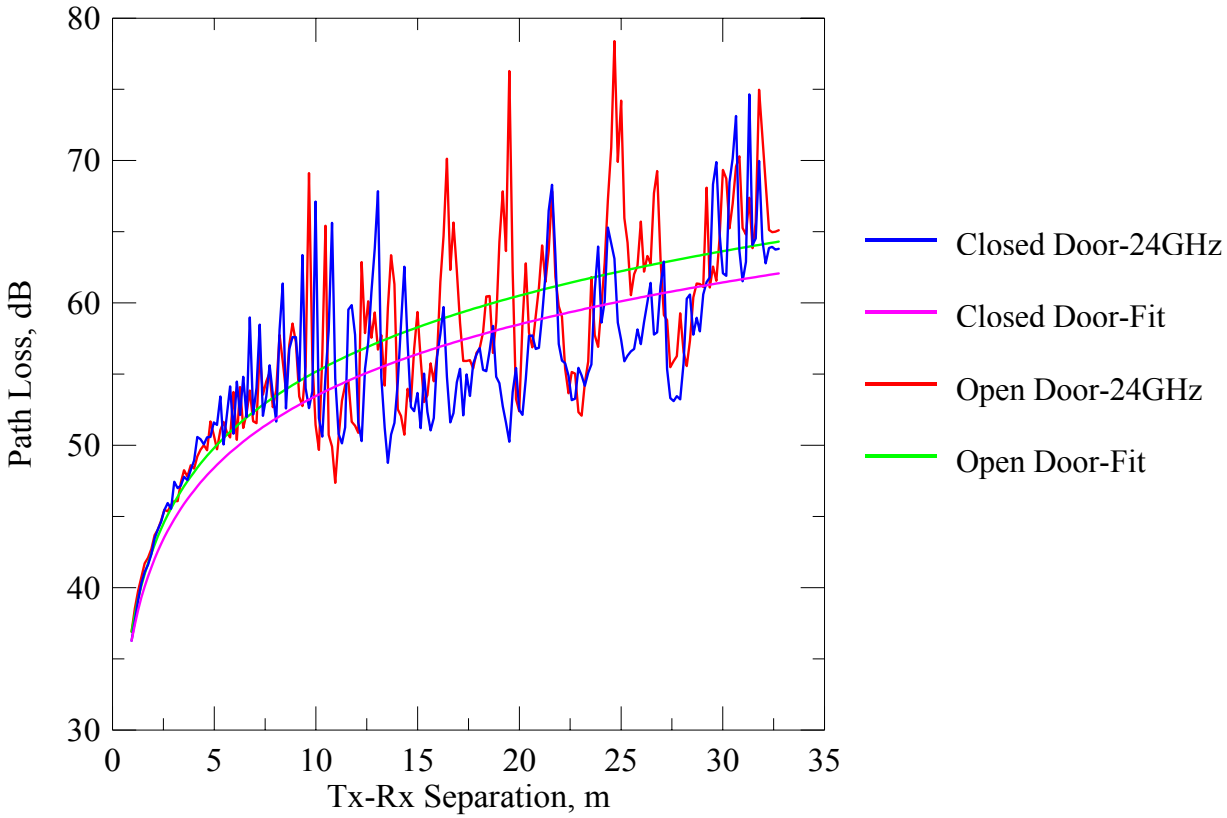

Figure 4.16 Path loss in LOS: open doors vs. closed doors (24 GHz)

Figure 4.12 to 4.16 also show the path loss as a function of Tx and Rx distance for all the hallway office doors closed and opened. It seems that he difference of these cases are not so big, which means open or close door will not affect wireless signal levels much. Another conclusion we can draw from the plots is that the frequency dependent path loss characteristics may give us a frequency diversity option for future wireless system.

4.3 Delay Spread Measurements

RMS delay spread (τ_{rms}) is frequently used to characterize the multipath properties of a channel [63]. We measured RMS delay spreads over a bandwidth of 250 MHz at the five frequency bands mentioned before in a 7×10 m^2 office (room 362 in Figure 4-3) and a 3×7 m^2 office (room 357 in Figure 4-3). The results are shown in Figure 4.17. It seems that delay spread is high in a large room, and also it decrease with frequency.

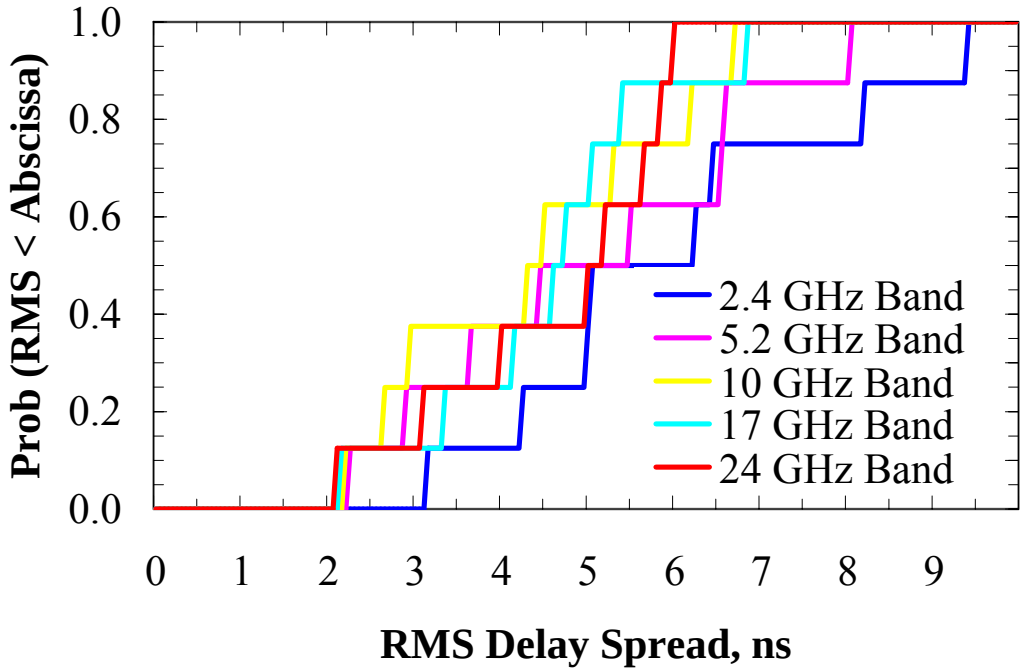

(a)

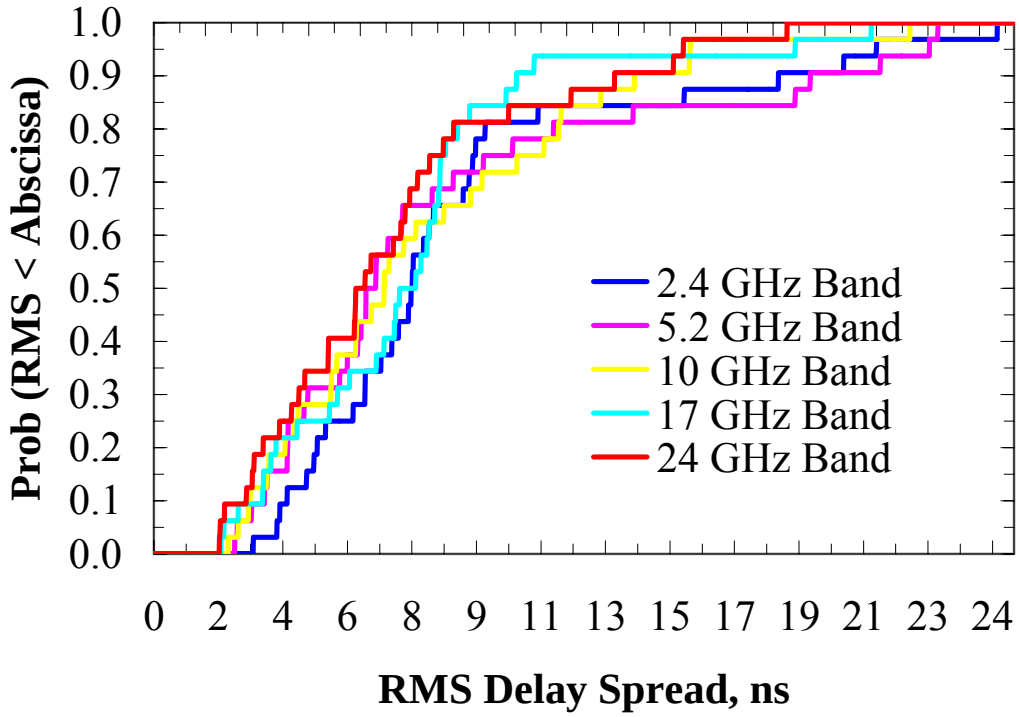

(b)

Figure 4.17 Delay spread measurements: (a) room 357 (b) room 362

Figure 4.18 shows the delay spread for the LOS and NLOS path in the 3rd floor hallway. As we can see, the average delay spread in LOS is smaller than that of NLOS. Also, as the frequency goes high, the average delay spread is more likely to be smaller. 10 GHz and 17 GHz seem to have the best delay spread in the LOS and NLOS scenarios.

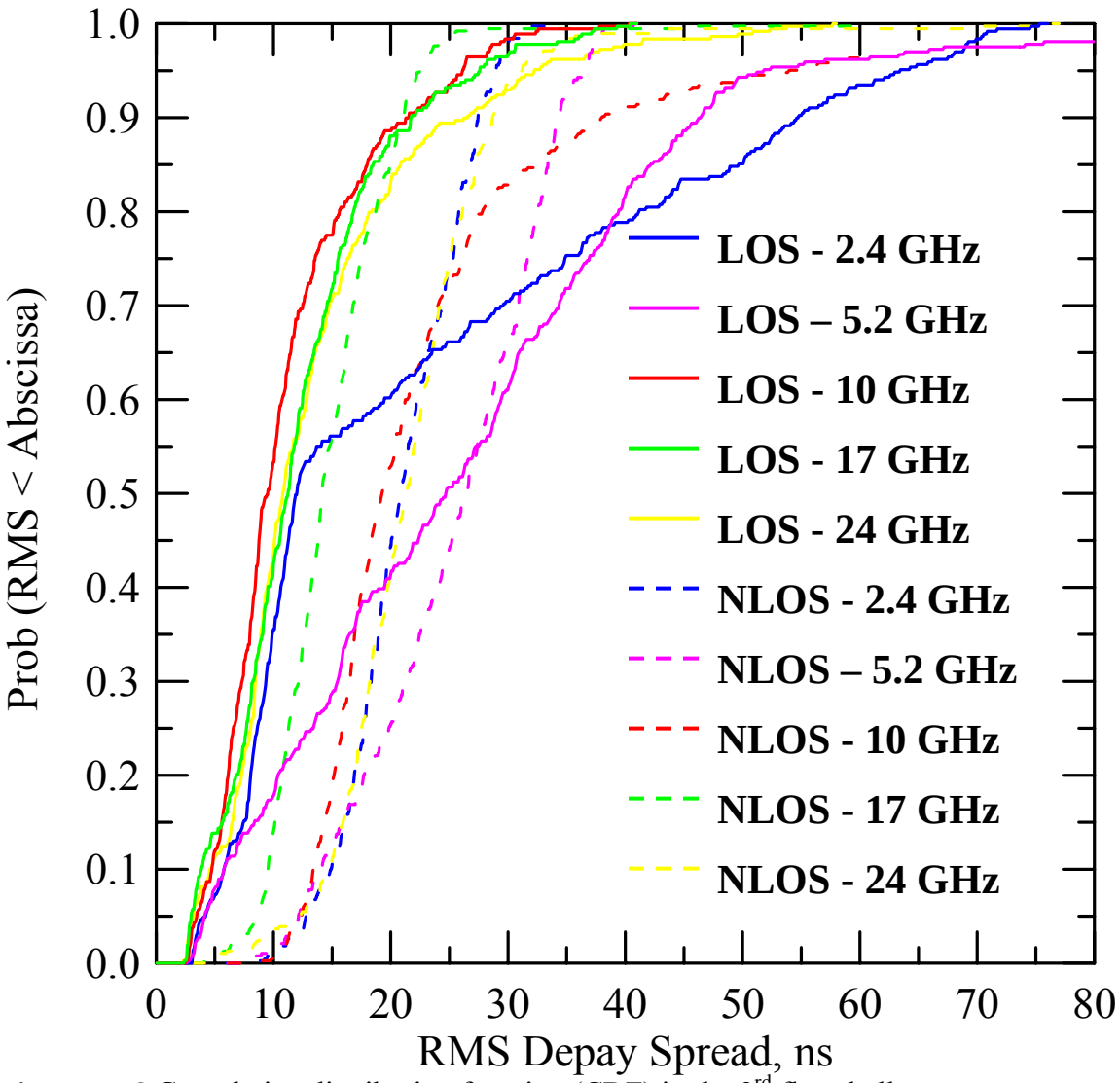

Figure 4.18 Cumulative distribution function (CDF) in the 3rd floor hallway.

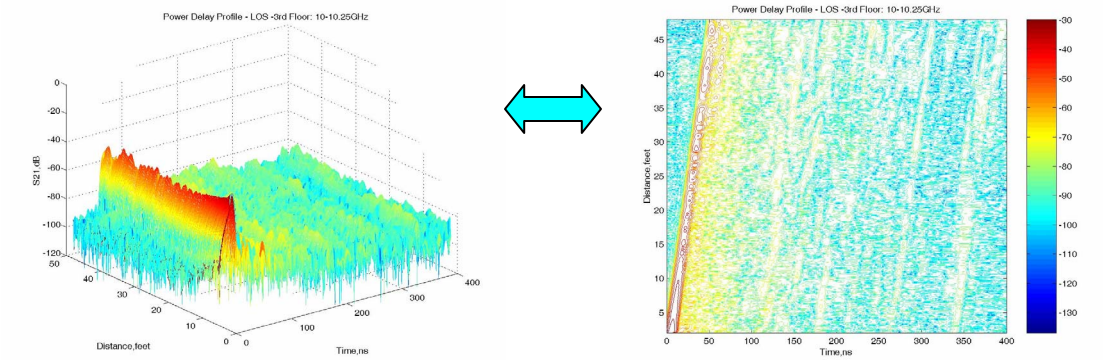

Figure 4.19 Another view to look at 3D PDP (Power Delay Profile)

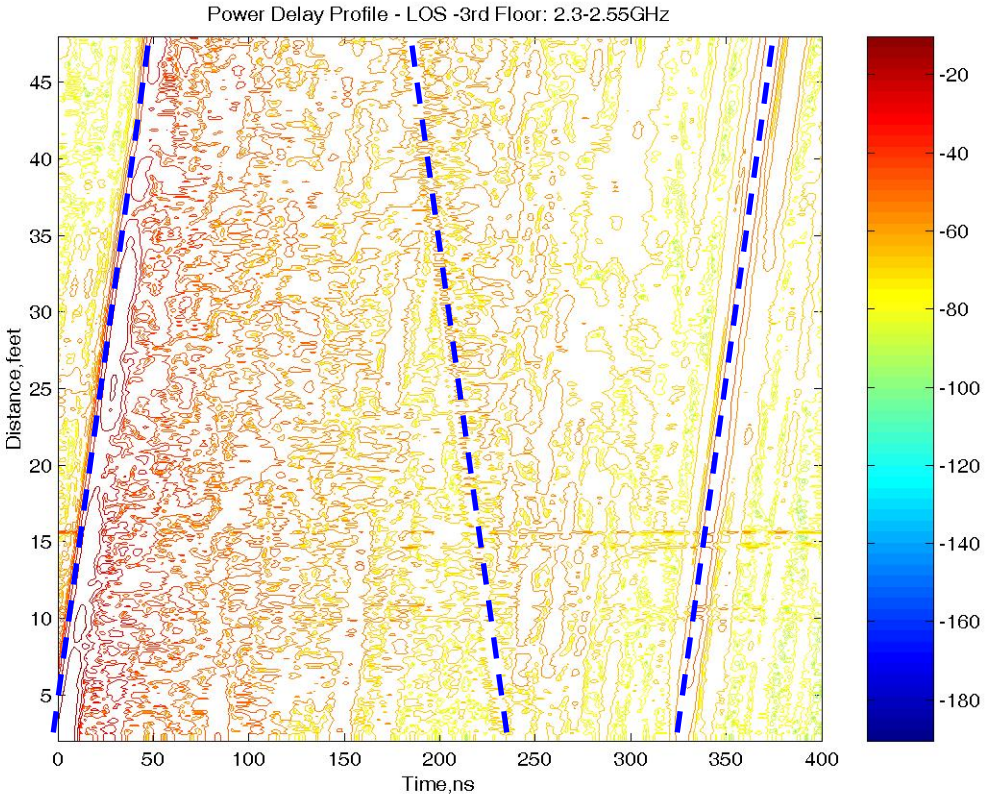

Figure 4.20 Contour map of the 3D PDP at 2.4 GHz

3D power delay profile can be made by plotting the delay profile as a function of both delay time and offset Tx-Rx distance as shown in Figure 4.19. If projected on the horizontal plane, it becomes a contour map of the power delay profile. This contour map

gives us an easy way to visualize the multipath in the channel under investigation. For example, Figure 4.20 shows the contour map of power delay profile at 2.4 GHz (LOS). Three signal paths are clearly seen from the map and marked by blue broken lines. The first path is the direct path from Tx and Rx as Rx moves away from Tx. The third path has the same slope as the direct path, so it could be the double reflection path from both end of the hallway. But the second path has the opposite slope as the direct path, so it should be the single reflection path from one end of the hallway.

In Figure 4.21, the path loss is plotted versus the delay spread for both LOS and NLOS situations. It can be seen that at the same path loss, the NLOS has small delay spread but at the same delay spread, the LOS has a smaller path loss.

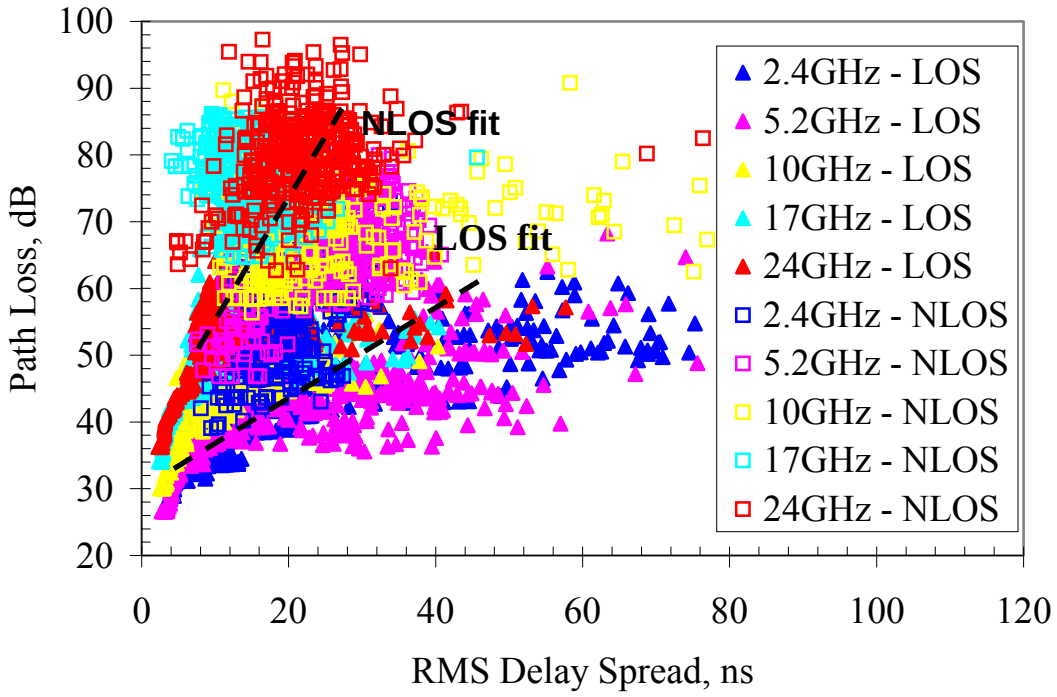

Figure 4.21 Delay spread vs loss for LOS path and the NLOS path (open door).

Chapter 5

A Combined E/H-Plane 2-D Ray-Tracing Method

For future applications of wireless local area networks (WLANs) and personal communication systems (PCSs), accurate CAD tools are needed not only to calculate coverage, but also to estimate radio-channel performance. The ultimate details of multipath propagation may be obtained, in principle, by solving Maxwell's equations with boundary conditions that express the physical properties of the walls and other structures. But this method is in general not economical and sometimes even unsolvable.

Saleh, Valensuela and other researchers had tried statistical models and formula based models on indoor and outdoor radio propagation [68]–[70]. Even neural network concept has been used to predict path loss [71]. But it seems that all these models are too general that it does not work well when transferring from one site to another. Recently, site-specific models such as ray-tracing have gained more acceptances. The Brute-force ray-tracing or shooting-and-bouncing ray (SBR) technique was first used by Ling [72] to calculate RCS. Later researchers such as Honcharenko [73] and Rappaport [74] have used this and image theory based ray-tracing methods to predict indoor radio wave propagation. To obtain a close prediction, 3-D ray-tracing is always used, which is not efficient and quite time consuming. But general 2-D ray-tracing tool such as CINDOOR

cannot obtain an accurate enough result. So I did this research trying to find a both efficient and fast method to predict channel performance.

5.1 Research Background

Current and future wireless network standards support data rates from 2 Mbps to over 100 Mbps. The IEEE 802.11 (a, b and g) products are widely used these days. They are operating at 2.4 GHz and 5 GHz. In addition, future wireless systems have been proposed at 17 GHz (HIPERLAN II) and 60 GHz for a large available bandwidth and a high data rate. In chapter 4, we have presented measurement results of an indoor-channel investigation at five selected frequency bands from 2.4 to 24 GHz [62]. In addition to 2.4, 5 and 17 GHz, the 10 GHz (amateur radio) and 24 GHz (Industrial, Scientific and Medical) bands have been added for comparison. To implement a successful wireless system at those frequency bands, an accurate prediction tool is very valuable in the system planning stage. Compared to the regular empirical method of channeling modeling, it can save a lot of time. 3D ray tracing methods [75]-[76] can handle this channel prediction but need detailed 3D information and require long processing time. In this chapter, a novel combined E/H-plane 2D ray-tracing method is proposed and developed in MATLAB. It gives quite good results in predicting the measurement data and saving a lot of processing time.

5.2 A Combined E/H-Plane 2D Ray Tracing Method

We did indoor channel measurements in the hallway of the 3rd floor of the Moore building. Since the width of the hallway is not large, there exist many strong reflection

paths from the walls on both sides. Also, many air ducts and light strips on the ceiling contribute strong additional multipaths to the channel. It is almost impossible to get a reasonable prediction of the channel by any 2D ray-tracing method. However, it seems quite impractical to draw all those details in 3D geometry and build a general 3D ray-tracing tool to handle it. Therefore, a combined E/H-plane 2D ray tracing method has been developed to save time and retain some degree of accuracy.

In the LOS scenario of this method, two principal planes (vertical and horizontal) are cut through both the transmitter (Tx) and the receiver (Rx), (Figure 5.1). The regular 2D ray tracing code is applied to both these planes and the results are summed up to obtain a complete set of signal paths. By considering these two principal planes, most strong paths are included except paths that cross the planes. The processing time is now proportional to $2N^2$ instead of N^3 as required for a general 3D ray-tracing method. Even though some accelerating algorithms have been developed recently for 3D ray-tracing [77], this combined 2D method is still a very promising way to handle channel prediction in a complex indoor environment with reasonable time and accuracy. Another advantage of this method is that the ray calculations can be naturally divided for parallel processing. This further reduces the simulation time, which is extremely helpful for a large size problem.

In the NLOS scenario, there is no way to cut the vertical plane to include both the transmitter and the receiver. We have come up with new transmitter sources to handle this problem (Figure 5.2). All additional sources are generated by diffractions from the

original Tx, or its image reflected by the ceiling or floor. All sources have a LOS path to the Rx. After finding the values of these sources from diffraction formulas, we can apply the normal 2D ray-tracing method as before and sum them with the horizontal ray-tracing results. This procedure is quite similar to the LOS case. The only difference here is that each new source requires the consideration of an additional vertical plane. This calculation is also included as an option in the numerical ray-tracing code. The NLOS case has a computation time proportional to mN^2, where m is an integer ($m > 2$), depending on how many diffraction sources are taken into account. The room geometry determines the number of diffraction sources necessary.

The formula for the multipath calculation is given in (5-1), where R_i is the product of the reflection, transmission and diffraction coefficients associated with the i^{th} path, L_i is the total length of the i^{th} path, and G^{Tx} and G^{Rx} are antenna pattern functions for the transmitter and receiver. Pattern measurements were made in an anechoic chamber. The Hann window function and IFFT are applied to find the time domain power delay profile for RMS delay spreads calculation (Appendix C).

$$S_{21}(f) = \sum_{E/H\_Plane} \sum_{i=1}^{M_{E/H\_Plane}} R_i \cdot \left(\frac{\lambda}{4\pi L_i}\right) \cdot e^{-j \cdot kL_i} \cdot G_{E/H}^{Tx}\left(\theta_{E/H\_Plane}\right) \cdot G_{E/H}^{Rx}\left(\theta_{E/H\_Plane}\right) \qquad (5\text{-}1)$$

A graphical user interface program has been developed using MATLAB. It takes the positions of the transmitter and receiver and the 2D E/H cutting plane geometry files as input parameters for a ray-tracing calculation. Different sets of programs are made to handle LOS and NLOS scenarios as described before.

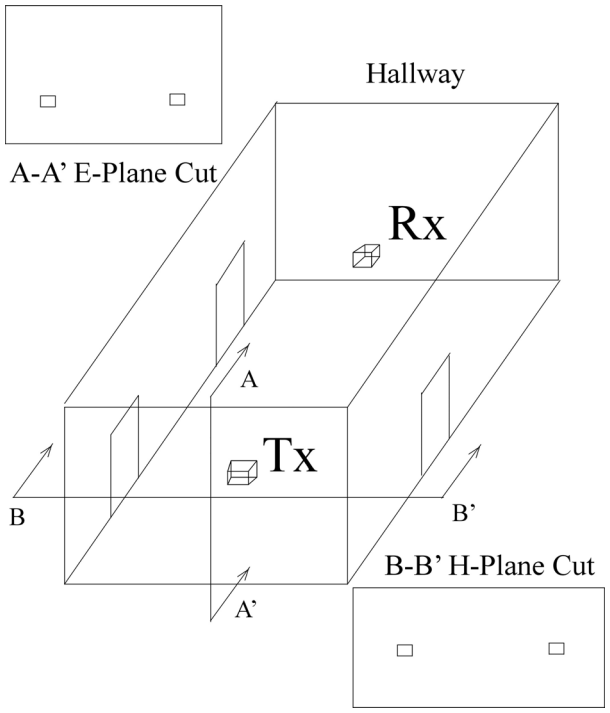

Figure 5.1 Combined 2D ray tracing for LOS.

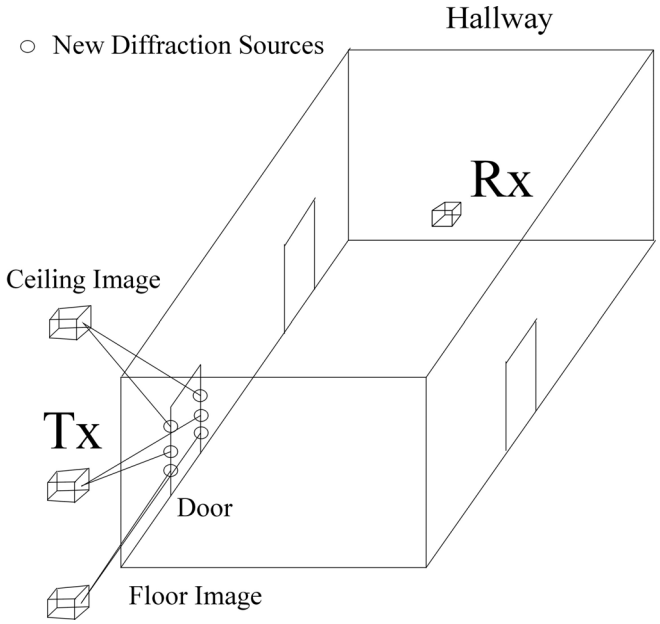

Figure 5-2 Modified 2D ray tracing for NLOS.

5.3 Calibration Measurement

In any ray-tracing model, physical properties of the indoor construction materials are needed for the calculation of reflection, transmission and diffraction coefficients. A

correct material model is very important for an accurate ray-tracing calculation. In the past, people have published results on the electrical properties of materials at microwave frequencies [78], [79]. In this work, we made both reflection tests with short reference and free-space TRL measurements (Figure 5.3) to find the microwave properties of three construction materials (plasterboard, glass and wood) at five selected frequency bands from 2.4 to 24 GHz. The reflection test involves reflection S21 measurement at difference incident angles and uses a metal plane as a short reference. The TRL measurement extracts data by fitting the S21 measurement data with material properties. The extracted material properties of those materials are shown in Figure 5.4. For example, the permitivities obtained for glass, wood and plasterboard are 6, 2,2 and 2. They are comparable to the results which have been published before [80].

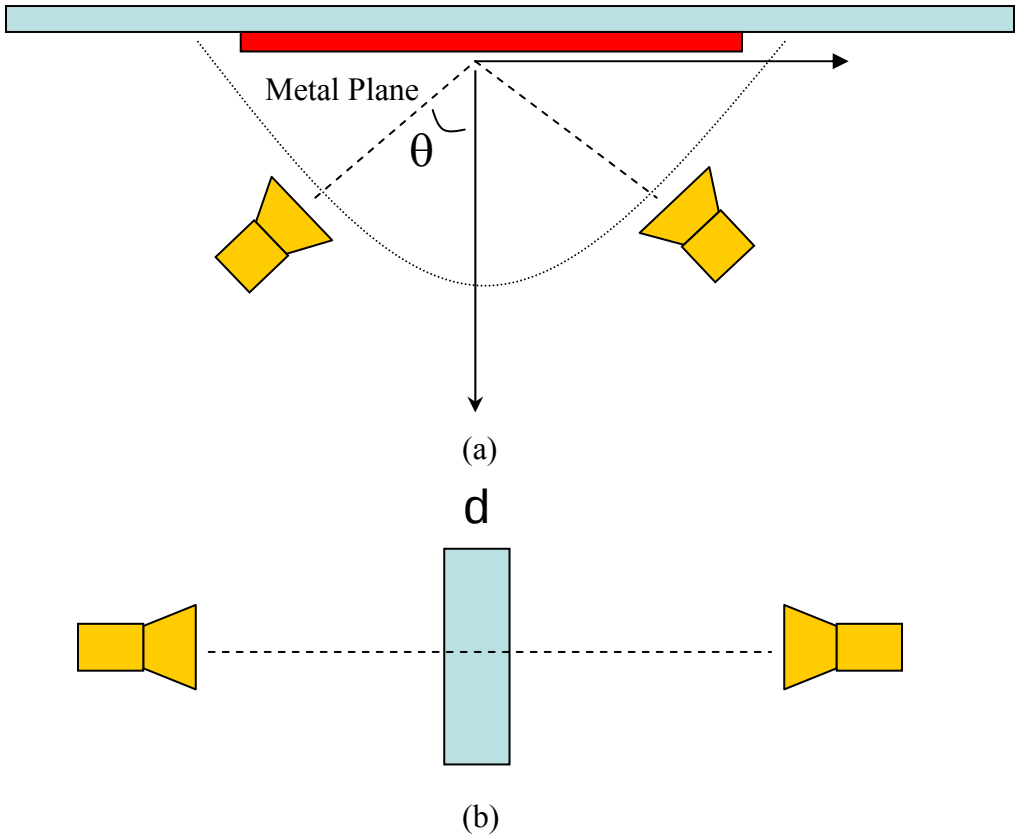

Figure 5.3 Reflection (a) and TRL measurements for material calibration

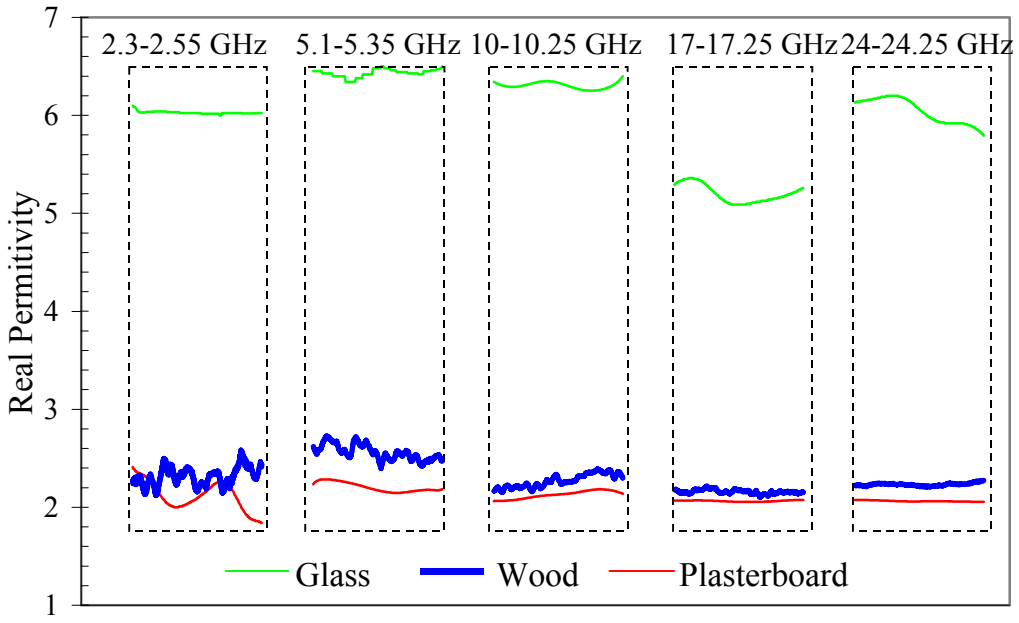

(a)

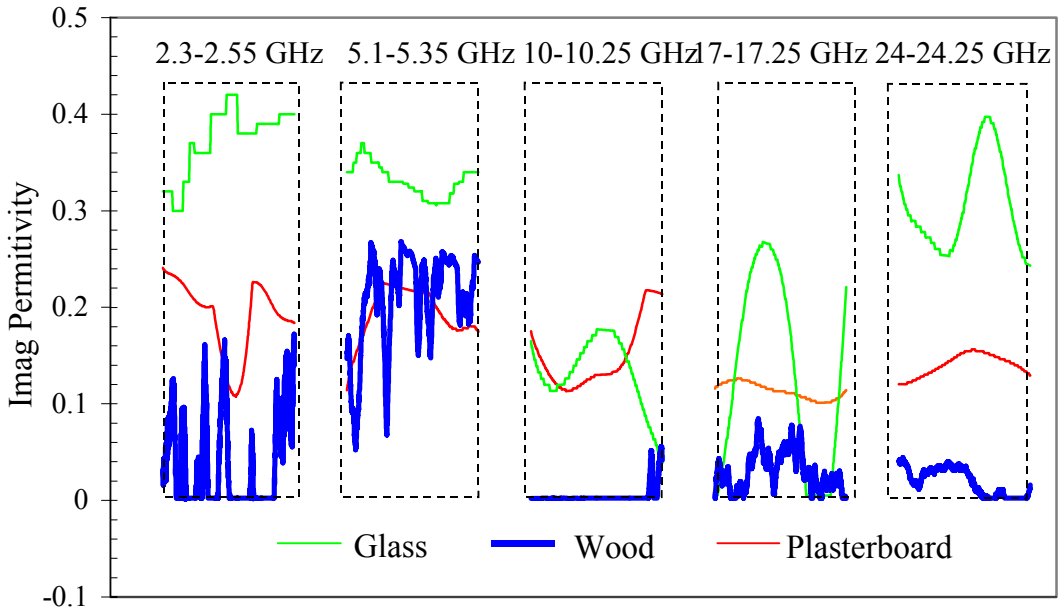

(b)

Figure 5.4 Extracted material dielectric constants: (a) real part, (b) imaginary part

5.4 A More Accurate Approximation for the Fresnel Integral

In the ray tracing code, the Fresnel integral (5-1) is involved in the formula of diffraction coefficient ([81]). For fast calculation of its value, asymptotic expression (5-2) can be applied ([82]). I found that the expression is not so accurate in the section between 0.3 and 5.5 when interpolation is used. An improved expression is made (5-3) and the comparison result is shown in Figure 5.5.

$$F(x) = 2j\sqrt{x}\cdot e^{jx}\cdot\int_{\sqrt{x}}^{\infty} e^{-j\tau^2}\,d\tau \tag{5-1}$$

$$F(x) = \begin{cases} \left[\sqrt{\pi x} - 2xe^{j\pi/4} - \frac{2}{3}x^2 e^{-j\pi/4}\right]e^{j(\pi/4+x)} & \text{x<0.3} \\ \text{Interpolation} & \text{0.3<x<5.5} \\ \left[1 + j\frac{1}{2x} - \frac{3}{4}\frac{1}{x^2} - j\frac{15}{8}\frac{1}{x^3} + \frac{75}{16}\frac{1}{x^4}\right] & \text{5.5<x} \end{cases} \tag{5-2}$$

$$F(x) = \begin{bmatrix} -0.493 + 1.312x^{0.09} - 0.009(x-0.8)(x-3.7) + \\ 0.004(x-0.616)(x-2.516)(x-4.889) \end{bmatrix}\cdot e^{j\left(1.74-1.46x^{0.08}\right)} \quad 0.3<X<5.5 \tag{5-3}$$

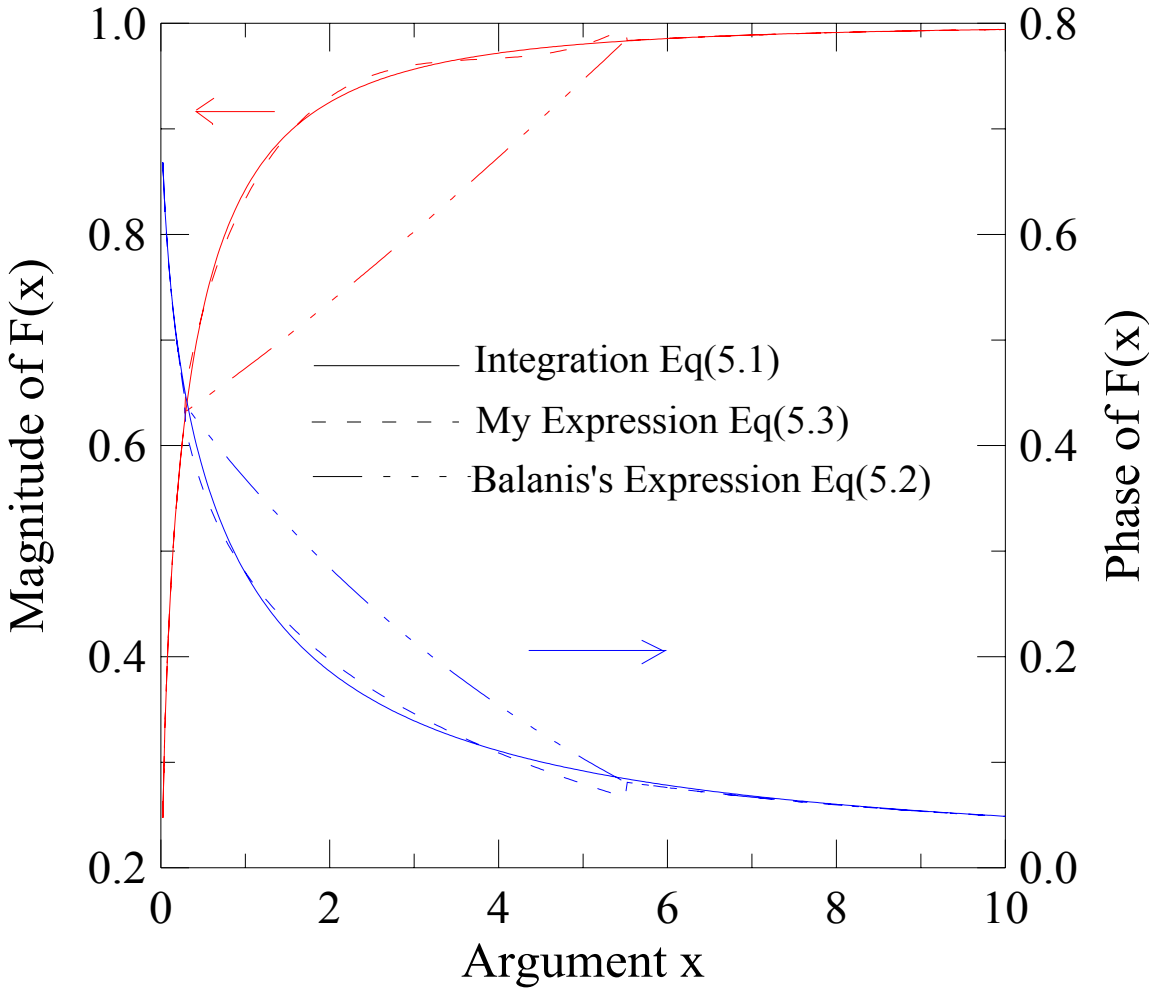

Figure 5.5 Modified expression of the Fresnel integral

5.5 Comparison of Ray-tracing Simulation and Measurement

Simulations were performed and measurements made for the 3rd floor of Moore building (Figure 5.6). In the LOS scenario, the transmitter is located in the center of the hallway, and in the NLOS scenario, the transmitter is located in one of the side rooms. The receiver is moved along the hallway controlled by the computer on the cart, while path loss and power delay profile data were measured. The cart is moving quite slowly (< 1 cm/s) to avoid frequency shifts. The cart can also be controlled in step mode to take measurements while stopped.

Figure 5.7 (a)-(e) shows the simulation and measurement result of path losses from 2.4 to 24 GHz for both LOS and NLOS. As can be seen from the figure, the algorithm gives a good prediction of path loss in both LOS and NLOS environment. The simulation does not have as many ripples as the measurement due to the limited number of paths considered. If dielectric properties of the construction materials are provided, this ray-tracing code can be applied to any indoor environment to find out the path loss. Also, this code can be modified to do channel prediction for even outdoor wireless communication systems.

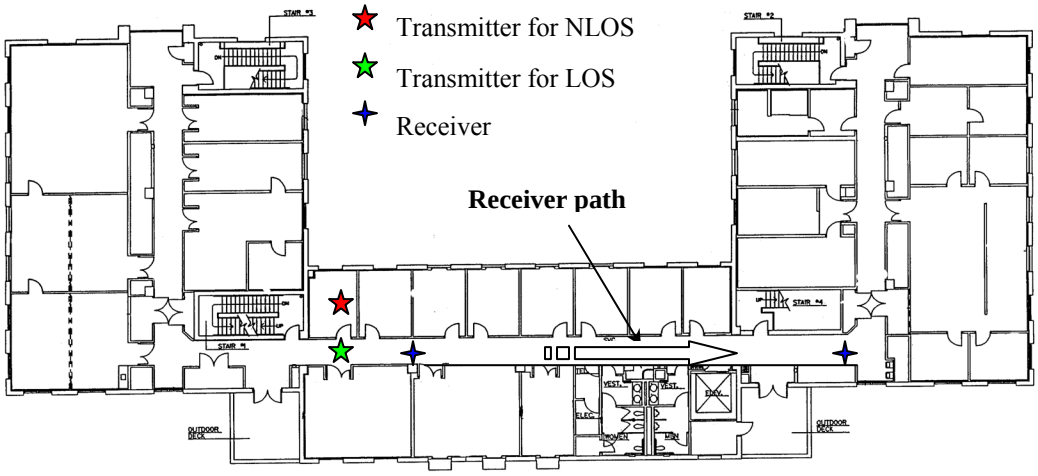

Figure 5.6 3rd floor of Caltech's Moore building (Department of Electrical Engineering)

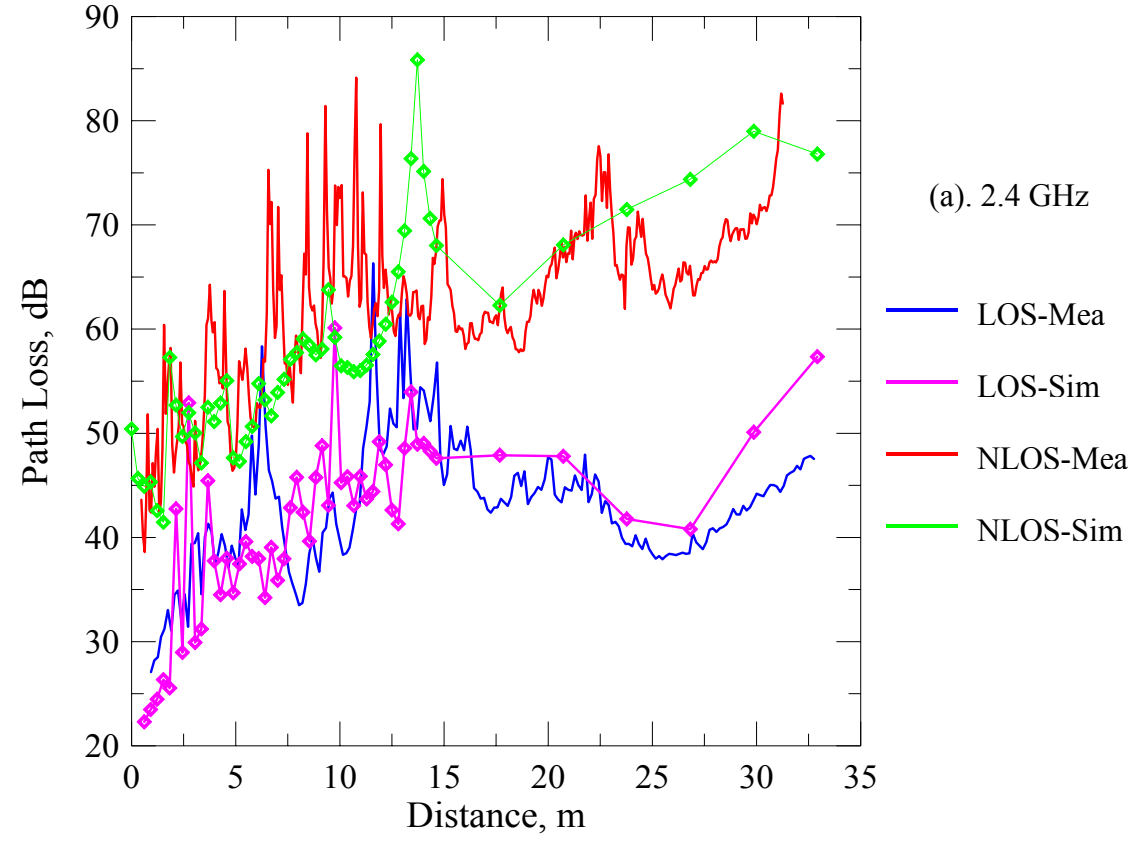
Path Loss, dB
Distance, m
(a). 2.4 GHz
LOS-Mea
LOS-Sim
NLOS-Mea
NLOS-Sim

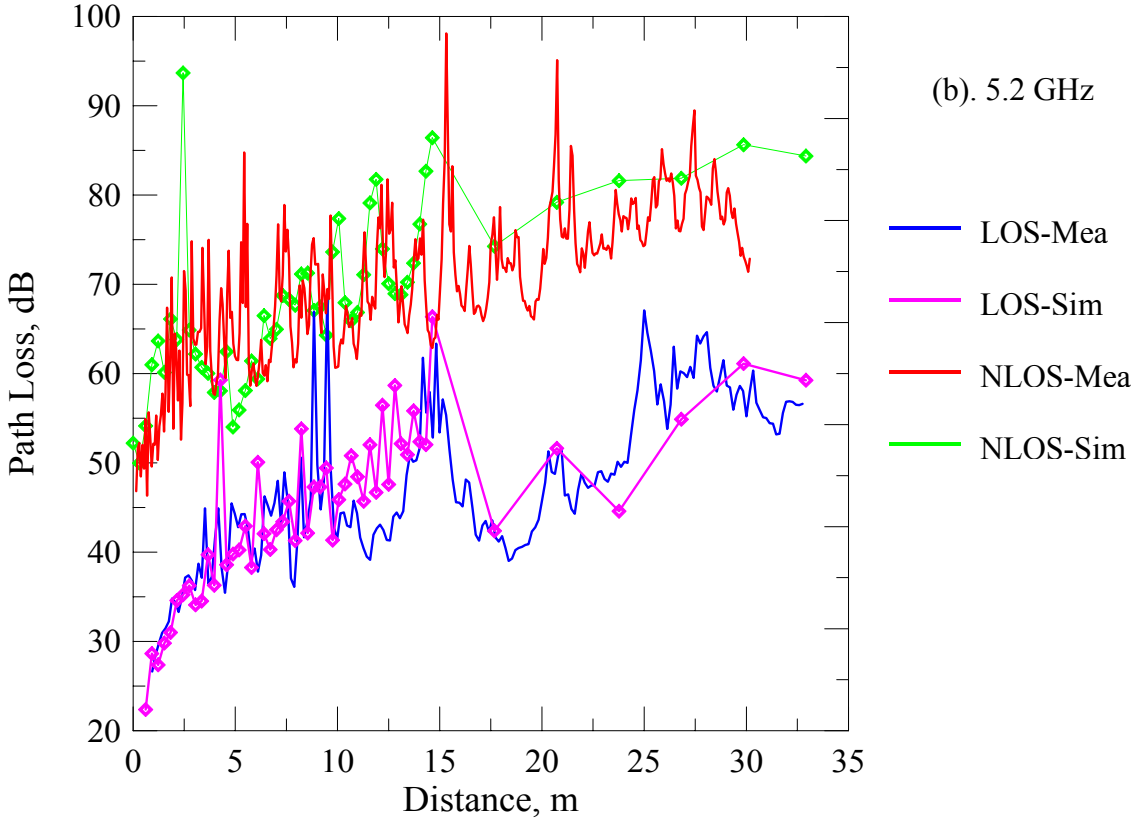
Path Loss, dB
Distance, m
(b). 5.2 GHz
LOS-Mea
LOS-Sim
NLOS-Mea
NLOS-Sim

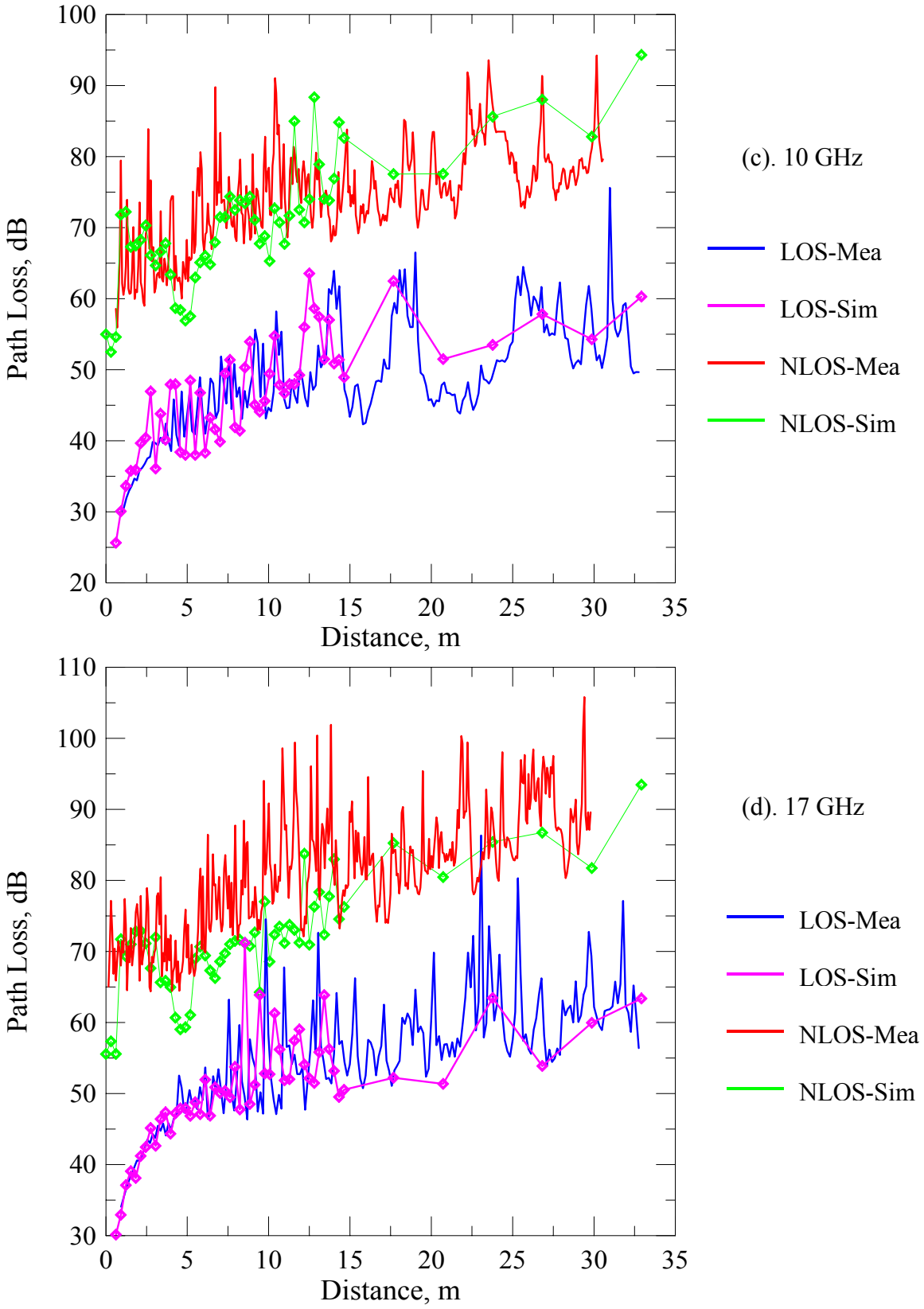
Path Loss, dB
Distance, m
(c). 10 GHz
LOS-Mea
LOS-Sim
NLOS-Mea
NLOS-Sim
Path Loss, dB
Distance, m
(d). 17 GHz
LOS-Mea
LOS-Sim
NLOS-Mea
NLOS-Sim

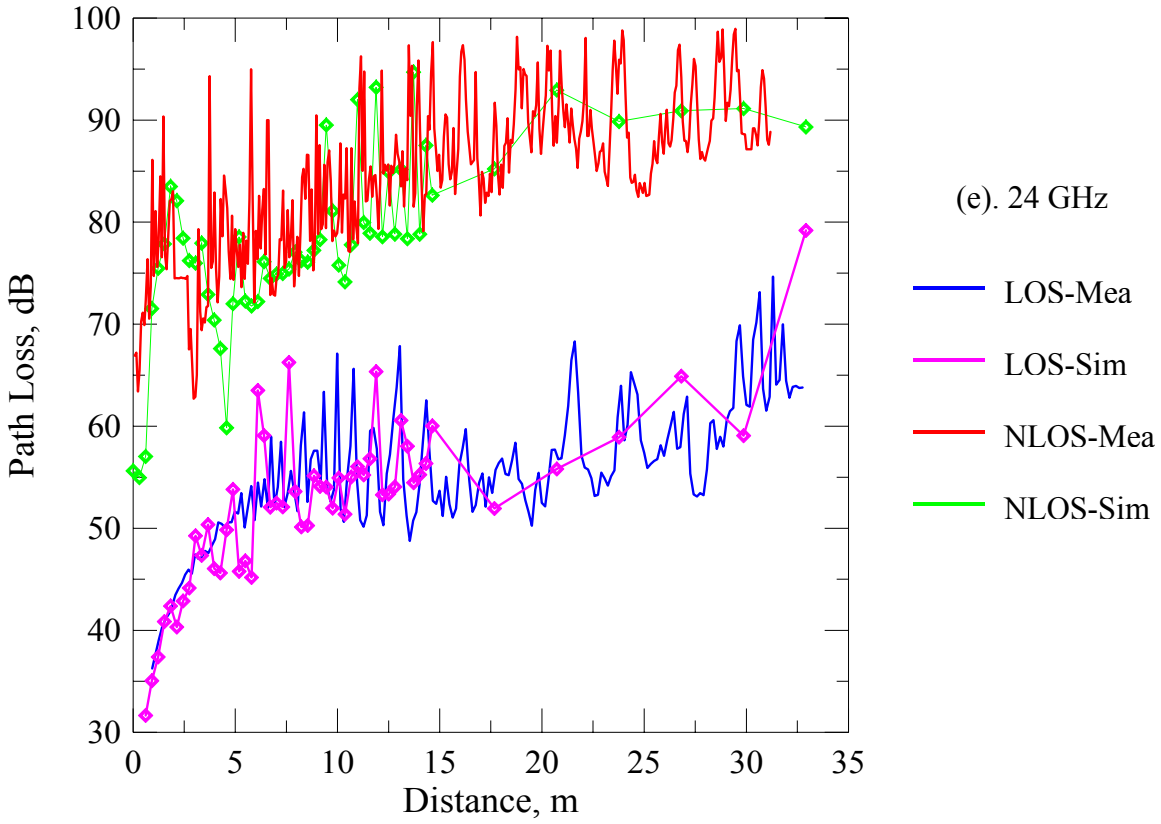

Figure 5.7 Path loss measurement and simulation comparison

Since this ray-tracing code provides a very close prediction of path loss information, it can be used to determine wireless system operating range and also study fading effects as a function of distance. In that case, a much higher simulation resolution is needed. As we found from measurement and prediction, the high frequency general has more frequent and large magnitude of fading.

Another important channel property is RMS delay spread. Since it requires a coherent frequency sounding method, a VNA (Vector Network Analyzer) 8022D is used. The CDF (Cumulative Distribution Function) of the delay spread from both simulation and measurements are shown in Figure 5.8 in five selected frequency bands. As can been seen

from the figure, the delay spread prediction in LOS is better than NLOS. Also, it seems that the simulated delay spread is always lower than the measured one. This effect is expectable since the combined E/H 2D ray-tracing method only counts up to the 2nd order rays and ignores all the cross-plane and higher order paths. So it is just an approximate method. Also the indoor environment file has been simplified for analysis. There are some paths that have not been taken into account in the simulation.

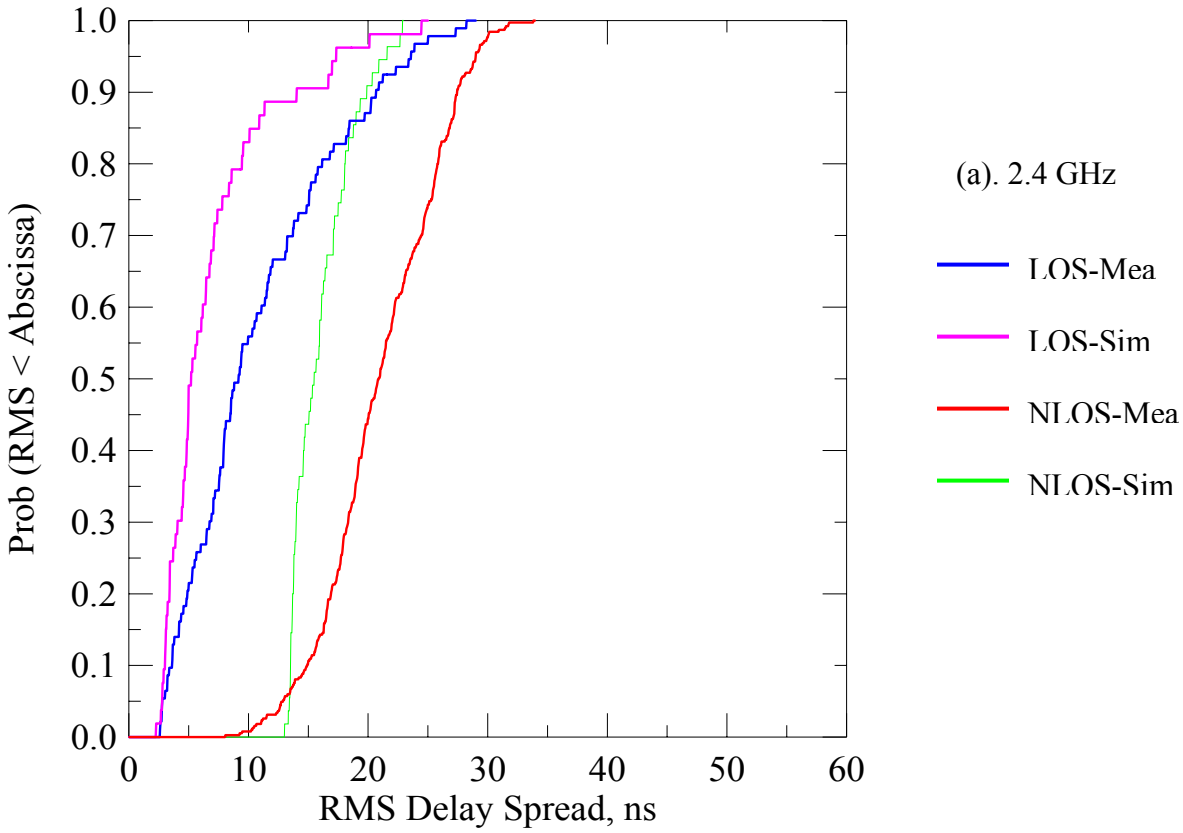

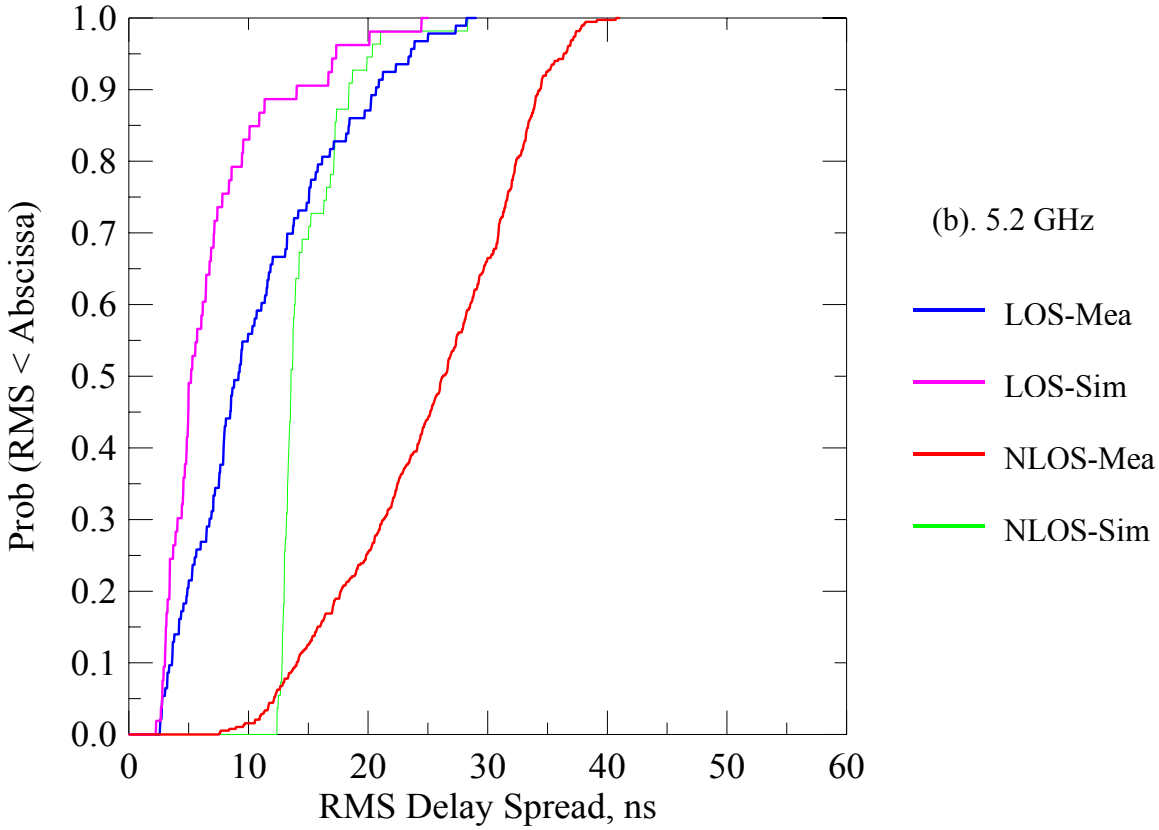
Prob (RMS < Abscissa)
RMS Delay Spread, ns
0.0
0.1
0.2
0.3
0.4
0.5
0.6
0.7
0.8
0.9
1.0
0
10
20
30
40
50
60
(b). 5.2 GHz
LOS-Mea
LOS-Sim
NLOS-Mea
NLOS-Sim

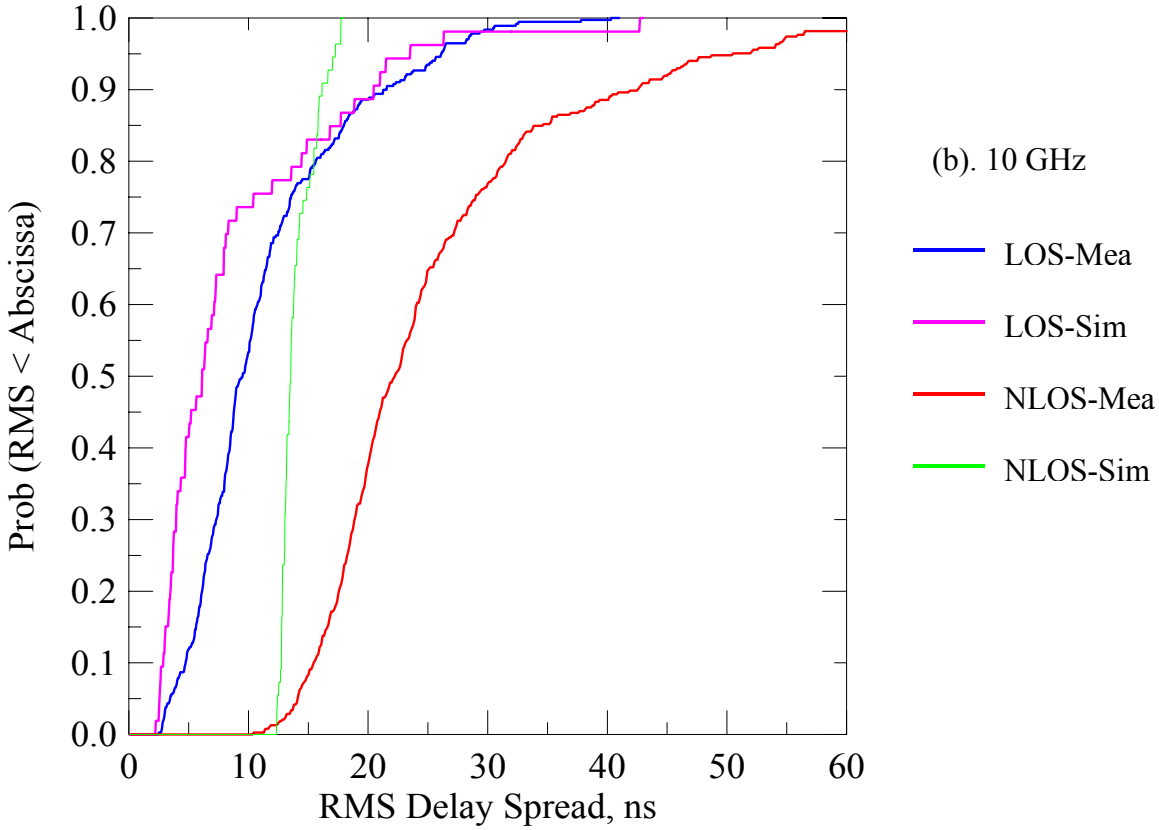
Prob (RMS < Abscissa)
RMS Delay Spread, ns
0.0
0.1
0.2
0.3
0.4
0.5
0.6
0.7
0.8
0.9
1.0
0
10
20
30
40
50
60
(b). 10 GHz
LOS-Mea
LOS-Sim
NLOS-Mea
NLOS-Sim

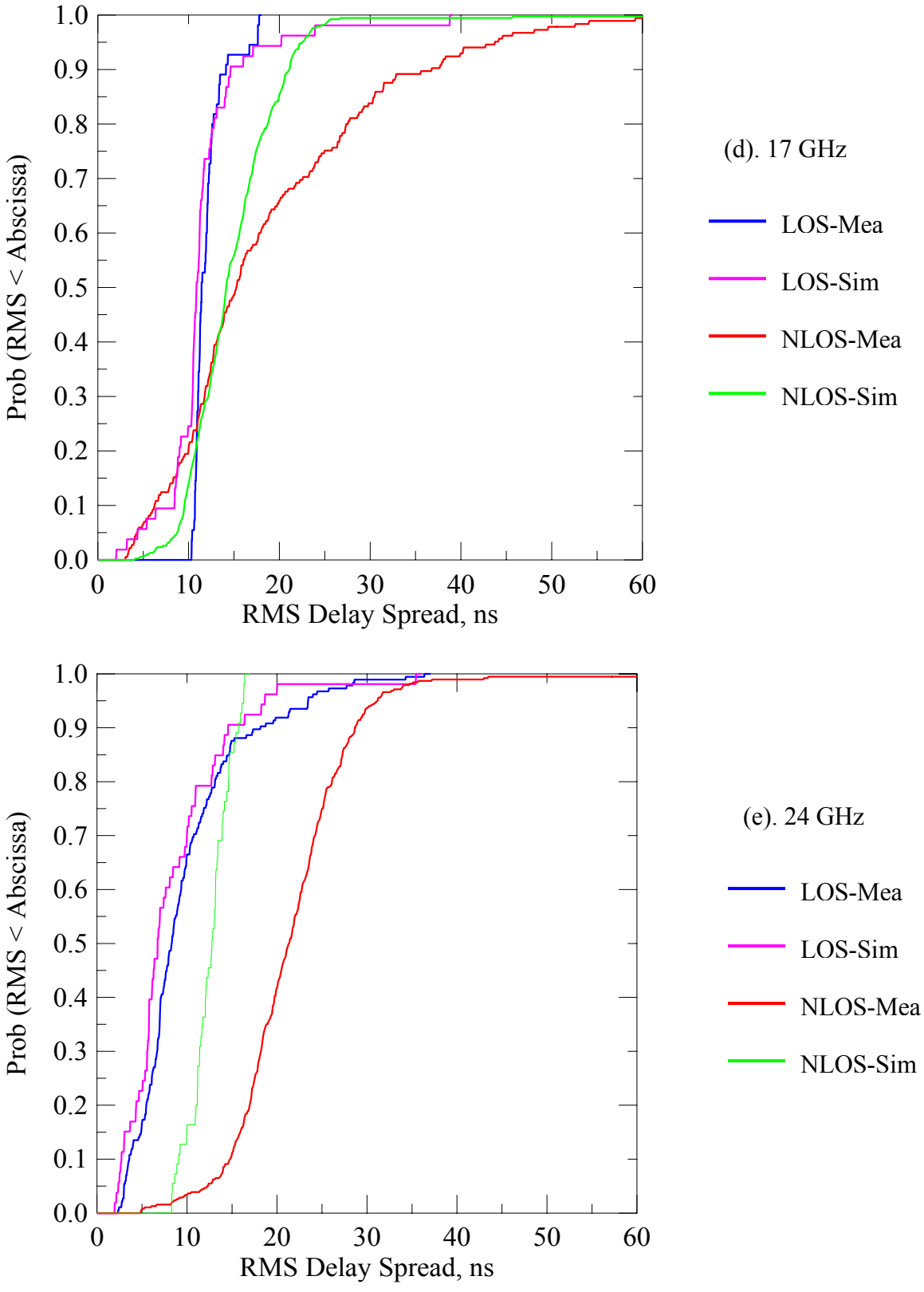

Figure 5.8 CDF of the RMS delay spread along the 3rd floor hallway: LOS and NLOS

The RMS delay spread as a function of transmitter - receiver distance is also plotted as shown in Figure 5.9. The S21 measurements have been made up to a maximum distance of 15 meters due to the limited length of cable available. In the section where both measurement and simulation data are available, the prediction is quite good. The simulated delay spread followed a similar shape of curve as compared to the measurement. There are multiple local maximums for the delay spread along the path. According to Robert Bultitude's paper [83], the delay spread should have a maximum value inside the range but our simulations show that there are maximum delay spreads at almost end of the path (hallway).

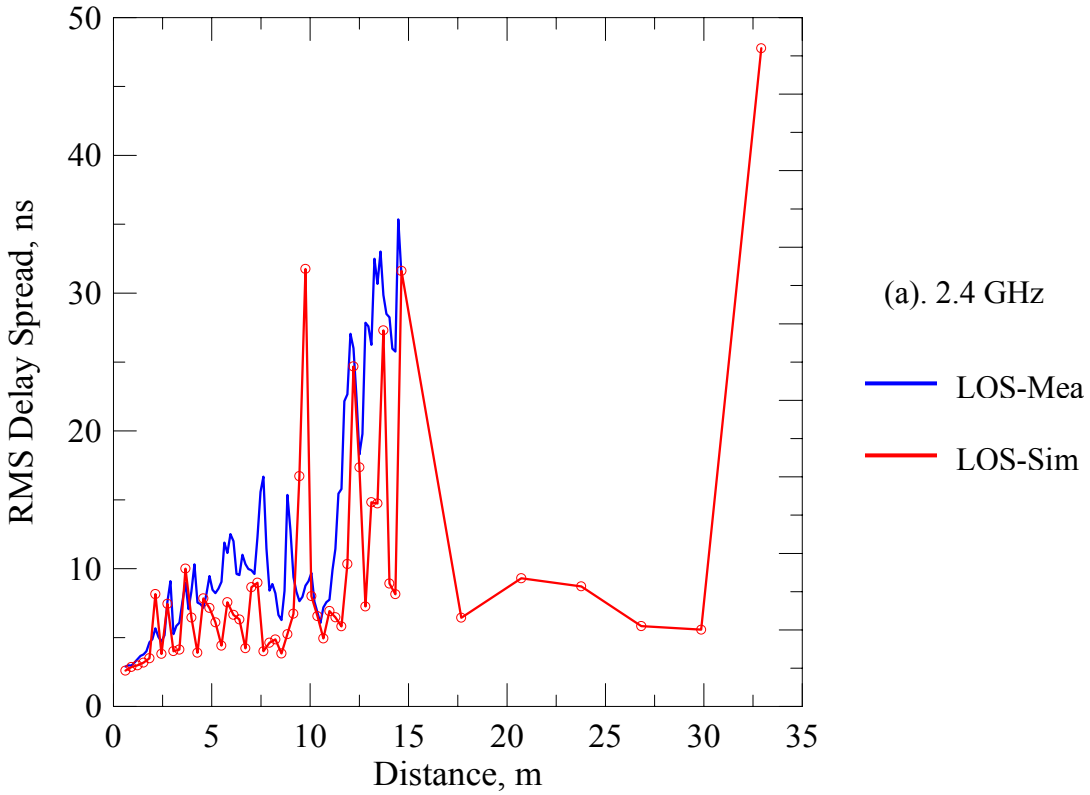

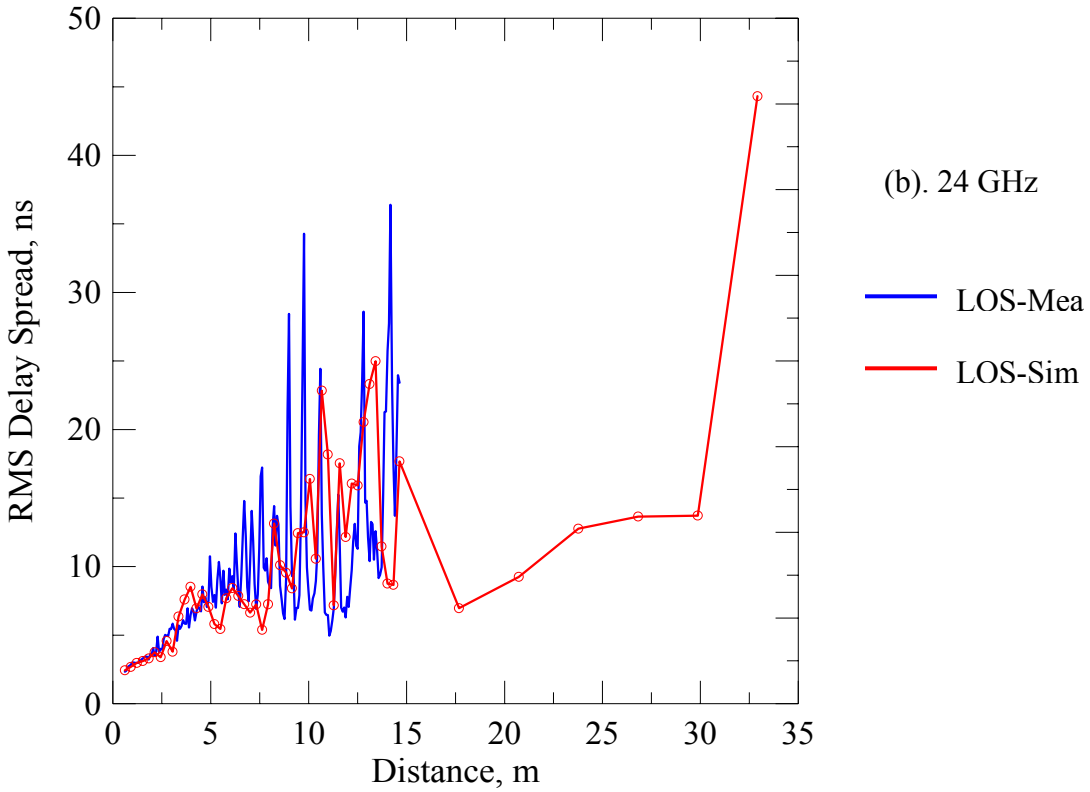

Figure 5.9 RMS delay spread as a function of Tx-Rx distance (LOS)

Since there are no measurements at that point, it is hard to decide which result is right. One possible explanation for the large RMS delay spread at the end of the hallway is that since the location of that point has reached the intersection with another hallway, it may introduce more multipaths to the channel.

5.6 Discussion of Possible Weakness of This Method

As can be seen from the simulation results, the weakness of this method is that it cannot be used to predict non-line-of-sight (NLOS) channel property such as delay spread. This means that either the electrical properties of the construction materials are not so accurate or the equivalent sources are not perfect enough to express all the

multipaths. To improve this method, future work should be done on both these sides to make sure that the materials and sources are accurately modeled. If the second problem is the dominant factor of error, it may be better to try simplified 3D ray-tracing method (Chapter 6).

Chapter 6

Access Point Optimization and Study of Shadowing Effects at 2.4 and 24 GHz

As described in previous chapters, currently higher frequencies have been investigated for future wireless system for available bandwidth and high data rate. But the large path loss due to the small wavelength of millimeter wave and availability of RF power has limited its range of application. In addition, complex indoor environment has created lots of multipaths to the communication systems, which further limits how much data rate can be achieved in a certain range. So an optimal installation of an access point has become more and more important. In the previous chapter, a combined 2D ray-tracing method has been shown to be quite useful and accurate in predicting the channel performance except on the RMS delay spread in NLOS environment. In this chapter, a simple 3D ray-tracing method is developed to improve the NLOS calculation. Based on this 3D ray-tracing model, investigation is done to find the optimal location for access point (AP). Also, simulation is carried out to find the shadowing effects of human bodies indoor at 2.4 and 24 GHz.

6.1 Previous Research on Access Point Optimization

Currently, the dominant commercial WLAN 802.11 (a, b and g) systems operate at 2.4 and 5 GHz band. Researchers are looking for even higher frequencies such as 17 GHz (HIPERLAN II by ERC) and 60 GHz (Swedish Foundation for Strategy Planning) for

future wireless communications. When frequency is high, path loss is larger than at low frequency for a same distance. Also RF power at higher frequencies is hard to get and the FCC has limit on the maximum radiated power. So future wireless system is more likely to be confined in a small cell, probably including only one or two office rooms. It is thus very important to select the location of access point for best performance. Nagy, Hills, Wright and Kamenesky did primary research on this issue [84] – [87].

In my opinion, two evaluation criteria should be considered to decide the optimal location of the access point: the coverage percentage of path loss and RMS delay spread. Previously researchers such as Nagy and Kamenesky all focused only on the path loss value for a good access point (base station) location and paid little attention to the delay spread value. In this paper, I have adopted a weighted sum to take both of them into account. In terms of optimization method, researchers have used previously either empirical or analytic methods such as the Nelder-Mead method [86], genetic method [84] or Hooke and Jeeve's, quasi-Newton and conjugate gradient method [88] to find the best AP location. In this chapter, we start by analyzing AP installation in an empty office room in order to understand the physics inside. Then we introduce a newly developed GSS (Generating Set Search) method which can be used to find the optimal access point location in a furnished office room. Battiti,

When an access point is installed inside a room, the path between the access point and the mobile device is sometimes blocked by human body, which changes channel performance significantly. In this chapter, we build a simple human body model using the

electrical properties of human tissues published [4] and analyze shadowing effects of human body at both 2.4 and 24 GHz bands.

6.2 Simplified 3D Ray-tracing Model and Its Verification

A simplified 3D ray-tracing code is developed in MATLAB. The code takes two input data files to define the indoor structure under investigation. The first input defines the outside boundary of the whole indoor environment. It can be outside walls of the interested region or air (free space). The second input defines the detailed indoor structures such as office doors, windows, furniture and human bodies. To make it easy for programming, the current code currently only considers indoor objects with vertical edges from ground. Also, it takes only vertical edge diffractions into account in simulation. Horizontal edge diffractions need to be added specifically in the code.

To verify this 3D ray-tracing model, S21 measurement has been done in the side hallway at the $3P^{rdP}$ floor of Moore lab (Figure 6.1). The transmitter (Tx) and the receiver (Rx) antennas are both AEL broadband horns which cover from 2 to 24 GHz bands. The plasterboard sidewalls, wooden office doors and glass windows were all included in the 3D ray-tracing model for simulation. Their physical parameters are derived from past calibration measurements. The S21 comparison of measurement and simulation at 2.4 and 24 GHz (bandwidth = 250 MHz) with Tx-Rx distance of 1.5 meters (LOS) is given in Figure 6.2. It can be seen from the figure that even horizontal diffractions have not been considered, the simulated S21 matches quite well with measurement. This verifies that

our 3D ray-tracing model with the material properties extracted before can be used to predict indoor wireless channels at both 2.4 and 24 GHz.

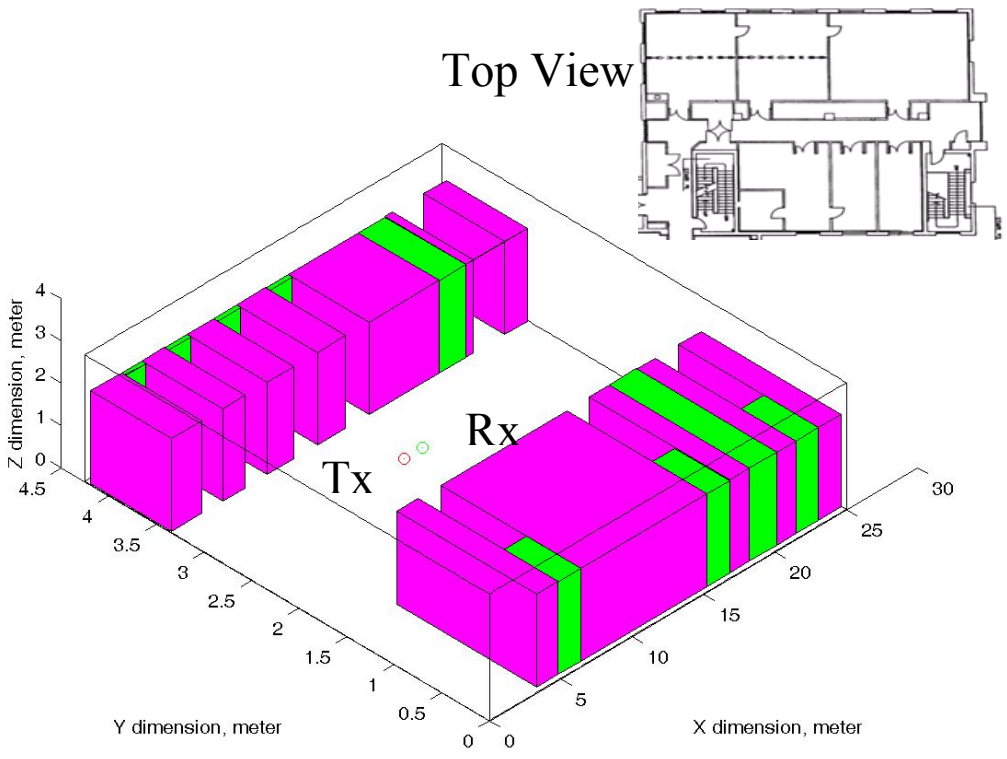

Figure 6.1 Side hallway at the 3rd floor of Moore lab

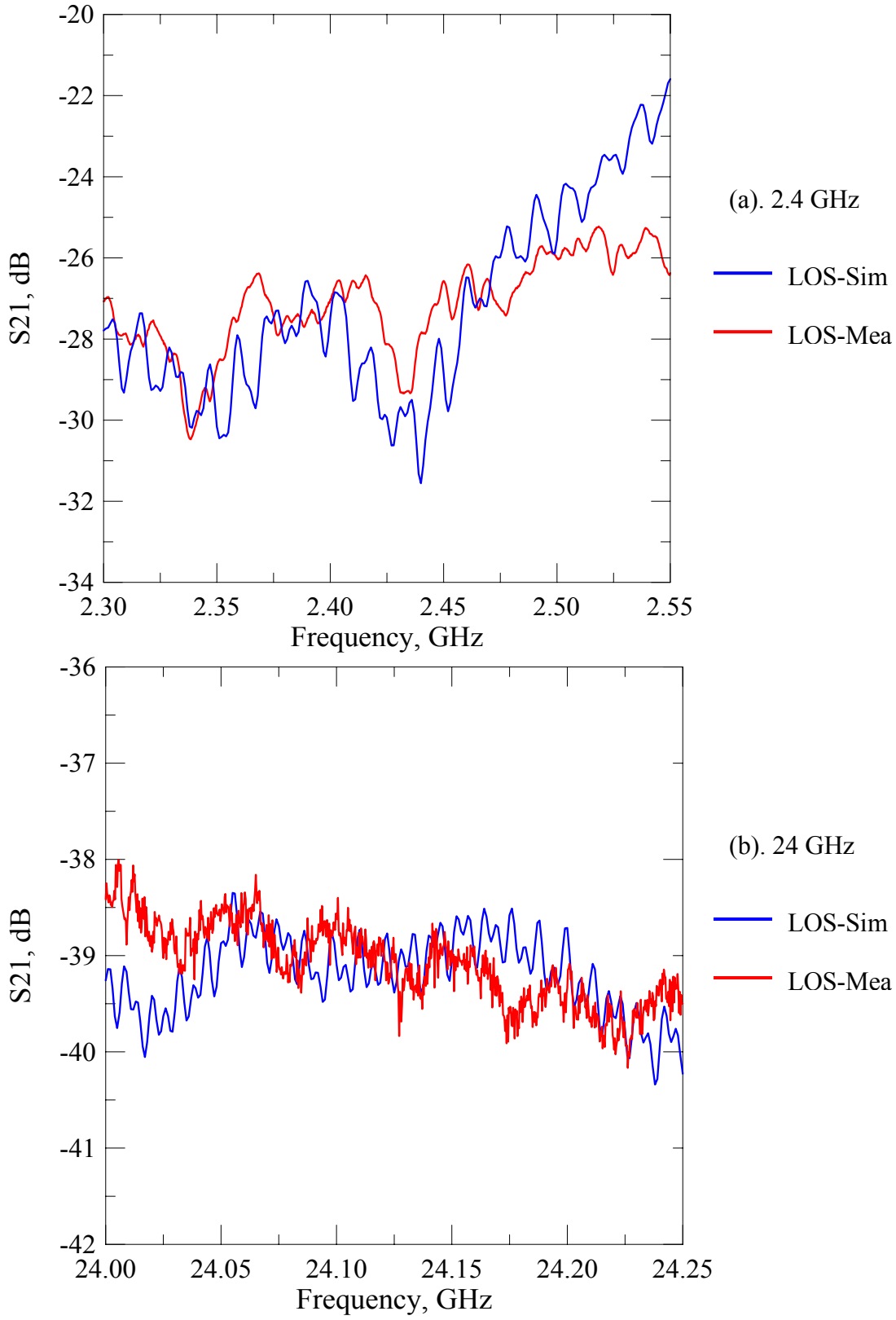

Figure 6.2 S_{21} comparison of simulation and measurement (2.4 and 24 GHz)

6.3 Optimization of Access Points: Empty and Furnished Office Room

An optimally designed wireless system always requires the largest percentage of simultaneous signal coverage in the interested region. In terms of system performance, path loss property of the system determines the available signal level or S/N ratio at the receiver, while the RMS delay spread determines the maximum data rate the receiver can obtain to avoid Inter-Symbol Interference (ISI). These two properties are both important values we need to pay attention to when implementing a wireless system, especially when installing an access point. In the past, people always focused on the signal level when designing an indoor wireless system. Now, we used a weighted sum as the evaluation criteria for the performance of the wireless system under investigation (6-1). It takes into consideration both path loss and RMS delay spread. If the most limiting factor of the system is one of them, the weighting coefficient α can be changed to emphasize this effect.

$$F\left(P_{access}; S, \alpha, PL_0, \tau_0\right) = \alpha \cdot \frac{Number(PL < PL_0)}{Number_{Total}} + (1-\alpha) \cdot \frac{Number\left(\tau_{RMS} < \tau_0\right)}{Number_{Total}} \tag{6.1}$$

where P_{access} is the coordinate of access point, S defines the desired wireless service region, α is the weight for signal level and delay spread coverage, PL_0 and τ_0 set the threshold level for signal level and delay spread. Number is a function that counts the number of grid points satisfying the condition in the service region. The default Tx and Rx antennas are isotropic, but they can be any antennas if pattern files are provided.

CASE-I: Empty Office Room (6×8×3 m^3)

We built up an empty 6×8×3 m room model in the MATLAB 3D ray-tracing program to get some general ideas of placement of access point. The side walls in the model are

made of plasterboard; ceiling and floor are made by brick. Beside the wooden door, there is nothing inside the room. Full-scanning (brute-force) method is applied to find the optimal access point position in this empty room. First, we set up three groups of access point locations: ceiling mount, corner mount and center wall mount. After simulation of access point in each of groups, we obtain the optimal points in each group and also find the best position among the three groups defined. This can give us an idea what should be the best way to install access point. Signal coverage percentage is calculated in predefined interesting region. This can be any place where the mobile computer can be set. In the simulation, the height of receiver is set 1 m above ground (Figure 6.3). The ceiling base AP coverage at 2.4 GHz is shown in Figure 6.4 (PL_0=-50dB, τ_0=5.5 ns). The rest coverage plots are omitted due to space limitation.

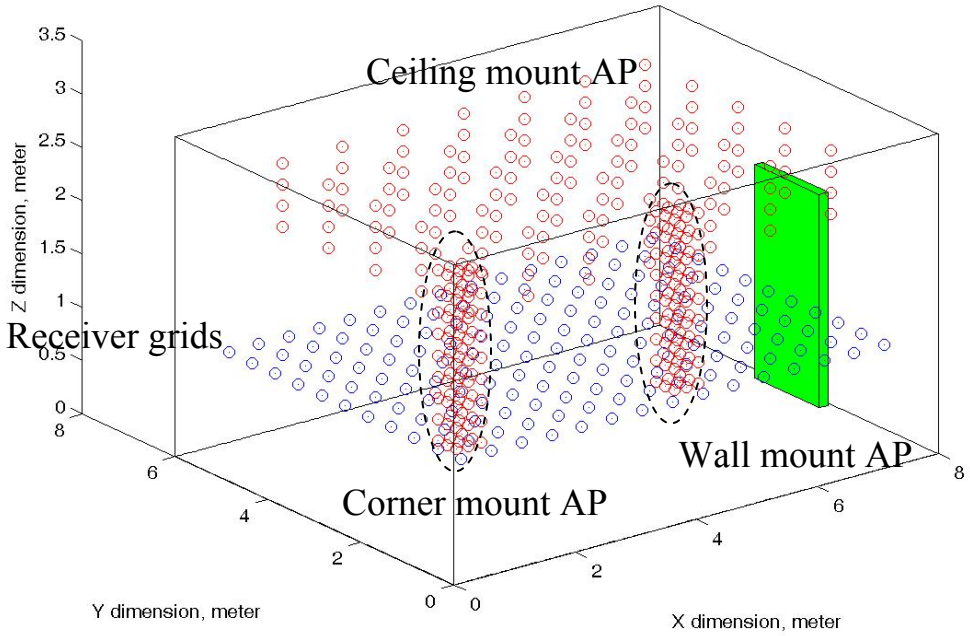

Figure 6.3 A Brute force method to find out the optimal AP position

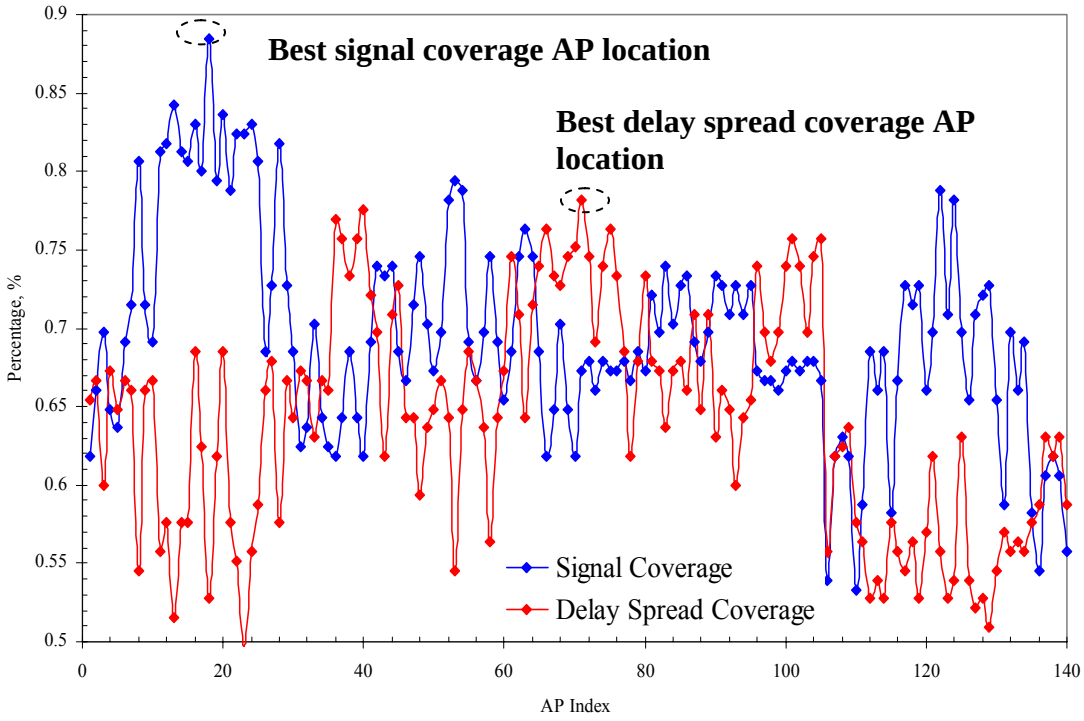

Figure 6.4 Coverage percentages for ceiling mount APs at 2.4 GHz

As can be seen from Figure 6.4, the best AP locations for signal level and delay spread are different. In the 3-meter high office room model (Figure 6.3), and the best AP location for signal level coverage is found at the center of the room and 2.2-meter from ground. This result is true for both 2.4 and 24 GHz. The coverage percentage at 24 GHz is similar to 2.4 GHz as shown in Figure 6.4. But the best AP location for maximum delay spread coverage (α=0) is off the center. According to simulation, the best AP locations for maximum delay spread coverage are (1, 1, 2.6) at 2.4 GHz and (1, 4, 2.6) at 24 GHz. The best ceiling mount AP has been picked to show the distribution of signal level and delay spread in the room. Figure 6.5–6.8 show 2-D contour maps and 3-D maps of signal levels and delay spreads distribution inside the room when the AP is mount in the center of the room (best signal AP position) at 2.4 GHz. It is easy to see

from the plots where the receiver will have best performance in terms of SNR and delay spread.

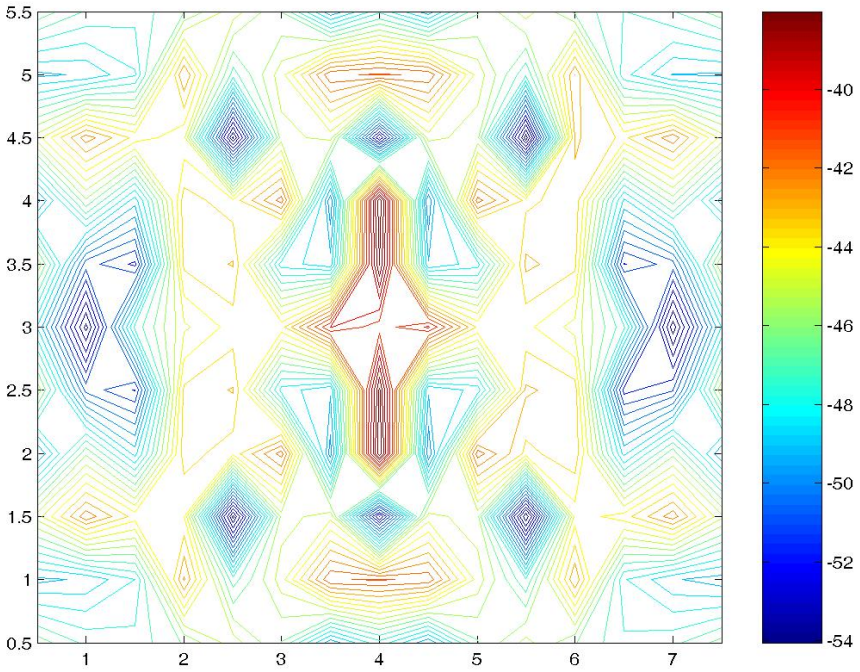

Figure 6.5 The 2D contour map of signal levels by a center ceiling mount AP

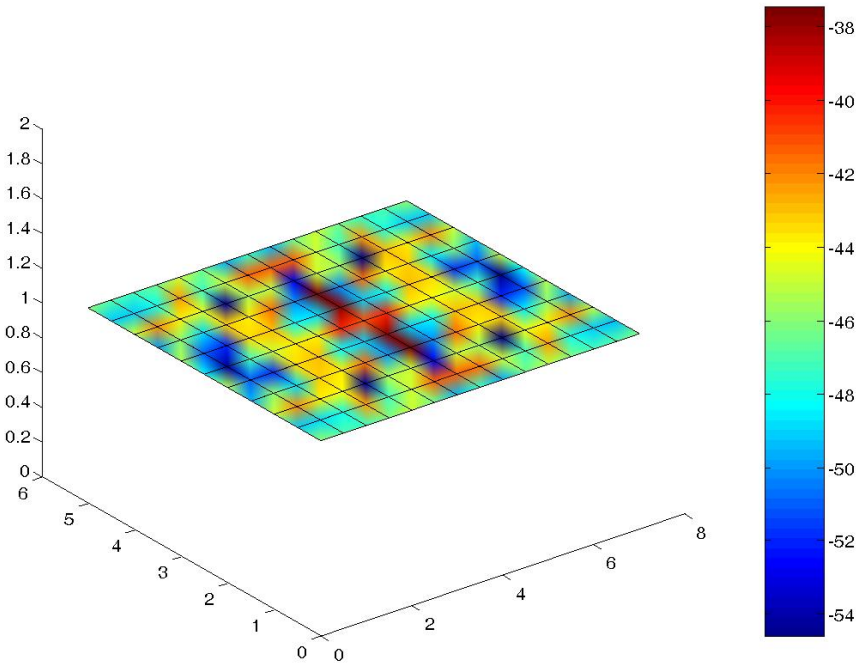

Figure 6.6 The 3D map of signal levels by a center ceiling mount AP

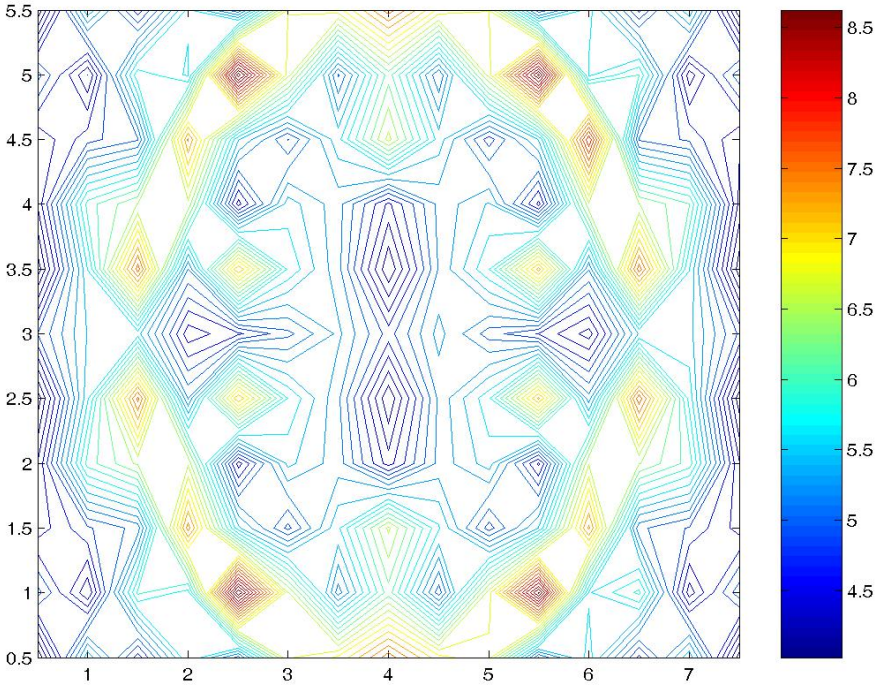

Figure 6.7 The 2D contour map of delay spreads by a center ceiling mount AP

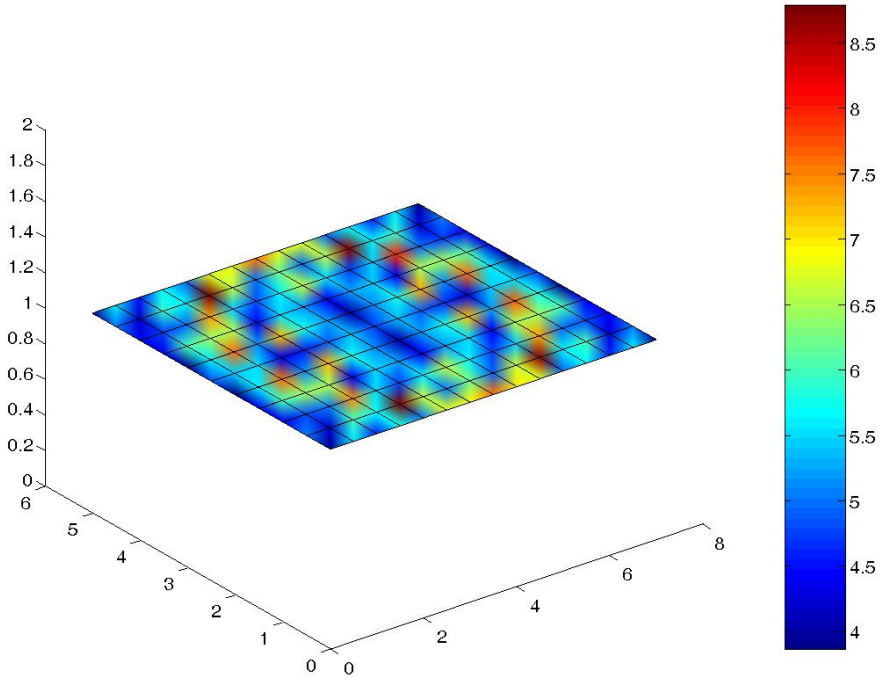

Figure 6.8 The 3D map of delay spreads by a center ceiling mount AP

In addition to the ceiling mount APs, wall mount and corner mount APs have also been considered. The analysis was done at both 2.4 and 24 GHz. Similar trends are found for these two frequencies. We found that among all three groups of AP positions, the best AP location for signal level coverage is at center of ceiling but the best location for delay spread coverage is at either at corner or center of wall.

AP1 – 2.4	**AP1 - 24**	**AP2 –2.4**	**AP2 – 24**	**AP3 – 2.4**	**AP3– 24**
(4, 1, 2.2)	(4, 1, 2.6)	(0.2, 0.6, 2)	(0.2, 0.6, 2)	(4.2, 0.2, 2)	(4, 0.6, 2)

Table 6.1 Best AP location (Case-I α=0.5): AP1-Ceiling based, AP2-Corner based, AP3-Wall based (2.4 GHz or 24 GHz)

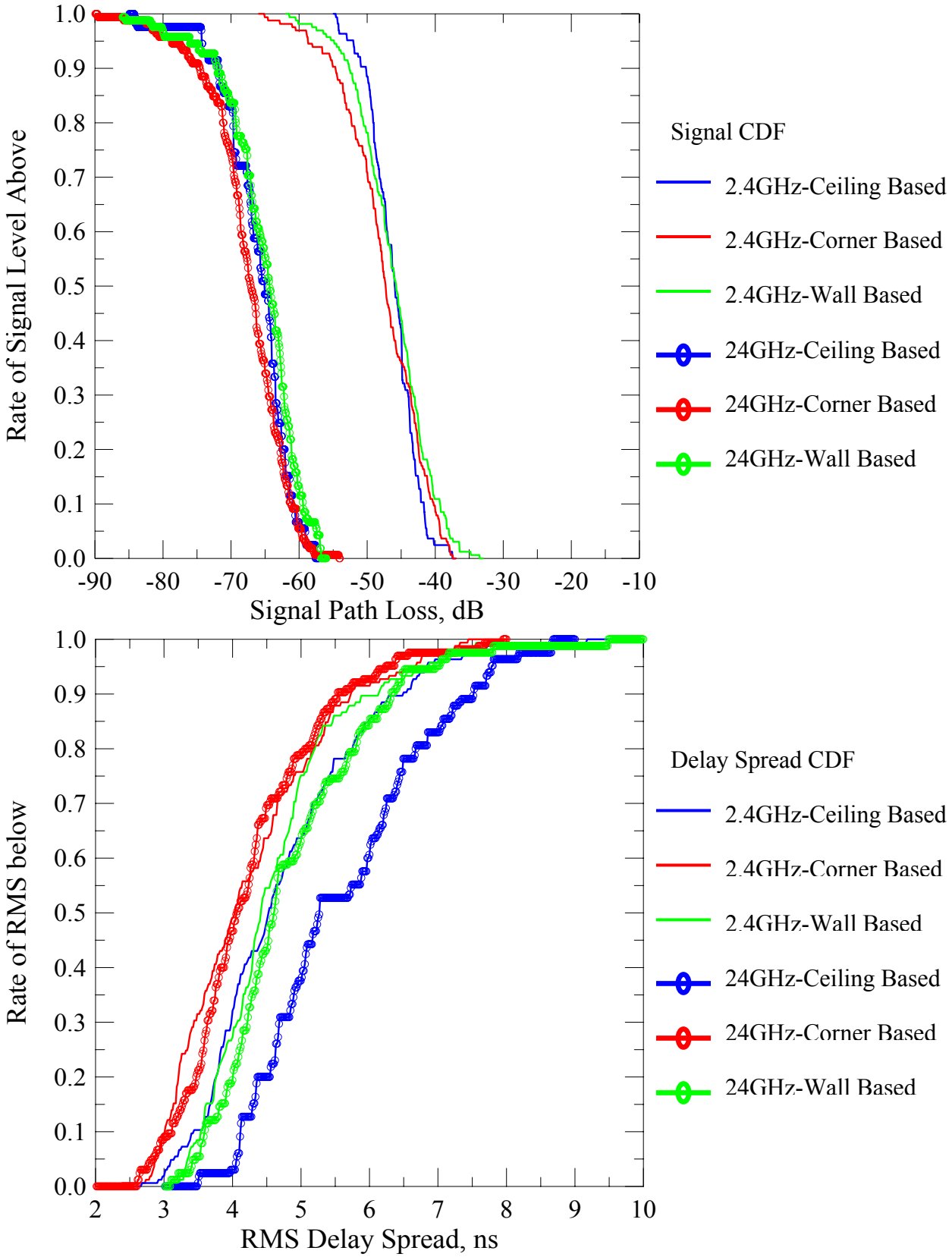

Figure 6.9 CDF of signal level and RMS delay spread coverage in the empty office room

CASE-II: Furnished Office Room

In a real system, access point will be installed in a full-furnished office room. It may have a desk, chair, bookshelf and cubicle, etc. Also human bodies should be considered too. So the AP optimization has to take all these into account. Since more multipaths are created by reflections and diffractions due to those objects, the ray-tracing calculation is more time-consuming. The previous full-scanning (brute-force) search is no longer an efficient way to find the optimal point. New method for optimization is needed. After reviewing previous researchers' work on applied mathematics, I decide to apply the GSS (General Set Search) algorithm for linear constraint problem [90]:

$f : R^3 \to R$ **is the evaluation function** $(= -F(P; S, \alpha, PL_0, \tau_0))$**, Let Ω define the feasible region**

Step 1. Let $D_k=G_k \cup H_k$, where G_k satisfy condition (8.4 or 8.5 and 8.8 in [5]), $\beta_{\min} \le \|d\| \le \beta_{\max}$ for all $d \in G_k$, H_k is a finite set of additional search direction such that $\beta_{\min} \le \|d\|$ for all $d \in H_k$.

Step 2: For $d_k \in D_k$, let $\alpha_k(d)$ be the largest non- negative value of α for which $x_k+\alpha d \in \Omega$, Let $\Delta_k(d) = \min(\Delta_k, \alpha_k(d))$.

Step 3: if there exists $d_k \in D_k$ such that $f(x_k + \Delta_k(d_k)d_k) < f(x_k) - \rho(\Delta_k(d_k))$, then do the following:

-Set $x_{k+1} = x_k + \Delta_k(d_k)d_k$.

-Set $\Delta_{k+1} = \Phi_k \Delta_k$, where $1 \le \Phi_k \le \Phi_{\max}$.

Step 4: $f(x_k + \Delta_k(d)d) \ge f(x_k) - \rho(\Delta_k(d))$ is true otherwise, for all $d \in D_k$, do the following:

-Set $x_{k+1} = x_k$

-Set $\Delta_{k+1} = \theta_k \Delta_k$,where $0 < \theta_k < \theta_{\max} < 1$.

-If the directions satisfy Con 8.5, set $\varepsilon_{k+1} = \theta_\varepsilon \varepsilon_k$

-If $\Delta_{k+1} < \Delta_{tolerance}$, then terminate.

The GSS algorithm has been proved for convergence, is easy to implement and has more freedom to control the search direction as compared to the previous work. The optimal search is carried out for a furnished room with a desk and a 1.7-meter tall person inside as shown in Figure 6.11. The GSS search starts at (4,1,2.2) and stops at optimal point (6, 2, 2.6). Another promising optimal search method is called Nelder-Mead method, also called Amoeba method. Basically, it defines a couple of possible direction of movements and compare. This is a downhill simplex method. The advantage is that it is easy to program but the convergence for higher dimension needs to be proved.

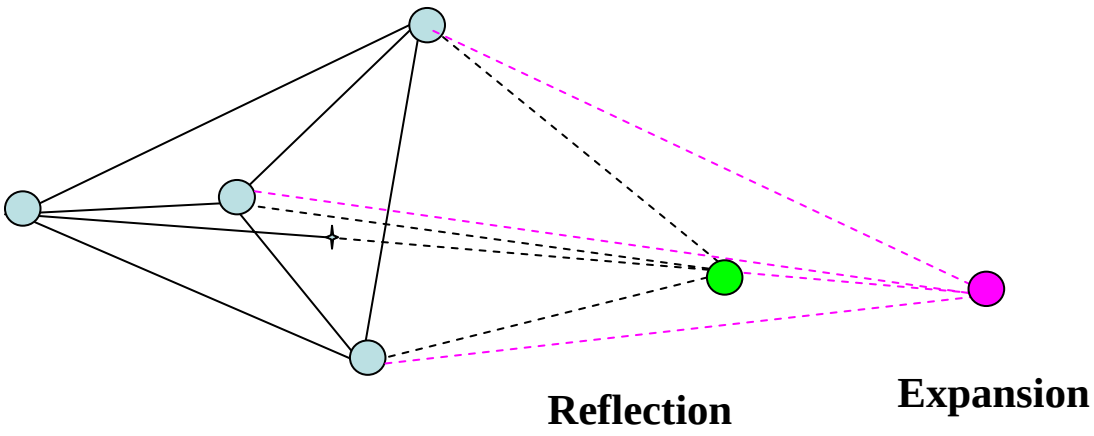

Figure 6.10 Reflection and expansion in Nelder Mead search method

6.4 Study of Human Body Effects in Wireless Communication

In recent years, people have paid more and more attention to the human body effects on the indoor wireless communication [91]. This is because microwave and millimeter-wave channel is more likely to be LOS and human body constitutes an insurmountable obstacle for microwaves. Previous researchers' work on the human effects involved much on some empirical analytic models, and statistics is always applied. Also blocking is the dominant type of effects being studied. I think that the previous statistical method is not good enough as guidance for system implementation. In addition, the human body contributes not only blocking, but also strong reflection and diffraction. So in this paper, a new body effect model is proposed to deal this problem.

	2.4 GHz			**24 GHz**		
	Conductivity	Permittivity	Loss	Conductivity	Permittivity	Loss
Blood	2.5024	58.347	0.32123	32.951	27.077	0.91147
SkinDry	1.4407	38.063	0.2835	22.841	18.993	0.90073
Muscle	1.7050	52.791	0.24191	29.437	27.395	0.80483
Average	1.8827	49.734	0.2822	28.409	24.488	0.87234

Table 2. Dielectric properties of body tissues (Camelia Gabriel – Final Report AL/OE-TR-1996-0037 [89])

To build the model of human bodies, we used the results from a recent published paper [89]. The average property of blood, skin and muscle is calculated and treated as the effective property of human body. As shown in Figure 6.11, the most possible place

of human body is the crossing trace from each center of walls. So the model takes equal possibility that the human will stand at the grid on the trace. The simulation results are given in Figure 6.12.

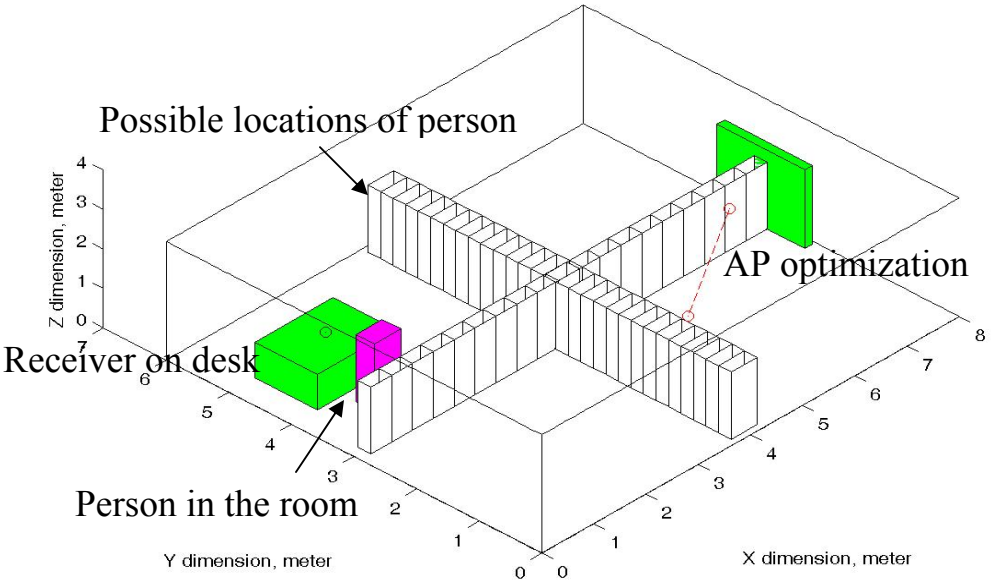

Figure 6.11 Study of human body effects in an office room

As can be seen from Figure 6.12, there is not much difference in delay spread but signal levels drops a lot when the frequency goes high. In the signal level CDF plot, it seems that the ceiling mount AP always has the worst signal levels at both frequencies when human body is present in the room. In addition, 2.4 GHz seems to have a smaller variation of signal levels as compared to 24 GHz. In the delay spread CDF plot, it seems that the best delay spread is achieved in different groups at different frequencies. The best delay spread is obtained in wall based AP at 2.4 GHz but in ceiling based AP at 24 GHz.

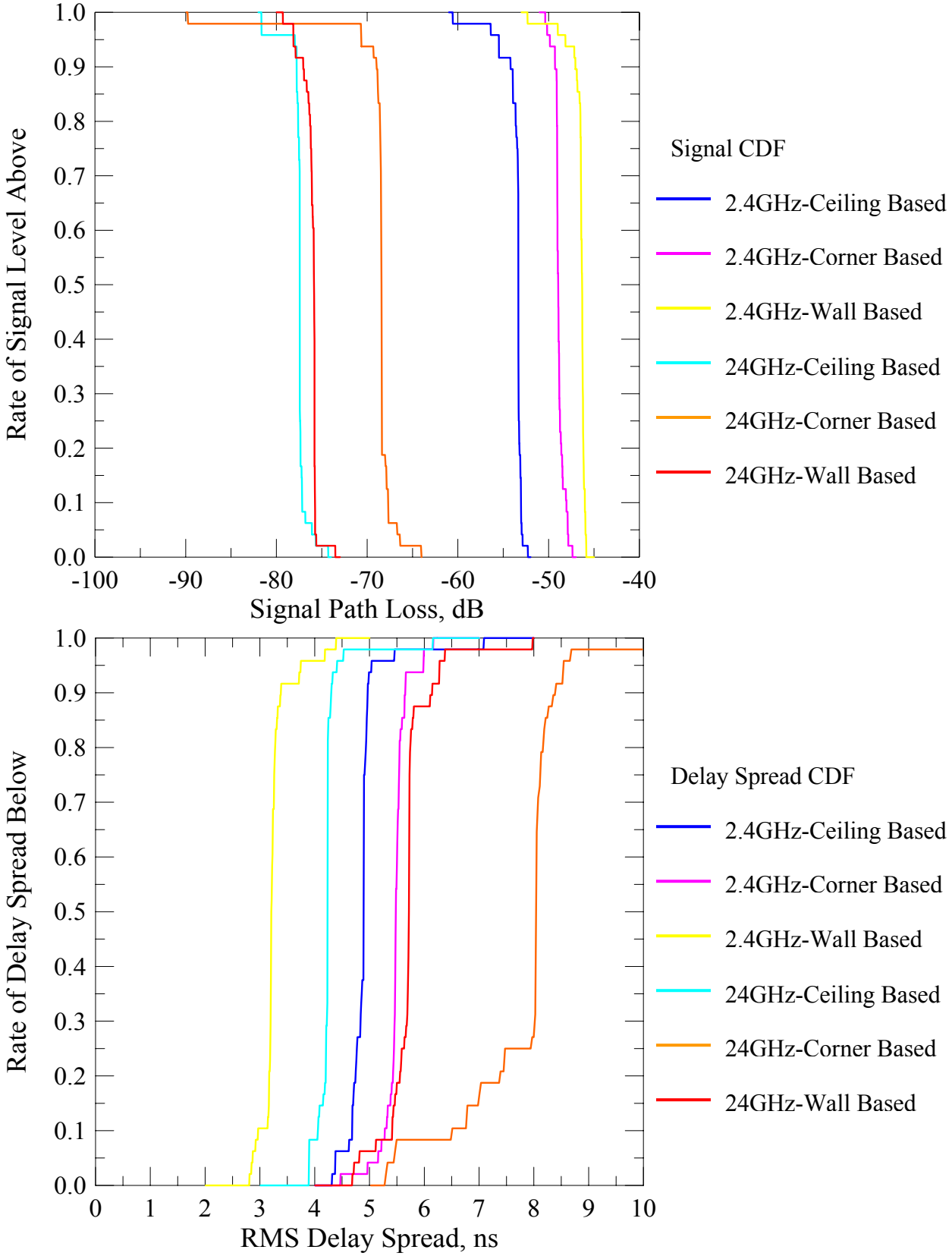

Figure 6.12 Shadow effect of human body at 2.4 and 24 GHz

6.5 Discussion on Future Improvement of this Model

In this chapter, a simple 3D ray-tracing program is built and verified. It has been applied to an empty and furnished room to find out the optimal location for access point. GSS algorithm is developed to achieve the optimal search. It has the advantages of easy to implement and has been proved convergence. Also, human shadow effects are studied at 2.4 and 24 GHz. From simulation, we found that the shadowing effect is about 5 to 10 dB AT 2.4 GHz and 10 to 25 dB at 24 GHz.

But there are still many places that need further improvement. First, this model is verified by a series LOS measurement in the side hallway. Actually this is not a so accurate way to verify the model since the antenna gain is high and the direct path dominates the channel. It will be quite hard to distinguish the multipath effects in the ray calculation as compared to the measurement. A better way to verify the channel should be a NLOS measurement. Second, this is a simplified 3-D ray-tracing model which ignores some of the ray calculations such as horizontal object diffractions and multiple diffractions and reflections by indoor objects. To obtain a more accurate model, those ignored weak multipaths must be added in the whole calculation. Third, another very challenging work is that how to modify this model to handle problems of outdoor environment. This is a very interesting area since currently people are thinking about designing meshed network for future outdoor wireless LAN. If there is some tool people can use to optimize their base stations, it will be beneficial to the whole wireless industry.

Appendix A
Design of a Compact Anechoic Chamber System

To provide a controlled environment, an all-weather capability, and security, and to minimize electromagnetic interference, indoor anechoic chambers have been developed as a useful testing tool of antennas for years. Presently there are two basic types of anechoic chamber: the rectangular and the tapered chamber (Figure A.1). The design of each is based on geometrical optics techniques, and each attempts to reduce or minimize specular reflections.

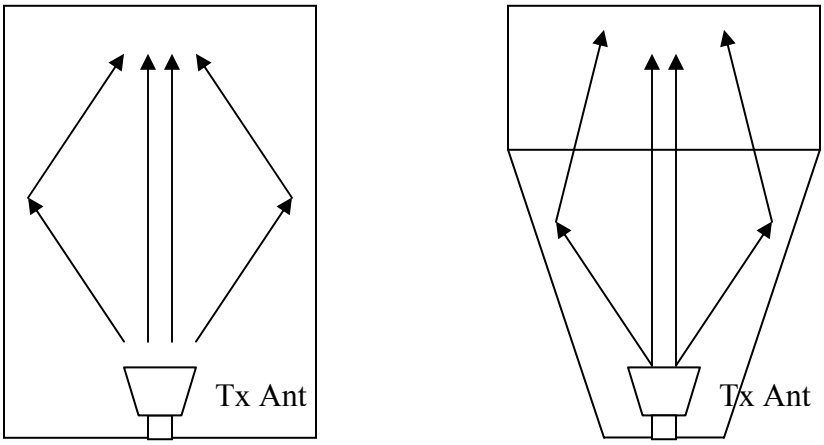

Figure A.1 Rectangular and tapered anechoic chambers and the corresponding side-wall specular reflections.

The old rectangular anechoic chamber in the RF & Microwave lab was designed by former Caltech students. It occupies a space of $1.5 \times 1.5 \times 3$ m^3. After more than ten years usage, some of the pyramidal absorbing materials have already fallen apart from the chamber wall. This deteriorates the RF performance of the absorber and makes the

pattern measurement inaccurate. To solve this problem and also to save the space in the lab, a much smaller tapered anechoic chamber is designed to replace the old one.

In theory, the tapered anechoic chamber takes the form of a pyramidal horn. It begins with a tapered chamber which leads to a rectangular configuration at the test region. At the lower end of the frequency band at which the chamber is designed, the source is usually placed near the apex so that the reflections form the side wall tend to have big incident angles, which will be guided along the chamber wall all the way to the bottom of test region and get absorbed. In this way, the multipaths are greatly reduced and the direct path remains to be the dominant path in the measurement. This can be illustrated by ray tracing techniques. Also, reflections from the walls of the chamber are further suppressed by using high gain source antennas whose radiation towards the walls is minimal.

A new chamber designed at RF & Microwave Lab is shown in Figure A.2. It takes a space of 0.75 x 0.75 x 1.80 m^3. And a computer program is developed using Visual C++ to control the stepper motor system and to communicate with the HP8722D network analyzer to obtain the measurement data.

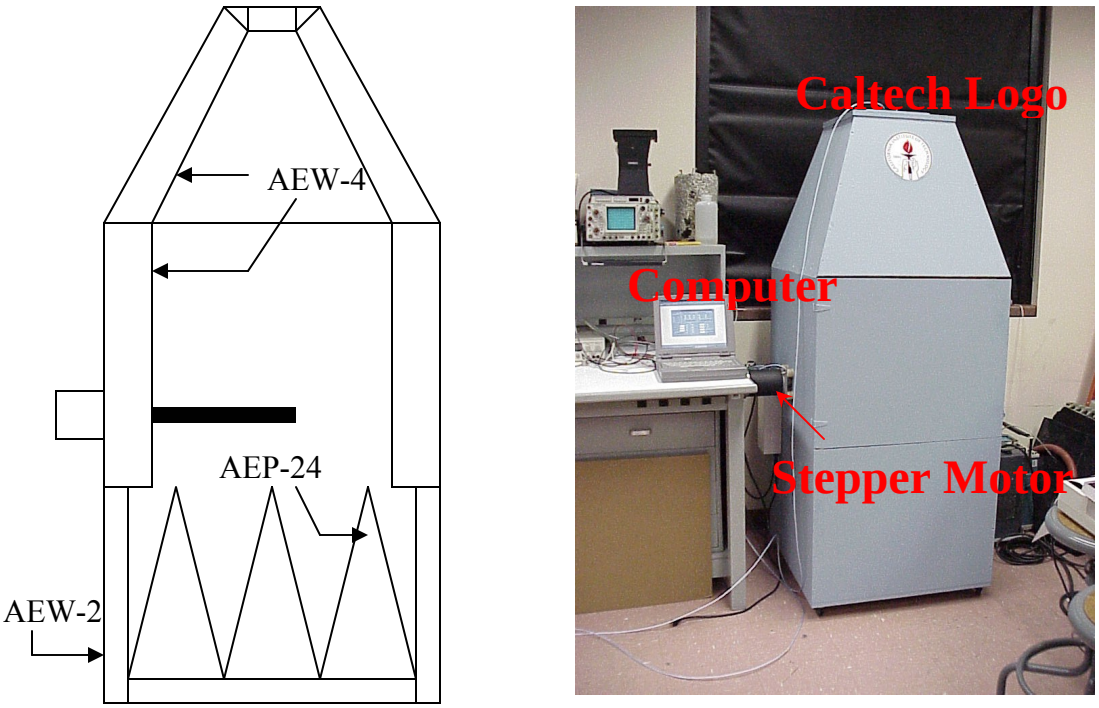

Figure A.2 The schematic diagram and the photo of the compact anechoic chamber.

A.1 Absorber Material

The absorber materials are often used in the anechoic chamber to lower the forward scatter, i.e. angle of incidence equals angle of reflection, and offer favorable back scatter properties at off-normal incidence. Normally manufacture provides the absorber materials in a variety of thickness and shapes, giving the chamber designer the opportunity to choose grades appropriate for specific frequencies and incidence angles.

In this design, the author chose two types of absorbing materials: broadband pyramidal absorbers (AEP) and broadband wedge absorbers (AEW). The first material is used to provide good absorb termination for the chamber. And the second material is used to direct energy in a given path so that it may be efficiently absorbed by large high

performance terminal absorber material. *Advanced ElectroMagnetics, Inc*. is the manufactory of these absorbers. Their related properties are listed in the following table.

Type	**Length**	**Pys/blk**	**0.25**	**0.50**	**1.0**	**3.0**	**6.0**	**10.0**	**15.0**	**30.0**	**Power**
AEW-4	4”	12				30	35	40	45	50	0.5w/in^2
AEP-24	24”	9	30	35	40	45	50	50	50	50	0.5w/in^2

Table A.1 Absorption at normal incidence (-dB, Freq. in GHz)

AEW-2 is a 2-inch version of wedge material similar to AEW-4, but the data is not listed. It is used in the region near of AEP-24 (Figure A.2), where the EM waves have been significantly absorbed by that pyramidal material (AEP-24).

A.2 Motion Control System

In the anechoic chamber, there should be a way to rotate the AUT (Antenna Under Test) so that the radiation pattern can be measured. To simplify the design, only one-degree freedom rotation system is made through the stepper motor and motor driver. With the mount of another rotation stage for the transmitter horn, this system is able to measure the normal antenna E and H plane pattern easily.

The initial goal of this chamber design is to make a system which can work for any kind of antennas, so the stepper motor is chosen in a conservative way that it has a driving force large enough for different antenna loads. But to make the whole system work, a proper driver must be chosen which can match the properties of the motor. In

this design, the step motor and motor driver are purchased from the same company - *Anaheim Automation*, which specializes in reliable and cost-effective motion control systems.

A.2.1 Stepper Motor

The two most important properties of the step motor are its holding torque and size. A bigger motor is meant by a higher torque value and a larger frame shaft. A conservative motor (Model 42D212S) is chosen to for the chamber design. Here, 42 means the size of the mount frame is 4.2 inches, and S shows that this motor has single ended shaft. Some of the related properties of this motor are listed in the following Table A.2.

Voltage (V/phase)	**Current (I/phase)**	**Resistance (R/phase)**	**Inductance (mH/phase)**	**Residual Torque (oz in)**	**Holding Torque (Min oz in)**
3.6	6.1	0.59	5.94	30.0	1125
Slew Torque (oz in)	**Rotor Inertia (nominal)**	**Torque to Inertia Ratio**	**Shaft DIA (in)**	**Motor Length (Max in)**	**Weight (lbs)**
840	110.5	10.2	0.625	6.99	15.7

Table A.2 Specifications of model 42D212S

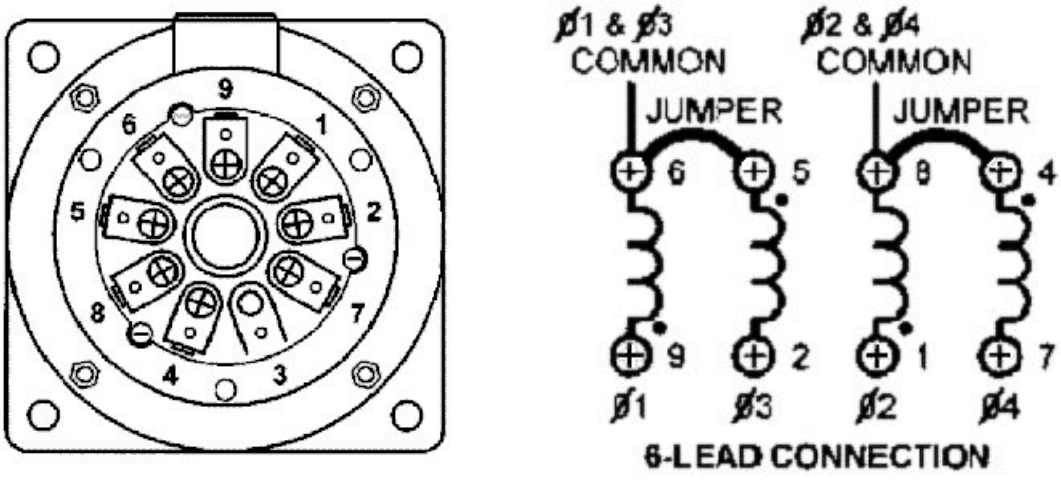

Figure A.3 Cross section of the 42D212S stepper motor and its 6-lead connection.

6-lead connection is used to minimize the phase current when the phase voltage is fixed (Figure A.3). In this configuration, the maximum current in each phase is about 6.1Amp.

A.2.2 Stepper Motor Driver

There are two factors to be considered in the choice of motor driver. First, the driver should be able to generate enough current to drive the stepper motor 42D212S. Second, there should be an appropriate microstep operation mode in the driver so that a required resolution of antenna pattern can be achieved. Model MBC08081 is one of the economic versions of motor driver by *Anahein Automation* which can support microstep operation up to 1600 steps/rev (0.225 ^{o} / step), and it has a output current capability of 8.3 Amps maximum. So in principle, this driver should be able to work with the chosen stepper motor in the anechoic chamber.

The MBC08081 microstep motor driver has an output current capability of 2.3 A minimum to 8.3A maximum (peak rating). It will operate from +24VDC minimum to +85VDC maximum. The clock input is set to receive negative edge clocks with a maximum frequency of 100 kHz. With MBC08081, various step resolutions can be implemented by the on board dip switch. These divisions range from 200 steps per revolution to 1600 steps per revolution. An additional power supply (PSA 80V4A) is used to provide the +85V voltage.

Hookup configuration for current sinking inputs is select for the connection as shown in the following Figure A.4. The external pulse generator inside the graph is realized by

the I/O port of the control labtop computer. The computer also works as a central processor to communicate with the HP8722D network analyzer and do data acquisition.

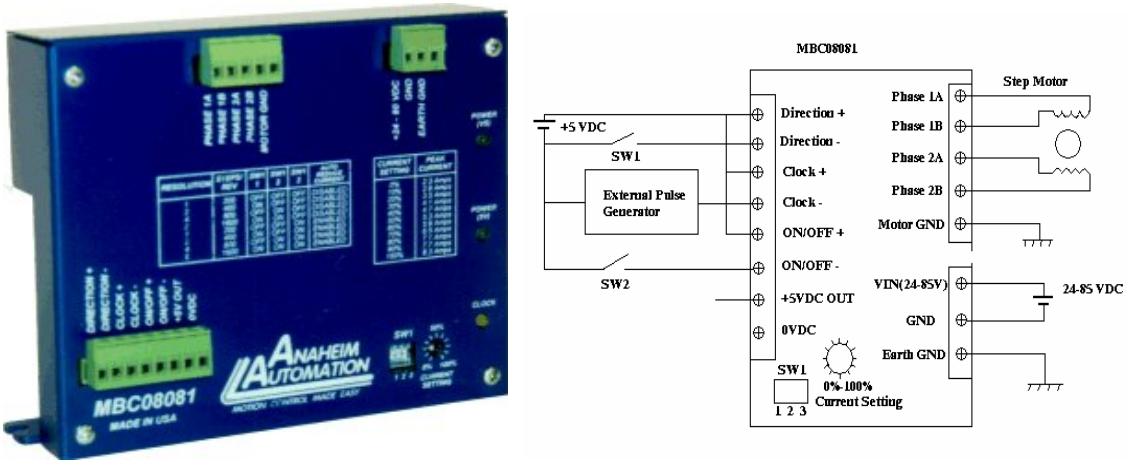

Figure A.4 MBC08081 microstep motor driver and its hookup circuit (current sinking)

A.3 System Control by Laptop Computer

The schematic diagram of this chamber testing system is shown in Figure A.5. As can be seen from the figure, control signal is sent from the laptop computer to operate the stepper motor driver through its I/O port. At the same time, GPIB interface is used to communicate between the laptop computer and vector network analyzer (HP 8722D). Proper codes are written to synchronize the operations of network analyzer and the motor driver. For an appropriate antenna measurement, lots of design issues must be carefully considered. For example, after the motor makes every step rotation, the program should wait for a short period of time before taking any measurement to let the motor reach a stable position. Otherwise, the measurement pattern will see some ripples due to the shaking effects of the motor in motion.

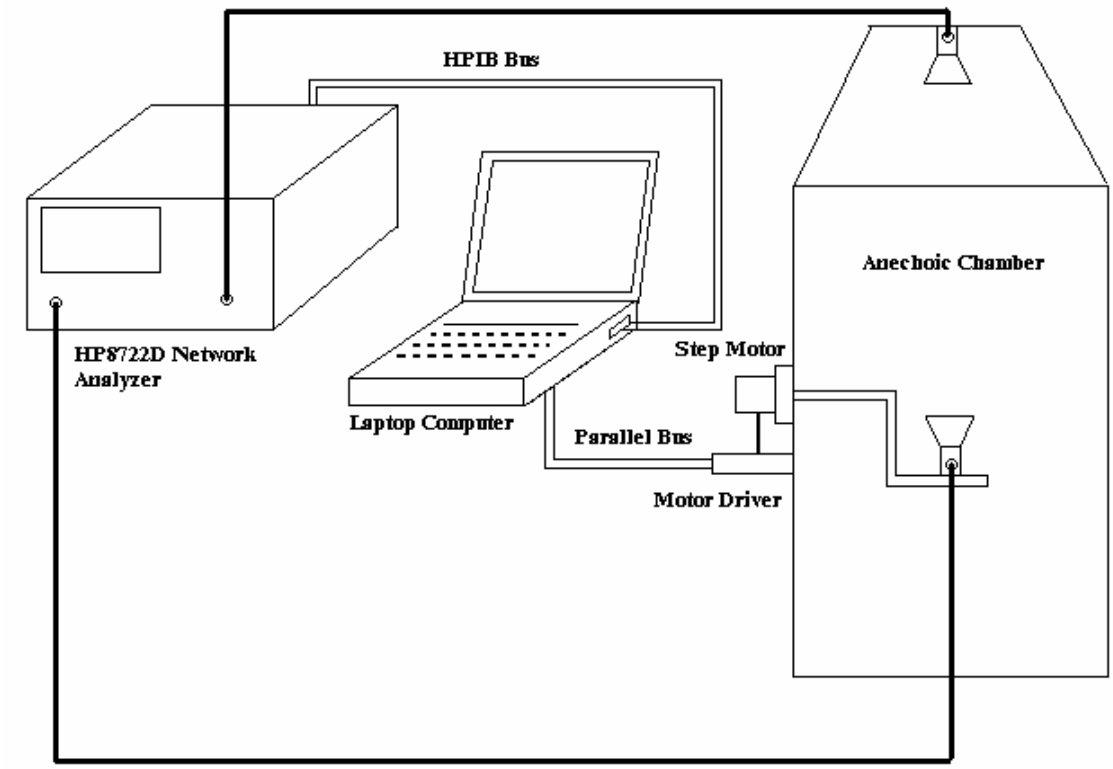

Figure A.5 Schematic diagram of the anechoic chamber testing system

A.3.1 First I/O Control: Parallel Printer Port (PPP)

There are many ways to send out the control signals from the I/O ports of a computer. For example, GPIB bus is an international standard supported by many instruments. But probably the simplest way to do I/O is through the parallel printer port. There are driver programs in C/C++ which you can use directly to write to the printer port.

As we know, the original IBM-PC's PPP has a total of 12 digital outputs and 5 digital inputs accessed via 3 consecutive 8-bit ports in the processor's I/O space. Various enhanced versions of the original specification have been introduced over the years:

- Bi-directional (PS/2)

- Enhanced Parallel Port (EPP)
- Extended Capability Port (ECP)

So now the original is commonly referred to as Standard Parallel Port (SPP). The picture of the 25-way connector is shown in Figure A.6.

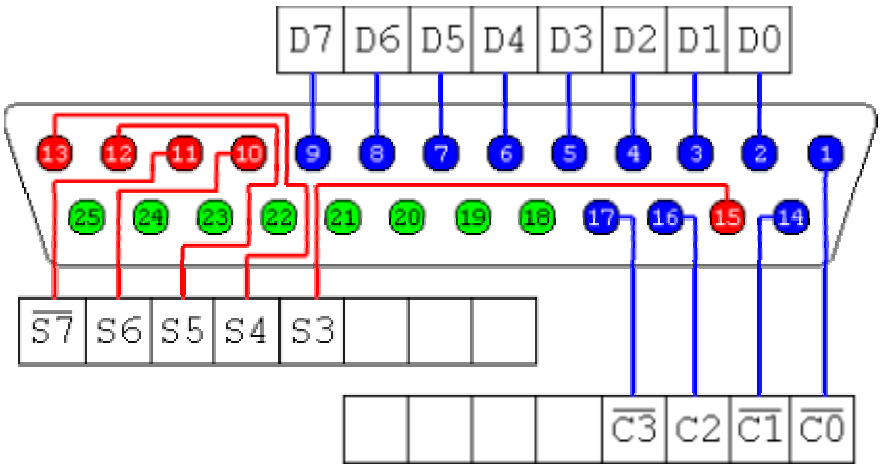

Figure A.6 25-way female D-type connector. (blue-8 output pins accessed via the DATA Port, 4 output pins accessed via the CONTROL Port; red-5 input pins access via the STATUS Port; green-the remaining 8 pins are grounded)

The printer adapter responds to five I/O instructions: two outputs and three inputs. The output instructions transfer data into two latches whose outputs are presented on the pins of a 25-pin D-type female connector.

Two of the three input instructions allow the processor to read back the contents of the two latches. The third allows the processor to read the real-time status of a group of pins on the connector.

A description of each instruction follows

1. Output to address 278/378/3BC Hex - The instruction captures data from the data bus and is present on the respective pins. These pins are each capable of sourcing 2.6 mA and sinking 24 mA. It is essential that the external device not try to pull these lines to ground.

2. Output to address 27A/37A/3BE Hex - This instruction causes the latch to capture the least significant bits of the data bus. The four least significant bits present their outputs, or inverted versions of their outputs, to the respective pins shown above. If bit 4 is written as 1, the card will interrupt the processor on the condition that pin 10 transitions high to low. These pins are driven by open collector drivers pulled to +5 Vdc through 4.7 k-ohm resistors. They can each sink approximately 7 mA and maintain 0.8 volts down-level.

3. Input from address 278/378/3BC Hex - This command presents the processor with data present on the pins associated with the corresponding output address. This should normally reflect the exact value that was last written. If an external device should be driving data on these pins (in violation of usage groundrules) at the time of an input, this data will be ORed with the latch contents.

4. Input from address 279/379/3BD Hex - This command presents real-time status to the processor from the pins.

5. Input from address 27A/37A/3BE Hex - This instruction causes the data present on pins 1, 14, 16, 17 and the IRQ bit to be read by the processor. In the absence of external

drive applied to these pins, data read by the processor will exactly match data last written to the corresponding output address in the same bit positions. Note that data bits 0-2 are not included. If external drivers are dotted to these pins, that data will be ORed with data applied to the pins by the output latch.

Microsoft Visual C/C++ provides access to the I/O ports on the 80x86 CPU via the predefined functions _inp / _inpw and_outp / _outpw.

```
int _inp(unsigned portid); /* returns a byte read from the I/O port portid */

unsigned _inpw(unsigned portid); /* returns a word read from the I/O port portid */

int _outp(unsigned portid,  /* writes the byte value to the I/O port portid */
        int value);       /* returns the data actually written          */

unsigned _outpw(unsigned portid,  /* writes the word value to the I/O port portid */
        unsigned value);  /* returns the data actually written          */
```

portid can be any unsigned integer in the range 0-65535. Here the printer port address 278H is used in the I/O function. To operate the motor, a data byte is written to this port address to for direction and clock signals. Originally, D3 & D2 are assigned as the clock- & clock+ signals. And D1 & D0 are assigned as direction- & direction+ signals. So you can send 0x05 and 0x0D periodically to printer port 278H for positive rotation and 0x04

and 0x0C for negative rotation. But it is found later on that the high voltage level of the direction signal is not stable to work with the motor driver. So a separate AC/DC +5V power supply is made to provide the +5V voltage. The schematic diagram of this DC power supply is shown in Figure A.7.

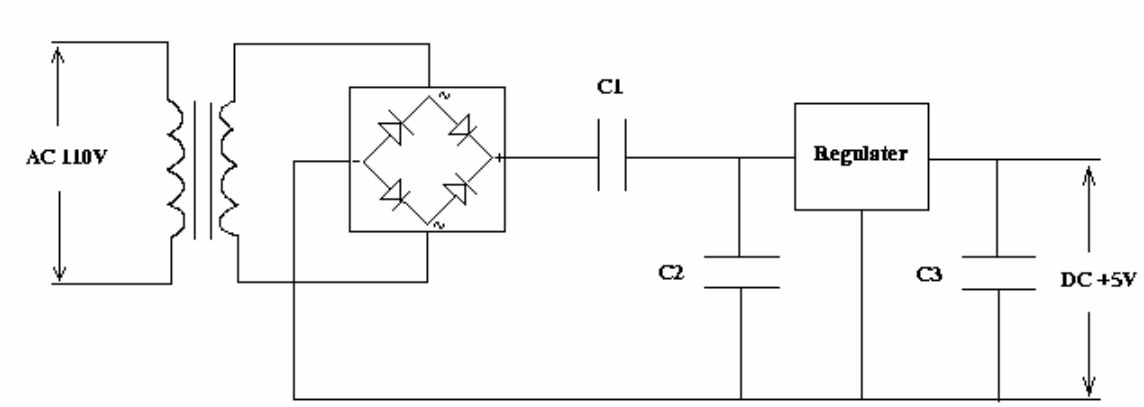

Figure A.7 AC/DC +5V power supply

Transformer	Bridge	C_1	C_2	C_3	Regulator
Stancor SW412	Fager W04F	1000 μF	0.22 μF	0.1 μF	LM 340F5

Table A.3 Components used in +5V power supply

A.3.2 Second I/O Control: PCMCIA Interface

PCMCIA (Personal Computer Memory Card International Association) is an international standards body and trade association with over 200 member companies that was founded in 1989 to establish standards for Integrated Circuit cards and to promote interchangeability among mobile computers where ruggedness, low power, and small size were critical. As the needs of mobile computer users has changed, so has the PC Card

Standard. By 1991, PCMCIA had defined an I/O interface for the same 68 pin connector initially used for memory cards. At the same time, the Socket Services Specification was added and was soon followed by the Card Services Specification as developers realized that common software would be needed to enhance compatibility.

In more recent years, PCMCIA has realized the need for higher speed applications such as multimedia and high-speed networking. From this realization came the CardBus and Zoomed Video Specifications which allow blazing speed in such applications as MPEG video and 100 Mbit Ethernet. Along with these speed enhancements, PCMCIA has continued to add to its specification to enhance compatibility and allow for such other mobile-oriented concerns as 3.3V operation and Power Management.

Today, PCMCIA promotes the interoperability of PC Cards not only in mobile computers, but in such diverse products as digital cameras, cable TV, set-top boxes, and automobiles. As the variety of products that need modular peripheral expansion has grown, so has the diversity of the capabilities of modular peripherals. As such, PCMCIA has recently changed its mission statement: "To develop standards for modular peripherals and promote their worldwide adoption."

For the purpose of following the application trend in PCMCIA, we decide to modify the original control program so that it can communicate with stepper motor through PCMCIA instead of SPP.

We chose the *Quatech* product IOP-241 to realize this task. The IOP-241 is a Type II PCMCIA card (Figure A.8) which allows parallel communication between personal computers with PCMCIA sockets and external devices. It is PCMCIA Card Standard Specification 2.1 compliant, and provides up to 24 digital input/output signals.

Figure A.8 Quatech IOP-241 : 24 channel digital input / output PCMCIA card

Each signal may be individually configured as input or output. In addition, each of the 24 signals is buffered to enhance the IOP-241's drive capability. Eight of the digital signals may be used as interrupt sources. Each interrupt source may be programmed as level sensitive or pulse triggered. An additional interrupt is available when all 24 I/O lines are needed. The interrupt signal may be mapped to any one of IRQ3-7, 9-12 or 14 and 15. The IOP-241 occupies 16 I/O address locations, and the address location may be selected by the user. It is easily programmed from host high level programming languages.

The outputs that need to be set is the same as the case in SPP. We have to decide five outputs: Direction-, ON/OFF+, ON/OFF-, Clk- and ground. The standard output for this IOP-241 PCMCIA card is a DSUB-37 female connector. The meaning of each pins is given below:

PIN 1: GND

PIN 2-9: DATA0 – DATA7

PIN 10: GND

PIN 11: DATA8

PIN 12-18: DATA9 – DATA15

PIN 19: GND

PIN 20-27: DATA16-23/INT1-7

PIN 28: GND

PIN 29: EXT-IRQ

PIN 30-37: GNE

In the implementation, we used PIN 3, 4, 5, 6, 10. Also, to use the pre-defined C/C++ functions supplied by manufacturer, we have to put some of library definition in:

```
char *device_type = "IOP-241";
char *DLL_name    = "iop241.dll";
char *config_file = "iop-241.dat";
```

The feature of the outside PINs should be reset first to “output” in stead of “input” so that the program can actually write data there.

A.3.3 Instrument Control: IEEE 488.2 / GPIB

IEEE-488 refers to the Institute of Electrical and Electronics Engineers (IEEE) Standard number 488. This standard was first established in 1978, 13 years after Hewlett Packard (HP) began work on GPIB to enable its range of instruments to communicate with one another and with host computers. At the time of its development, IEEE-488 was particularly well suited for instrument applications when compared with the alternatives. IEEE-488 comprises a 'bus on a cable,' providing both a parallel data transfer Path on eight lines and eight dedicated control lines. Given the demands of the times, its nominal 1Mbyte/sec maximum data transfer rate seemed quite adequate; even today IEEE-488 is sufficiently powerful for many highly sophisticated and demanding applications. During the 1980s, a new layer was added to the IEEE-488 standard, IEEE-488.2. The original standard was re-designated IEEE-488.1. IEEE-488.2 provides for a minimum set of capabilities among 'controllers' and 'devices,' as well as for more specific content and structure of messages and communications protocols. IEEE-488.2 is fully backward compatible with IEEE-488.1; the use of a '488.2' compliant controller affords the ability to use the new protocols available with '488.2' instruments while retaining the ability to communicate with and control '488.1' compliant instruments and associated supplier idiosyncrasies. Today, IEEE-488 is the most widely recognized and used method for communication among scientific and engineering instruments. Major stand-alone general-purpose instrument makers include IEEE-488 interfaces in their products. Many specialist market instrument makers also rely on IEEE-488 for data communications and control. IEEE-488 interfaces can be connected to most computers, by means of plug-in boards (e.g. ISA, PCMCIA, NUBUS), serial (e.g. RS232) and other cabled parallel

interfaces (e.g. Centronics). All provide at least IEEE-488.1 in compliance, with newer models adhering to IEEE488.2.

The IEEE-488 interface, often called the General Purpose Interface Bus (GPIB) or in Hewlett Packard case HPIB, is a general purpose digital interface system that can be used to transfer data between two or more devices. It is particularly well suited for interconnecting computers and scientific instruments.

Some of its key features are

Up to 15 devices may be connected to one bus all though a choice of address from 0-30 is usually available. Total bus length may be up to 20m and the distance between devices may be up to 2m Communication is digital and messages are sent one byte (8 bits) at a time. Message transactions are hardware handshaked. Data rates may be up to 1 Mbyte/sec. The above, original features can, in many cases, be enhanced with newer hardware. Typical examples are devices which increase the bus length, bus speed and number of devices. For example, the 4889 Fast Bus Extender, allows the bus to extend to 25km and still allows greater than 300kbytes per second transfer rate.

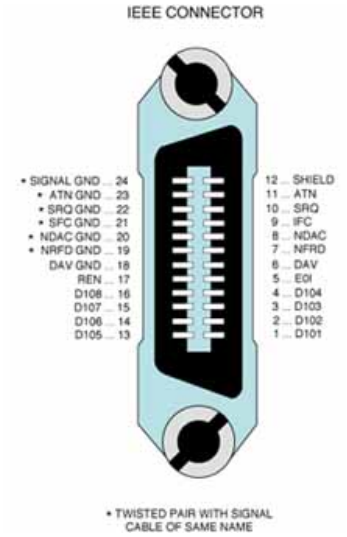

Figure A.9 IEEE GPIB interface

NI-488.2 is the version by National Instrument Corporation, and support C/C++ programming under Windows 9x/NT and Dos environments. The author chose the Microsoft visual c++ to make windows interface mush easier. Some of the most frequently used GPIB function calls are listed below:

*Void Send (int boardID, Addr4882_t address, void *buffer, long count, int eotmode)*

*Void Receive (int boardID, Addr4882_t address, void *buffer, long count, int termination)*

As their names can tell, they are basically used to send and receive data bytes to and from a device. This is the way how the laptop communicates with network analyzer HP8722D. There are also other function calls are used such as *SendIFC* which reset the GPIB by sending interface clear.

A.4 *MotorDriver* Version 1.0 @ Caltech

A windows program is developed (Visual C++) to control and motor and manage the data measurement. Different rotation speed and angles can be set for the step motor, and there is a way to do the port calibration, time gating and angle sweep measurement in the chamber and also the measurement data can be saved in a text file on the computer. Maximum 3 frequency points can be measured during one sweep measurement. The photo below gives a brief look of the software interface.

One of the most important features of this software is that it can display in real-time how the antenna pattern looks like. If there is something wrong, we can quickly detect it and stop it immediately. As you can see from this picture, multiple frequencies can be measured at the same time.

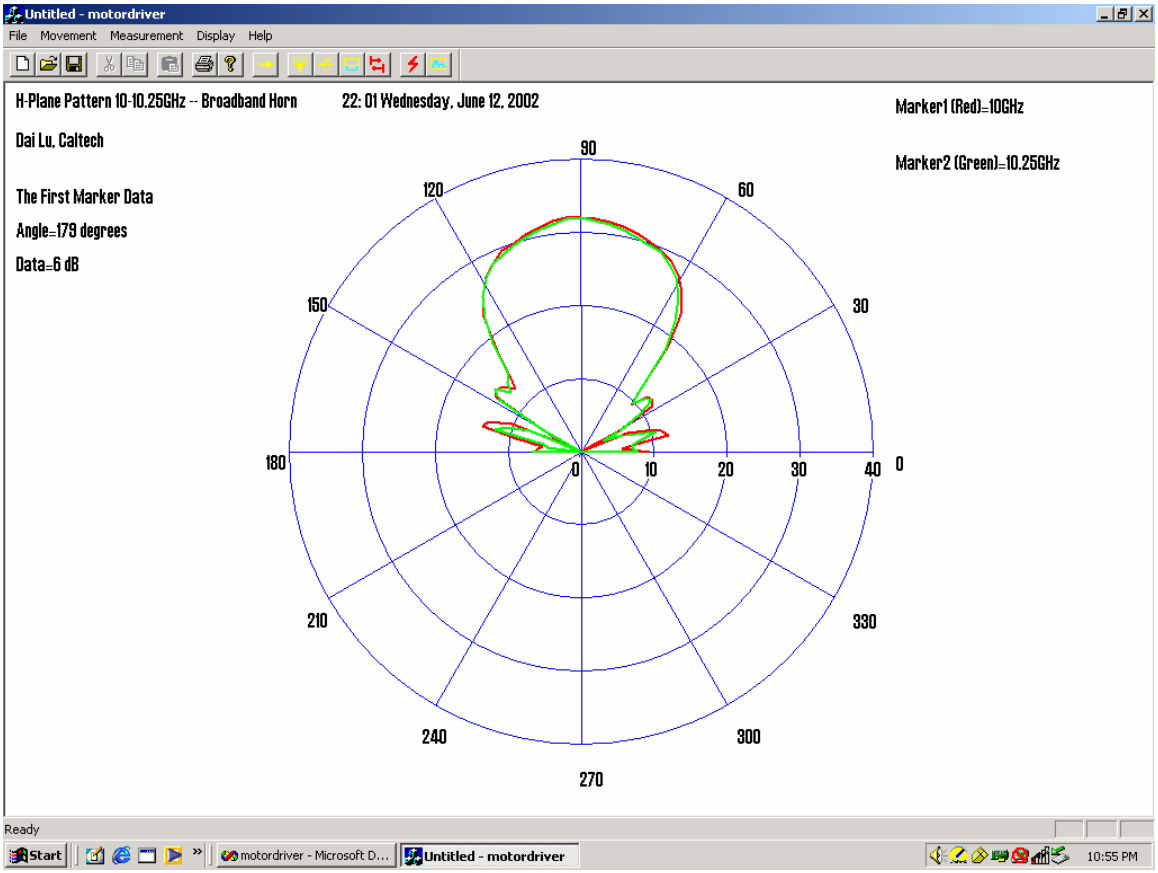

Figure A.10 *MotorDriver V1.0*

A.4.1 Radiation Testing of the Anechoic Chamber

To test the performance of the anechoic chamber, the author did the pattern measurement for two pyramidal horns. The first is a 2-18GHz broadband horn and the second is an 18-26.5GHz WR42 standard gain horn.

Friis Transmission Equation (A-1) is used to evaluate the performance of the chamber. The formula given here is for reflection and polarization-matched antennas aligned for maximum directional radiation and reception. It relates the power P_r (delivered to the receiver) to the P_t (radiated from transmitter). This power ratio is also

$$\frac{p_r}{p_t} = \left(\frac{\lambda}{4\pi R}\right)^2 G_t G_r \qquad \text{(A-1)}$$

called the *free-space loss factor*, and it takes into account the losses due to the spherical spreading of the energy by the antenna.

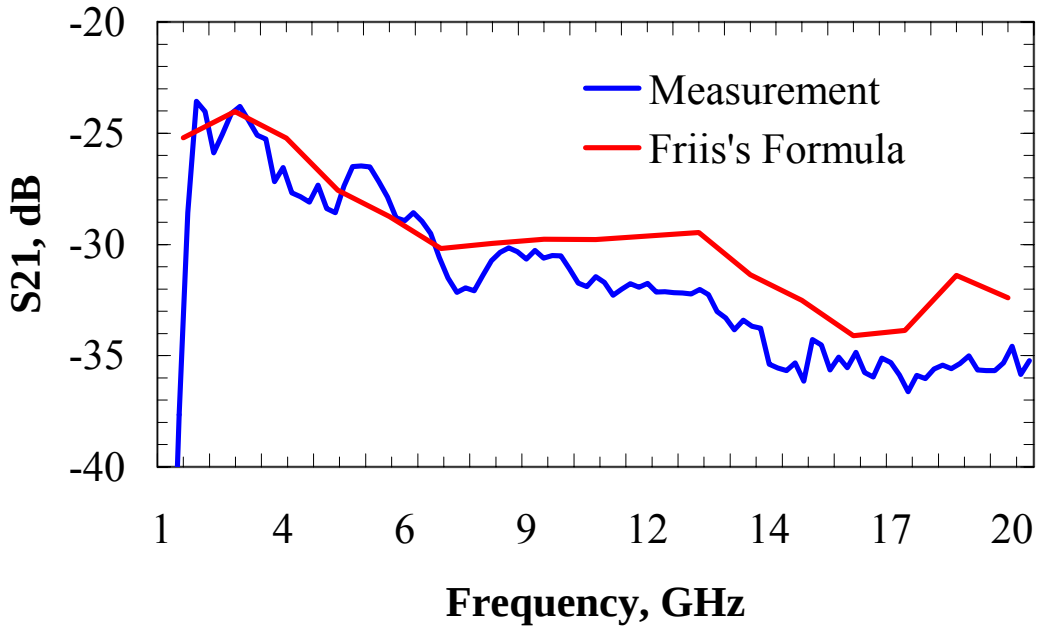

(a) Broadband horn (2-18 GHz)

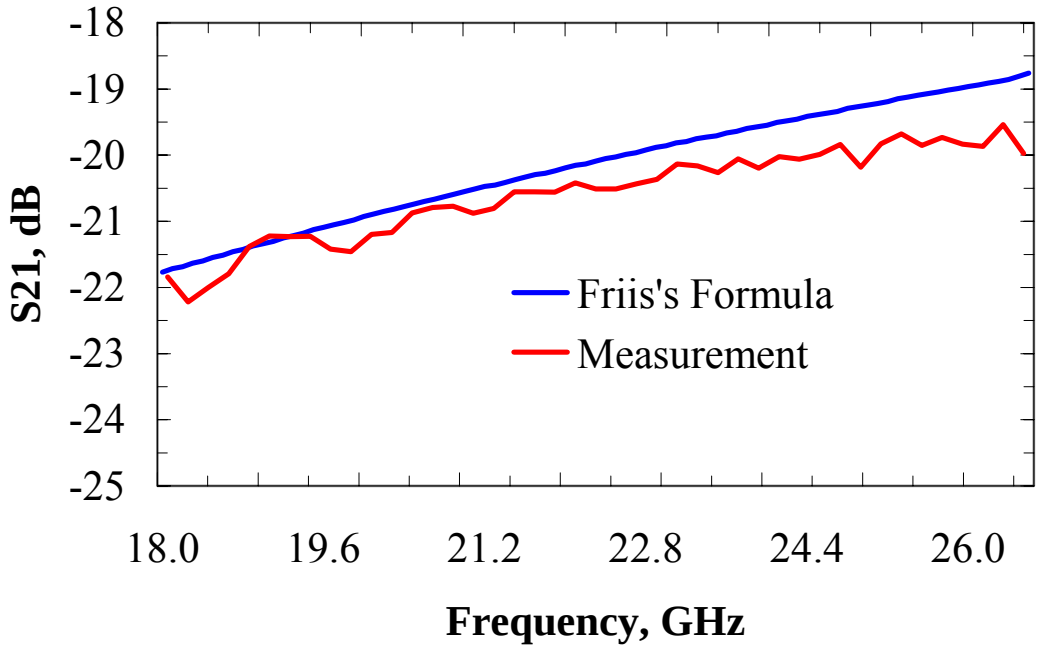

(b) Standard gain horn: WR42

Figure A-11 S_{21} comparison of calculation and measurement

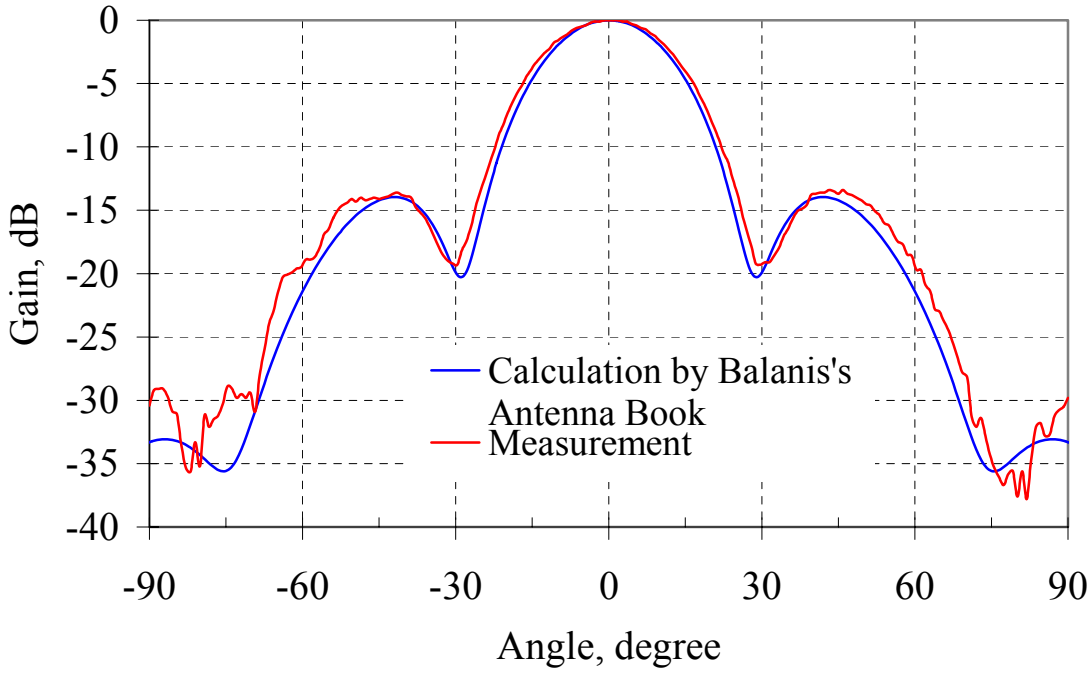

(a)

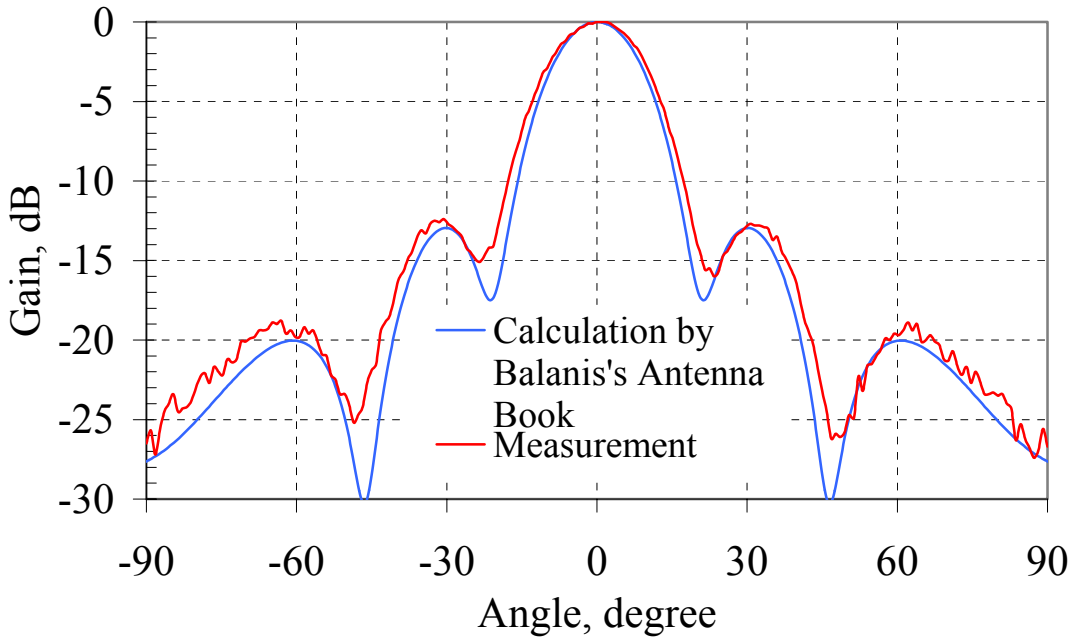

Figure A-12 E-plane pattern measurement compared to Balanis's book

As can be seen from the plot, the measurement and calculation data is quite close. This certifies that our anechoic chamber is well designed. It can be used to do RF / Antenna measurement from 2 GHz to almost 40 GHz.

Appendix B
Automatic Indoor Measurement

In order to make the indoor channel measurements accurately and fast, an ATS (Automatic Testing System) is made. As shown in Figure 4.1, there are two kinds of testing setup: scalar and vector measurements. In both cases, the receiver is sitting on a movable cart. There is a DC motor installed on the cart and driven by a power supply (AC/battery powered). Depending on how much the control voltage is, the cart can move fast, slow or stop. And the voltage control signal is sent from the laptop computer B on the cart. There is another laptop computer A on the fixed transmitter site. A can send out signal to B for all the movements and data acquisition involved through WLAN. To avoid communication interference in band, 802.11b and 802.11a are used alternatively.

B.1 Motor Servo System

The DC motor used is a permanent magnet servomotor from Electro-Craft (Part No. 0542-01-000). It is a 24 volt motor and always driven in the range of 0-15 volts.

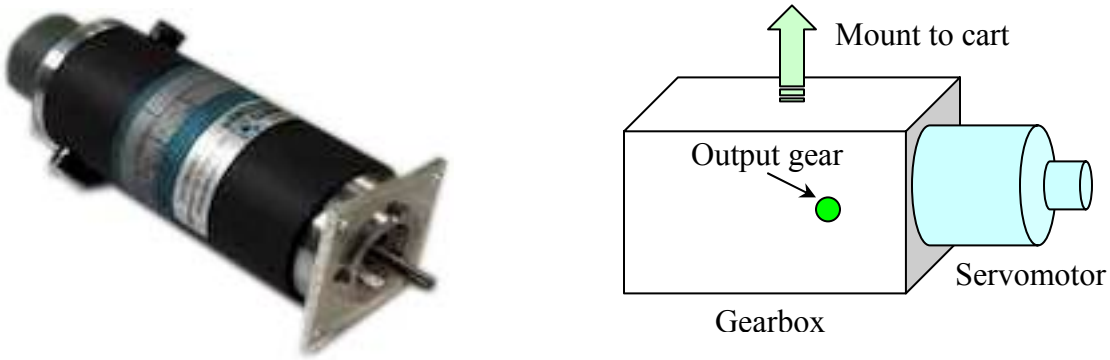

Figure B.1 DC servomotor from Electro-Craft and combined gear box

The DC control voltage decides how fast this motor can rotate when the load is fixed. A gearbox is used to slow down the speed of this servomotor to provide a large torque in the testing system (Figure B-1). Experiment has shown that it can drive the car with an adult (170 pounds) sitting on quite easily.

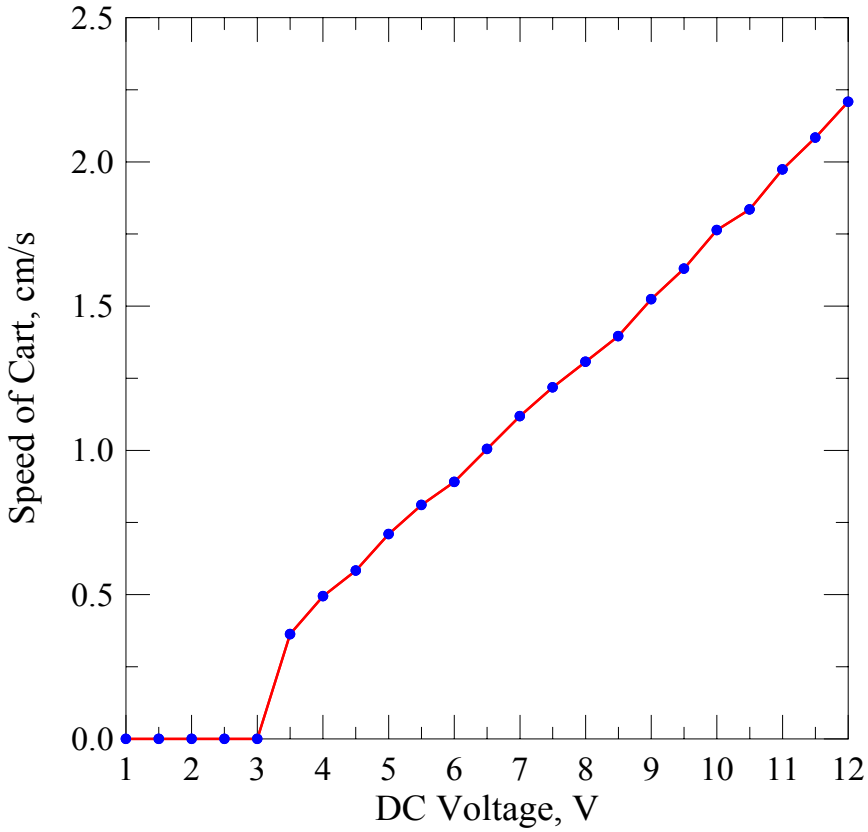

Figure B.2 The speed of cart as a function of control voltage.

Figure B.2 shows the speed of the cart when DC voltage is applied. The threshold voltage for the cart to move is about 3 volts. During the measurement, the speed of the cart is very slow to keep the Doppler shift small. Also it is necessary for the tracking tool to keep a straight moving trace.

B.2 System Assembly and LABVIEW Programming

The receiver testing system is shown in Figure B.3. The height of both transmitter and receiver is 1.1 m. A piece of absorbing material has been put in front of the cart.

(a) Back view

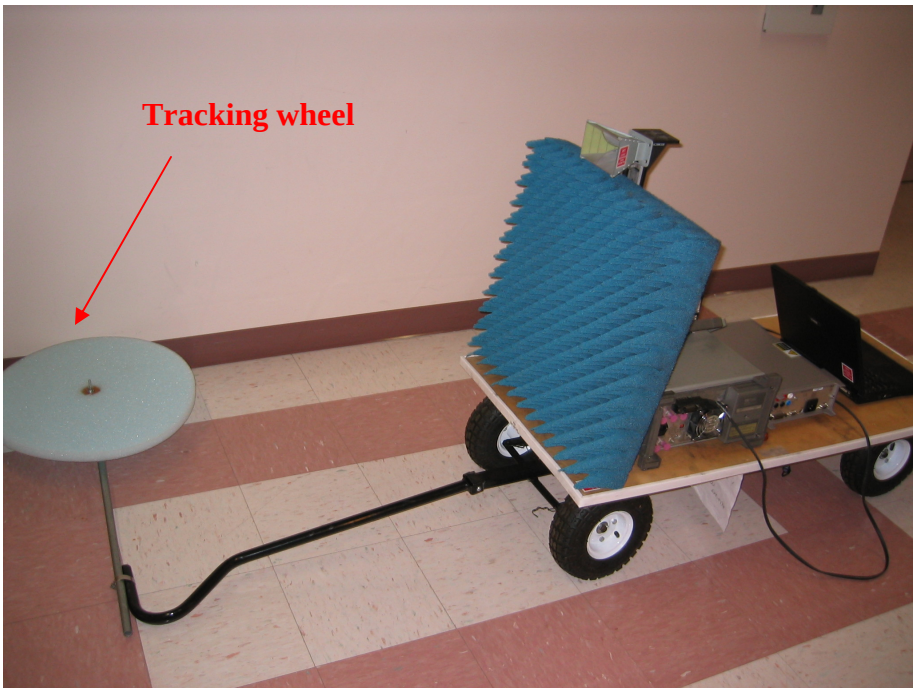

(b) Side view

Figure B.3 indoor receiver testing system

The purpose of this absorbing material is to keep the multipaths caused by the instruments as small as possible. Also it can be noticed from the photo that there is a big circular wheel made by Styrofoam is fixed to the cart. The function of the wheel is to keep the moving trace in a straight line.

The motor control and data acquisition program are made in LABVIEW. An advantage of use LABVIEW is that it offers a simple and easy way to manipulate the measurement and control. For example, program controls and data can be transferred easily by *Datasocket* technology. Basically it is a data structure in LABVIEW which can be used to exchange data between the computers on TCP/IP standards.

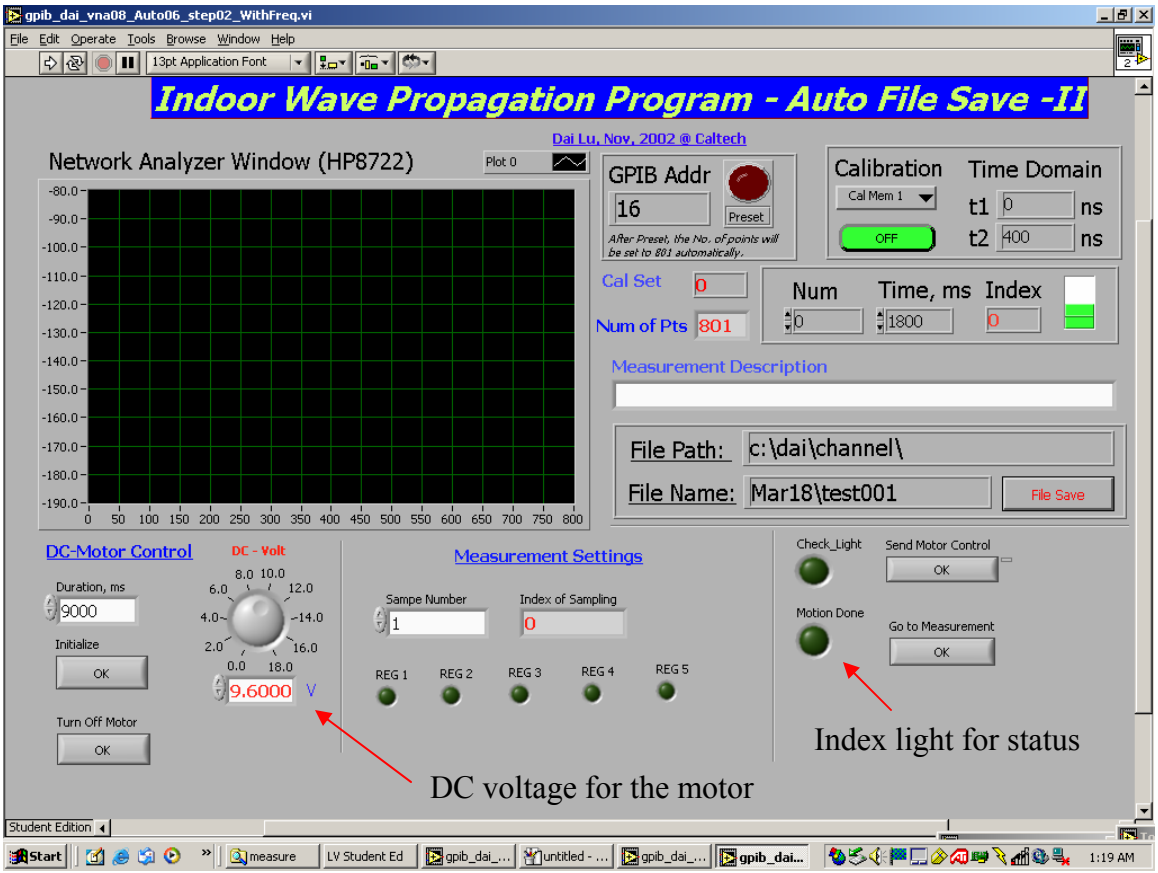

Figure B.4 Datasocket client program interface in LABVIEW

The command from the client to the server can be the control signals to change the cart speed of the cart, make it stop or set a different frequency range, resolution bandwidth of the spectrum analyzer (Figure B.4).

The data extracted from the instrument can be stored locally in the server computer or sent back to the client computer. In the real system, it is saved locally to save the hand-shaking requirement.

B.3 Safety Concern of RF Exposure during the Measurement

The FCC (Federal Communications Commission) has limits for Maximum Permissible Exposure (MPE) on human body. The NCRP and ANSI/IEEE exposure criteria and most other standards specify "time-averaged" MPE limits. This means that it is permissible to exceed the recommended limits for short periods of time as long as the average exposure (over the appropriate period specified) does not exceed the limit. The limit for Occupational/Controlled Exposure in 1.5 – 100 GHz range is 5 mW/ cm^2 × 6 minutes.

The received power P_r can be calculated by the Friis formula:

$$P_r = P_t \cdot G_t \left(\frac{\lambda}{4\pi \cdot r} \right)^2$$

Since maximum radio frequency exposure density is 5 mw/cm^2. We can computer safety range of testing by assuming that the receiver gain is 1 and the effective area is 1 cm^2, which is about the dimension of an eye. Also we assume the period of the indoor

measurement is about 8 hours = 480 minutes. So the average safe exposure is

$$P_{av} = \frac{5 \times 6}{480} = 0.0625mW = -12dBm$$

1). At f = 2.4 GHz, if G_1 = 8 dB (front), and the maximum output power is 30 dBm, then

$$P_r < -12dBm \Rightarrow G_1 \cdot 20 * \log\left(\frac{c}{4\pi \cdot 2.4 \cdot r}\right) < -12 \Rightarrow r > 3.14m$$

if G_1 = 0 dB (back and side), and the maximum output power is 30 dBm, then

$$P_r < -12dBm \Rightarrow G_1 \cdot 20 * \log\left(\frac{c}{4\pi \cdot 2.4 \cdot r}\right) < -12 \Rightarrow r > 1.25m$$

2). At f = 24 GHz, if G_1 = 12 dB (front), the maximum output power is 36 dBm, then

$$P_r < -12dBm \Rightarrow G_1 \cdot 20 * \log\left(\frac{c}{4\pi \cdot 24 \cdot r}\right) < -12 \Rightarrow r > 0.99m$$

if G_1 = 0 dB (back and side), and the maximum output power is 36 dBm, then

$$P_r < -12dBm \Rightarrow G_1 \cdot 20 * \log\left(\frac{c}{4\pi \cdot 24 \cdot r}\right) < -12 \Rightarrow r > 0.25m$$

As we can see from the above calculation, to keep safe during the long period (8 hours) measurement, human body should be 3 m away in front of the transmitter and 1 m away even from the back side of transmitter.

Appendix C
Ray-Tracing Programming by MATLAB

In recent years, ray-tracing techniques have proven to be very useful as computer tools for the design and planning of wireless systems both in urban microcells and in indoor picocells. At present, the optimization of these techniques enables a great number of rays (reflected, refracted, diffracted, and multiple combination of these effects) to be taken into account, which reach the receiver through multiple paths and contribute to the received signal. The degree of precision in the calculation of the signal levels makes it possible to estimate accurately enough not only the signal mean level but also its variations and consequently its statistics. In Chapter 5, the prediction of indoor channels by combined 2-D E/H ray-tracing method has been presented to achieve good results in path loss and delay spread. Here, some of the programming issues and ray-tracing concepts are discussed.

C.1 Choice of Window Functions

In order to compare the simulated PDP (Power Delay Profile) from the ray-tracing code with the calculated PDP by VNA (Vector Network Analyzer), it is necessary to know how PDP is generated in VNA. The analyzer provides a windowing feature that makes time domain measurements more useful for isolating and identifying individual responses. Windowing is needed because of the abrupt transitions in a frequency domain measurement at the start and stop frequencies. Since this function is sealed to the user by Agilent, it is important to find it out before doing further simulation.

First, a complex S parameter measurement is done using the VNA. Both time domain and frequency domain complex S parameters are saved. Different window functions are applied to the frequency domain S parameter. Then inverse FFT is done to see how close the result is compared to the time domain data from VNA. If the result is close enough, it is thought that the window function is matched. Five different window functions are evaluated using this method, they are: Hamming, Hann, Bohman, Kaiser Chebyshev.

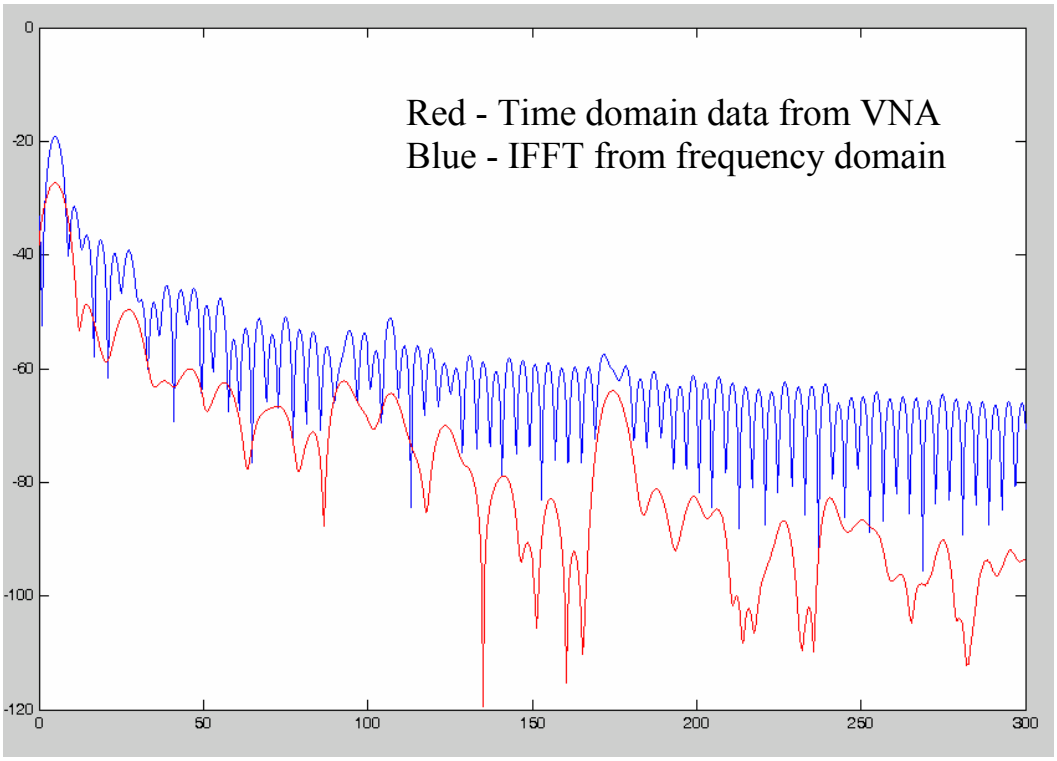

Figure C.1 Power delay profile without window function

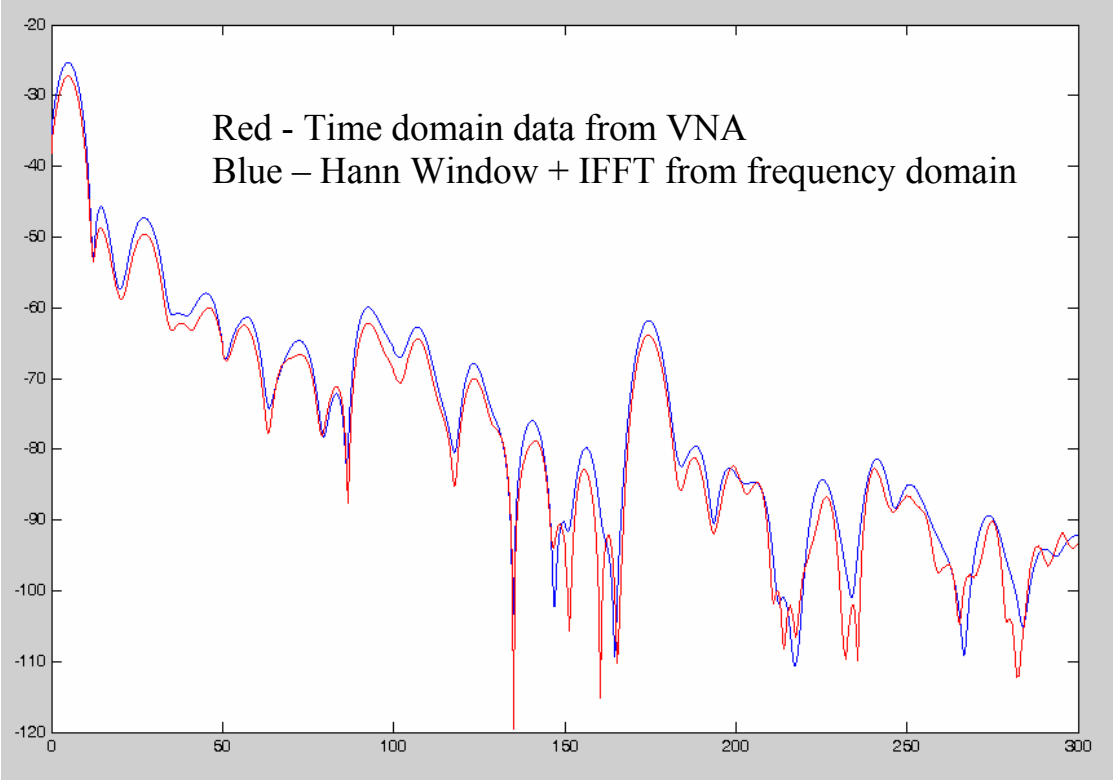

Figure C.2 Power delay profile with window function

Some window function may also have parameter to fit in such as Hamming and Han. As can been seen from Figure C.1 and C.2, the Hann window with $\alpha = 0.5$ is shown to get good fit compared to VNA data. The formula for Hann function is shown below.

$$H(x,\tau,\alpha) = \begin{cases} \alpha + (1-\alpha)\cdot\cos(\pi \cdot x/\tau) & |x| < \tau \\ 0 & else \end{cases}$$

C.2 Concept of the Illumination Zone

In general, there are two different kinds of ray-tracing method. The first method is called SBR (Shooting-and-Bouncing Ray) launching algorithm. First, a ray is launched from the transmitting antenna (Tx), then the ray is traced in all directions to see if it hits

any object or is received by the receiving antenna. When an object is hit, reflection, transmission, diffraction or scattering will occur, depending on the geometry and the electric properties of the object. The second method is called image method. First, multiple images of the Tx is found and then the reflection paths to the Rx are determined. Compared to SBR, this method is much faster. But when number of walls is large, the reflection time is high. This method is used in my ray tracing code and also to make accurate simulation, illumination zone concept is applied (Figure C.3).

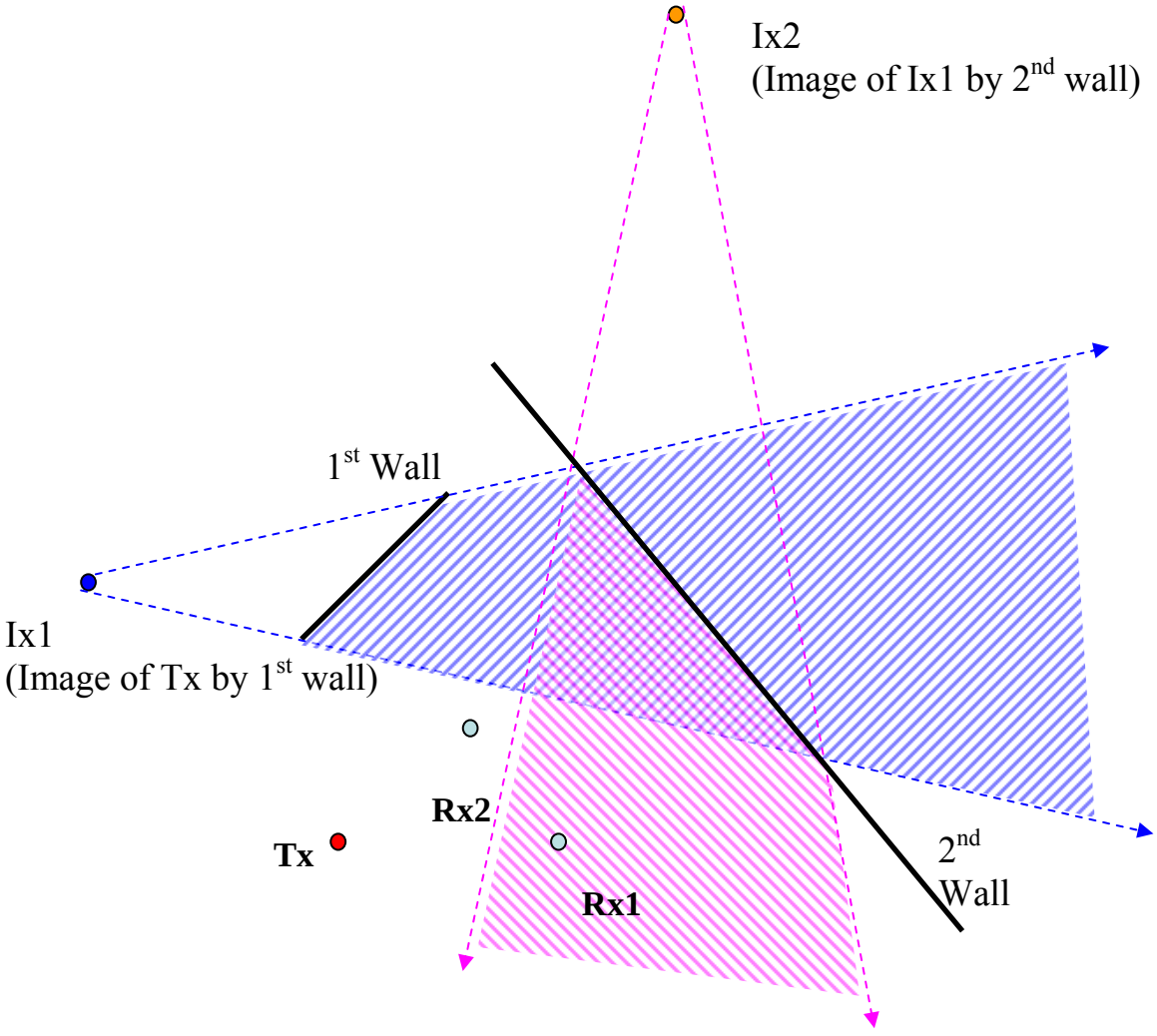

Figure C.3 Concept of illumination zone

As can be seen from Figure C.3, Tx has an image Ix1 by the 1st wall, and this image Ix1 also induces an image Ix2 by the 2nd wall. The illumination zones of these two images (Ix1 and Ix2) are shown as the blue region and pink region. This explains why only Rx1 can be illuminated by the Ix2 since Rx2 is not inside the illumination zone of Ix2. By applying the concept of illumination zone, we can ignore many non-physical paths in the ray calculation and this improves both accuracy and time.

C.3 Ray-tracing Program

The ray-tracing program used to do indoor channel prediction in Chapter 5 and 6 is made in MATLAB. The reason of choosing MATLAB is the availability of many math functions and it is also very easy to build a GUI based program. The subroutines defined for the combined E/H 2D ray-tracing program is shown in Figure C.4.

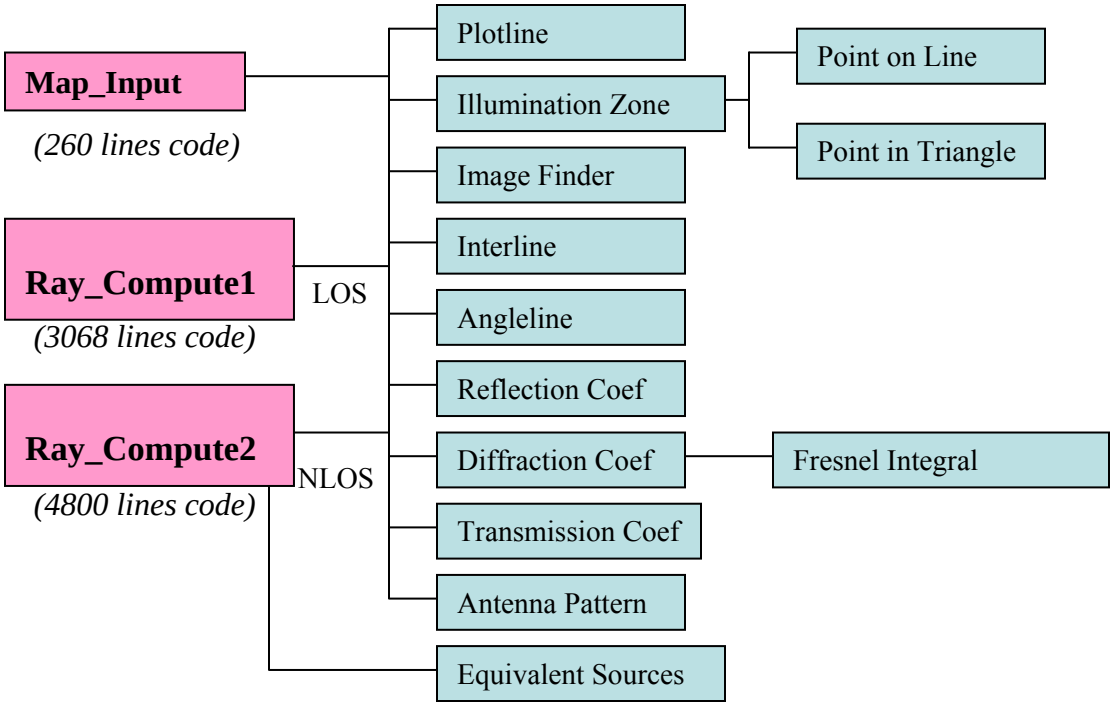

Figure C.4 Subroutines defined for the combined E/H plane 2D ray-tracing

The propagation mechanisms considered in this 2-D ray-tracing code are direct path, 1st reflection, 2nd reflection, 1st diffraction, 1st diffraction + 1st reflection, 1st reflection + 1st diffraction, 2nd diffraction. Basically, this includes all 2nd order paths and higher order paths are ignored. The function of those pre-defined subroutines in Figure C.4 are listed below. Map Input is a GUI program for 2-D geometry input and Ray_Compute is a GUI program for ray-tracing simulations for either LOS or NLOS.

Plot line – This subroutine is used to draw 2D lines on the GUI program. The lines can be geometry outline or ray tracing paths.

Illumination Zone – This is subroutine is used to calculate and store multiple images and their illumination zone regions.

Image Finder – This subroutine is used to compute the coordinate of the image when the position of wall is given.

Interline – This subroutine is used to calculate the intersection point of two lines in space.

Angleline – This subroutine is used to calculate the angle of intersection of two lines. For example, it is possible to decide the incident angle of a reflected path.

Reflection Coef – This subroutine is used to calculate the reflection coefficient given the parameter of the wall and the incident angle.

Diffraction Coef – This subroutine is used to calculate the diffraction coefficient given the parameter of the wall and the direction of diffraction paths

Transmission Coef – This subroutine is used to calculate the transmission coefficient given the parameter of the wall and the incident angle.

Antenna Pattern – This subroutine is used to calculate the antenna pattern in a certain direction based on anechoic chamber measurement.

Equivalent Sources – This subroutine is used to find out those equivalent radiation sources which can be applied in the LOS 2D ray-tracing code.

Point on Line – This subroutine is used to determine if a point is on a certain line.

Point on Triangle – This subroutine is used to determine if a point is in or on a certain triangle.

Fresenel Integral – This subroutine is used to calculate the Fresnel integral which is needed in diffraction coefficient calculation.

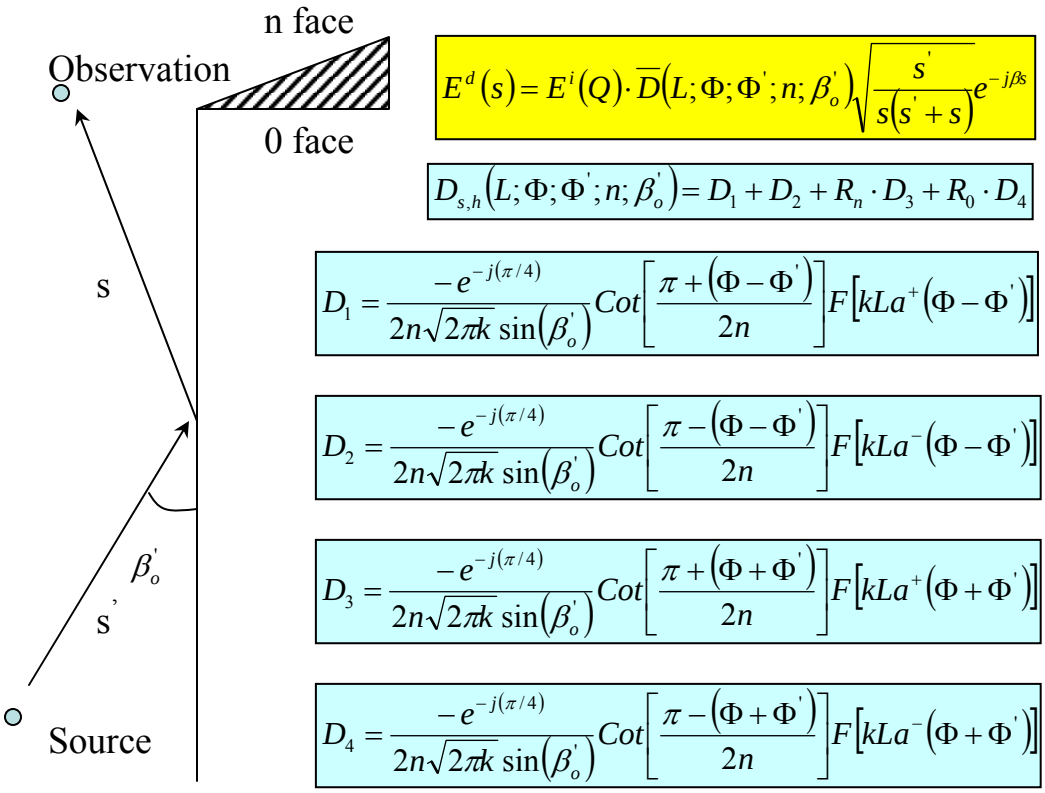

Figure C.5 Diffraction coefficient in the ray calculation

View window

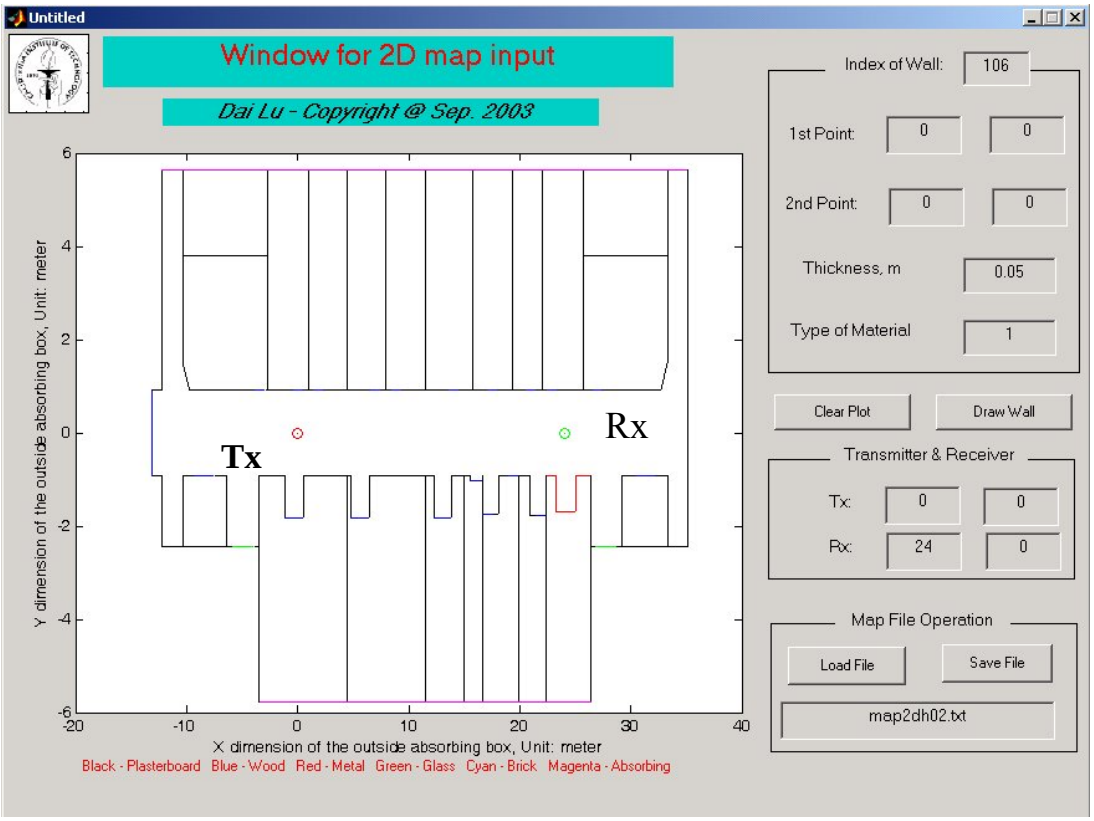

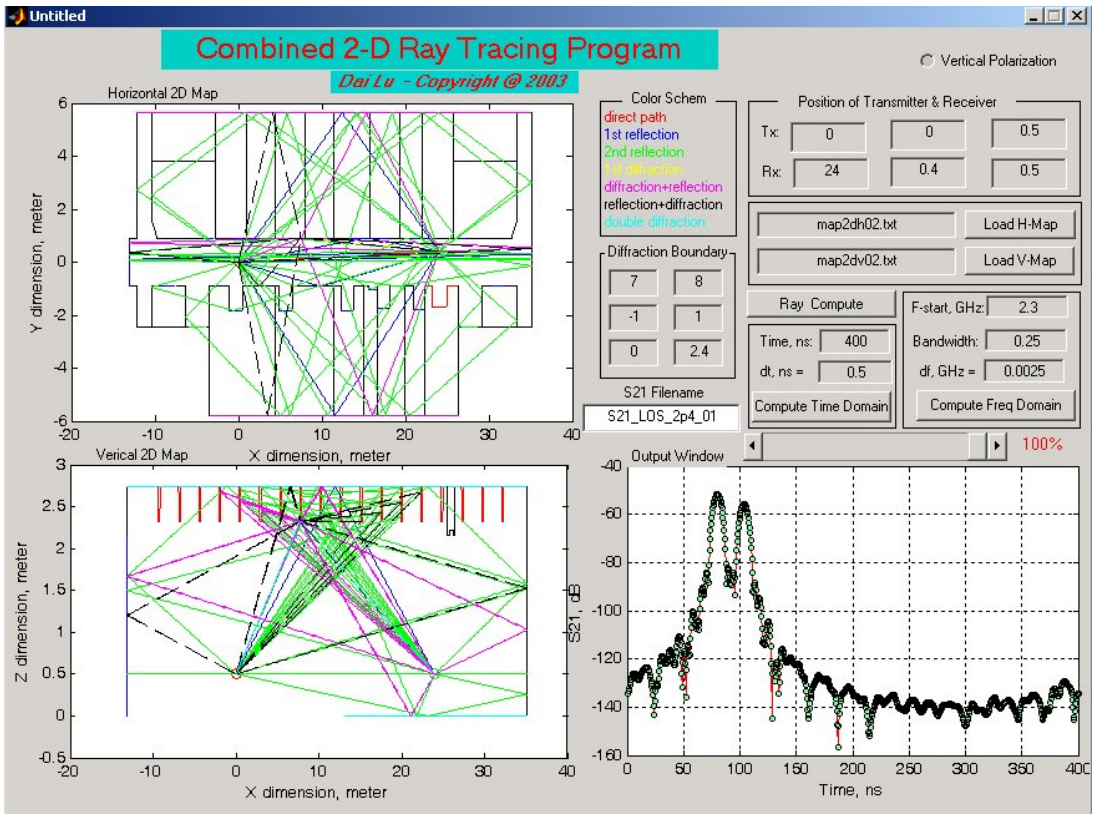

Figure C.6 2D E/H ray-tracing program: Top - Geometry Input, Bottom - Simulation

Bibliography

[1] Jenshan Lin, Tatsuo Itoh, "Active Integrated Antennas," *IEEE Trans. Microwave Theory Tech.*, MTT-42, pp. 2186-2194, Dec. 1994.

[2] Hall PS, Gardner P, Ma GZ, "Active Integrated Antennas," *IEICE Trans. Communications,* E85B (9), pp.1661-1667, Sep. 2002.

[3] Chang K, York RA, Hall PS, et al. "Active Integrated Antennas," *IEEE Trans. Microwave Theory Tech.*, MTT-50, pp.937-944, MAR 2002.

[4] Qian YX, Itoh T, "Progress in Active Integrated Antennas and Their Applications." *IEEE Trans. Microwave Theory Tech* MTT-46 (11): pp.1891-1900 (2) Nov. 1998.

[5] Wong C. H., "A Steerable Planar Antenna System for Wireless LAN", *B. Eng. Thesis*, University of Queensland, 1996.

[6] Meng CC, Deng KL, Lee HD, et al. "10 GHz GaAs Monolithic Twin-Dipole Antenna FET Mixer," *Microwave Opt. Tech Let.* 30 (6): pp.436-438 Sep. 20 2001.

[7] Don Parker, David C. Zimmermann, "Phased Arrays—Part I: Theory and Architectures" *IEEE Trans. Microwave Theory Tech*, MTT-50 (3), pp.678-687, March 2002.

[8] E. Brookner, "Practical Phased-Array Antenna Systems. Norwood," *Artech House*, MA, 1991.

[9] *IEEE Int. Phased-Array Syst. Technol. Symp. Dig.*, Boston, MA, Oct.15–18, 1996.

[10] G. W. Stimson, "Introduction to Airborne Radar," *2nd ed. Mendham, NJ: Science*, 1998, 37–39.

[11] S. Panaretos, C. Shoda, R. Relatores, J. Gordon, P. Curtis, and D. Parker, "A Broadband, Low-Sidelobe, Dynamic Weighting Three-Channel Receive, X -band Active Array," *IEEE MTT-S Int. Microwave Symp. Dig.*, vol. III, San Francisco, CA, pp. 1573–1576, June 1996.

[12] R. J. Mailloux, "Phased Array Antenna Handbook," *Norwood, MA: Artech House*, 1994.

[13] H. Wu and A. Hajimiri, "Silicon-Based Distributed Voltage Controlled Oscillators," *IEEE Journal of Solid-State Circuits*, vol. 36, no. 3, pp. 493-502, March 2001.

[14] X. Guan and A. Hajimiri, "A 24GHz CMOS Front-End," *Proc. of IEEE European Solid-State Circuits Conference (ESSCIRC)*, Sept. 2002.

[15] H. Wu and A. Hajimiri, "A 19GHz, 0.5mW, Frequency Divider with Shunt-Peaking with Shunt-Peaking Locking Range Enhancement," *Proc. of IEEE International Solid-State Circuits Conference*, pp. 412-413, Feb. 2001.

[16] D. Ham and A. Hajimiri, "Complete Noise Analysis for CMOS Switching Mixers via Stochastic Differential Equations," *Proc. of IEEE Custom Integrated Circuits Conference*, pp. 439-442, May 2000.

[17] Bruce A. Kopp, Michael Borkowski, and George Jerinic, "Transmit/Receive Modules," *IEEE Trans. Microwave Theory Tech*., MTT-50, pp. 827-834, March 2002.

[18] "1.7-2.7GHz Power Amplifier And T/R Switch MMIC –AN24," *Application Notes*, Bookham Technology.

[19] Niranjan Talwalkar, C.Patrick Yue and Simon Wong, "An Integrated 5.2GHz CMOS T/R Switch with LC-Tuned Substrate Bias," *ISSCC Session 20*, Paper 20, 2003

[20] John R. Sellin, Stow; Donald N. Jessen, Sudbury, "Transmit and Receiver Switch," *US Patent,* No. 4,637,073, Jan. 1987.

[21] Tzu Kiu Lee, Wing Shing Chan and T.Y.M. Siu, "Power amplifier/low noise amplifier RF switch," *Electronics Letters,* Vol.36, No.24, pp.1983-1984, Nov. 2000.

[22] Tze Kiu Lee, Wing Shing Chan, and Yun Ming Siu, "Integrated Broadband Power Amplifier/Low Noise Amplifier Switch for Time Division Diplexer," *Microwave and Optical Tech. Letters*, Vol. 36, No. 2, January 20 2003.

[23] Kevin W. Kobayashi, "An AlGaAs/GaAs HBT PA-LNA Transceiver MMIC Chip for 1.9 GHz PHS Digital Cordless Telephones," *Microwave Journal,* Jan. 1998.

[24] K. Yamamoto, K. Maemura, N. Kasai, Y. Yoshii, Y. Miyazaki, M. Nakayama, "A Single-chip GaAs RF Transceiver for 1.9 GHz Digital Mobile Communication System," *IEEE JSSC*, Vol.31, No.12, pp. 1964-1973, Dec. 1996.

[25] S. Weinreb, E. Fisher, B. Kane, N. Byer, M. Zimmerman, "W-band 0.3 W pHEMT MMIC power amplifier module," *IEEE Microwave and Millimeter-Wave Monolithic Circuits Symposium* 1995, pp. 25-28.

[26] Ping-Yu Chen, Zou-Min Tsai, Shey-Shi Lu et al., "An Ultra Low Phase Noise W-Band GaAs-Based PHEMT MMIC CPW VCO," *European Microwave Conference*, 2003.

[27] Yuh-Jing Hwang, Chun-Hsien Lien, HueiWang, Malcolm W. Sinclair, Russell G. Gough, Henry Kanoniuk, and Tah-Hsiung Chu, "A 78–114 GHz Monolithic Subharmonically Pumped GaAs-Based HEMT Diode Mixer," *IEEE Microwave and Wireless Components Letters*, Vol.12, No. 6, pp.209-211, June 2002

[28] Emilio A. Sovero, Youngwoo Kwon, Don S. Deakin, John Hong, "Watt Level GaAs PHEMT Power Amplifiers 26GHz and 40 GHz for Wireless Applications," *1999 RAWCON Digest*, pp. 309-312.

[29] Kwon Y, Kim K, Sovero EA, Deakin DS, "Watt-level Ka- and Q-band MMIC power amplifiers operating at low voltages," *IEEE Trans. Microwave Theory Tech.*, MTT-48, pp.891-897 JUN 2000

[30] Agilent Technologies, "Circuit Components Nonlinear Devices," *Advanced Design Systems Manual 2002*.

[31] Hau-Yiu Tsui and Jack Lau, "SPICE Simulation and Tradeoffs of CMOS LNA Performance with Source-Degeneration Inductor," *IEEE Trans. Circuits and Systems II-Analog and Digital Signal Processing*, Vol.47, No.1, pp.62-65, Jan. 2000.

[32] Kuo KC, Leuciuc A, "A Linear MOS Transconductor Using Source Degeneration and Adaptive Biasing," *IEEE Trans. Circuits* - II 48 (10): pp.937-943 Oct 2001.

[33] Goo JS, Ahn HT, Ladwig DJ, et al. "A Noise Optimization Technique for Integrated Low-Noise Amplifiers," *IEEE Jour Solid-State Circuit* 37 (8) pp.994-1002 Aug. 2002

[34] D. K. Shaeffer, and T. H. Lee, "The Design and Implementation of Low-Power CMOS Radio Receivers," *Kluwer Academic Publishers*, Boston, 1999.

[35] Pietro Andreani, Henrik Sjöland, "Noise Optimization of an Inductively Degenerated CMOS Low Noise Amplifier," *IEEE Trans. On Circuits and Systems – II: Analog and Digital Signal Processing*, 48, NO. 9, Sep 2001.

[36] Jung-Suk Goo, Hee-Tae Ahn, Donald J. Ladwig, Zhiping Yu, Thomas H. Lee, and Robert W. Dutton, "A Noise Optimization Technique for Integrated Low-Noise Amplifiers," *IEEE Jour. of Solid State Circuits*, Vol.37, No.8, Aug. 2002.

[37] Behzad Razavi, "RF Microelestronics," *Prentice Hall*, NJ, 1998.

[38] M. L. Edwards and J. H. Sinsky, "A new criterion for linear 2-port stability using geometrically derived parameters," *IEEE Trans. on Microwave Theory Tech*., Vol. 40, No. 12, pp. 2303-2311, Dec. 1992.

[39] Ramesh Grag, Prakash Bhartia, Inder Bahl and Apisak Ittipiboon, "Microstrip Antenna Design Handbook," Chapter 12 - *Design and Analysis of Microstrip Antenna Arrays*, Artech House, 2001.

[40] Thomas Metzler, "Microstrip Series Arrays," *IEEE Trans. Antennas and Propagat.*, AP-29, pp. 174-178, Jan. 1981.

[41] Derneryd, A.G., "Linear Polarized Microstrip Antennas," *IEEE Trans. Antennas and Propagation.*, Vol. AP-24, pp. 846-851, 1976.

[42] David M. Pozar, "Microwave Engineering," *Wiley Text Books*, 2nd Ed, 1997.

[43] Agilent Technologies , "Noise Figure Measurement Accuracy – The Y Factor Method," *Application Note 57-2*, http://cp.literature.agilent.com/litweb/pdf/5952-3706E.pdf.

[44] H. Hashemi, X. Guan and A. Hajimiri, "A Fully Integrated 24-GHz 8-Path Phased-Array Receiver in Silicon," *IEEE International Solid-State Circuits Conference*, San Francisco, February 2004.

[45] Sheung Li, "Channel Bonding Will Move WLANs past 100 Mb/s," *Atheros Communications,* www.iApplianceWeb.com 01/17/04, 08:40:13 PM EDT.

[46] C. E. Shannon, "The Mathematical Theory of Information," *Urbana, IL:University of IllinoisPress*, 1949.

[47] FCC regulation, "Part 15 – Radio Frequency Devices", *Federal Communications Commission*, December 8, 2003.

[48] FCC regulation, "Part 97 – Amateur Radio Service", *Federal Communications Commission*, October 8, 1998.

[49] CEPT/ERC TR/22-06: "Harmonised Radio Frequency Bands for High Performance Radio Local Area Networks (HIPERLANs) in the 5 GHz and 17 GHz Frequency Range."

[50] Norbert Schroeder and Mel Murray (prepared), “Radio Frequency Spectrum Allocations in the United States,” *NTIA/Department of Commerce,* Washington, DC 20230, January 2004.

[51] FCC, First report and order, ET Docket 98-153, “Revision of Part 15 of the Commission’ Rules Regarding Ultra-Wideband Transmission Systems,” adopted Feb, 2002.

[52] P. A. Bello, "Characterization of Randomly Time-Variant Linear Channels," *IEEE Trans. Commun. Syst*., vol. COM-11, pp. 360-393, Dec. 1963.

[53] D. Parsons, “The Mobile Radio Propagation Channel,” *John Wiley & Sons Press*, reprinted 1996.

[54] J.D. Gibson, "The Mobile Communications Handbook", *Second Edition, IEEE Press* 1999.

[55] A. Leon-Garcia. “Probability and Random Processes for Electrical Engineering,” *Addison-Wesley Publishing Company, Inc.*, 2 edition, 1994.

[56] J.G. Proakis, “Digital Communications”, *McGraw Hill*, 1995.

[57] John S. Sadowsky, and Venceslav Kafedziski, “On the Correlation and Scattering Functions of the WSSUS Channel for Mobile Communications,” *IEEE Trans. Vehicular Tech.*, VOL. 47, NO. 1, Feb 1998.

[58] Theodore S. Rappaport, "Wireless Communications: Principles and Practice," *Prentice Hall PTR*, 1996.

[59] G.J.M. Janssen, "Robust receiver techniques for interference-limited radio channels", *Ph.D. Thesis*, Delft University Press, The Netherlands, 1998

[60] K. Witrisal, Y.-H. Kim and R. Prasad, "Frequency-Domain Simulation of the MM-Wave Multipath Fading Radio Channel Applying the Hilbert Transform", *PIMRC'98*, Boston 1998.

[61] K. Witrisal, Y.-H. Kim, R. Prasad, "RMS Delay Spread Estimation Technique Using Non-Coherent Channel Measurements", *Electronics Letters*, Vol. 34, No. 20, pp.1918-1919, October 1998.

[62] L. Dai, D. Rutledge, M. Kovacevic and J. Hacker, "A 24-GHz Active Patch Array with a Power Amplifier / Low Noise Amplifier MMIC," *International Jour. Infrared and Millimeter Waves*, May 2002, pp. 693-704.

[63] T. Wysocki, H.-J. Zepernick ., "Characterization of the Indoor Radio Propagation Channel at 2.4 GHz", *Journal of Telecommunications and Information Technology*, 3-4, 2000, pp. 84-90.

[64] "Propagation Measurements of the 5.2 GHz Radio Band in Commercial and Domestic Environments," *HP Tech Report*, HPL-97-87, No. 970718,

[65] M. Lobeira, A.G. Armada, R.P. Torres and J.L. Garcia , "Channel modeling and characterization at 17GHz for indoor broadband WLAN," IEEE Jour. on Selected Areas in Communications, 20, 2002, pp. 593-601.

[66] S.Y. Seidel and T.S. Rappaport, "914 MHz Path Loss Prediction Model for Indoor Wireless Communications in Multifloor Buildings," *IEEE Trans. Antennas Propagat.*, Vol.40, pp207-217, Feb. 1992.

[67] Intel Labs, "A Path Loss Comparison between the 5 GHz UNII Band (802.11a) and 2.4 GHz ISM Band (802.11b)," http://impulse.usc.edu/resources/802_11a-vs-b_report.pdf.

[68] Adel. A. M. Saleh and Reinaldo A. Valenzuela, "A Statistical Model for Indoor Multipath Propagation," *IEEE Jour. Selected Areas in Communications*, Vol SAC-5, No.2 February 1987.

[69] Li KH, Ingram MA, Van Nguyen A, "Impact of Clustering in Statistical Indoor Propagation Models on Link Capacity," *IEEE Trans on Communications*, 50 (4): 521-523 April 2002.

[70] Xiongwen Zhao, Jarmo Kivinen, Pertti Vainikainen and Kari Skog, "Propagation Characteristics for Wideband Outdoor Mobile Communication at 5.3 GHz," *IEEE Jour. Selected Areas in Communications*, Vol.20, No.3, pp 507-514, April 2002.

[71] Ileana Popescu, Athanasios Kanatas, Evangelos Angelou, Ioan Nafornita, Philip Constantinou, "Applications Of Generalized Rbf-Nn For Path Loss Prediction," *http://citeseer.ist.psu.edu/552751.html*.

[72] H. Ling, R.C. Chou, and S. W. Lee, "Shooting and Bouncing Rays: Calculating the RCS of an Arbitrarily Shaped Cavity," *IEEE Trans Antennas Propagation*, Vol. 37, No.2, pp. 194-205, February 1989.

[73] W. Honcharenko, H.L. Bertoni, J.L. Darling, J.Qian and H.D. Lee, "Mechanism Governing UHF Propagation on Single Floors in Modern Office Buildings,", *IEEE Trans. Vehicular Technology*, VT-41, 4, pp. 496-504, 1992.

[74] T.S. Rappaport, S.Y. Seidel and K.R. Schaubach, "Site-Specific Propagation Prediction for PCS System Design," Chapter 17 in *Wireless Personal Communications*, Kluwer Academic Publishers, 1993.

[75] K.Rizk, A. Mawira, J.F. Wagen and F. Gariol, "Propagation in Urban Microcells with High Rise Buildings", *IEEE VTS 46th Vehicular Tech Conf.*, Atlanta, GA, pp. 859-863, April, 1996.

[76] Geoge Liang and Herry L. Bertoni, "A New Approach to 3-D Ray Tracing for Propagation Prediction in Cities", *IEEE Trans on Antennas and Propagations*, Vol.46, No.6, pp. 853-863, June 1998.

[77] F.A. Agelet et.al, "Efficient Ray-tracing Acceleration Techniques for Radio Propagation Modeling", *IEEE Trans on Vehicular Technology*, Vol.49, No.6, pp.2089-2104, November 2000.

[78] V.V. Varadan, R.D. Hollinger, D.K. Ghodgaonkar and V.K. Varadan, "Free-Space, Broadband Measurements of High-Temperature, Complex Dielectric Properties at Microwave Frequencies," *IEEE Trans. Instrum. Meas.*, vol.40, pp.842-846, Oct. 1991.

[79] Inigo Cuinas and Manuel Garcia Sanchez, "Building Material Characterization from Complex Transmissivity Measurement at 5.8 GHz," *IEEE Trans. Antennas and Propagation, vol.48,* no.8, pp.1269-1271, Aug. 2000.

[80] Kurt Fenske and Devendra Misra, "Dielectric Materials at Microwave Frequencies," *Applied Microwaves and Wireless*, Vol. 12, No. 12, pp. 92-100, October 2000.

[81] R.G. Kouyoumjian and P.H. Pathak, "A Uniform Geometrical Theory of Diffraction for An Edge in a Perfectly Conducting Surface," *Proc. IEEE*, vol. 62, no.11, pp.1448-1461, November 1974.

[82] P.C. Clemmow, “The Plane wave Spectrum Representation of Electromagnetic Fields”, *Pergamon, Elmsford*, NY, 1966.

[83] Rober J. C. Bultitude, P. Melancon, H. Zaghioul, G. Morrison, and M. Prokki, “The Dependence of Indoor Radio Channel Multipath Characteristics on Transmit/Receive Ranges,” *IEEE Jour on Selected Areas in Communications*, Vol.1, No.7, pp. 979-990, Sept. 1993.

[84] L. Nagy and L. Farkas, “Indoor Base Station Location Optimization Using Genetic Algorithms,” *IEEE PIMRC 2000*, vol. 2, 2000, pp. 843–846.

[85] A. Hills, “Large-Scale Wireless LAN design,” *IEEE Communications Magazine*, vol. 39, pp. 98–107, 2001.

[86] M. H. Wright, “Optimization Methods for Base Station Placement in Wireless Applications,” *Proceedings of IEEE Vehicular Technology Conference*, vol. 89, 1998, pp. 11 513–11 517.

[87] M. Kamenetsky and M. Unbehaun, “Coverage Planning for Outdoor Wireless LAN Systems,” *International Zurich Seminar on Broadband Communications,* Access, Transmission, Networking, vol. 49, 2002, pp.1–6.

[88] H.D. Sherali, C.M. Pendyala and T.S. Rappaport, "Optimal Location of Transmitters for Mico-Cellular Radio Communication System Design," *IEEE Jour. Selected Area in Comm.*, Vol.14, pp. 662-673, 1996.

[89] C. Gabriel, *Final report AL/OE-TR-1996-0037*, http://safeemf.iroe.fi.cnr.it/cgi-bin/tissprop/

[90] T.G. Kolda, R.M. Lewis and V. Torczon, "Optimization by Direct Search: New Perspectives on Some Classical and Modern Methods", *SIAM Review*, Vol.45, No.3, pp. 385-482, 2003.

[91] S. Obaysshi, J. Zander, "A body-shadowing model for indoor radio communication environments", *IEEE Trans. Antennas and Propagation*, Vol. 46, No. 6, pp. 920-927, June 1998.

[92] FCC, "Questions and Answers about Biological Effects and Potential Hazards of Radio Frequency Electromagnetic Fields", *OET BULLETIN 56*, Fourth Edition, August 1999.

[93] J.W. McKown and R.L. Hamilton, Jr., "Ray-Tracing as A Design Tool for Radio Networks," *IEEE Network Mag.*, pp. 27-30, Nov. 1991.

[94] S.Y. Tan and H.S. Tan, "A Microcellular Communications Propagation Model Based on the Uniform Theory of Diffraction and Multiple Image Theory," *IEEE Trans. Antennas Propagation*, Vol.44, pp. 1317-1326, Oct. 1996.

[95] R.A. Valenzuela, "Ray Tracing Prediction of Indoor Radio Propagation," in *Proc. 5th IEEE Int. Symp. Personal, Indoor , Mobile Radio Communication*, pp.140-144, Sept. 1994.

[96] L. Piazzi and H.L. Bertoni, "Achievable Accuracy of Site-Specific Path Loss Predictions in Residential Environments," *IEEE Trans. Vehicle Technology*, Vol.48, pp. 922-930, May 1999.